

Magazine of Civil Engineering

107(7), 2021

ISSN
2712-8172





ПОЛИТЕХ
Санкт-Петербургский
политехнический университет
Петра Великого

Инженерно-строительный институт
Центр дополнительных профессиональных программ
195251, г. Санкт-Петербург, Политехническая ул., 29,
тел/факс: 552-94-60, www.stroikursi.spbstu.ru,
stroikursi@mail.ru

**Приглашает специалистов организаций, вступающих в СРО,
на курсы повышения квалификации (72 часа)**

Код	Наименование программы	Виды работ*
Курсы по строительству		
БС-01-04	«Безопасность и качество выполнения общестроительных работ»	п.1,2, 3, 5, 6, 7, 9, 10, 11, 12, 13, 14
БС-01	«Безопасность и качество выполнения геодезических, подготовительных и земляных работ, устройства оснований и фундаментов»	1,2,3,5
БС-02	«Безопасность и качество возведения бетонных и железобетонных конструкций»	6,7
БС-03	«Безопасность и качество возведения металлических, каменных и деревянных конструкций»	9,10,11
БС-04	«Безопасность и качество выполнения фасадных работ, устройства кровель, защиты строительных конструкций, трубопроводов и оборудования»	12,13,14
БС-05	«Безопасность и качество устройства инженерных сетей и систем»	15,16,17,18,19
БС-06	«Безопасность и качество устройства электрических сетей и линий связи»	20,21
БС-08	«Безопасность и качество выполнения монтажных и пусконаладочных работ»	23,24
БС-12	«Безопасность и качество устройства мостов, эстакад и путепроводов»	29
БС-13	«Безопасность и качество выполнения гидротехнических, водолазных работ»	30
БС-14	«Безопасность и качество устройства промышленных печей и дымовых труб»	31
БС-15	«Осуществление строительного контроля»	32
БС-16	«Организация строительства, реконструкции и капитального ремонта. Выполнение функций технического заказчика и генерального подрядчика»	33
Курсы по проектированию		
БП-01	«Разработка схемы планировочной организации земельного участка, архитектурных решений, мероприятий по обеспечению доступа маломобильных групп населения»	1,2,11
БП-02	«Разработка конструктивных и объемно-планировочных решений зданий и сооружений»	3
БП-03	«Проектирование внутренних сетей инженерно-технического обеспечения»	4
БП-04	«Проектирование наружных сетей инженерно-технического обеспечения»	5
БП-05	«Разработка технологических решений при проектировании зданий и сооружений»	6
БП-06	«Разработка специальных разделов проектной документации»	7
БП-07	«Разработка проектов организации строительства»	8
БП-08	«Проектные решения по охране окружающей среды»	9
БП-09	«Проектные решения по обеспечению пожарной безопасности»	10
БП-10	«Обследование строительных конструкций и грунтов основания зданий и сооружений»	12
БП-11	«Организация проектных работ. Выполнение функций генерального проектировщика»	13
Э-01	«Проведение энергетических обследований с целью повышения энергетической эффективности и энергосбережения»	
Курсы по инженерным изысканиям		
И-01	«Инженерно-геодезические изыскания в строительстве»	1
И-02	«Инженерно-геологические изыскания в строительстве»	2,5
И-03	«Инженерно-гидрометеорологические изыскания в строительстве»	3
И-04	«Инженерно-экологические изыскания в строительстве»	4
И-05	«Организация работ по инженерным изысканиям»	7

*(согласно приказам Минрегионразвития РФ N 624 от 30 декабря 2009 г.)

**По окончании курса слушателю выдается удостоверение о краткосрочном повышении
квалификации установленного образца (72 ак. часа)**

Для регистрации на курс необходимо выслать заявку на участие, и копию диплома об образовании по телефону/факсу: 8(812) 552-94-60, 535-79-92, , e-mail: stroikursi@mail.ru.

Magazine of Civil Engineering

SCHOLAR JOURNAL

ISSN 2712-8172

Свидетельство о государственной регистрации:
Эл № ФС77-77906 от 19.02.2020,
выдано Роскомнадзором

Специализированный научный журнал.

Выходит с 09.2008.

Включен в Перечень ВАК РФ

Индексируется в БД Scopus

Периодичность: 8 раз в год

Учредитель и издатель:

Санкт-Петербургский политехнический университет
Петра Великого

Адрес редакции:

195251, СПб, ул. Политехническая, д. 29

Главный редактор:

Екатерина Александровна Линник

Научный редактор:

Виталий Владимирович Сергеев

Заместитель главного научного редактора:

Галина Леонидовна Козинец

Редакционная коллегия:

PhD, проф. Т. Аввад;
д.т.н., проф. М.И. Бальзанников
д.т.н., проф. А.И. Белостоцкий;
к.т.н., проф. А.И. Боровков;
д.т.н., проф. А. Бородинец;
PhD, проф. М. Велькович;
PhD, проф. Р.Д. Гарг;
PhD, М.Р. Гарифуллин;
Dr.-Ing, проф. Т. Грис;
д.т.н., проф. Т.А. Дацюк;
д.т.н., проф. В.В. Елистратов;
Dr.-Ing., проф. Т. Кэрки;
д.т.н., проф. Д.В. Козлов;
д.т.н., доцент С.В. Корниенко;
д.т.н., проф. Ю.Г. Лазарев;
д.т.н., проф. М.М. Мухаммадиев;
Dr.-Ing. Habil., проф. Х. Пастернак;
Dr.-Ing., проф. Ф. Рёгинер;
д.т.н., проф. Т.З. Султанов;
д.т.н., проф. М.Г. Тягунов;
акад. РАН, д.т.н., проф. М.П. Федоров;
Dr.-Ing., проф. Д. Хецк;
д.г.-м.н. А.Г. Шашкин;
д.т.н. В.Б. Штильман

Дата выхода: 30.11.2021

© ФГАОУ ВО СПбПУ, 2021

© Иллюстрация на обложке: Илья Смагин

Magazine of Civil Engineering

SCHOLAR JOURNAL

ISSN 2712-8172

Peer-reviewed scientific journal

Start date: 2008/09

8 issues per year

Publisher:

Peter the Great St. Petersburg Polytechnic University

Indexing:

Scopus, Web of Science (ESCI, RSCI), Compendex,
EBSCO, Google Academia, Index Copernicus, ProQuest,
Ulrich's Serials Analysis System, CNKI

Corresponding address:

29 Polytechnicheskaya st., Saint-Petersburg, 195251,
Russia

Editor-in-chief:

Ekaterina A. Linnik

Science editor:

Vitaly V. Sergeev

Deputy chief science editor:

Galina L. Kozinetc

Editorial board:

T. Awwad, PhD, professor
M.I. Balzannikov, D.Sc., professor
A.I. Belostotsky, D.Sc., professor
A.I. Borovkov, PhD, professor
A. Borodinecs, Dr.Sc.Ing., professor
M. Veljkovic, PhD, professor
R.D. Garg, PhD, professor
M. Garifullin, PhD, postdoctorant
T. Gries, Dr.-Ing., professor
T.A. Datsyuk, D.Sc., professor
V.V. Elistratov, D.Sc., professor
T. Kärki, Dr.-Ing., professor
D.V. Kozlov, D.Sc., professor
S.V. Korniyenko, D.Sc., professor
Yu.G. Lazarev, D.Sc., professor
M.M. Muhammadiev, D.Sc., professor
H. Pasternak, Dr.-Ing.habil., professor
F. Rögener, Dr.-Ing., professor
T.Z. Sultanov, D.Sc., professor
M.G. Tyagunov, D.Sc., professor
M.P. Fedorov, D.Sc., professor
D. Heck, Dr.-Ing., professor
A.G. Shashkin, D.Sc.
V.B. Shtilman, D.Sc.

Date of issue: 30.11.2021

© Peter the Great St. Petersburg Polytechnic University.
All rights reserved.

© Coverpicture – Ilya Smagin

Contacts:

E-mail: mce@spbstu.ru

Web: <http://www.engstroy.spbstu.ru>

Contents

Ponomarenko, A.A. Technogenic anhydrite binder for high-strength concrete	10701
Alkhalwaldeh, A., Al-Rousan, R. Behavior of RC beams with different bond strength	10702
Mai, V.C., Luu, X. B., Nguyen, V. T. Ultra High-Performance Fiber Reinforced Concrete panel subjected to high velocity impact	10703
Solovyev, S.A., Soloveva, A.A. Structural reliability analysis using evidence theory and fuzzy probability distributions	10704
Yurchenko, V.V., Peleshko, I.D. Methodology for solving parametric optimization problems of steel structures	10705
Serpik, I.N., Shkolyarenko, R.O. Algorithm of correcting bimoments in calculations of thin-walled bar systems	10706
Tyukalov, Yu.Ya. Arbitrary quadrangular finite element for plates with shear deformations	10707
Tarasevsky, P.G., Badenko, V.L., Goryunov, I.V. The open flow damper in effluent control system	10708
Musorina, T.A., Zaborova, D.D., Petrichenko, M.R., Stolyarov, O.N. Flexural properties of hogweed chips reinforced cement composites	10709
Ibrahim, M., Nasir, M., Hussaini, S.R., Najamuddin, S.K., Ewebajo, A.O. Performance of structurally viable green concrete derived from natural pozzolan and nanosilica	10710
Nguyen, S., Thai, Q., Ho, L. Properties of fine-grained concrete containing fly ash and bottom ash	10711
Semenov, A.S., Grishchenko, A.I., Artiukh, V.G., Melnikov, B.E. Long-term strength of polyethylene pipes with increased temperature resistance without reinforcement	10712
Schreiberova, H., Trtik, T., Chylik, R., Prosek, Z., Seps, K., Fladr, J., Bily, P., Kohoutkova, A. Self-healing in cementitious composite containing bacteria and protective polymers at various temperatures	10713
Al-Kutti, W.A., Chernykh, T.C. An isotropic damage model to simulate failure in reinforced concrete beam	10714
Kozin, A.V., Fediuk, R.S., Yarusova, S.B., Gordienko, P.S., Lesovik, V.S., Mosaberpanah, M.A., Mugahed Amran, Y.A., Murali, G. Improvement of mechanical characteristics of mortar by using of wollastonite	10715



DOI: 10.34910/MCE.107.1

Technogenic anhydrite binder for high-strength concrete

A.A. Ponomarenko 

Ural Federal University named after first president of Russia B.N. Yeltsin, Ekaterinburg, Russia

E-mail: ponfox@mail.ru

Keywords: hydrofluoric acid, slags, fly ash, grinding (machining), setting, compressive strength, strength of material, concretes

Abstract. Currently the global trend is to expand the range of construction materials produced using resource-saving technologies that do not generate CO₂ emissions. An important role in this is given to gypsum-anhydrite binders and concretes which can be obtained using a non-burning technology with the involvement of technogenic wastes which excludes the emission of carbon dioxide into the environment in comparison with Portland cement technology. The article is devoted to the results of studies on obtaining anhydrite binder from the by-product of sulfuric acid decomposition of fluorite concentrate – fluorine-anhydrite using other by-products of industry (metallurgical, mining and heat power) acting as active mineral additives. The influence patterns of such additives composition and quantity on the kinetics of milling and neutralization of fluorine-anhydrite are established. It is shown that the milling capacity of the anhydrite binder depends on the degree of binding of the acid component as well as the stoichiometry of chemical reactions between sulfuric acid contained in fluorine-anhydrite and additives minerals. The process of the acid component binding proceeds most actively with the addition of steel-refining slag in an amount of 12.3 % which allows to achieve a high milling rate of the binder. The resulting products of neutralization reactions are centers of crystallization which increases the hydraulic activity of fluorine-anhydrite. As a result, anhydrite binder comparable to Portland cement by physical and mechanical properties have been obtained. This binder is suitable for producing high-strength concrete of B30 class in which granules from neutralized fluorine-anhydrite are used as a coarse aggregate. Thus, the study made an important contribution to the material science of technogenic materials expanding their use in construction.

1. Introduction

One of the most important directions in the construction materials science is the production of clinker-free binders as well as concretes based on them excluding the use of Portland cement which is produced by material-intensive and energy-consuming technology. At the same time a significant reduction in the construction cost is achieved due to significant resource and energy savings. Gypsum and gypsum-anhydrite binders are materials which characterized by low energy consumption in production and better environmental performance compared to Portland cement. Special attention among them is given to non-fired anhydrite cement obtained from a by-product of sulfuric acid decomposition of fluorite concentrate – fluorine-anhydrite (FA) formed in enterprises of various industries (chemical, nuclear and non-ferrous metallurgy). The FA use in construction is constrained by the lack of information about its composition and properties depending on the formation conditions as well as the presence of harmful impurities in the form of sulfuric acid and chemically active fluorine compounds. Therefore it is very prospectively to study the influence of the decomposition mode of fluorine-containing raw materials on composition and properties of FA and also to transform impurities contained in the FA which are harmful to the quality of the binder and enterprises staff and in a useful and environmentally safe one. Similar studies were carried out to get a binder from phosphogypsum using the technologies of Nissan Chemical (Japan) and Central Prayon (France) which allow to decompose phosphate raw materials in such a way that the precipitate of calcium sulfate is recycled into construction materials with cost-effective and technically effective technologies similar to natural gypsum raw materials [1–3].

Ponomarenko, A.A. Technogenic anhydrite binder for high-strength concrete. Magazine of Civil Engineering. 2021. 107(7). Article No. 10701. DOI: 10.34910/MCE.107.1

© Ponomarenko, A.A., 2021. Published by Peter the Great St. Petersburg Polytechnic University.



This work is licensed under a [CC BY-NC 4.0](https://creativecommons.org/licenses/by-nc/4.0/)

Gashkova V.I., Tolkacheva L.E. also propose to consider the process of FA obtaining not as the formation of wastes but the formation of a semi-product with properties that meet the requirements of the appropriate standards for raw materials of construction use. However they found that obtaining two high-quality products namely HF and FA simultaneously in one technological cycle is impossible [4]. In this regard the FA utilization can be carried out only separately from the main process of decomposition of fluorine-containing raw materials. According to many researchers for this purpose various mineral and chemical additives can be used; they can neutralize the acidic component of FA, activate its hardening as well as reinforce the structure and increase the water resistance of technogenic anhydrite binder for its use in concrete [5–22]. But in these works there is no single approach justifying the choice of certain additives and the method of their introduction to obtain a binder from FA suitable for high-strength concrete. According to this paper such approach should be based on the understanding and choice of external energy effects on the FA in accordance with the combined laws of thermodynamics providing five types of energy effects aimed at reducing the free energy of the system: mechanical, additional milling leading to the formation of a new surface, chemical, electro-physical and thermal. As it is known the lower the value of free energy the more work is performed by the cement system during hardening and the stronger the formed concrete structure [23]. Technogenic materials containing metastable phases in which a large amount of energy is accumulated fully correspond to this criterion.

Based on the thermodynamic approach the activation of FA during its mechanical-chemical treatment with the use of technogenic mineral additives of different composition neutralizing the acidic component and being the centers of crystallization of new formations during hardening of the binder, providing high strength of concrete on its basis was investigated.

The aim of present work is to investigate the possibility of obtaining of anhydrite binder using mineral additives which are technological wastes of various industries and high-strength concrete based on it.

To achieve this goal the following tasks were solved:

1. to determine the composition and properties of FA as well as mineral additives to neutralize it;
2. to study the kinetics of milling and neutralization of FA in joint milling with mineral additives;
3. to determine the physical and mechanical properties of the binder based on neutralized FA;
4. to obtain artificial porous aggregate for concrete on the basis of fluorine-anhydrite and mineral additive;
5. to determine the properties of the resulting aggregate;
6. to prepare the concrete mix, to mold the samples and to determine the concrete properties.

2. Methods

Anhydrite binder was obtained by joint milling of acidic fluorine-anhydrite (FA) with mineral additives in a laboratory ball mill. During the milling process samples were taken at regular intervals and were exposed for determination of the content of free sulfuric acid, calcium fluoride and dispersion. Milling was carried out in a mill of 5.5 liters volume. Dispersion was controlled by the residue on the sieve No. 008 (not more than 10 %). The kinetics of milling and neutralization of acidic FA with mineral additives was studied using formal kinetics equations:

$$R_{\tau} = R_o \cdot e^{-k_1 \tau^m}, \quad (1)$$

$$\alpha = 1 - e^{-k_2 \tau^n}, \quad (2)$$

where R_{τ} is the content of the coarse fraction in the material through time τ , %;

R_o is the content of coarse fraction in the initial material, %;

k_1 is the milling rate constant, $\text{min}^{\text{is}1}$;

m is the relative milling rate;

τ is milling time, min;

α is degree of neutralization;

k_2 is the reaction rate constant, $\text{min}^{\text{is}1}$;

n is kinetic parameter.

Steel-refining slag, ferrochrome slag, fly ash and limestone crushing screening formed at the crushing and grinding complex of microcalcite production were used as mineral additives.

The chemical composition of acidic FA was determined by the methods of Russian State Standards GOST 5382-9, 19181-78, 7619.5-81 and 7619.6-8; the quantity of crystallization water in FA – according to Russian State Standard GOST 4013-82 (after removal of sulfuric acid with alcohol). Determination of sulfuric acid content in FA is based on its neutralization by sodium hydroxide in an alcohol solution in the presence of methyl red indicator. The FA sample dried to a constant mass in an amount of 40–50 g was crushed until it completely passed through a sieve No. 008; 0.5 g of powder was taken from it (up to a quarter of the decimal point) and was placed in a dry glass with a volume of 100 cm³. 10 cm³ of ethyl alcohol was poured into it, an indicator was added until the bright red coloring of the solution which was periodically stirred for 10 minutes and then titrated with a NaOH solution until the color transition from red to yellow-green. The arithmetical mean of two parallel tests was taken as the result of the analysis, the permissible difference between them should not exceed 0.15 % with a variation coefficient of 0.95.

The quantity of sulfuric acid (W) was calculated by the formula:

$$W = \left(\frac{V \cdot K \cdot 0.004904 \cdot 100}{m} \right), \quad (3)$$

where V is the volume of sodium hydroxide solution of 0.1 mol/dm³ concentration which was used to titration of the tested solution, cm³;

K is the correction to the titer of a solution of NaOH;

0.004904 is the mass of sulfuric acid corresponding to 1 cm³ of sodium hydroxide solution with a concentration of exactly 0.1 mol/dm³, g;

m is mass of the sample to be tested, g.

The quantity of CaSO₄ in FA was determined by the CaO quantity obtained from the difference between the content of total CaO (according to chemical analysis) and CaO associated with fluorine. The fluorine ion is determined by potentiometric titration.

The FA macrostructure was studied using a Levenhuk 2ST binocular microscope with a photo-nozzle. Electronic-microscopic studies were carried out on a scanning electron microscope JSM 6490 with specialized SEM and micro X-ray diffraction analysis tools. The image of the FA structure was obtained in the following mode: back-scattered electrons, the pressure in the chamber is 100 Pa, the accelerating voltage on the gun is 20 kV, the beam length is 60 nm.

The chemical composition of mineral additives was determined according to Russian State Standard GOST 5382-2019, as well as using the electronic-raster device “Superprobe 733” by “Joel” company with the box for energy dispersion analysis. Determination of the mineral composition of slag and ash was performed by the method based on the complete solubility of two- and tricalcium silicates and free lime in a 5 % solution of boric acid and on insolubility of the intermediate phase. 10 % aqueous solution of sugar completely decomposes calcium aluminates and lime soluble in sugar during the treatment of residue insoluble in boric acid corresponds to CaO bound in calcium aluminates.

The quantity of mineral additives taken to FA neutralization was calculated taking into account stoichiometry of chemical reactions of interaction of minerals with sulfuric acid. The possibility of reactions was estimated by the Gibbs energy.

The granulometric composition of the raw materials was determined according to Russian State Standard GOST 8269.0-97, the open, total porosity and apparent density – according to Russian State Standard GOST 2409-2014, the true density by pycnometrical method, bulk density – according to Russian State Standard GOST 9758-2012, the specific surface – by Blaine and BET method.

The hardening kinetics of the samples, the composition of the hydration and neutralization products were controlled by x-ray phase analysis (XPA), differential thermal analysis (DTA) and SEM. XPA was carried out at the DRON-3 device by the following mode: cobalt radiation (with an iron filter), 2θ from 10 to 50°, 2 s accumulation time, 35 kV voltage, 20 mA anode current were used. Differential thermal analysis was performed on the Q-1500 device under the following conditions: material mass – 200 mg, crucible material – Pt, reference substance – Al₂O₃, sensitivity – 200 units, maximum temperature – 1000 °C, heating rate – 10 °C/min.

Physical and mechanical properties of the binder based on neutralized FA were determined using mortar with normal sand (1:3) according to DIN 4208 and the addition of 0.3 % superplasticizer Melment F15G produced by “BASF Construction Solutions” (Trostberg, Germany) together with mixing water. Further the FA neutralized with a mineral additive was used as a binder for the concrete preparation. Natural quartz sand with a size modulus of 2.5 according to Russian State Standard GOST 8736-2014 was used as a fine aggregate. Granules on the basis of the binding mix consisting of FA and neutralizing mineral additive taken in certain

proportions were a coarse aggregate. Granules were obtained on a disc granulator having a bowl diameter of 0.7 m and tilt angle to the horizon of 45°. 10 kg of binding mix were used to obtain granules of 8–10 mm in quantity not less than 90 %, aqueous solution of superplasticizer been added during granulation. The granules mentioned above hardened in air-wet conditions. The properties of granules were determined according to Russian State Standard GOST 9758-2012 and then they were used as an aggregate in the concrete composition. The concrete mix was formed into samples-cubes with an edge of 70 mm. The mobility grade was P2 (5–9 cm) according to Russian State Standard GOST 7473-2010. Physical and mechanical tests of concrete were carried out in accordance with the requirements of Russian State Standard GOST 26633-2015. The coefficient of constructive quality was calculated as relation of the strength and density of concrete.

3. Results and Discussion

The composition and properties of FA selected from a revolving drum furnace with a diameter of 3.2 m, a length of 50 m with internal heating are shown in Table 1. The material temperature at the furnace outlet was 200 °C.

Table 1. The composition and the properties of FA for conditioning.

Fractions quantity, mass %, mm				Material composition of fractions, mass %			Apparent density, kg/m ³	Open porosity, %	Total porosity, %	Closed porosity, %
1-5	5-20	20-40	40-60	CaSO ₄	H ₂ SO ₄	CaF ₂				
30.0	–	–	–	93.20	5.80	1.00	2100	27.8	28.1	0.3
–	22.2	–	–	92.90	5.10	2.00	2285	21.1	21.7	0.6
–	–	18.0	–	86.23	6.77	3.00	2300	14.2	20.6	6.4
–	–	–	30.0	89.92	6.08	4.00	2350	10.8	19.5	8.7

It is established that FA from the furnace is a granular material. It has a grain size of 1–60 mm, with a total porosity of 19.5–28.1 %, a free sulfuric acid content of 5.1–6.7 %, and 1–4 % calcium fluoride. X-ray phase analysis showed that calcium sulfate in FA is represented by a low-activity modification – insoluble anhydrite (β -CaSO₄) ($d = 3.50; 2.84 \text{ \AA}$). Lines belonging to CaSO₄·2H₂O and γ -CaSO₄ (soluble anhydrite) were not found. It was found that when FA is heated in the temperature range of 100–400 °C, two phase transitions are observed on the derivatogram; these transitions are accompanied by endothermic effects and mass changes of the sample: the first – in the temperature range of 120–169 °C (mass loss is 2.6 and 4.0 %) and the second – in the range of 234–310 °C (mass loss is 6.0 %), Fig. 1(1).

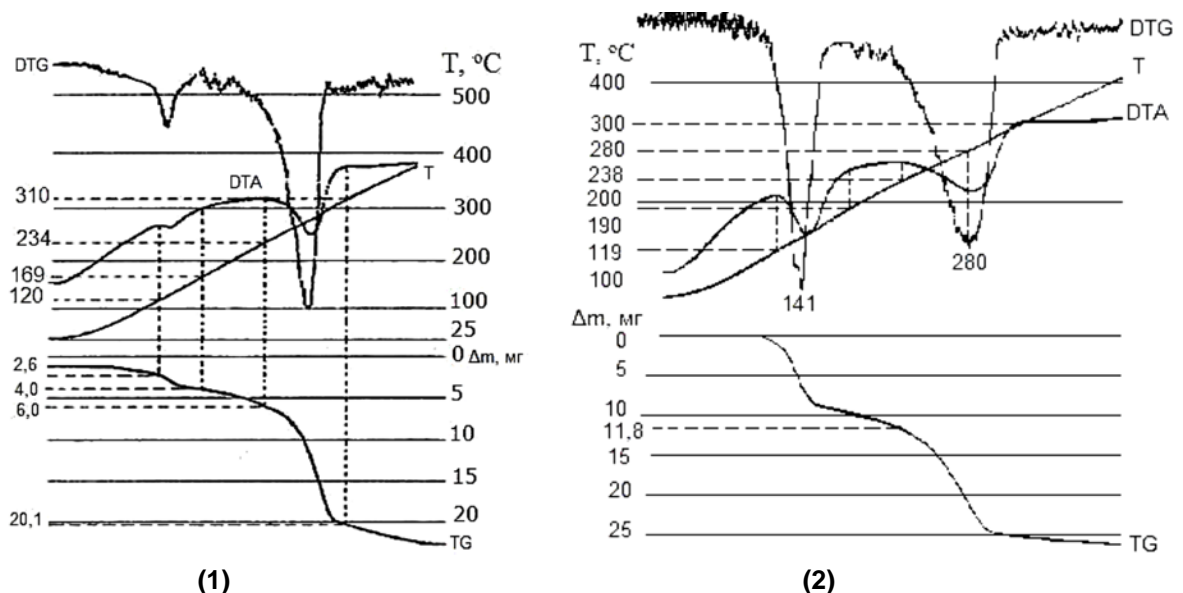


Figure 1. Results of DTA of FA from furnace (1) and fluorine-anhydrite stone at the age of 28 days of air hardening (2).

The first phase transition is associated with the desorption of moisture from the surface of the FA and the evaporation of fluorosulfonic acid (HSO₃F) and the second – with the evaporation of free sulfuric acid and the decomposition of calcium fluoro-sulfonate (Ca(SO₃F)₂). When mixing water with the powder of acidic FA of specific surface area of 200 m²/kg a paste of 42 % normal density is formed, its initial setting time is after 14 h and the final setting time is after 17 h. Fluorine-anhydrite stone slowly hardens in the early stages but it has a compressive strength of 3-5 MPa by 28 days. According to DTA hardened acidic FA has an endothermic effect at 141 °C associated with the decomposition of dihydrous gypsum to semi-aqueous and an endothermic

effect at 280 °C indicating the removal of the rest of the crystallization water from semi-aqueous gypsum and the formation of anhydrous calcium sulfate. Also at 310 °C free sulfuric acid evaporates, Fig. 1(2).

Fig. 2 shows the macrostructure and microstructure of the original FA. Channel and isometric pores located randomly are mainly dominated. The length of the channel pores is from 188 to 1000 microns and their diameter is from 63 to 178 microns. The number of isometric pores are as follows, %: 40–57 – less than 60 microns, 35–45 – from 60 to 125 microns, 5–10 – from 60 to 310 microns, 3–5 – more than 310 microns. It was found that part of the pores in the FA were filled with a white substance presumably calcium fluoro-sulfonate.

According to the SEM data the FA of the current output has a loose-grained rather homogeneous structure composed of prismatic anhydrite crystals of 1-4 microns size, Fig. 3.

Thus the FA of the current output is represented by granules of inhomogeneous composition, it contains a significant amount of insoluble anhydrite, sulfuric acid as well as impurities of hydraulically inert calcium fluoride and easily volatile calcium fluoro-sulfonate. Acidic FA has weak binder properties so it is necessary to neutralize the acidic component to improve them and increase the environmental safety of the material for its use in construction. For this purpose mineral additives were used; its chemical composition, physical and hydrophysical properties are presented in Tables 2-3.

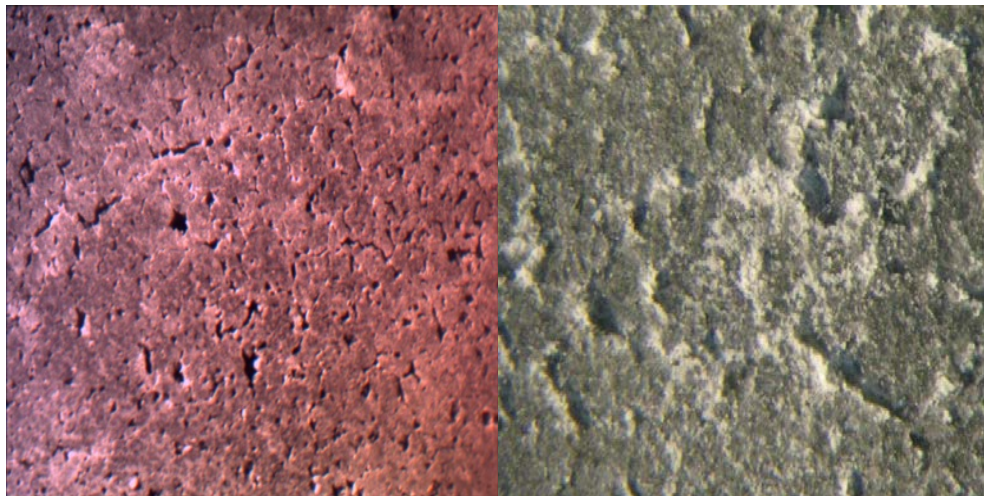


Figure 2. FA macrostructure (×16, ×40).

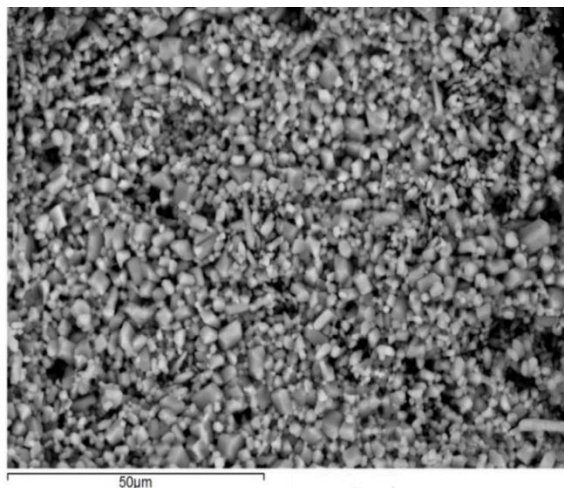


Figure 3. FA microstructure.

Table 2. Chemical composition of mineral additives

Additive	The content of oxides, mass %								Loss of ignition, mass %
	CaO	SiO ₂	Al ₂ O ₃	Fe ₂ O ₃	MgO	SO ₃	R ₂ O	Other	
Refining slag	43.27	15.14	27.16	0.86	5.93	4.70	0.07	2.24	+0,63
Ferrochrome slag	50.90	26.10	5.83	0.83	8.79	–	–	5.74	1.81
Fly ash	36.00	31.30	6.16	11.54	6.25	2.36	–	0.92	5.45
Limestone crushing screening	50.40	3.53	0.63	0.33	1.92	0.06	0.42	0.79	41.92

Table 3. Physical and hydrophysical properties of mineral additives.

Additive	Granulometric composition, mass %			ρ , kg/m ³	W/S, %	Setting time, min	
	of fractions, mm					initial	final
	0.16-0.315	0.08-0.16	<0.08				
Refining slag	3.3	33.4	63.3	2846	38	8	30
Ferrochrome slag	2.1	32.3	65.6	2790	42	720	1440
Fly ash	–	28.1	71.9	2600	50	30	50
Limestone crushing screening	–	13.9	86.1	2720	–	–	–

Mineral additives are basic by chemical composition. According to XPA the crystalline phase of refining slag contains $12\text{CaO} \cdot 7\text{Al}_2\text{O}_3$ ($d = 4.90; 2.68; 2.19 \text{ \AA}$), β - and γ - C_2S ($d = 4.06; 3.22; 2.78 \text{ \AA}$) and MgO ($d = 2.11 \text{ \AA}$). The actual phase composition of this slag is 43.2 % $12\text{CaO} \cdot 7\text{Al}_2\text{O}_3$; 31.5 % $2\text{CaO} \cdot \text{SiO}_2$; 5.9 % MgO and 18.0 % vitreous phase. Ferrochrome slag mainly consists of β - C_2S ($d = 5.60; 3.01; 2.73 \text{ \AA}$), a solid solution of the composition $(\text{Mg}, \text{Fe})(\text{Cr}, \text{Al}, \text{Fe})_2\text{O}_4$ ($d = 4.77; 2.48 \text{ \AA}$), periclase ($d = 2.11 \text{ \AA}$) and okermanite ($d = 2.67; 2.21 \text{ \AA}$) which is typical for ferrochrome slag of low-carbon ferrochrome. Fly ash contains bicalcium silicate ($b = 3.49; 2.76; 2.68 \text{ \AA}$), ferromagnetic spinel ($d = 2.97; 2.57 \text{ \AA}$), quartz ($b = 3.34 \text{ \AA}$) and free calcium oxide ($b = 2.39; 2.76 \text{ \AA}$).

However it was found that the amount of bicalcium silicate in fly ash is less than in metallurgical slags. Limestone crushing screening contains calcite with quartz admixture. Metallurgical slags and fly ash have different water demand and setting time when mixing with water. The amount of mineral additives taken to neutralize sulfuric acid and calculated taking into account the thermodynamics and stoichiometry of chemical reactions according to the equations presented in Table 4 was as follows, %: 12.3 of refining slag; 13.4 of ferrochrome slag; 24.8 of fly ash and 6.1 of limestone crushing screening.

Table 4. Results of thermodynamic calculation of enthalpy and Gibbs energy of formation of possible products of sulfuric acid neutralization from minerals of metallurgical slags, fly ash and limestone crushing screening in the system "FA-mineral additive".

No	The chemical reaction of neutralization	The calculated ΔH°_{298} , kJ/mol H_2SO_4	The calculated ΔG°_{298} , kJ/mol H_2SO_4
1	$\text{C}_{12}\text{A}_7(\text{sol.}) + 6\text{H}_2\text{SO}_4(\text{liq.}) + 71\text{H}_2\text{O}(\text{gas.}) \rightarrow 2\text{C}_3\text{AC}\hat{\text{S}}_3\text{H}_{31}(\text{sol.}) + 10\text{AH}_3(\text{sol.})$	-477	-344
2	$\text{C}_{12}\text{A}_7(\text{sol.}) + 3\text{H}_2\text{SO}_4(\text{liq.}) + 45\text{H}_2\text{O}(\text{liq.}) \rightarrow 3\text{C}_3\text{AC}\hat{\text{S}}\text{H}_{12}(\text{sol.}) + 8\text{AH}_3(\text{am.})$	-655	-430
3	$\text{C}_{12}\text{A}_7(\text{sol.}) + 12\text{H}_2\text{SO}_4(\text{liq.}) + 33\text{H}_2\text{O}(\text{liq.}) \rightarrow 12\text{C}\hat{\text{S}}\text{H}_2(\text{sol.}) + 14\text{AH}_3(\text{am.})$	-312	-264
4	$\text{C}_2\text{S}(\text{sol.}) + \text{H}_2\text{SO}_4(\text{liq.}) + 2\text{H}_2\text{O}(\text{r.}) \rightarrow \text{C}\hat{\text{S}}\text{H}_2(\text{sol.}) + \text{CSH}(\text{sol.})$	-713	-581
5	$\text{MgO}(\text{sol.}) + \text{H}_2\text{SO}_4(\text{liq.}) \rightarrow \text{MgSO}_4(\text{sol.}) + \text{H}_2\text{O}(\text{gas.})$	-67	-131
6	$\text{MgFe}_2\text{O}_4(\text{sol.}) + 4\text{H}_2\text{SO}_4(\text{liq.}) \rightarrow \text{MgSO}_4(\text{sol.}) + \text{Fe}_2(\text{SO}_4)_3(\text{sol.}) + 4\text{H}_2\text{O}(\text{gas.})$	-20	-19
7	$\text{CaCO}_3(\text{sol.}) + \text{H}_2\text{SO}_4(\text{liq.}) \rightarrow \text{C}\hat{\text{S}}\text{H}_2(\text{sol.}) + \text{CO}_2(\text{gas.}) + \text{H}_2\text{O}(\text{gas.})$	-65	-127
8	$2\text{Al}(\text{OH})_3(\text{sol.}) + 3\text{H}_2\text{SO}_4(\text{liq.}) \rightarrow \text{Al}_2(\text{SO}_4)_3(\text{sol.}) + 6\text{H}_2\text{O}(\text{liq.})$	-82	-91
9	$\text{Mg}(\text{OH})_2(\text{sol.}) + \text{H}_2\text{SO}_4(\text{liq.}) \rightarrow \text{MgSO}_4(\text{sol.}) + 2\text{H}_2\text{O}(\text{liq.})$	-41	-30

Table 4 shows that lower Gibbs energy values by 1 mole of H_2SO_4 correspond to reactions (4) and (2) the products of which are dihydrate calcium sulfate and calcium hydrosulfoaluminate in monosulfate form. This paper suggests that these compounds can serve as centers of crystallization of new formations in particular secondary dihydrous gypsum during the hardening of neutralized FA having a positive effect on its binding properties. However to obtain thermodynamically stable centers of new formations crystallization at least two conditions are to be met. In accordance with the statements of the classical theory of the process of new phase nucleation described by equations (4) and (5) the formation of stable crystallization centers is possible; firstly, if the surface of the phase boundaries is large and secondly, the size of the crystal germ should reach the limit value at which the effective crystallization of new formations is provided. The joint milling of acidic FA with mineral additives is satisfied by these two conditions.

$$P = C \cdot \exp \left[- \frac{16\pi \cdot \sigma^3 \cdot M^3 \cdot N_A}{3R^3 \cdot T^3 \cdot \ln^2 \left(\frac{c}{c_\infty} \right) \cdot p^2} \right], \quad (4)$$

$$\ln \frac{C}{C_{\infty}} = \frac{2M \cdot \sigma}{R \cdot T \cdot \rho \cdot r_{\kappa}}, \quad (5)$$

where P is possibility of formation of an equilibrium crystal germ;

C is constant;

M is molar mass;

c is solubility of small crystals;

c_{∞} is solubility of large crystals;

σ is the specific interfacial energy;

N_A is Avogadro number;

r_{κ} is the critical radius of the crystal germ;

ρ is the density of the solid phase;

R is gas constant;

T is temperature.

When studying the kinetics of milling and neutralization of FA with mineral additives it was found that refining and ferrochrome slag and fly ash introduced into FA in stoichiometric quantities provide a high degree of H_2SO_4 neutralization which was equal to 92.0; 73.4 and 71.8 % respectively. Herewith the rate constants of material milling and sulfuric acid neutralization were 0.344; 0.279; 0.119 and 0.848; 0.435; 0.323 min^{-1} respectively. With the introduction of limestone crushing screening in stoichiometric amount the degree of H_2SO_4 neutralization was 41 % and the constant of the milling rate of FA and the neutralization of sulfuric acid in it was 0.075 and 0.137 min^{-1} respectively. It is seen from the experimental data that metallurgical slags especially refined one react most intensively with sulfuric acid because the acid content after FA milling decreased from 6.10 to 0.48 %. The reason is that the refining slag contains a chemically active and easily milling mineral $C_{12}A_7$ for which the Gibbs energy of interaction with sulfuric acid by 1 mol of H_2SO_4 is from -264 to -430 kJ. When using ferrochrome slag less intensive acid neutralization and milling rate are due to that it mainly contains of hard-to-mill C_2S , okermanite and a solid solution of the composition (Mg, Fe)(Cr, Al, Fe) $_2O_4$ and does not contain chemically active and easy-to-mill $C_{12}A_7$. Fly ash and limestone crushing screening have a low ability to neutralize sulfuric acid during joint milling with FA because the amount of chemically active mineral C_2S in the ash was about 2-3 times less than in metallurgical slags and the surface of free CaO particles in the ash is covered with a vitreous phase that limits the binding of sulfuric acid. In addition the interaction of sulfuric acid with minerals MgO·Fe $_2O_3$, MgO of ash and CaCO $_3$ of limestone crushing screening according to reactions (5)–(7) is less thermodynamically probable compared to calcium-containing minerals of metallurgical slags.

The quantity of CaF $_2$ in the ground FA with the addition of refining slag increased from 2.3 to 3.4 % what indicates the neutralization of HF which may be formed by the interaction of heated water vapor released during the binding of sulfuric acid with HSO $_3$ F and Ca(SO $_3$ F) $_2$.

Thus it can be concluded that there is an interrelation between the Gibbs energy of chemical reactions, the rate of neutralization of sulfuric acid (neutralization degree) in FA as well as the composition of mineral additives. The lower the Gibbs energy of the interaction reactions of minerals with sulfuric acid of FA the greater the work performed by the system and the more intensively the acid is neutralized during the FA milling.

The presence of dihydrous gypsum ($d = 7.63; 4.29 \text{ \AA}$) and calcium hydrosulphaluminate ($d = 5.63; 2.61 \text{ \AA}$) in FA milling together with refining slag was established by XPA (Fig. 4) what confirms the thermodynamic possibility of chemical reactions (1)–(4), Table 4. There is still an unreacted mineral $C_{12}A_7$ in FA after milling and sulfuric acid neutralization what is confirmed by strong lines at interplane distances of 4.90 and 2.54 \AA . This indicates that the formation of a dihydrous gypsum is possible both by reaction (3) and reaction (4) which is more likely by Gibbs energy.

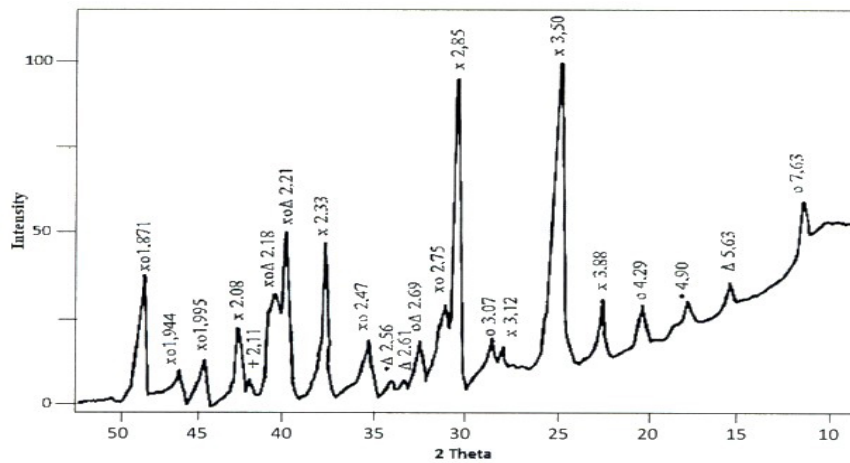


Figure 4. XPA results of FA milled together with refining slag
 Δ – $3\text{CaO}\cdot\text{Al}_2\text{O}_3\cdot 3\text{CaSO}_4\cdot 31\text{H}_2\text{O}$; o – $\text{CaSO}_4\cdot 2\text{H}_2\text{O}$; x – CaSO_4 ; • – $12\text{CaO}\cdot 7\text{Al}_2\text{O}_3$; + – MgO .

From the kinetic point of view the process of FA neutralization when milling with mineral additives can be divided into two stages. The first stage includes mechanical deformation of solid components, the second – the formation of neutralization products. In the first stage due to a powerful hydrodynamic impact of grinding bodies porous grains of FA are destroyed and sulfuric acid located in the pores is squeezed out and gets to the surface of the particles of the mineral additive.

The neutralization process proceeds at a low rate and is determined by the increase in the specific surface area of the material (the rate of milling) as well as the amount of acidic composition. After that in the second stage a layer of fine neutralization products is removed from the surface of the particles due to mechanical abrasion and the neutralization rate increases. Thus FA neutralization and activation of the binding properties are provided as a result of constant updating of the surface during FA milling with mineral additives. At the same time it was observed that long-term milling of FA (more than 2 hours) does not cause an increase of the neutralization rate of the acidic component because the surface of the particles of the mineral additive is covered with a thin layer of remilled and aggregated FA. In addition the temperature of the medium in the mill has a great influence on the process of FA neutralization during its milling with mineral additives. Thermodynamic calculations showed that the process of acidic component neutralization of FA is accompanied by the release of heat and heating of the material which was observed during the experiments. With the increase of temperature the growth of the material surface area and the degree of neutralization decreased. For these reasons FA after milling contains up to 0.5 % unbound sulfuric acid. The study of physical and mechanical properties of the binder based on FA neutralized by refining slag with the addition of 0.3 % superplasticizer showed that it has a high specific surface area indicating a greater reactivity and is characterized by shorter setting times, high mechanical strength and water resistance of gypsum slag stone (softening coefficient is 0.75) compared to acidic FA from the furnace, Table 5.

Table 5. Physical and mechanical properties of the binder based on neutralized FA.

Specific surface area, m^2/g	W/S ratio, %	Setting time, min		The strength, MPa after			
		initial	final	3 days		28 days	
				bending	compression	bending	compression
10.0	28	45	120	4.5	15.4	6.7	43.0

Fig. 5 shows the microstructure of hardened binder based on FA neutralized by refining slag and with plasticizer Melment F 15 G after 28 days.

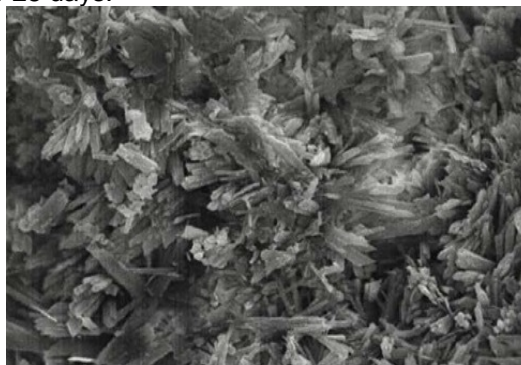


Figure 5. Microstructure of hardened binder based on FA neutralized by refining slag and with plasticizer Melment F 15 G at the age of 28 days (x1000) SEM.

Thus gypsum and calcium hydrosulfoaluminate formed during the FA neutralization by refining slag positively affected the binding properties of the FA.

When granulating of the obtained technogenic anhydrite binder (TAB) with the addition of an aqueous solution of plasticizer in a quantity of 12 % it was found that this amount of the liquid phase is sufficient for the formation of isometric granules of 8–10 mm in size but not enough for the processes of their hydration and hardening. Formed granules reach the strength of about 2.6–2.8 N/granule which is not sufficient for their use as an aggregate in high-strength concrete composition, Fig. 6. When more water was added to the granulation process of the binder an overmoistened sticky mass was formed that could not be granulated.

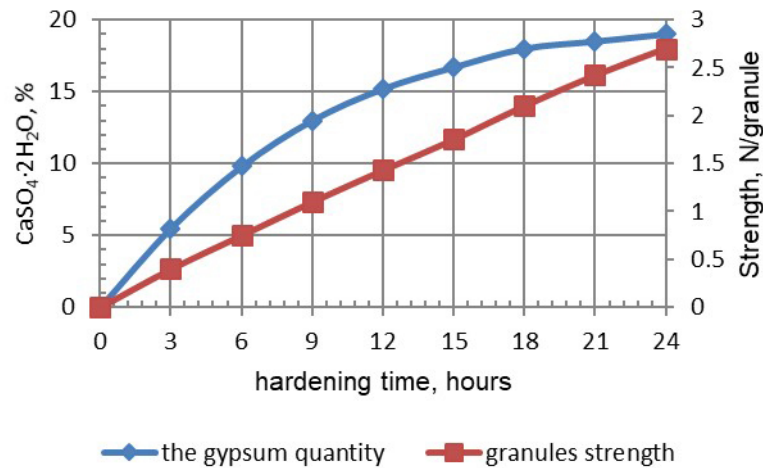


Figure 6. Hardening kinetics of granules on the basis of the neutralized FA.

Therefore during granulation of FA neutralized by refining slag its binding potential is very limited while the binding potential of the refining slag proper containing high-basic calcium aluminate (mayenite) and the vitreous phase is practically not used. In this regard the amount of refining slag in relation to acidic FA should be increased to obtain strong granules. As it is known binders including calcium aluminates and calcium sulfate are characterized by increased strength in the early stages of hardening. One of these binders is gypsum-alumina expanding cement developed by Soviet scientists and consisting of 70 % high-alumina slag and 30 % gypsum or anhydrite [24].

It was found that during granulation of a binder composition pre-milled to a fraction of less than 80 microns and consisting of 70 % of refining slag and 30 % of acidic FA, granules are formed with the following properties according to Russian Standard 9757-90: bulk density – 1100 kg/m³, average density – 1800 kg/m³, compressive strength in the cylinder – 17.0 MPa. High physical and mechanical indicators allow to use such granules as an artificial porous aggregate for concrete (non-fired slag-anhydrite gravel – NFSAG) [25]. The composition and properties of concrete with a binder based on FA neutralized by refining slag and aggregate from NFSAG are presented in Table 6.

Table 6. Composition and properties of concrete.

TAB	NFSAG	Quartz sand	Water	Plasticizer Melment F 15 G	Concrete density, kg/m ³	Compressive strength, MPa after		Coefficient of constructive quality
						7 days	28 days	
300	900	600	150	1	1895	24.7	43.4	23

The test results show that obtained concrete has B30 compressive strength class. Such concrete on an anhydrite binder, in contrast to concrete on Portland cement (high-strength concrete on Portland cement is usually referred to as concrete with a strength class from B55-B65 and higher) can be considered high-strength. It can be assumed that the strengthening of concrete is due to the high strength of non-fired slag-anhydrite gravel and slag-anhydrite stone synthesized during the hardening of FA neutralized by refining slag in the superplasticizer presence, which is also indicated in [26, 27]. In addition an important factor is the structure of the contact zone between the aggregate and the cement stone which in this case has the highest possible strength due to the chemical affinity of the binder and the aggregate.

Such concretes may be in demand in the manufacture of wall stones or to obtain large-size structures and the construction of high-rise buildings by monolithic technology due to their high coefficient of structural quality and water resistance of the binder. It should be noted that the concrete hardening proceeds in an accelerated mode and does not need curing. From a material and technical point of view, the transition to the use of anhydrite binders and concretes based on them allows reducing the cement intensity of construction

that is increasing the share of linker-free binders instead of Portland cement. At the same time, labor productivity increases and construction costs decrease due to significant resource and energy savings, while solving environmental problems in the production of binders.

4. Conclusions

1. It was established that acidic FA is a porous granular material which contains insoluble anhydrite with a crystal size of 1–4 microns as well as sulfuric acid, calcium fluoride, fluorosulfonic acid and calcium fluorosulfonate which subjected to hydrolytic decomposition in air.

2. The influence of the composition and quantity of mineral additives on the kinetics of sulfuric acid neutralization and FA properties during milling was studied. The neutralization process of sulfuric acid in FA proceeds most actively with the introduction of stoichiometric amount of additives: 6.1 % of microcalcite, 12.3 % of steel-refining slag, 13.4 % of ferrochrome slag and 24.8 % of fly ash.

3. Anhydrite binder on the basis of fluorine-anhydrite neutralized by refining slag and with superplasticizer was obtained. The binder is normally hardening, sufficiently high strength and water resistant so it can be used for the manufacture of construction materials applied in conditions with high humidity.

4. Cement-free high-strength concrete of B30 strength class which does not require curing was obtained on the basis of anhydrite binder and non-fired gravel.

References

- Zhang, P. Comprehensive recovery and sustainable development of phosphate resources. *Procedia Engineering*. 2014. Pp. 37–51.
- Garg, M., Minocha, A.K., Jain, N. Environment hazard mitigation of waste gypsum and chalk: Use in construction materials. *Construction and Building Materials*. 2011. Vol. 25. Pp. 944–949.
- Prasad, M.N.V. Resource Potential of Natural and Synthetic Gypsum Waste. *Environmental Materials and Waste: Resource Recovery and Pollution Prevention*. 2016. Pp. 307–337.
- Gashkova V.I., Tolkacheva L.Ye., Pureskina O.A., Katyshev S.F. Issledovaniye vliyaniya rezhima raboty reaktivnykh pechey na svoystva ftorangidrita iz pechi [Investigation of the influence of the reaction furnace operation mode on the properties of fluorine anhydrite from the furnace]. *Khimicheskaya promyshlennost*. 2008. No 7. Pp. 331–338. (rus)Singh, M., Garg, M. Activation of fluorogypsum for building materials. *Journal of Scientific and Industrial Research*. 2009. Vol. 68(2). Pp. 130–134.
- Pureskina, O.A., Gashkova, V.I., Petrov, N.S., Katy'shev, S.F. Sposob polucheniya angidritovogo vyazhushhego [Method for producing anhydrite binder]. 2010. Patent Russia no. 2382743, 2010. (rus)Zhou, M., Zhang, W., Hou, H., Huang, X., Wang, W. The activation of fluorgypsum with slag activator and the fluorine solidification mechanics. *Journal Wuhan University of Technology, Materials Science Edition*. 2011. Pp. 1023–1026.
- Batalin, B.S., Eremin, O.G., Ivenskix, D.V., Popov, V.S. Sul'fatnosilikatnoe vyazhushhee i sposob ego polucheniya [Sulfate-silicate binder and method of its preparation]. Patent Russia no. 2450989. 2012. (rus)Žvironaitė, J., Pundienė, I., Gaidučis, S., Kizinievič, V. Effect of different pozzolana on hardening process and properties of hydraulic binder based on natural anhydrite. *Journal of Civil Engineering and Management*. 2012. Vol. 18(4). Pp. 530–536.
- Sychugov, S., Tokarev, Y., Plekhanova, T., Kazantseva, A., Gaynetdinova, D. Binders based on natural anhydrite and modified by finely-dispersed galvanic and petrochemical waste. *Procedia Engineering*. 2013. Pp. 1022–1028.
- Garg, M., Pundir, A. Investigation of properties of fluorogypsum-slag composite binders – Hydration, strength and microstructure. *Cement and Concrete Composites*. 2014. Vol. 45. Pp. 227–233.
- Khalil, A.A., Tawfik, A., Hegazy, A.A., El-Shahat, M.F. Effect of some waste additives on the physical and mechanical properties of gypsum plaster composites. *Construction and Building Materials*. 2014. Vol. 68. Pp. 580–586.
- Magallanes-Rivera, R.X., Escalante-García, J.I. Anhydrite/hemihydrate-blast furnace slag cementitious composites: Strength development and reactivity. *Construction and Building Materials*. 2014. Vol. 65. Pp. 20–28.
- Magallanes-Rivera, R.X., Escalante-García, J.I. Hemihydrate or waste anhydrite in composite binders with blast-furnace slag: Hydration products, microstructures and dimensional stability. *Construction and Building Materials*. 2014. Vol. 71. Pp. 317–326.
- Huang, X., Jiang, M., Zhao, X., Tang, C. Mechanical properties and hydration mechanisms of high-strength fluorogypsum-blast furnace slag-based hydraulic cementitious binder. *Construction and Building Materials*. 2016. Vol. 127. Pp. 137–143.
- Bigdeli, Y., Barbato, M. Use of a low-cost concrete-like fluorogypsum-based blend for applications in underwater and coastal protection structures. *OCEANS 2017 – Anchorage 2017*. Pp. 1–5.
- Sychugov, S., Tokarev, Y., Plekhanova, T., Mikhailova, O., Pudov, I., Faizullin, R., Gaifullin, A., Sagdiev, R. Line of Approach to a Problem of Water Resistance of Anhydrite Cements. *Procedia Engineering*. 2017. Pp. 982–990.
- Tokarev, Y., Ginchitsky, E., Sychugov, S., Krutikov, V., Yakovlev, G., Buryanov, A., Senkov, S. Modification of Gypsum Binders by Using Carbon Nanotubes and Mineral Additives. *Procedia Engineering*. 2017. Pp. 1161–1168.
- Bigdeli, Y., Barbato, M., Gutierrez-Wing, M.T., Lofton, C.D. Use of slurry fluorogypsum (FG) with controlled pH-adjustment in FG-based blends. *Construction and Building Materials*. 2018. Vol. 163. Pp. 160–168.
- Bigdeli, Y., Barbato, M., Gutierrez-Wing, M.T., Lofton, C.D., Rusch, K.A., Jung, J., Jang, J. Development of new pH-adjusted fluorogypsum-cement-fly ash blends: Preliminary investigation of strength and durability properties. *Construction and Building Materials*. 2018. Vol. 182. Pp. 646–656.
- Pedreño-Rojas, M.A., Flores-Colen, I., De Brito, J., Rodríguez-Liñán, C. Influence of the heating process on the use of gypsum wastes in plasters: Mechanical, thermal and environmental analysis. *Journal of Cleaner Production*. 2019. Vol. 215. Pp. 444–457.
- Cordon, H.C.F., Cagnoni, F.C., Ferreira, F.F. Comparison of physical and mechanical properties of civil construction plaster and recycled waste gypsum from São Paulo, Brazil. *Journal of Building Engineering*. 2019. Vol. 22. Pp. 504–512.

20. Sychova, A.M., Svatovskaya, L.B., Starchukov, D.S., Soloviova, V.Y., Gravit, M.V., The improving of the concrete quality in a monolithic clip. Magazine of Civil Engineering. 2018. 80(4). Pp. 3–14. doi: 10.18720/MCE.80.1
21. O vliyaniy sostava modifitsirovannogo gipsoglinozemistogo rasshiryayushhegosya cementa na prochnost' i temp tverdeniya [On the influence of the composition of modified gypsum-alumina expanding cement on the strength and rate of hardening] [Online]. URL: <http://naukovedenie.ru/PDF/01TVN615.pdf> (reference date: 01.11.2019).(rus)Behera, M., Minocha, A., Bhattacharyya, S., Deoliya, R. Durability and In Situ Performance Evaluation of Sustainable Recycled Aggregate Concrete Using Fluorogypsum as Cementitious Binder: Select Proceedings of SEC 2016. Lecture Notes in Civil Engineering. 2019. Pp. 985–997.
22. Tolstoy, A.D., Lesovik, V.S., Milkina, A.S. Improving New Generation Concretes (NGCs) by Introducing Technogenic Materials. IOP Conference Series: Materials Science and Engineering. 2018. Vol. 463(2). DOI: 10.1088/1757-899X/463/2/022095
23. Khezhev, T.A., Pukharenko, Y.V., Khezhev, K.A., Klyuev, S.V. Fiber gypsum concrete composites with using volcanic tuff sawing waste. ARPN Journal of Engineering and Applied Sciences. 2018. No. 13(8). Pp. 2935–2946.

Contacts:

Alexander Ponomarenko, ponfox@mail.ru



DOI: 10.34910/MCE.107.2

Behavior of RC beams with different bond strength

A. Alkhalwaldeh*, R. Al-Rousan 

Jordan University of Science and Technology, Irbid, Jordan

*E-mail: aalkhalwaldeh91@gmail.com

Keywords: materials science, civil engineering, structural, concrete, engineering

Abstract. This study investigates the impact of carbon fiber reinforced polymers (CFRP) composite to concrete bond strength degradation on the flexural response of CFRP strengthened reinforced concrete (RC) beams by using nonlinear finite element analysis (NLFEA). After reasonable validation of NLFEA simulated beams with the experimental test results of companion beams, NLFEA was expanded to provide a parametric study of twenty-two beams that correlates the ultimate flexural strength of RC beams to degradation in concrete compressive strength, degradation in bond strength, CFRP bond surface with concrete, and the number of layers and the size effect. The results show that the increase of CFRP-to-concrete contact area, concrete strength degradation, and epoxy bond strength degradation percentage had a significant impact on ultimate load capacity, ultimate deflection, stiffness, and energy absorption. Finally, new guidelines were proposed for designers and researchers to find the reduction in concrete strength as well as CFRP-to-concrete contact area at any ultimate load capacity of RC beams.

1. Introduction

The alarming deterioration of world's infrastructure has lead engineers to search for new techniques of rehabilitating deficient structures. The major reason of deterioration in concrete infrastructure facilities such as buildings, bridges, waterfront, marine constructions, and chemical plants is corrosion of steel reinforcement. Even though a variety of solutions like cathodic protection, epoxy coatings, polymer concrete, and increased concrete cover have been tried in the past, none of the procedures have provided long-term solutions. The construction industry is in ominous necessitate of alternative materials to steel, which do not corrode.

Concrete or steel jacketing considered as traditional strengthening techniques of existing deficient structures. Although these techniques are practicable and resolve just the strength issue, issues associated with them such as enlarge in the self-weight and strengthened member dimensions; the time necessary to carry out the strengthening work is moderately significant. In some situations, such as a bridge on a demanding highway or in issue of factories it may be complicated to take them out of service during application strengthening system. The consumption of advanced composite materials shows enormous possible in the area of structural rehabilitation. Composites offer several advantages in structural uses, such as lighter weights, higher strengths, design flexibility that enables the creation of complex and large shapes, and corrosion resistance. Other factors which call for the use of carbon fiber reinforced polymers (CFRP) composites in the strengthening and rehabilitation of deficient structures is tailor and time ability, CFRP strengthening techniques allow for cost-efficient retrofit alternative although the initial cost of CFRP composites is higher than traditional strengthening techniques. As a result, several papers on various aspects related to the paper subject have been published such as rehabilitation of damaged and deficient bridges and buildings [1–4], investigation the durability performance and safety factors of reinforced concrete (RC) beams [5–9], type of composite [10–11], severe conditions [12], type of loading [13], type of concrete [14–18], precast concrete [19], and low thermal transmittance [20].

Alkhalwaldeh, A., Al-Rousan, R. Behavior of RC beams with different bond strength. Magazine of Civil Engineering. 2021. 107(7). Article No. 10702. DOI: 10.34910/MCE.107.2

© Alkhalwaldeh, A., Al-Rousan, R., 2021. Published by Peter the Great St. Petersburg Polytechnic University.



This work is licensed under a CC BY-NC 4.0

Nonlinear Finite Element analysis (NLFEA) is an essential and efficient tool in the analysis and simulating of complex structures. The major benefits that NLFEA provided are: 1) significant savings in the time, cost, and effort compared with the experimental fabrication and testing of real structure elements, 2) freedom to modify any interest parameter to assess its influence on the structure, such as the strength of concrete in tension and compression, 3) and freedom to get the strain, stress, and displacement values at any load level and at any location. Recently, few researchers have attempted to simulate the complexity behavior of reinforced concrete externally strengthened with CFRP composites using NLFEA in the area of prestressed concrete [21–22], two-way slabs subjected to drop-weight [23], cable-stayed bridges [24], RC columns [25], thermal shock [26], bending and torsion [27], and hybrid FRP/steel technique [28]. Therefore, essential issues to produce effective, economical, and successful CFRP strengthening were discussed. Also, the impact of CFRP composite to concrete bond strength degradation on the flexural response of CFRP strengthened RC beams by using NLFEA received miniature consideration. The scientific problem considered in the study is indeed one of the problems in the modern theory of reinforced concrete. Despite a significant number of studies on the problem of bond between CFRP and concrete are limited to date. There are no sufficiently reliable solutions to this problem that most fully reflect the physical nature of the problem. In this study, the main subject is investigated the novel application in which was implemented in which the CFRP sheet was integrated as external flexural strengthening for RC beams. A lack of literature regarding the behavior of simply supported RC beams strengthened externally with CFRP composite and subjected to degradation in bond strength are necessitated conducting the present investigation. The main objectives of this study are to investigate the effect of CFRP contact area with concrete ($0.00A_t$, $0.25A_t$, $0.50A_t$, $0.75A_t$, and $1.00A_t$), concrete compressive strength (55, 51.6, 48.1, 44.7, 41.3, 37.8, 34.4, 30.9, 27.5, and 24.1 MPa), and epoxy bond strength degradation percentage (0, 15, 25, 35, 45, 55, 65, 75, and 85 %) in order to provide procedures and guidelines for researchers and designers.

2. Method

The goal of this analysis is to determine the effect of CFRP contact area with concrete, concrete compressive strength, and epoxy bond strength degradation percentage in the behavior of reinforced concrete (RC) flexural beams. Twenty-two beams were created analyzed in order to study the ultimate flexural strength of RC beams to degradation on concrete compressive strength, degradation in bond strength, CFRP bond surface with concrete, and number of layers.

2.1. Design constants

Twenty-two identical RC Strengthened beams with CFRP sheet layers were modelled using NLFEA. The cross section of all simulated beams is 150 mm × 250 mm with a length is 1200 mm. The beams were reinforced with three bars of $\phi 12$ at the bottom, two bars of $\phi 8$ bars at the top, and $\phi 8$ stirrups spaced at 75 mm on centers (Fig. 1).

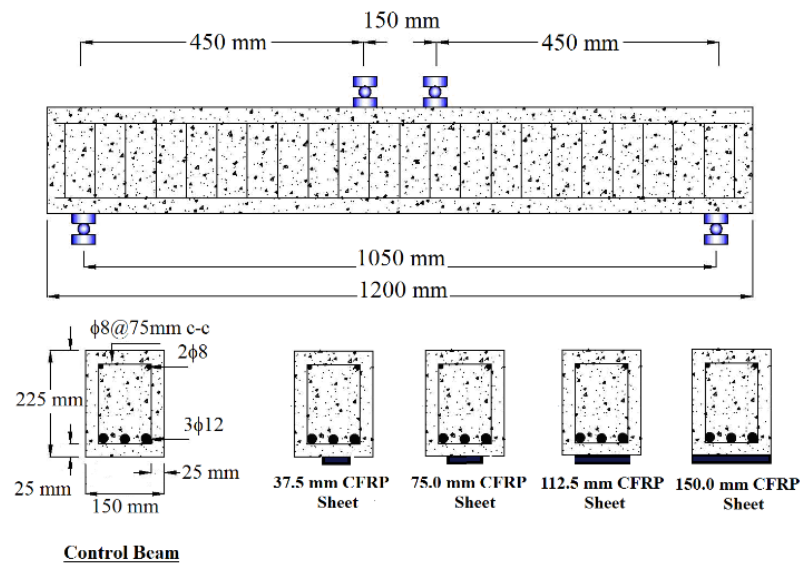


Figure 1. Typical layout of the simulated beams.

The first group includes five beams which simulated with different CFRP width (w_f) of 0 mm ($0.00A_t$), 37.5 mm ($0.25A_t$), 75 mm ($0.50A_t$), 112.5 mm ($0.75A_t$), and 150 mm ($1.00A_t$) to study the effect of CFRP contact area with concrete (Table 1). The second group includes ten control beams which simulated with different concrete compressive strength (f/c) of 55, 51.6, 48.1, 44.7, 41.3, 37.8, 34.4, 30.9, 27.5, and

24.1 MPa to study the degradation in concrete compressive strength (Table 2). The third group includes nine beams which simulated with different bond layer strength reduction percentage of 0, 15, 25, 35, 45, 55, 65, 75, and 85 % to study the epoxy bond strength degradation percentage (Table 3).

Table 1. Beams with different CFRP contact area.

Specimen	CFRP sheet width (w_f), mm	f'_c , MPa	Epoxy bond strength degradation (EBD), %	Ultimate deflection, mm (%)	Ultimate load, kN (%)	Stiffness, kN/mm (%)	Energy Absorption, kN.mm (%)
Bfc55wf0er0	0.0 (0.00 A_t)	55	0	40.0 (100)	170.5 (100)	26.2 (100)	5917 (100)
Bfc55wf37.5er0	37.5 (0.25 A_t)	55	0	38.8 (97)	180.8 (106)	29.7 (113)	6240 (105)
Bfc55wf75er0	75.0 (0.50 A_t)	55	0	37.5 (94)	192.7 (113)	32.6 (124)	6392 (108)
Bfc55wf112.5er0	112.5 (0.75 A_t)	55	0	36.1 (90)	201.7 (118)	35.4 (135)	6433 (109)
Bfc55wf150er0	150.0 (1.00 A_t)	55	0	34.5 (86)	207.7 (122)	38.4 (146)	6484 (110)

Note: A_t : Area of the tension side = length of the beam (L) × width of the beam (b)

Table 2. Beams with different concrete strength.

Specimen	CFRP sheet width (w_t), mm	f'_c , MPa	Epoxy bond strength degradation (EBD), %	Ultimate deflection, mm (%)	Ultimate load, kN (%)	Stiffness, kN/mm (%)	Energy Absorption, kN.mm (%)
Bfc55.0wf0er0	0.0 (0.00 A_t)	55.0	0	40.0 (100)	170.5 (100)	26.2 (100)	5917 (100)
Bfc51.6wf0er0	0.0 (0.00 A_t)	51.6	0	36.9 (92)	162.5 (95)	25.0 (91)	5192 (88)
Bfc48.1wf0er0	0.0 (0.00 A_t)	48.1	0	34.1 (85)	155.8 (91)	24.0 (87)	4533 (77)
Bfc44.7wf0er0	0.0 (0.00 A_t)	44.7	0	31.8 (79)	150.5 (88)	23.2 (84)	4077 (69)
Bfc41.3wf0er0	0.0 (0.00 A_t)	41.3	0	29.9 (75)	145.6 (85)	22.4 (81)	3735 (63)
Bfc37.8wf0er0	0.0 (0.00 A_t)	37.8	0	28.4 (71)	142.5 (84)	21.9 (79)	3455 (58)
Bfc34.4wf0er0	0.0 (0.00 A_t)	34.4	0	27.3 (68)	140.3 (82)	21.6 (78)	3246 (55)
Bfc30.9wf0er0	0.0 (0.00 A_t)	30.9	0	26.6 (67)	138.5 (81)	21.5 (77)	3085 (52)
Bfc27.5wf0er0	0.0 (0.00 A_t)	27.5	0	26.3 (66)	137.1 (80)	21.2 (76)	2998 (51)
Bfc24.1wf0er0	0.0 (0.00 A_t)	24.1	0	25.9 (65)	134.8 (79)	21.0 (75)	2883 (49)

Note: A_t : Area of the tension side = length of the beam (L) × width of the beam (b)

Table 3. Beams with different epoxy bond strength degradation percentage.

Specimen	CFRP sheet width (w_f), mm	f'_c , MPa	Epoxy bond strength degradation (EBD), %	Ultimate deflection, mm (%)	Ultimate load, kN (%)	Stiffness, kN/mm (%)	Energy Absorption, kN.mm (%)
Bfc55wf150er0	150.0 (1.00 A_t)	55.0	0	34.5 (100)	207.7 (100)	38.4 (100)	6484 (100)
Bfc55wf150er15	150.0 (1.00 A_t)	55.0	15	33.4 (97)	203.8 (98)	37.7 (93)	6148 (95)
Bfc55wf150er25	150.0 (1.00 A_t)	55.0	25	32.7 (95)	200.4 (96)	37.1 (92)	5904 (91)
Bfc55wf150er35	150.0 (1.00 A_t)	55.0	35	32.0 (93)	198.0 (95)	36.6 (91)	5708 (88)
Bfc55wf150er45	150.0 (1.00 A_t)	55.0	45	31.2 (90)	194.1 (93)	35.9 (89)	5449 (84)
Bfc55wf150er55	150.0 (1.00 A_t)	55.0	55	30.5 (88)	189.2 (91)	35.0 (87)	5189 (80)
Bfc55wf150er65	150.0 (1.00 A_t)	55.0	65	30.0 (87)	183.5 (88)	33.9 (84)	4950 (76)
Bfc55wf150er75	150.0 (1.00 A_t)	55.0	75	29.1 (84)	176.5 (85)	32.6 (81)	4598 (71)
Bfc55wf150er85	150.0 (1.00 A_t)	55.0	85	27.9 (81)	172.2 (83)	31.8 (79)	4287 (66)

Note: A_t : Area of the tension side = length of the beam (L) × width of the beam (b)

2.2. Elements

The concrete material was modelled by using SOLID65 which can be used for the 3-D modelling of solids with or without steel reinforcing bars. SOLID65 is eight nodes element with three degrees of freedom at each node with translations in the nodal x, y, and z directions. The most significant aspects of SOLID65

are the conducting of nonlinearity of concrete material and capable of crushing, cracking (in three orthogonal directions), creep, and plastic deformation. The steel reinforcement bars were modelled by using LINK8 element (3-D spar element) with a uniaxial compression-tension element with three degrees of freedom at each node with translations in the nodal x, y, and z directions. Steel plates at the supports and load applications were modelled by using SOLID45 in the models with eight nodes having three degrees of freedom at each node with 8 translations in the nodal x, y, and z directions. Finally, CFRP composite sheet was modelled by using SOLID46 (layered element of the 8-node structural solid) which allows up to 250 different material layers with different orthotropic material properties and orientations in each layer. SOLID46 has three degrees of freedom at each node with translations in the nodal x, y, and z directions. Fig. 2 shows the types of used elements used in the NLFEA simulated beams.

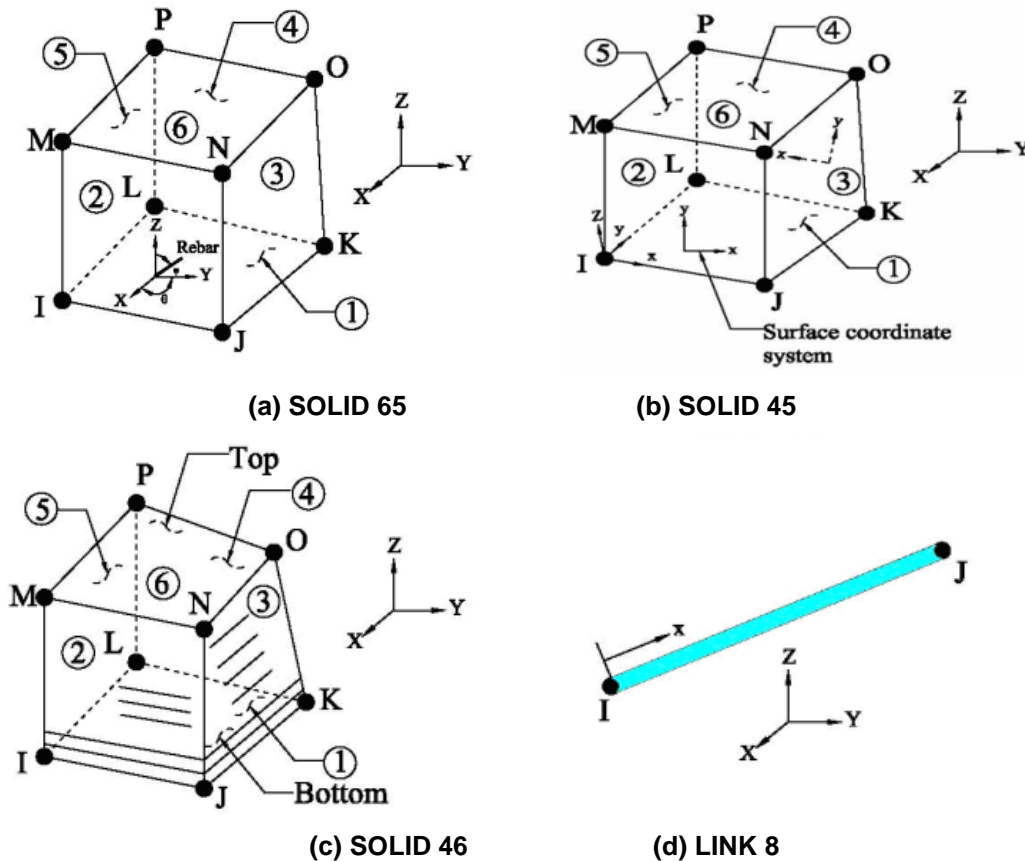


Figure 2. Types of the used elements used in the NLFEA.

2.3. Materials

Concrete material is classified as quasi-brittle material with different performance in tension and compression. The used SOLID65 element can predict the nonlinear performance of concrete materials via a smeared crack approach which predicts concrete material failure and accounts for both crushing and cracking failures. Therefore, the main two input strength parameters required to define a failure surface for the concrete material are ultimate uniaxial compressive and tensile strengths. As a result, a failure criterion of concrete due to a multi axial stress state should be calculated [31]. In addition, a Poisson's ratio of 0.2 was used for all simulated beams. The conditions of the crack face can be represented by shear transfer coefficient (β_t). Generally, the β_t value ranges from 0.0 (a smooth crack with complete loss of shear transfer) to 1.0 (a rough crack with no loss of shear transfers). The β_t value ranges from 0.05 to 0.25 was used in many studies of reinforced concrete structures [31]. Thus, a β_t value of 0.2 was used in this study. The concrete properties include f'_c of 55, 51.6, 48.1, 44.7, 41.3, 37.8, 34.4, 30.9, 27.5, and 24.1 MPa, initial young's modulus (E_c) of 34856, 33762, 32596, 31423, 30205, 28896, 27566, 26126, 24647, and 23073 MPa, respectively. In tension stage, the concrete stress-strain curve is assumed to be linearly elastic up to the ultimate strength. After this limit, the concrete started to crack and the strength decreases to zero. Figure 3(a) shows the concrete simplified uniaxial stress-strain relationship that is used in this study for f'_c of 55 MPa.

The steel reinforcement bars for the simulated models was assumed to be an elastic-perfectly plastic material with the same properties in compression and tension as shown in Fig. 3 (b). Yield stress and

Poisson's ratio of 413 MPa and 0.3, respectively were used for defining the steel reinforcement bars. A more even stress distribution over the support areas were provided by adding steel plates at both ends of the beams. The performance steel plates were assumed to be linear elastic materials with Poisson's ratio of 0.3 and an elastic modulus of 200 GPa.

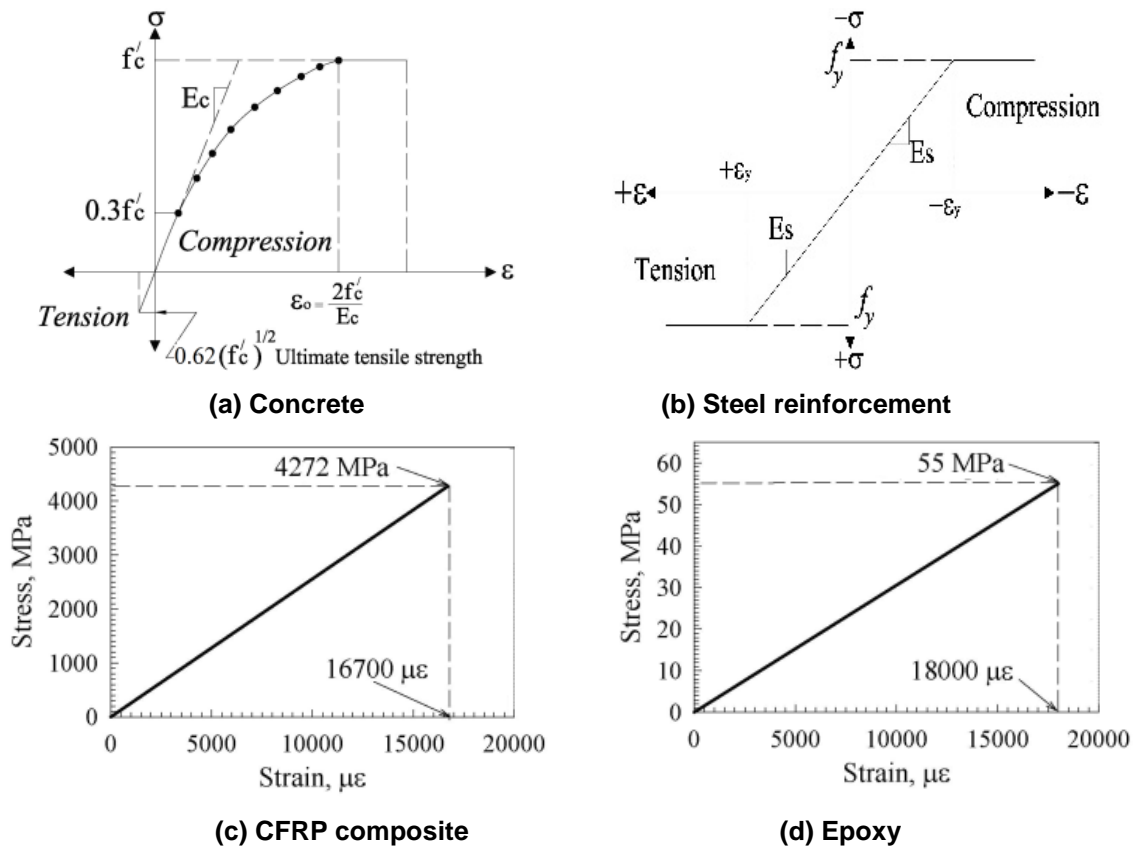


Figure 3. Stress-strain curves: (a) concrete, (b) steel Reinforcement, (c) CFRP composite sheet, and (d) epoxy.

The CFRP composite sheet is assumed an orthotropic material of tensile strength of 3790 MPa, 0.165 mm thick, ultimate tensile strain of 0.017 in/in, and elastic modulus of 228 GPa as shown in Fig. 3(c). The epoxy material is assumed an isotropic material of ultimate tensile strength 55 MPa, 0.343 mm thick, ultimate tensile strain of 0.018 mm/mm, and elastic modulus of 30 GPa as shown in Fig. 3(d). The elastic modulus of CFRP composite sheet was assumed to be 10^{-6} times that of the main direction for the other directions perpendicular to the fibre direction. Linear elastic property performance was assumed for both CFRP composite sheet and epoxy.

2.4. Models

Quarter of the simulated beam with appropriate boundary conditions was used in the NLFEA simulation by taking advantage of the symmetry in the reinforced concrete beam configuration and the applied loading. This advantage can reduce the computer disk space requirements and computational time. The appropriate mesh density was determined by carried a convergence study. Fig. 4 shows the finite element meshing of quarter of the RC beam. Perfect bond was assumed between the concrete and steel reinforcement epoxy as well as between CFRP composite sheet and epoxy. Close up views of appropriate boundary conditions and finite element meshing of the beams is shown in Fig. 5.

The applied load was divided into a series of load steps or load increments. Convergence at the end of each load increment within tolerance limits is equal to 0.001 which is provided by Newton–Raphson equilibrium iterations. The maximum and minimum load step sizes were automated by ANSYS program. The cracking created when the principal tensile stress in any direction occurred outside the failure surface of concrete. After creation of crack, the concrete elastic modulus is set to zero in the direction parallel to the direction of principal tensile stress. Crushing occurs when all compressive principal stresses are lies outside the failure surface of concrete, afterwards, the elastic modulus is set to zero in all directions, and the element efficiently disappears. The simulated finite element model fails impetuously when the crushing concrete capability is turned on. Concrete crushing started to grow in elements situated directly under the load locations and significantly reducing the local stiffness. Ultimately, the simulated model showed a large displacement and the solution diverged. Consequently, the concrete crushing capability was turned off and

concrete cracking inhibited the failure of the simulated finite element models. The loads were applied steadily with smaller load increments at concrete cracking and ultimate load stages. Failure for each simulated model was recognized when the solution for 0.0045 kN load increment was not converging.

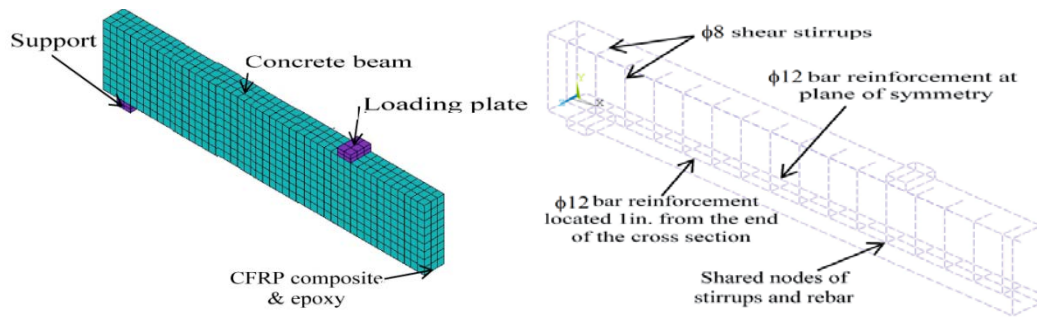


Figure 4. Typical finite element meshing of quarter of the beam.

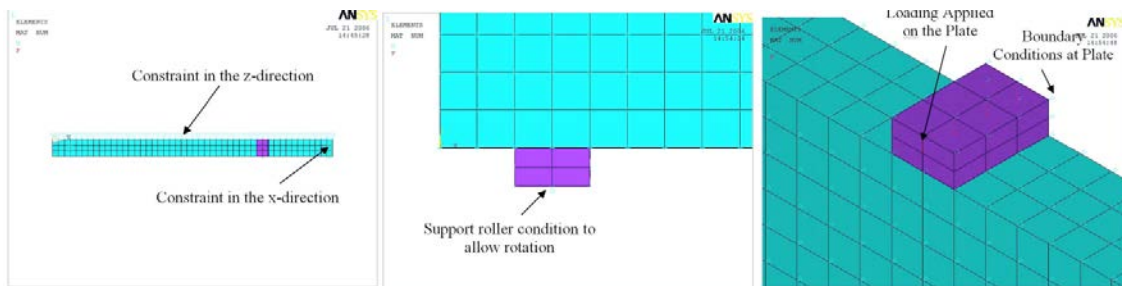


Figure 5. Close up view of the finite element meshing of the beams and boundary conditions.

3. Results and Discussion

3.1. Validation of models

Fig. 6 shows the load deflection response of the NLFEA simulated beams and tested beams reported by Al-Rousan and Issa [12]. The load-deflection response of CFRP strengthened beams, as with the virgin (control) beams, was linear behaviour until the creation of the flexural cracks as well as the main steel reinforcement is starting to yield. After the steel reinforcement yielding point, the deflection increased rapidly with tiny reduction in ultimate load capacity. Also, the CFRP sheets had a significant impact on the ultimate load capacity and corresponding deflection as well as redistribution of stresses occurred and thus increasing the beam's strength at yielding. In comparison with the control beams, the load-deflection performance of the CFRP strengthened beams was enhanced by the addition of CFRP sheets as indicated by the enhancement of the ultimate load capacity, and the reduction in the corresponding deflection at any load level. Inspection of Fig. 6 reveals that there is a good agreement between the NLFEA simulated beams and the experimental test results in terms of ultimate strength and load response. Fig. 7 shows a typical NLFEA deformed shape deformed of control beam and stress contours of concrete beam externally strengthened with one layer of CFRP composites.

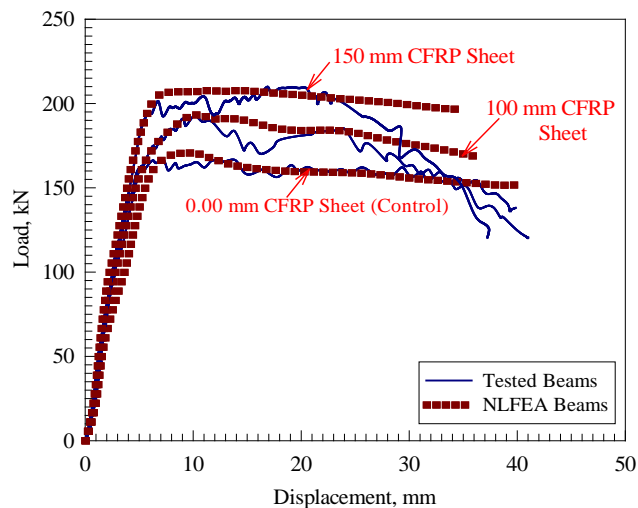


Figure 6. Load-deflection curve of NLFEA and tested beams [12].

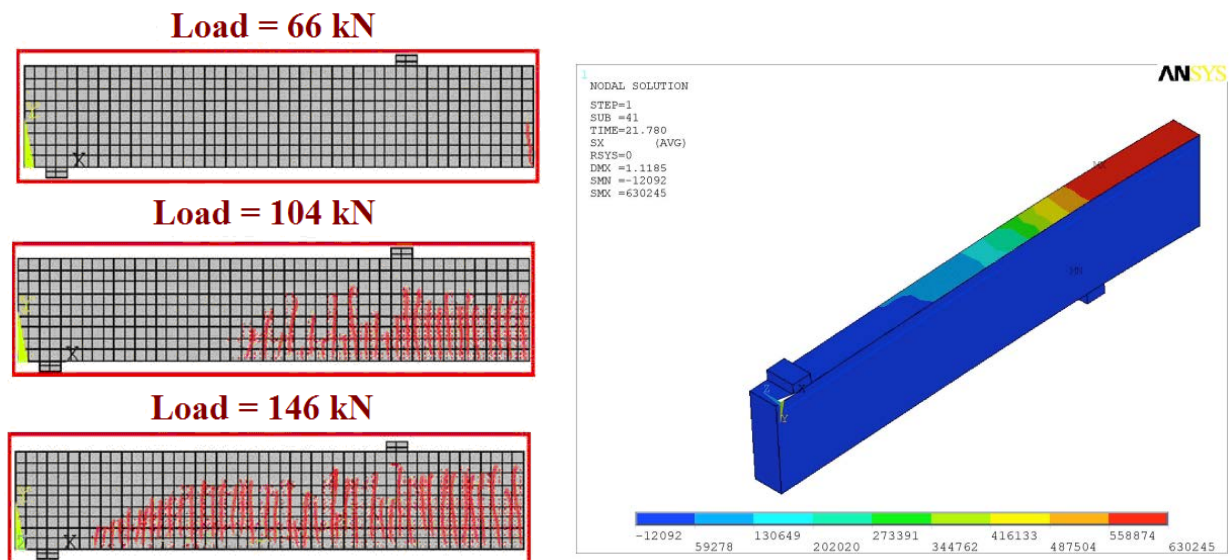


Figure 7. Typical NLFEA (a) deformed shape of control beam and (b) stress contours of 1 layers CFRP beam.

3.2. Effect of CFRP contact area

Table 1 shows the effect of CFRP contact area with concrete for beams strengthened with CFRP contact area of 0 CFRP sheet layer ($0.00A_t$), 0.25 CFRP sheet layer ($0.25A_t$), 0.50 CFRP sheet layer ($0.50A_t$), 0.75 CFRP sheet layer ($0.75A_t$), and 1.00 CFRP sheet layer ($1.00A_t$) for w_f of 0 mm, 37.5 mm, 75 mm, 112.5 mm, and 150 mm, respectively, and concrete compressive strength of 55 MPa. Inspection of Table 1 reveals that the enhancement ultimate capacity strength of beams strengthened 0.25 CFRP sheet layer ($0.25A_t$), 0.50 CFRP sheet layer ($0.50A_t$), 0.75 CFRP sheet layer ($0.75A_t$), and 1.00 CFRP sheet layer ($1.00A_t$) with respect to control beam was 6 %, 13 %, 18 %, and 22 %, respectively. Whereas, the deflection of the strengthened beams decreased with the increase of CFRP contact area with a reduction percentage of 3 %, 6 %, 10 %, and 14 % for 0.25 CFRP sheet layer, 0.50 CFRP sheet layer, 0.75 CFRP sheet layer, and 1.00 CFRP sheet layer, respectively. The stiffness scored the maximum enhancement percentage of 13%, 24 %, 35 %, and 46 % for 0.25 CFRP sheet layer, 0.50 CFRP sheet layer, 0.75 CFRP sheet layer, and 1.00 CFRP sheet layer, respectively, which is almost twice the enhancement in the ultimate capacity strength. While, the energy absorption scored the minimum enhancement percentage of 5 %, 8 %, 9 %, and 10 % for 0.25 CFRP sheet layer, 0.50 CFRP sheet layer, 0.75 CFRP sheet layer, and 1.00 CFRP sheet layer, respectively, which is almost one third of the enhancement in the stiffness. As a result, when the CFRP contact area increased 100 % of beam strengthened with CFRP sheet layer (150 mm contact area with concrete) with respect to the control beam strengthened, the ultimate flexural strength, stiffness, and energy absorption increased 22 %, 46 %, and 10 %, respectively. Fig. 8 shows the load deflection response of the NLFEA simulated beams with different CFRP contact area. Inspection of Fig. 8 reveals that the load-deflection response can be divided into two stages. The first stage represents the linear part from zero loading up to yielding of the steel reinforcement bars in which the load was carried by steel reinforcement. Then, the second stage represents almost a linear part with tiny reduction in ultimate load capacity and large increasing in deflection in which the load was carried by CFRP sheet.

Fig. 9 shows the effect of CFRP contact area on the CFRP delamination profile of beams strengthened with different configuration. Inspection of Fig. 9 reveals that the initial CFRP sheet delamination length of the beams strengthened decreased with the increase of CFRP contact area in which the CFRP sheet delamination length is 250 mm (2.5 times the CFRP sheet delamination length of the beam strengthened with 1.00 CFRP sheet layer), 200 mm (2 times the CFRP sheet delamination length of the beam strengthened with 1.00 CFRP sheet layer), 150 mm (1.5 times the CFRP sheet delamination length of the beam strengthened with 1.00 CFRP sheet layer), and 100 mm for 0.25 CFRP sheet layer, 0.50 CFRP sheet layer, 0.75 CFRP sheet layer, and 1.00 CFRP sheet layer, respectively.

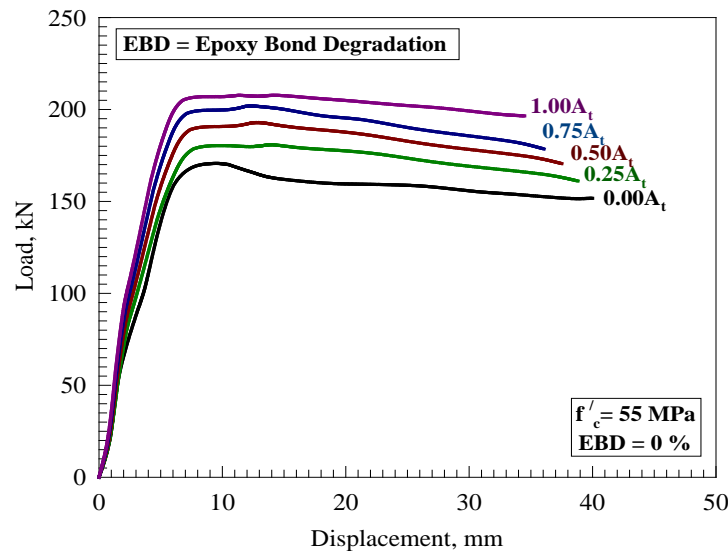


Figure 8. Load-deflection curve of beams with different CFRP contact area.

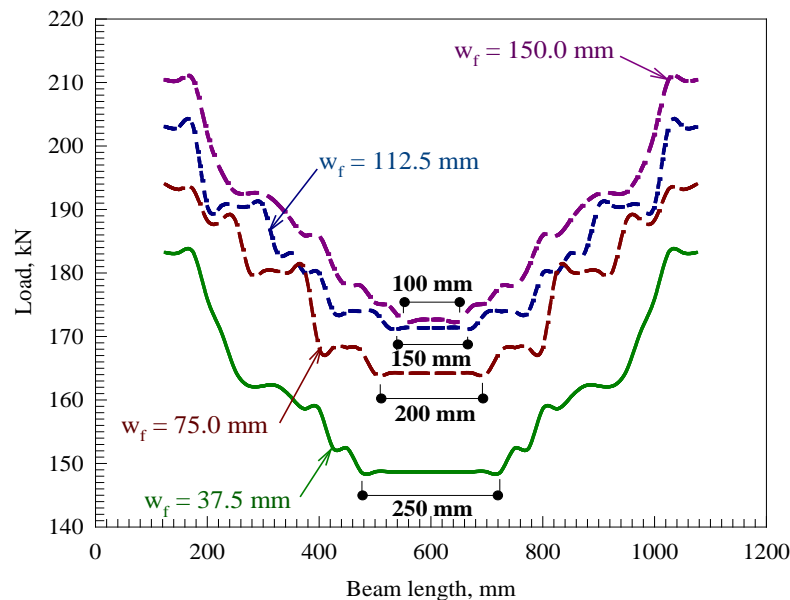


Figure 9. CFRP delamination profile of beams with different CFRP contact area.

3.3. Effect of concrete strength degradation

Fig. 10 shows the load deflection response of the NLFEA simulated beams with different concrete strength. Inspection of Fig. 10 reveals that the load-deflection response can be also divided into two stages. The first stage represents the linear part from zero loading up to yielding of the steel reinforcement bars in which the load was carried by steel reinforcement. Then, the second stage represents a descending linear part from yielding of the steel reinforcement bars up to failure with slope increase with the decrease of concrete strength.

Table 2 shows the effect of concrete strength for control beams with f/c of 55, 51.6, 48.1, 44.7, 41.3, 37.8, 34.4, 30.9, 27.5, and 24.1 MPa. Inspection of Table 2 reveals that the reduction in ultimate capacity strength of control beams with f/c of 55, 51.6, 48.1, 44.7, 41.3, 37.8, 34.4, 30.9, 27.5, and 24.1 MPa was 5 %, 9 %, 12 %, 15 %, 16 %, 18 %, 19 %, 20 % and 21 %, respectively. Whereas, the reduction in deflection of the control beams is almost 1.5 times the reduction in ultimate capacity strength. The reduction in stiffness is almost the same the reduction in ultimate capacity strength. While, the energy absorption scored the maximum reduction percentage of 12 %, 23 %, 31 %, 37 %, 42 %, 45 %, 48 %, 49 % and 51 %, for f/c of 55, 51.6, 48.1, 44.7, 41.3, 37.8, 34.4, 30.9, 27.5, and 24.1 MPa, respectively, which is almost twice the reduction in the ultimate capacity strength.

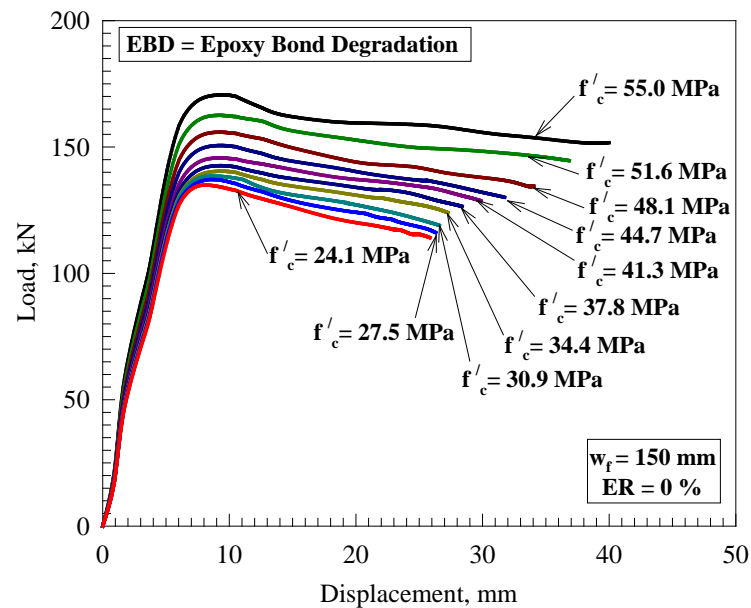


Figure 10. Load-deflection curve of beams with different concrete strength.

Table 4 shows the ultimate flexural load capacity of CFRP strengthened reinforced concrete beams exposed for three years for the room temperature, cyclic ponding in 15 % salt-water solution, hot-water of 65 °C, and rapid freeze/thaw cycles reported by Al-Rousan and Issa [12]. Fig. 11 shows that the damage percentage in concrete had a parabolic relation with the ultimate strength of control beams. Inspection of Fig. 11 reveals that the damage percentage in concrete strength of freeze and thaw beams of 166.8 kN ultimate load capacity was 3.2 % (53.2 MPa) which almost 2 times the reduction in ultimate load capacity with respect to the control beam under room temperature. Also, the damage percentage of the salt and hot water beams was 4.8 % (31.7 MPa) and 23.0 % (42.4 MPa), respectively, which corresponded to almost 2 times the reduction in ultimate load capacity with respect to the control beam under room temperature. In the real life, the beams always subject under more than two conditions and sometimes all the conditions. Therefore, the damage percentage for the beams subjected to freeze-thaw and salt water cycles by using the experimental results reported by Al-Rousan and Issa [12] was 8 % (50.6 MPa) as shown in Fig. 11. The damage percentage for the beams subjected to hot and salt water cycles was 26.7% (40.2 MPa). For all conditions, the damage percentage was 29 % (39.1 MPa) as shown in Fig. 11. As a result, Fig. 11 provided guidelines for designers and researchers to find the reduction in concrete strength at any ultimate load capacity of RC beams.

Table 4. The details of the tested beam specimens [12].

Group	Beam Designation	Type of strengthening with CFRP	Ultimate load, kN
I (Room Temperature)	BRC0	Unstrengthened (control)	169.9
	BRC1	1-layer Sheet	211.3
II (Freeze and Thaw)	BFC0	Unstrengthened	166.8
	BFC1	1-layer Sheet	202.8
III (Heat Tank Water)	BHC0	Unstrengthened	147.2
	BHC1	1-layer Sheet	186.4
IV (Ponding Salt Water)	BSC0	Unstrengthened	165.0
	BSC1	1-layer Sheet	198.8

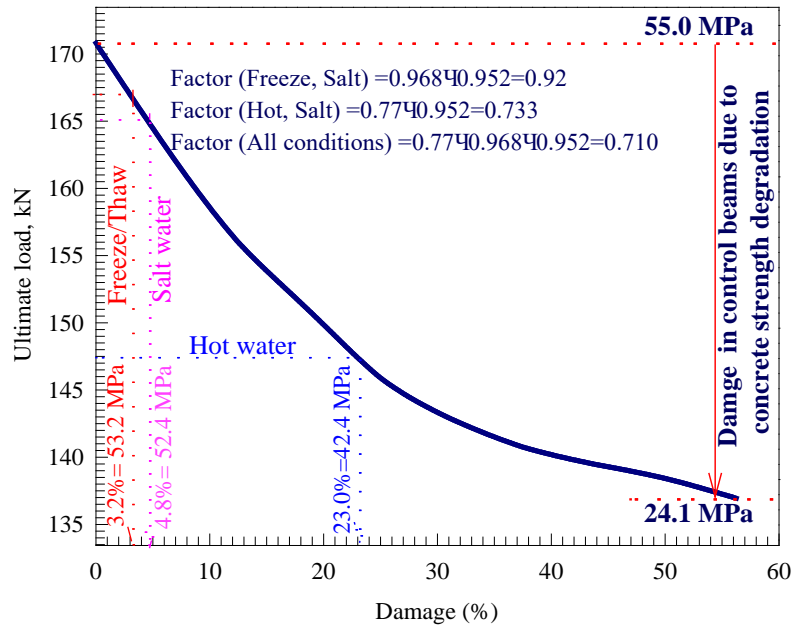


Figure 11. Damage percentages versus ultimate load capacity of control beam.

3.4. Effect of epoxy bond strength degradation

Fig. 12 shows the load deflection response of the NLFEA simulated beams with different epoxy bond strength degradation percentage. Inspection of Fig. 12 reveals that the load-deflection response can be also divided into two stages. The first stage represents the linear part from zero loading up to yielding of the steel reinforcement bars in which the load was carried by steel reinforcement. Then, the second stage represents almost a liner part with small reduction in ultimate load capacity and large increasing in deflection in which the load was carried by CFRP sheet. Also, Fig. 12 shows that the area under the curve as well as the ultimate ductility decreased with the increase of epoxy bond strength degradation percentage.

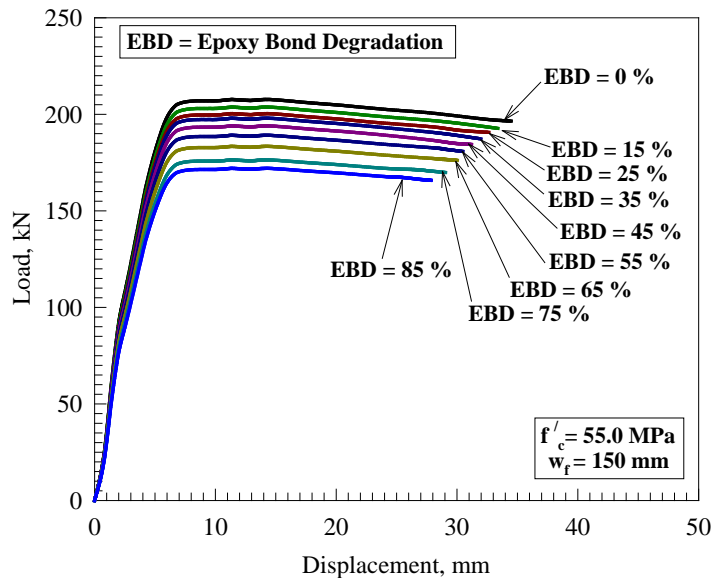


Figure 12. Load-deflection curve of beams with different epoxy bond strength degradation percentage.

Fig. 13 shows the effect of epoxy bond strength degradation percentage on the CFRP delamination profile. Inspection of Fig. 13 reveals that the initial CFRP sheet delamination length of the beams strengthened increased with the increase of epoxy bond strength degradation percentage. Fig. 13 shows that the increase in CFRP sheet delamination length of strengthened beams is 11 %, 16 %, 21 %, 26 %, 32 %, 42 %, 53 %, 63 %, and 79 % of the CFRP bonded length for epoxy bond strength degradation percentage of 0 %, 15 %, 25 %, 45 %, 55 %, 65 %, 75 %, and 85 %, respectively. As a result, the increase in CFRP sheet delamination length of strengthened beams is almost equal to an average percentage of 83 % of epoxy bond strength degradation percentage.

Table 3 shows the effect of epoxy bond strength degradation percentage for CFRP strengthened beams with f/c of 55. Inspection of Table 3 reveals that the reduction in ultimate capacity strength with respect to CFRP strengthened beam without reduction in epoxy bond strength was 3 %, 5 %, 7 %, 10 %, 12 %, 13 %, 16 %, and 19 % for EBD of 15 %, 25 %, 45 %, 55 %, 65 %, 75 %, and 85 %, respectively. Whereas, the reduction in deflection of the CFRP strengthened beams is almost 0.95 times the reduction in ultimate capacity strength. The reduction in stiffness is almost 1.05 times the reduction in ultimate capacity strength. While, the energy absorption scored the maximum reduction percentage of 5 %, 9 %, 12 %, 16 %, 20 %, 24 %, 29 %, and 34 % for EBD of 15 %, 25 %, 45 %, 55 %, 65 %, 75 %, and 85 %, respectively, which is almost twice the reduction in the ultimate capacity strength.

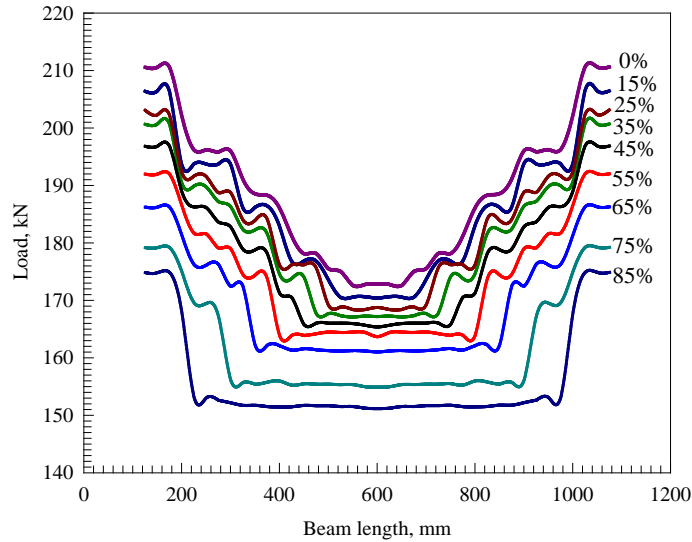


Figure 13. CFRP delamination profile of beams with different epoxy bond strength degradation percentage.

Fig. 14 shows bond strength degradation on ultimate load capacity. Inspection of Fig. 14 reveals that the bond strength degradation of freeze and thaw beams of 166.8 kN ultimate load capacity was 18 % which almost 10 times the reduction in ultimate load capacity with respect to the beam under room temperature. Also, the bond strength degradation of the salt and hot water beams was 24 % and 35 %, respectively, which corresponded to almost 9 times and 3 times the reduction in ultimate load capacity with respect to the beam under room temperature. For the beam subjected to freeze-thaw and salt water cycles, the bond strength degradation was 37.6 %. For the beam subjected to hot and salt water cycles, the bond strength degradation was 50.6 %. For all conditions, the bond strength degradation was 59.6 % as shown in Fig. 14. As a result, Fig. 14 provided guidelines for designers and researchers to find the bond strength degradation at any ultimate load capacity or RC beams.

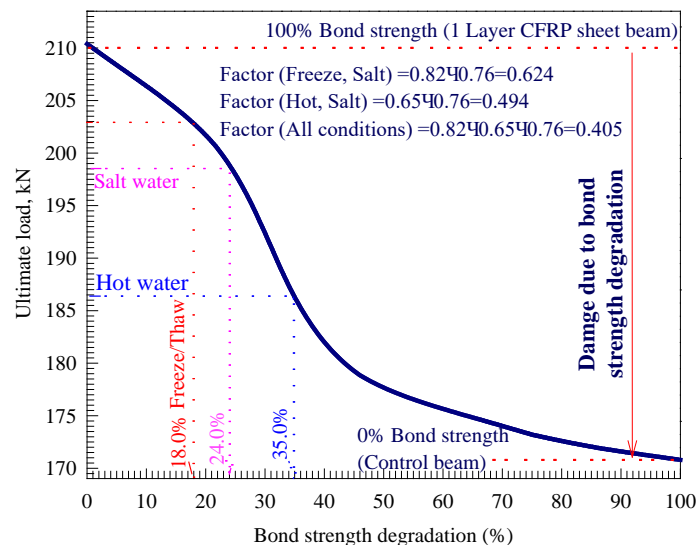


Figure 14. Bond strength degradation versus ultimate load capacity of control beam.

4. Conclusions

1. The load deflection response of the NLFEA simulated beams can be divided into two stages. The first stage represents the linear part from zero loading up to yielding of the steel reinforcement bars in which the load was carried by steel reinforcement. Then, the second stage represents a descending linear part from yielding of the steel reinforcement bars up to failure with decreased slope based on the investigated parameters.

2. The increasing of CFRP contact area of beam strengthened with CFRP sheet layer (150 mm contact area with concrete) with respect to the control beam strengthened, the ultimate flexural strength, stiffness, and energy absorption increased 22 %, 46 %, and 10 %, respectively.

3. The ultimate capacity strength of control beams decreased with the decrease of concrete strength. Whereas, the reduction in deflection of the control beams is almost 1.5 times the reduction in ultimate capacity strength. The reduction in stiffness is almost the same the reduction in ultimate capacity strength. While, the energy absorption scored the maximum reduction percentage of twice the reduction in the ultimate capacity strength.

4. The epoxy bond strength degradation percentage decreased the ultimate capacity strength with respect to CFRP strengthened beam. Whereas, the reduction in deflection of the CFRP strengthened beams is almost 0.95 times the reduction in ultimate capacity strength. The reduction in stiffness is almost 1.05 times the reduction in ultimate capacity strength. While, the energy absorption reduction percentage is almost twice the reduction in the ultimate capacity strength.

5. The damage in ultimate flexural load capacity of control beam subjected to freeze-thaw and salt water, hot and salt water cycles, and freeze-thaw and salt water and hot water cycles (all conditions) was 8 %, 26.7 %, and 29 %, respectively.

6. The damage in bond strength of reinforced concrete beam externally strengthened with 1 layer of CFRP composites subjected to freeze-thaw and salt water, hot and salt water cycles, and freeze-thaw and salt water and hot water cycles (all conditions) was 37.6 %, 50.6 %, and 59.6 %, respectively.

7. New guidelines were proposed for designers and researchers to find the reduction in concrete strength as well as CFRP to concrete contact area at any ultimate load capacity of RC beams.

References

1. Meier, U. Carbon Fiber-Reinforced Polymers: Modern Materials in Bridge Engineering. Structural Engineering International. 1992. 2(1). Pp. 7–12. DOI: 10.2749/101686692780617020
2. Durability Evaluation of Carbon Fiber-Reinforced Polymer Strengthened Concrete Beams: Experimental Study and Design. ACI Structural Journal. 2005. 102(1). Pp. 40–53. DOI: 10.14359/13529
3. Wenwei, W., Guo, L. Experimental study of RC beams strengthened with CFRP sheets under sustaining loads. Journal of Wuhan University of Technology-Mater. Sci. Ed. 2006. 21(3), Pp. 82–85. DOI: 10.1007/bf02840887
4. Benjeddou, O., Ouezdou, M.B., Bedday, A. Damaged RC beams repaired by bonding of CFRP laminates. Construction and Building Materials. 2007. 21(6). Pp. 1301–1310. DOI: 10.1016/j.conbuildmat.2006.01.00
5. Ekenel, M., Myers, J.J. Durability performance of RC beams strengthened with epoxy injection and CFRP fabrics. Construction and Building Materials. 2007. 21(6). Pp. 1182–1190. DOI: 10.1016/j.conbuildmat.2006.06.020
6. Almusallam, T.H. Load-deflection behavior of RC beams strengthened with GFRP sheets subjected to different environmental conditions. Cement and Concrete Composites. 2006. 28(10). Pp. 879–889. DOI: 10.1016/j.cemconcomp.2006.07.017
7. Tan, K.H., Saha, M.K., Liew, Y.S. FRP-strengthened RC beams under sustained loads and weathering. Cement and Concrete Composites. 2009. 31(5). Pp. 290–300. DOI: 10.1016/j.cemconcomp.2009.03.002
8. Ji, G., Li, G., Alaywan, W. A new fire resistant FRP for externally bonded concrete repair. Construction and Building Materials. 2013. 42(1). Pp. 87–96. DOI: 10.1016/j.conbuildmat.2013.01.008
9. Trentin, C., Casas, J.R. Safety factors for CFRP strengthening in bending of reinforced concrete bridges. Composite Structures. 2015. 128(1). Pp. 188–198. DOI: 10.1016/j.compstruct.2015.03.048
10. Ferrari, V.J., de Hanai, J.B., de Souza, R.A. Flexural strengthening of reinforcement concrete beams using high performance fiber reinforcement cement-based composite (HPFRCC) and carbon fiber reinforced polymers (CFRP). Construction and Building Materials. 2013. 48(1). Pp. 485–498. DOI: 10.1016/j.conbuildmat.2013.07.026
11. Attari, N., Amziane, S., Chemrouk, M. Flexural strengthening of concrete beams using CFRP, GFRP and hybrid FRP sheets. Construction and Building Materials. 2012. 37(1). Pp. 746–757. DOI: 10.1016/j.conbuildmat.2012.07.052
12. Al-Rousan, R.Z., Issa, M.A. Flexural behavior of RC beams externally strengthened with CFRP composites exposed to severe environment conditions. KSCE Journal of Civil Engineering. 2016. 21(6). Pp. 2300–2309. DOI: 10.1007/s12205-016-0570-x
13. Kolchunov, V.I., Dem'yanov, A.I. The modeling method of discrete cracks in reinforced concrete under the torsion with bending. Magazine of Civil Engineering. 2018. 81(5). Pp. 160–173. DOI: 10.18720/MCE.81.16
14. Travush, V.I., Konin, D.V., Krylov, A.S. Strength of reinforced concrete beams of high-performance concrete and fiber reinforced concrete. Magazine of Civil Engineering. 2018. No. 77(1). Pp. 90–100. DOI: 10.18720/MCE.77.8
15. Usanova, K., Barabanshchikov, Yu., Fedorenko, Yu., Kostyrya, S. Cold-bonded fly ash aggregate as a coarse aggregate of concrete. Construction of Unique Buildings and Structures. 2018. 9(72). Pp. 31–45. DOI: 10.18720/CUBS.72.2

16. Volkova, A., Rybakov, V., Seliverstov, A., Petrov, D., Smignov, A. Strength characteristics of foam concrete samples with various additives. MATEC Web of Conferences 245, 03015 (2018). doi.org/10.1051/mateconf/201824503015
17. Volkova, A., Rybakov, V., Seliverstov, A., Petrov, D., Smignov, A. Lightweight steel concrete structures slab panels load-bearing capacity. MATEC Web of Conferences 245, 08007 (2018). doi.org/10.1051/mateconf/201824508008
18. Rybakov, V.A., Kozinetc, K.G., Vatin, N.I., Velichkin, V.Z., Korsun, V.I. Lightweight steel concrete structures technology with foam fiber-cement sheets. Magazine of Civil Engineering. 2018. 82(6). Pp. 103–111. DOI: 10.18720/MCE.82.10
19. Vatin, N.I., Velichkin, V.Z., Kozinetc, G.L., Korsun, V.I., Rybakov, V.A., Zhuvak, O.V. Precast-monolithic reinforced concrete beam-slabs technology with claydit blocks. Construction of Unique Buildings and Structures. 2018. 70(7). Pp. 43–59. DOI: 10.18720/CUBS.70.4
20. Barabanshchikov, Y., Fedorenko, I., Kostyrya, S., Usanova, K. Cold-Bonded Fly Ash Lightweight Aggregate Concretes with Low Thermal Transmittance: Review. Advances in Intelligent Systems and Computing. 2019. 983(1). Pp. 858–866. DOI: 10.1007/978-3-030-19868-8_84
21. Bily, P., Fladr, J., Kohoutkova, A. Finite Element Modelling of a Prestressed Concrete Containment with a Steel Liner. Proceedings of the Fifteenth International Conference on Civil, Structural and Environmental Engineering Computing. Civil-Comp Press. 2015. DOI: 10.4203/ccp.108.1
22. Bílý, P., Kohoutková, A. Sensitivity analysis of numerical model of prestressed concrete containment. Nucl. Eng. Des. 2015. 295(1). Pp. 204–214. DOI: 10.1016/j.nucengdes.2015.09.027
23. Al-Rousan, R. Behavior of two-way slabs subjected to drop-weight. Magazine of Civil Engineering. 2019. 90(6). Pp. 62–71. DOI: 10.18720/MCE.90.6
24. Al-Rousan, R. The impact of cable spacing on the behavior of cable-stayed bridges. Magazine of Civil Engineering. 2019. 91(7). Pp. 49–59. DOI: 10.18720/MCE.91.5
25. Mirmiran, A., Shahawy, M. Behavior of Concrete Columns Confined by Fiber Composites. Journal of Structural Engineering. 1997. 123(5). Pp. 583–590. DOI: 10.1061/(asce)0733-9445(1997)123:5(583)
26. Al-Rousan, R. Behavior of strengthened concrete beams damaged by thermal shock. Magazine of Civil Engineering. 2020. 94(2). Pp. 93–107. DOI: 10.18720/MCE.94.2
27. Al-Rousan, R., Abo-Msamh, I. Bending and Torsion Behaviour of CFRP Strengthened RC Beams. Magazine of Civil Engineering. 2019. 92(8). Pp. 42–51. DOI: 10.18720/MCE.92.8
28. Kara, I.F., Ashour, A.F., Körog'lu, M.A. Flexural behavior of hybrid FRP/steel reinforced concrete beams. Composite Structures. 2015. 129(1). Pp. 111–121. DOI: 10.1016/j.compstruct.2015.03.073

Contacts:

Ayah Alkhaldeh, aalkhaldeh91@gmail.com

Rajai Al-Rousan, rzalrousan@just.edu.jo



DOI: 10.34910/MCE.107.3

Ultra high-performance fiber reinforced concrete panel subjected to high velocity impact

V.C. Mai^{*a} , X.B. Luu^a, V.T. Nguyen^b

^a Kumoh National Institute of Technology, Gumi, Gyeongbuk, South Korea

^b Institute of Techniques for Special Engineering, Le Quy Don Technical University, Ha Noi, Viet Nam

*E-mail: maivietchinh@lqdtu.edu.vn

Keywords: Ultra High-Performance Fiber Reinforced Concrete (UHPFRC), Holmquist-Johnson-Cook model, high velocity impact

Abstract. In the last few decades, several full-scale tests have been performed to study the behavior of Ultra High-Performance Fiber Reinforced Concrete (UHPFRC). However, only limited research has been devoted to simulate performance of UHPFRC subjected to special load and impact, such as high-velocity impact. Accurate modeling and simulation of the UHPFRC panel subjected to high velocity impact is a big challenge involving costly experimental characterization of material and verification of ballistic impact response with actual test data. This article investigates the dynamic behavior of UHPFRC panel against multiple bullet impacts using the Holmquist-Johnson-Cook damage model incorporating both the damage and residual material strength. The projectile used in this study is chosen with high-speed and low-weight like the fragments which can be formed by industrial accidents or in an explosion. The kinetic and internal energies of the UHPFRC panel are also evaluated. The analysis results are compared to the High Strength Concrete (HSC) in terms of capability to absorb energy and reduce the damage on target panel.

1. Introduction

Invented about three decades ago, the so-called ultra-high performance concretes (UHPC) result in high compressive strength values of 150 N/mm² and more [1]. UHPC is characterized by steel fibers, cement, silica fume, fine sand, super plasticizer, and very low water-cement ratio. UHPC possesses very high compressive strength, good tensile strength, enhanced toughness, and durability properties in comparison to conventional concrete [2–8]. However, one of the main drawbacks of UHPC is its brittleness property. To overcome brittleness of UHPC, fibers are often added to UHPC and this type of concrete is referred to as Ultra High-Performance Fiber Reinforced Concrete (UHPFRC). The inclusion of reinforcement fibers in UHPC improves its mechanical properties, reduces its brittleness, and alters the crack propagation behaviors [9]. The UHPC has high compressive and tensile strengths compared to normal or high performance concretes, including good durability due to the combination of the optimum packing density [10]. It is well known that high strength and fiber reinforced concrete (FRC) has good capacity to absorb impact energy [11]. However, compared to conventional concrete, several authors suggested that UHPFRC has much greater capability to absorb energy [12–15]. In addition, UHPFRC can significantly improve impact resistance of cladding panels and walls while maintaining its standard thicknesses and appearance [16]. Such advantages of UHPFRC give the potential to be used for some constructions like military structures or multipurpose complex subjected to the special load like projectile impact. In a broad sense, the projectile impact might be understood as a fragment generated from a high-speed rotating machine in industrial accidents or generated from a direct armed attack [16].

Due to the high technical requirements, high costs of manufacturing UHPFRC, and the security restrictions required for full-scale velocity impact tests, experimental studies on UHPFRC members under

Mai, V.C., Luu, X. B., Nguyen, V. T. Ultra High-Performance Fiber Reinforced Concrete panel subjected to high velocity impact. Magazine of Civil Engineering. 2021. 107(7). Article No. 10703. DOI: 10.34910/MCE.107.3

© Mai, V.C., Luu, X. B., Nguyen, V. T., 2021. Published by Peter the Great St. Petersburg Polytechnic University.



This work is licensed under a CC BY-NC 4.0

high-velocity impact are very limited. Moreover, UHPFRC is still a type of advanced concrete, and most investigations on its characteristics are predominantly quasi-static. Radoslav Sovják et al., 2013, took the experimental investigation of UHPFRC Slabs Subjected to Deformable Projectile Impact [17]. Several UHPFRC mixtures with different content of fibers were subjected to deformable projectile impact. A test with an ogive-nose projectile at average velocity shows that the plain UHPC specimen failed in a brittle manner, which makes the slab split into several pieces. Experimental results indicate that the implementation of high-strength steel microfibers significantly increased the resistance to projectile impact. It was stated that UHPFRC has much better resistance to projectile impact in comparison to conventional FRC. Erzar et al., 2017, has led an experimental and numerical research program in collaboration with French universities to evaluate the vulnerability of UHPFRC infrastructure to rigid projectile penetration [16]. They used the concrete model developed by Pontiroli, Rouquand and Mazars (PRM model), especially to take into account the contribution made by the fibers in the tensile fracture process. The collected result was significant, however, the PRM model is based on an isotropic formulation and the fiber ratio actually contributing to the material resistance needs to be more accurately determined. Sebastjan Kravanja, Radoslav Sovják, 2018, implemented cratering experiments, where the response of the Ultra-High Performance Fiber-Reinforced Concretes with various fiber volume fractions to the high-velocity projectile impact loading was investigated. Based on the experiment results, the increment of the fiber volumetric fraction did not have a significant influence on the depth of the penetration [18]. However, it plays an important role in reducing the crater area and volume. Jianzhong Lai et al., 2018, modeled the Ultra-High-Performance Concrete Subjected to Multiple Bullet. In this study, ultra-high-performance concrete (UHPC) was reinforced by hybrid fibers and corundum aggregates. The effects of hybrid fibers and corundum aggregates on bullet penetration depth and damage to UHPC subjected to multiple bullet impacts were researched. As a result, an empirical model was proposed to predict bullet penetration depths in UHPC based on the formula developed by Gomez [19].

This paper contributes to the development of UHPFRC and its application in the field, where high-impact energy absorption capacity is required. In this paper, a numerical model to predict the impact behavior of a UHPFRC panel penetrated by an ogive-nosed steel projectile is implemented. Due to the relatively high cost of large-scale experimental research, a means of modeling UHPFRC panel under impact load using a computer-aided program is needed to broaden the current knowledge. The numerical simulations were conducted using the ABAQUS software, which is a general FE analysis package for modeling the nonlinear mechanics of structures and their interactions. ABAQUS is based on implicit and explicit numerical methods for problems associated with large deformation and multi-loading environments. The UHPFRC panel has dimensions of 300 mm × 150 mm × 50 mm. The behavior of the UHPFRC panel is modeled using the Holmquist-Johnson-Cook damage model incorporating both the damage and residual material strength. The steel projectile has a small mass and a length of 26.6 mm, and is modeled as a deformable element under an impact velocity of 540 m/s. A general contact surface with nodal erosion is adapted to simulate the contact between the projectile and UHPFRC panel to be more appropriate. Accurate simulation of the structural response to such projectile impact using the Holmquist-Johnson-Cook damage model is a convenient way to radically decrease the cost of efforts relating to the field experiments. The model was also calculated with high strength concrete (HSC) and the results were also compared with UHPFRC to clarify the advantages of UHPFRC compared to conventional concrete under impact effect.

2. Materials and Methods

In terms of the existing dynamic constitutive model, the Holmquist-Johnson-Cook (HJC) model [20] represents a good compromise between simplicity and accuracy for large-scale computations, and has been implemented in ABAQUS for numerical simulations. The HJC model with damage is useful when modeling brittle materials subjected to large pressures, shear strain and high strain rates. The HJC model assumes that the damage variable increases progressively with plastic deformation. This model similarly consists of three components: strength, damage and pressure. The equivalent strength of material is expressed as a function of the pressure, strain rate and damage:

$$\sigma^* = \left[A(1 - D) + BP^* \right] \cdot \left(1 + C \ln \dot{\varepsilon}^* \right) \quad (1)$$

Where: P^* denotes the normalized pressure, shown as $P^* = P / f_c$;

P denotes pressure;

f_c is the quasi-static uniaxial compressive strength;

- * $\dot{\varepsilon}$ is the dimensionless strain rate, given by: $\dot{\varepsilon} = \dot{\varepsilon} / \dot{\varepsilon}_0$;
- $\dot{\varepsilon}$ is the actual strain rate;
- $\dot{\varepsilon}_0$ is the reference strain rate;

D ($0 \leq D \leq 1$) denotes the damage parameter. Additionally A , B , N , and C denote the material parameters.

The model accumulates damage both from equivalent plastic strain and plastic volumetric strain, and is expressed as:

$$D = \sum \frac{\Delta \varepsilon_p + \Delta \mu_p}{\varepsilon_p^f + \mu_p^f} \quad (2)$$

Where:

$\Delta \varepsilon_p, \Delta \mu_p$ are the equivalent plastic strain increment and plastic volumetric strain increment, respectively, during one cycle integral computation;

$\varepsilon_p^f + \mu_p^f$ is the plastic strain to fracture under a constant pressure, which can be expressed as follows:

$$\varepsilon_p^f + \mu_p^f = D_1 (P^* + T^*)^{D_2} \quad (3)$$

Where:

D_1 and D_2 represent damage constants, and $T^* = T / f_c$ is the normalized largest tensile strength (T represents the maximum tensile stress).

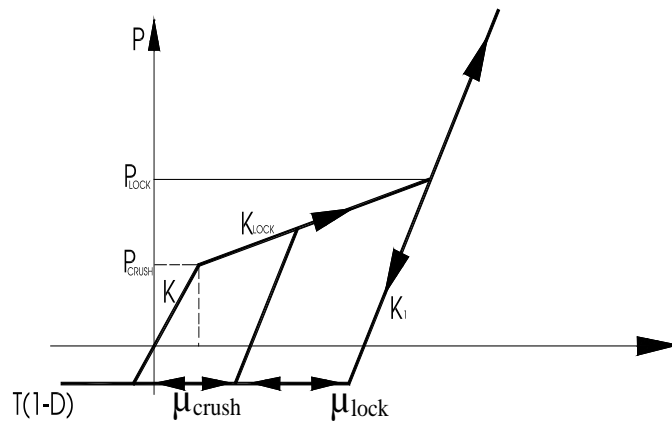


Figure 1. The relationship between hydrostatic pressure and material volumetric strain.

The equation of state of this model describes the relationship between hydrostatic pressure and volume. The loading and unloading process of concrete can be divided into three response regions. The first zone is the linear elastic zone, where the material is in elastic state. The elastic bulk modulus is given by:

$$k = \frac{P_{crush}}{\mu_{crush}} \quad (4)$$

Where:

P_{crush} and μ_{crush} represent the pressure and volumetric strain arising in a uniaxial compression test. Within the elastic zone, the loading and unloading equation of state is given by:

$$P = k \mu \quad (5)$$

Where:

μ is density parameter: $\mu = \rho / \rho_0 - 1$;

ρ is the current density and ρ_0 denotes the reference density.

The second zone arises at $P_{crush} < P < P_{lock}$, where the material is in the plastic transition state. In this area, the concrete interior voids gradually reduce in size as the pressure and plastic volumetric strain increase. The unloading curve is solved by the difference from the adjacent regions. The third area defines the relationship for fully dense material. The concrete has no air voids. The relationship between pressure and the volumetric strain is given by:

$$P = k_1 \bar{\mu} + k_2 \bar{\mu}^{-2} + k_3 \bar{\mu}^{-3} \quad (6)$$

where k_1, k_2, k_3 are constants and:

$$\bar{\mu} = \frac{\mu - \mu_{lock}}{1 + \mu_{lock}} \quad (7)$$

where μ_{lock} is the locking volumetric strain.

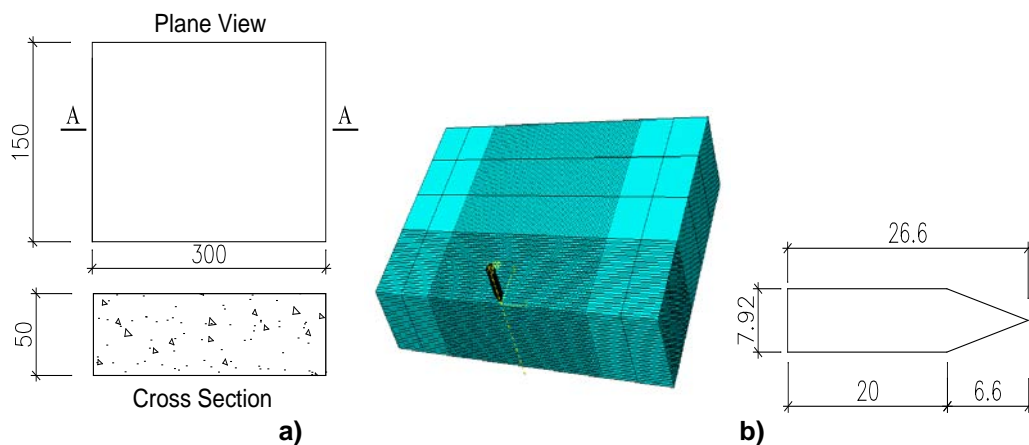
In this paper, the material model for UHPFRC and HSC panel is the Holmquist-Johnson-Cook model. The material model for deformable steel projectile is the Johnson-Cook model. The material parameters for UHPFRC panel, HSC panel and steel projectile are shown in Table 1, 2. Fig. 1 shows the geometry configurations of the panel, 3D mesh model and the steel projectile. The steel deformable projectile has 8 g of mass and a length of 26.6 mm, 7.92 mm in diameter and is modeled as a deformable element at velocity 540 m/s. The UHPFRC and HSC panel has dimensions of 300 mm x 150 mm x 50 mm, and is meshed using 8-node hexahedron solid elements in ABAQUS explicit software.

Table 1. The material parameters for UHPFRC and HSC panel.

Variable	Description	UHPFRC	HSC
ρ (Ton/mm ³)	Density	2.55e ⁻⁹	2.27e ⁻⁹
G (MPa)	Shear Modulus	18457	18457
C (MPa)	Strain Rate Law Constant	0.01209	0.01209
A	Failure Surface Constant	0.0017345	0.0075412
T (MPa)	Maximum Allowable Tensile Pressure	6.8946	4.3780
P_{lock} (MPa)	Equation of State Constant	792.88	640.46
μ_{lock}	Locking volumetric strain	0.10094	0.13814
P_{crush} (MPa)	Pressure arising in a uniaxial compression test	172.37	60.60
μ_{crush}	Volumetric strain in a compression test	0.00781	0.00683811
k_1 (MPa)	Equation of State Constant	7919.2	6429.9
k_2 (MPa)	Equation of State Constant	-29206	-47138.6
k_3 (MPa)	Equation of State Constant	187100	255724.2
D_1	Damage constant	0.00040598	0.000311742

Table 2. The material parameters for deformable steel projectile.

Variable	Description	UHPFRC
ρ (Ton/mm ³)	Density	7.86e ⁻⁹
G (MPa)	Shear Modulus	8.18e ⁴
E (MPa)	Elastic modulus	20.9e ⁴
PR	Poisson's ratio	0.28
A (MPa)	Yield stress	7.92 e ²
B (MPa)	Hardening constant	5.1e ²
C	Strain rate constant	0.014
EPSO (s ⁻¹)	Ref. strain rate	1
Failure parameter	D1	0.05
Failure parameter	D2	3.44
Failure parameter	D3	-2.12
Failure parameter	D4	0.002
Failure parameter	D5	0.61

**Figure 2. a – Geometry of UHPFRC and HSC panel; b – 3D mesh model in ABAQUS and geometry of steel projectile, unit mm.**

A three-dimensional eight-node reduced integration (C3D8R) element was adopted with a 2 mm × 2 mm × 2 mm mesh at the impact location, and 15 mm × 15 mm × 15 mm mesh in the outer region. With the aim to save computational costs and due to the symmetry of the model, half of the UHPFRC panel and projectile is considered. The projectile is meshed with 8-node hexahedron solid elements, with the mesh size of 0.5 mm.

3. Results and Discussion

The pressure distribution of the UHPFRC and High Strength Concrete panel during the impact process are shown in Fig. 3.

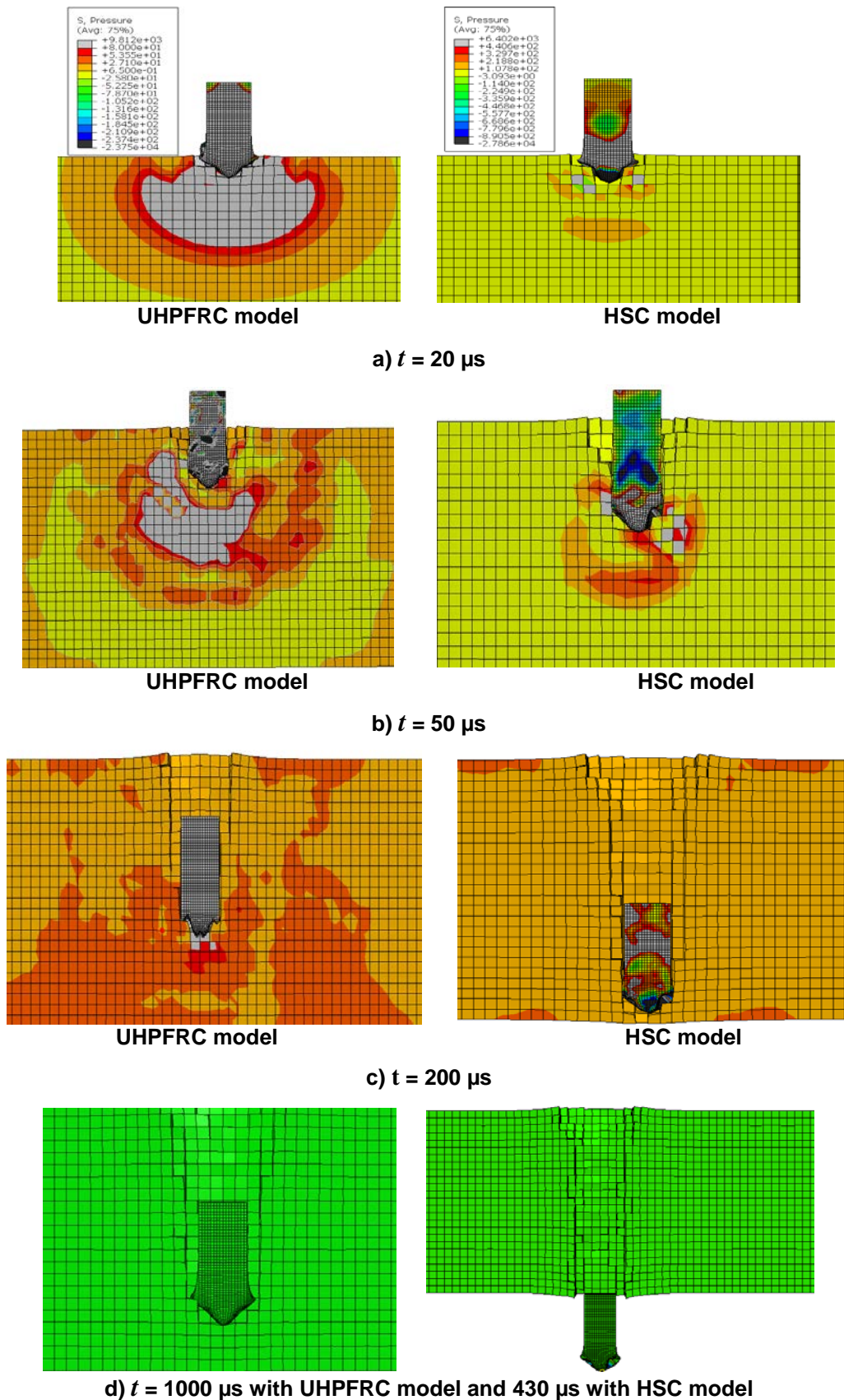


Figure 3. Pressure distribution of model in time step, unit MPa.

At the time after the impact ($20 \mu s$ and $50 \mu s$), pressure in the UHPFRC and HSC panel reached the highest value and concentrated around the projectile head and the crater. The highest stresses in UHPFRC panel and HSC panel is 9812 MPa and 6402 MPa , respectively. However, compared to HSC material, pressure in the UHPFRC dispersed faster in the larger region. In HSC panel, the projectile was still embedded in panel from $0 \mu s$ to $430 \mu s$ and HSC panel was perforated by the projectile at $t = 430 \mu s$.

Projectile movement speed through the HSC panel was faster than in UHPFRC panel. Residual velocity of the projectile for the HSC panel model was 110.62 m/s. On the other hand, in the UHPFRC panel, the projectile velocity decreased gradually after impacting. It bounced and moved in the opposite direction at time $t = 1000 \mu\text{s}$ without perforating the panel. Based on these results, compared to HSC material, UHPFRC can more effectively absorb the impact energy and reduce the velocity of the projectile.

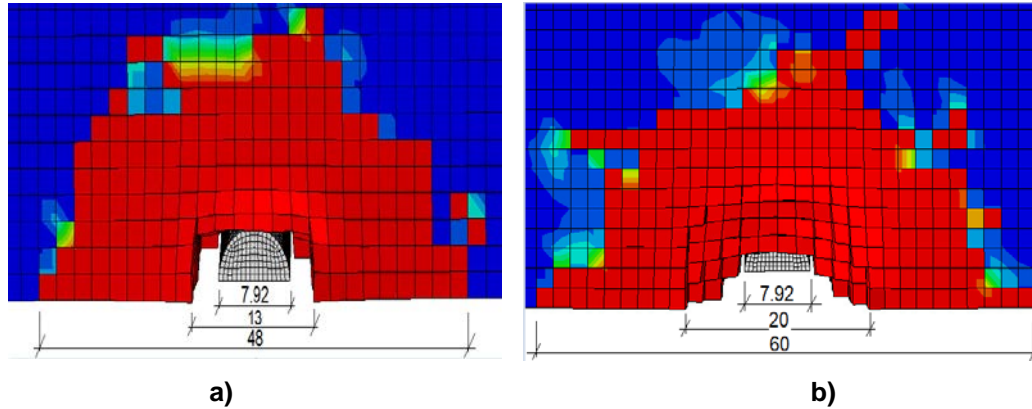


Figure 4. The damage in the front side (a) – UHPFRC panel; (b)– HSC panel.

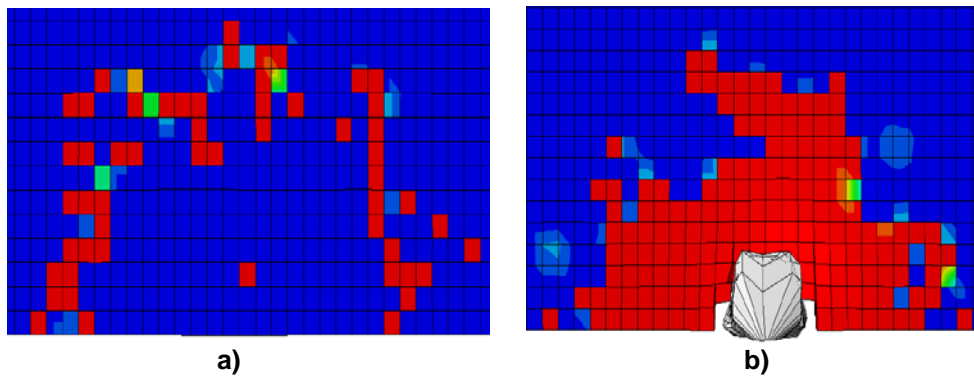


Figure 5. The damage in the back side (a) – UHPFRC panel; (b) – HSC panel.

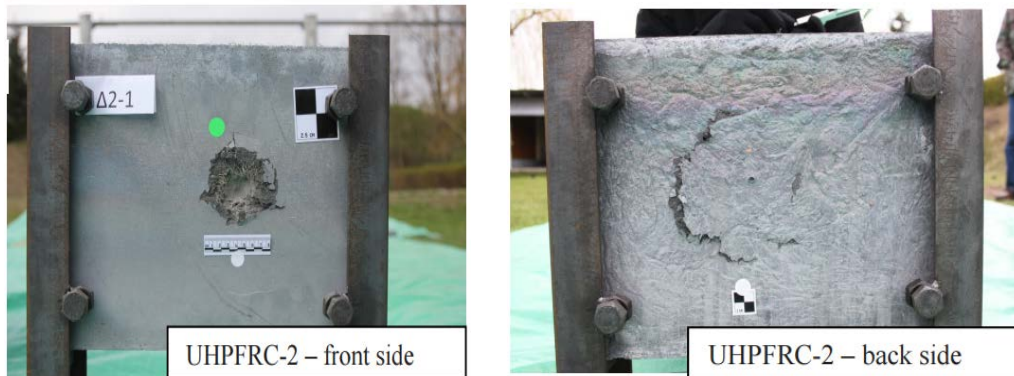


Figure 6. The experimental result of Radoslav Sovják et al. with UHPFRC Slab Subjected to Deformable Projectile Impact.

Table 3. Results after the impact.

Description	UHPFRC	HSC
Projectile	Was stuck	Passed through panel entirely
Residual velocity of Projectile (m/s)	110.62	0
Hole diameter (mm)	13	20
Crater diameter (mm)	48	60
Penetration depth (mm)	42	50

Damage state in the front side and backside of UHPFRC and HSC panels is shown in Figs 4-5 and Table 3. The damage variable had a value of 1.0 and 0.0, when the material was totally damaged (featured in red color) and undamaged, respectively. In the front side of UHPFRC and HSC panel, the damage started to initiate at the impact region with an expansion of the fracture around this region. As seen on the front side of the UHPFRC and HSC panel, the hole formed after the impact was slightly larger than the projectile diameter – 7.92 mm (13 mm in UHPFRC panel and 20 mm in HSC panel). However, the crater (totally damaged region) is about 6 times larger than projectile diameter with the UHPFRC panel and 7.6 times larger with HSC panel, respectively. On the other hand, comparing the hole and crater in UHPFRC and HSC panel, the UHPFRC panel shows a smaller hole diameter (by 35 %) and crater diameter (by 20 %) than the HSC panel. There was no serious damage in the back side of UHPFRC panel. These results are basically similar to the experiments that Radoslav Sovják et. al took with the UHPFRC slabs subjected to deformable projectile impact. UHPFRC material can effectively reduce the damage of impact action.

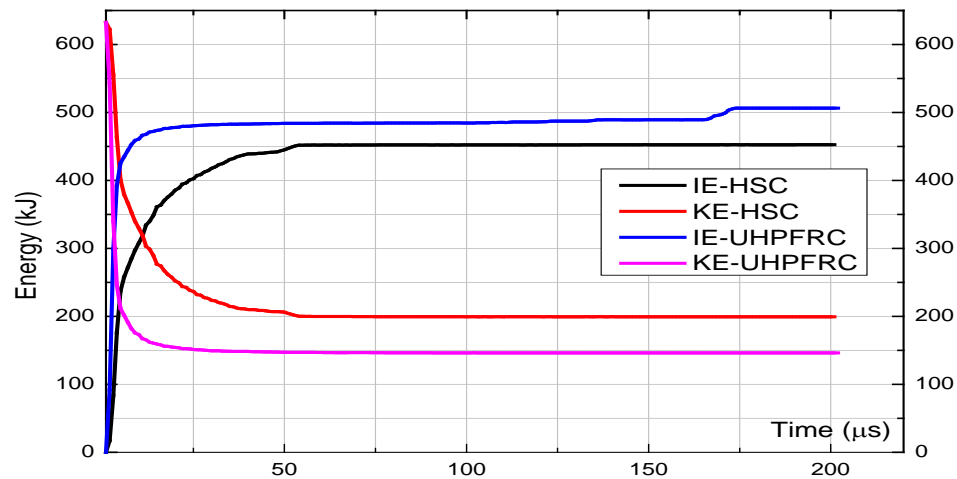


Figure 7. Kinetic energy (KE) of the projectile and internal energy (IE) of panel.

Fig. 7 shows the kinetic energy (KE) of the projectile and the internal energy of panel model (IE) under the 540 m/s of impact velocity. The kinetic energy of the projectile gradually decreased when the projectile penetrating the panel. However, the kinetic energy of the projectile in UHPFRC model (KE-UHPFRC) decreased faster with greater reduction compared to the kinetic energy of the projectile in HSC model (KE-HSC), whereas the internal energy of UHPFRC model (IE-UHPFRC) increased faster than the internal energy of HSC model (IE-HSC). These results should be attributed to the higher energy absorption capacity of the UHPFRC material.

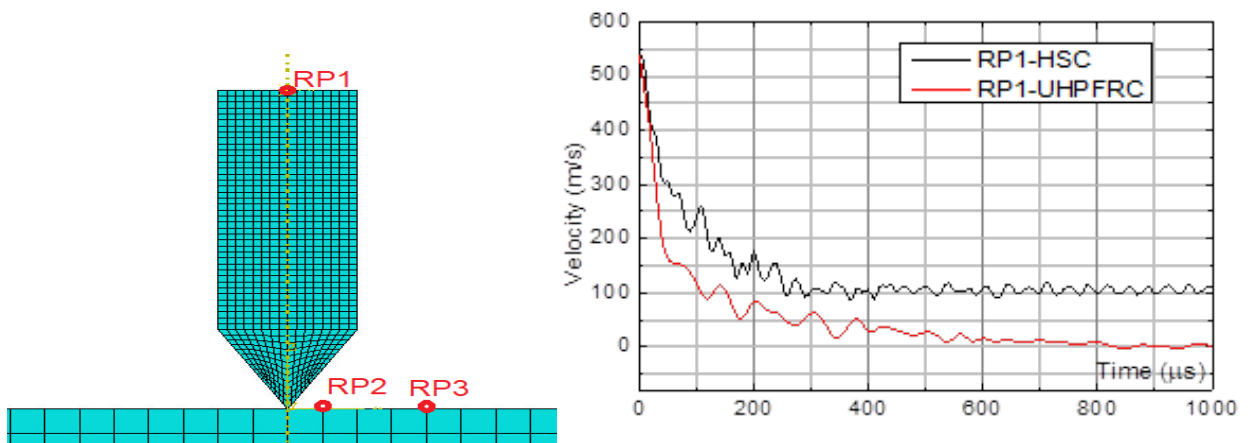


Figure 8. a – Reference points of the model; b – Velocity of RP1 in the projectile.

To evaluate the velocity and acceleration of the model during the impact process, some reference points on the model are chosen, as shown in Fig. 8a.

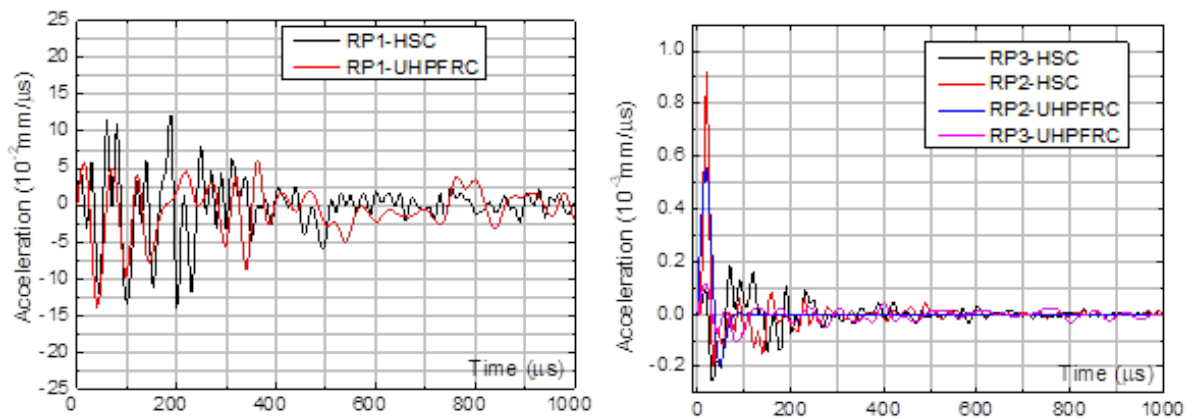


Figure 9. Acceleration of the RP1 in projectile and RP2, RP3 in panel.

Fig. 8b shows the initial velocity of the projectile was 540 m/s, which decreased after the penetration of the HSC panel at 430 μ s. The velocity of the projectile started to become stable, which is due to the full penetration of the projectile into the HSC panel. However, projectile movement speed through the UHPFRC panel was slower than in HSC panel. After the impact, the projectile velocity decreased gradually and was close to zero after 1000 μ s. Compared to HSC material, it can be clearly seen that UHPFRC material can effectively reduce the velocity of projectile.

From Fig. 9a, it can be noticed that the acceleration of RP1 in the projectile of the UHPFRC panel and HSC panel fluctuated at the beginning of the impact. Then, the acceleration of the projectile was close to zero. In Fig. 9b, the acceleration of RP2 and RP3 in the UHPFRC panel was smaller than the HSC panel. This result indicates that damage in HSC was serious than the UHPFRC panel.

4. Conclusions

This research presents the numerical simulation of the UHPFRC panel subjected to high velocity impact. The result of UHPFRC impact model was compared with the results of HSC impact model. The UHPFRC and HSC material was modeled using the Holmquist-Johnson-Cook model and the steel projectile was simulated as a deformable element by Johnson-Cook model. Analyses of the internal energy of the model and the kinetic energy of the steel projectile were conducted. The variations in velocity and acceleration of the projectile and UHPFRC panel, as well as the pressure, were also calculated. From the results addressed in this research, the following conclusions are drawn:

1. The kinetic energy of the projectile was shown to decrease and when the projectile penetrates into the UHPFRC and HSC panel, the panel tended to absorb the energy of the projectile. It was clearly that UHPFRC has much greater resistance to impact loading compared to HSC also in terms of reducing velocity of projectile and absorbing energy efficiently. Moreover, UHPFRC can reduce the crater and scabbing dimensions on the concrete plate, which decreased the mass loss significantly.
2. Holmquist-Johnson-Cook model can be successfully utilized to simulate the process of UHPFRC under high velocity impact of rigid projectile.
3. Through numerical simulations, the design of new protective structures using UHPFRC material and numerical simulation against high-velocity impact in industrial accidents or explosion generated fragments, can be undertaken. However, to avoid perforation and serious damage to the model, parameters like the thickness of the panel, properties of the UHPFRC are important and should be carefully considered.

5. Conflict of Interests

The authors declare that there is no conflict of interests regarding the publication of this paper.

References

1. Wang, D., Shi, C., Wu, Z., Xiao, J., Huang, Z., Fang, Z. A review on ultra high performance concrete: Part II. Hydration, microstructure and properties. *Construction and Building Materials*. 2015. 96. Pp. 368–377. <https://doi.org/10.1016/j.conbuildmat.2015.08.095>
2. Shi, C., Wu, Z., Xiao, J., Wang, D., Huang, Z., Fang, Z. A review on ultra high performance concrete: Part I. Raw materials and mixture design. *Construction and Building Materials*. 2015. 101. Pp. 741–751. <https://doi.org/10.1016/j.conbuildmat.2015.10.088>
3. Mai, V.-C., Nguyen, T.-C., Dao, C.-B. Numerical simulation of ultra-high-performance fiber-reinforced concrete frame structure under fire action. *Asian Journal of Civil Engineering*. 2020. 21. <https://doi.org/10.1007/s42107-020-00240-4>
4. Yoo, D.Y., Banthia, N. Mechanical properties of ultra-high-performance fiber-reinforced concrete: A review. *Cement and Concrete Composites*. 2016. 73. Pp. 267–280. <https://doi.org/10.1016/j.cemconcomp.2016.08.001>

5. Wu, Z., Shi, C., He, W., Wang, D. Static and dynamic compressive properties of ultra-high performance concrete (UHPC) with hybrid steel fiber reinforcements. *Cement and Concrete Composites*. 2017. 79. Pp. 148–157. <https://doi.org/10.1016/j.cemconcomp.2017.02.010>
6. Buttignol, T.E.T., Sousa, J.L.A.O., Bittencourt, T.N. Ultra High-Performance Fiber-Reinforced Concrete (UHPC): a review of material properties and design procedures, *Revista IBRACON de Estruturas e Materiais*. 2017. 10. Pp. 957–971. <https://doi.org/10.1590/s1983-41952017000400011>
7. Azmee, N.M., Shafiq, N. Ultra-high performance concrete: From fundamental to applications, *Case Studies in Construction Materials*. 2018. 9. <https://doi.org/10.1016/j.cscm.2018.e00197>
8. Mai, V.-C., Vu, N.-Q., Pham, H., Nguyen, V.-T. Ultra-High Performance Fiber Reinforced Concrete Panel Subjected to Severe Blast Loading. *Defence Science Journal*. 2020. 70. Pp. 603–611. <https://doi.org/10.14429/dsj.70.15835>
9. Farnam, Y., Mohammadi, S., Shekarchi, M. Experimental and numerical investigations of low velocity impact behavior of high-performance fiber-reinforced cement based composite. *International Journal of Impact Engineering*. 2010. 37. Pp. 220–229. <https://doi.org/10.1016/j.ijimpeng.2009.08.006>
10. Meng, W., Valipour, M., Khayat, K.H. Optimization and performance of cost-effective ultra-high performance concrete. *Materials and Structures/Materiaux et Constructions*. 2017. 50. <https://doi.org/10.1617/s11527-016-0896-3>
11. Pham, T.M., Hao, H. Impact Behavior of FRP-Strengthened RC Beams without Stirrups. *Journal of Composites for Construction*. 2016. [https://doi.org/10.1061/\(ASCE\)CC.1943-5614.0000671](https://doi.org/10.1061/(ASCE)CC.1943-5614.0000671)
12. Li, J., Wu, C., Hao, H. An experimental and numerical study of reinforced ultra-high performance concrete slabs under blast loads. *Materials and Design*. 2015. 82. Pp. 64–76. <https://doi.org/10.1016/j.matdes.2015.05.045>
13. Xu, J., Wu, C., Xiang, H., Su, Y., Li, Z.X., Fang, Q., Hao, H., Liu, Z., Zhang, Y., Li, J. Behaviour of ultra high performance fibre reinforced concrete columns subjected to blast loading. *Engineering Structures*. 2016. 118. Pp. 97–107. <https://doi.org/10.1016/j.engstruct.2016.03.048>
14. Yoo, D.Y., Banthia, N. Mechanical and structural behaviors of ultra-high-performance fiber-reinforced concrete subjected to impact and blast. *Construction and Building Materials*. 2017. 149. Pp. 416–431. <https://doi.org/10.1016/j.conbuildmat.2017.05.136>
15. Mai, V.-C., Vu, N.-Q. Assessment of Dynamic Response of 3D Ultra High Performance Concrete Frame Structure under High Explosion Using Johnson-Holmquist 2 Model. *KSCE Journal of Civil Engineering*. 2020. 00. Pp. 1–11. <https://doi.org/10.1007/s12205-020-1373-7>
16. Erzar, B., Pontiroli, C., Buzaud, E. Ultra-high performance fibre-reinforced concrete under impact: Experimental analysis of the mechanical response in extreme conditions and modelling using the Pontiroli, Rouquand and Mazars model. *Philosophical Transactions of the Royal Society A: Mathematical, Physical and Engineering Sciences*. 2017. 375. <https://doi.org/10.1098/rsta.2016.0173>
17. Sovják, R., Vavřínek, T., Máca, P., Zatloukal, J., Konvalinka, P., Song, Y. Experimental investigation of ultra-high performance fiber reinforced concrete slabs subjected to deformable projectile impact. *Procedia Engineering*. 2013. 65. Pp. 120–125. <https://doi.org/10.1016/j.proeng.2013.09.021>
18. Kravanja, S., Sovják, R. Ultra-high-performance fibre-reinforced concrete under high-velocity projectile impact. Part I. experiments. *Acta Polytechnica*. 2018. 58. Pp. 232–239. <https://doi.org/10.14311/AP.2018.58.0232>
19. Lai, J., Yang, H., Wang, H., Zheng, X., Wang, Q. Properties and modeling of ultra-high-performance concrete subjected to multiple bullet impacts. *Journal of Materials in Civil Engineering*. 2018. 30. Pp. 1–11. [https://doi.org/10.1061/\(ASCE\)MT.1943-5533.0002462](https://doi.org/10.1061/(ASCE)MT.1943-5533.0002462)
20. Holmquist, T.J., Johnson, G.R., Cook, W.H. A computational constitutive model for concrete subjected to large strains, high strain rates, and high pressures. *Proc 14th International Symposium on Ballistics, Quebec, 1993*.

Contacts:

Viet-Chinh Mai, maivietchinhce@gmail.com

Xuan-Bach Luu, xuanbachmta@gmail.com

Van-Tu Nguyen, nguyentu@lqdtu.edu.vn



DOI: 10.34910/MCE.107.4

Structural reliability analysis using evidence theory and fuzzy probability distributions

S.A. Solovyev* , **A.A. Soloveva**
Vologda State University, Vologda, Russia
*E-mail: ser6sol@yandex.ru

Keywords: durability, reliability, structural mechanics, failure probability, structural design, steel truss, safety, interval data, strength

Abstract. A structural element failure probability (as a structural reliability measure) is an indicator of the structural safety. Approaches for structural reliability analysis with incomplete statistical data are a special scientific problem. In the development of this scientific direction, the article proposed a method for structural reliability analysis based on a combination of evidence theory and fuzzy probability distributions when the problem of reliability analysis involves quantitative and qualitative uncertainty at the same time. The article presents an experimental study of reliability analysis for a steel truss by the truss members strength criterion based on various approaches to reliability analysis. The reliability interval $[0.99272; 1]$ of the proposed method covers the FOSM (First Order Second Moment) reliability value of 0.99354. From the experiment results, it follows that the proposed approach can be used in practice for a more cautious assessment of the structural reliability with incomplete statistical information. The proposed approach also allows reducing the number of tests and getting an operational (preliminary) assessment of the structural element reliability. The value of the acceptable reliability level in discrete or interval form should be set individually for each design situation taking into account the risk of economic and non-economic losses.

1. Introduction

Evaluation the safety of structural elements during manufacture, construction and operation is one of the most important tasks for a civil engineer. The structural reliability theory is often used for the quantitative assessment of structural safety.

The origin of research on the structural reliability theory is considered to be the beginning of the twentieth century. John Tucker Jr. [1], M. Mayer, N.F. Hocialov presented researches on probabilistic analysis of the structures behavior. Later, soviet scientists A.R. Rzhanitsyn, N.S. Streletsky made a significant contribution to the formation of the existing theory of structural reliability.

Structural reliability analysis for incomplete statistical information is one of the important current tasks of reliability theory as a science. Relevance of this direction is emphasized by the major conference – 13th International Conference on Applications of Statistics and Probability in Civil Engineering (ICASP13) in Seoul, South Korea. The article [2] notes that the structural reliability theory has become one of the main methods of structural safety design in recent years. Reliability analysis has been increasingly applied to structural design and structural assessment due the uncertainties involved with material, load and geometric properties [3]. The research [4] also notes that it is well known that the inevitable uncertainties inherent in both load and resistance of the structure will seriously affect its safety and serviceability, and hence, reliability analysis plays an important role in structural engineering. The subject of this paper is the reliability of a structural element which is expressed as a failure probability or a probability of non-failure (safety).

Solovyev, S.A., Soloveva, A.A. Structural reliability analysis using evidence theory and fuzzy probability distributions. Magazine of Civil Engineering. 2021. 107(7). Article No. 10704. DOI: 10.34910/MCE.107.4

© Solovyev, S.A., Soloveva, A.A., 2021. Published by Peter the Great St. Petersburg Polytechnic University.



This work is licensed under a CC BY-NC 4.0

FORM (First Order Reliability Method) [5], SORM (Second Order Reliability Method) [6] and Monte Carlo simulation (MSC) [7] are most common approaches for structural reliability analysis. These methods are based on complete statistical information when the cumulative distribution function (CDF), the parameters of CDF, information about the dependence / independence of random variables, etc. are known. The problem of a limited statistical data often arises in practical problems of reliability analysis. A quantitative limitation of statistical data is a small sample size. A qualitative limitation of statistical data is an inaccurate (interval) estimate of a single value from a general or sample population.

Special methods of structural reliability analysis were developed to take into account the factor of statistical data fuzziness. Methods based on the provisions of fuzzy set theory and the theory of possibilities has received great development. H. Li and X. Nie [8] present a novel structural reliability analysis method with fuzzy random variables from the perspective of error propagation. Fuzzy numbers are used in research [9] to define an equivalence class of probability distributions compatible with available data and corresponding upper and lower cumulative density functions. A procedure is then proposed to perform reliability analysis using extended fuzzy operations. It gives estimates of small and large fractiles of output variables which are conservative with respect to probability. The paper [10] presents a novel algorithm for obtaining membership function of fuzzy reliability with interval optimization based on Line Sampling (LS) method. Methods for structural reliability analysis were developed based on the evidence theory (or Dempster-Shafer theory) and random set theory for modeling random variables with limited statistical data. Evidence theory employs a much more general and flexible framework to quantify the epistemic uncertainty, and thereby it is adopted to conduct reliability analysis for engineering structures recently [11]. The paper [11] proposes a response surface (RS) method to evaluate the reliability for structures using evidence theory, and hence improves its applicability in engineering problems. The article [12] presents the evidence theory model based on the copula function and the related structural reliability analysis method. It is an effective tool for uncertainty modeling and reliability analysis with dependent evidence variables. Random set theory is used for calculating the upper and lower bounds on the failure probability in the research [13]. The method allows the modulation of dependence between the input variables by means of copulas.

The relevance of this research is due to the great interest of the scientific community to probabilistic methods of structural mechanics and a reliability theory for evaluating the structural safety. In addition, there are separate methods for reliability analysis based on evidence theory and fuzzy set theory, but there is no generalized approach to reliability analysis based on a combination of evidence theory and fuzzy probability distributions taking into account the impact on reliability of uncertainties in the form of a small number of intervals and the degree of confidence in expert estimates, instruments, methods, etc.

In this regard, the purpose of this research is to develop a method for structural reliability analysis based on the combination of the evidence theory and fuzzy probability distributions.

2. Methods

As noted above, some random variables can be represented by a subset of intervals as $x \in x_i^I = \{[\underline{x}_i, \bar{x}_i]\}$, where \underline{x}_i and \bar{x}_i are the lower and upper value of the i -th interval of a random variable. In practical problems, these can be intervals of measured values in different time periods, a set of confidence intervals when using different measurement tools and methods, etc. Random set theory and evidence theory can be used for statistical analysis of a subset of interval values. In the evidence theory, an interval random variable can be described by two boundary distribution functions. According to researches [14, 15], the upper boundary distribution function is called the "belief function" and denoted as $Bel(A)$ and the lower boundary distribution function is called the "plausible function" and denoted as $Pl(A)$, where A is a set consisting of subsets (A_i) in Ω (set of all values).

If random value X , then x_i^I is the subset of the x set. Let C_i is a number of observed subsets A_i . Then in according to [10]:

$$Bel(A) = \sum_{A_i: A_i \subseteq A} m(A_i), \quad (1)$$

$$Pl(A) = \sum_{A_i: A_i \cap A \neq \emptyset} m(A_i), \quad (2)$$

where $m(A_i) = C_i/N$ with N is a number of measurements (a number of intervals) and C_i is a number of observed subsets A_i .

Hence, $Bel(A)$ and $Pl(A)$ can be considered as the lower and upper probability of A as $Bel(A) \leq P(A) \leq Pl(A)$.

The limit state mathematical model for reliability analysis can be written in the form:

$$X \leq Y. \tag{3}$$

where X is a generalized load (load, stress, bending moment, etc.); Y is a generalized strength (maximum allowable stress, ultimate deformations, etc.).

The probability of non-failure P [16] of the condition $X \leq Y$ is defined by the equation:

$$P(X \leq Y) = \int_0^{\infty} f_Y(y) F_X(y) dy, \tag{4}$$

where $f_Y(y)$ is a probability density function of the random variable Y by variable y ; $F_X(y)$ is a probability density function of the random variable X by variable y .

Let X is described by a subset of intervals $\{[\underline{x}_i, \bar{x}_i]\}$, and Y is described by some fuzzy probability distribution functions. Conditional view of distribution function X and Y graphs is shown on Fig. 1.

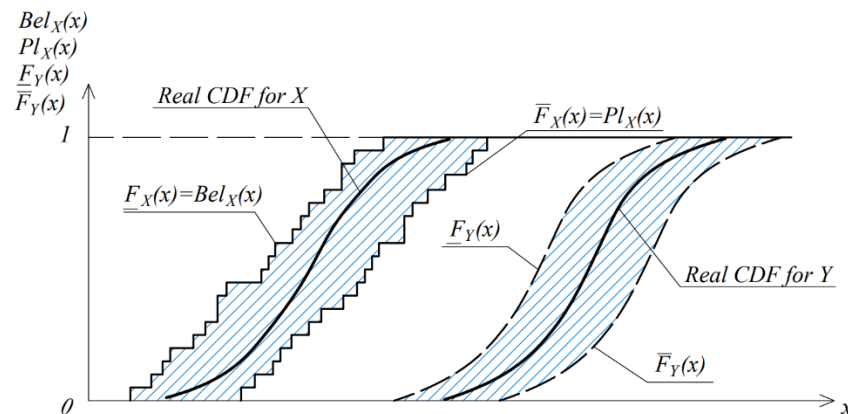


Figure 1. Graphs of the belief $Bel_X(x)$ and plausible $Pl_X(x)$ functions of the random value X and the probability distribution functions of the fuzzy value Y ; CDF – cumulative distribution function.

Graphically, as well as analytically from dependencies (1), (2) and (4), the equations can be figured out to calculate the lower \underline{Q} and upper \bar{Q} boundaries of the failure probability by (3) in general form:

$$\Pr(X \leq Y) = \begin{cases} \underline{Q} = n^{-1} \cdot \sum_{i=1}^n \bar{F}_Y(\underline{x}_i) \\ \bar{Q} = n^{-1} \cdot \sum_{i=1}^n F_Y(\bar{x}_i) \end{cases}. \tag{5}$$

where n is a number of intervals $\{[\underline{x}_i, \bar{x}_i]\}$.

The non-failure probability interval is related to the failure probability interval by the following equation $[\underline{P}; \overline{P}] = [1 - \overline{Q}; 1 - \underline{Q}]$. Structural reliability will be characterized by an interval $[\underline{P}; \overline{P}]$.

Such approach is also called a p -boxes (probability boxes) approach.

Let us consider the case where the "strength" Y is described by the fuzzy distribution functions (based on the possibility theory [17]) with the analytical form:

$$\overline{F}_Y(y) = \begin{cases} 1 - \exp\left[-\left(\frac{y - a_y}{b_y}\right)^2\right] & \text{if } y > a_y, \\ 0 & \text{otherwise} \end{cases}, \quad (6)$$

$$\underline{F}_Y(y) = \begin{cases} \exp\left[-\left(\frac{y - a_y}{b_y}\right)^2\right] & \text{if } y < a_y, \\ 1 & \text{otherwise} \end{cases}, \quad (7)$$

where a_y is a "mean" value which is calculated as $a_y = 0.5(Y_{\max} + Y_{\min})$; b_y is a measure of variance which is calculated as $b_y = 0.5(Y_{\max} - Y_{\min})/\sqrt{-\ln \alpha}$, where Y_{\max} and Y_{\min} is a maximum and a minimum value in the set of $\{Y\}$; α is a cut (risk) level [18, 19].

Other fuzzy distributions can be used to model an uncertainty as p -box. For example, the distribution functions based on the Chebyshev's inequality [20] with the analytical form:

$$\underline{F}_Y(y) = \begin{cases} \frac{S_Y^2}{(m_Y - y)^2 + S_Y^2}, & \text{for } y < m_Y, \\ 1, & \text{for } y \geq m_Y \end{cases},$$

$$\overline{F}_Y(y) = \begin{cases} 0, & \text{if } y < m_Y \\ 1 - \frac{m_Y}{y}, & \text{if } m_Y \leq y \leq m_Y + \frac{S_Y^2}{m_Y}, \\ \frac{(m_Y - y)^2}{(m_Y - y)^2 + S_Y^2}, & \text{if } y > m_Y + \frac{S_Y^2}{m_Y} \end{cases},$$

where m_Y , S_Y is an expected value and a standard deviation for random variable Y .

For a more convenient using of the proposed approach, let us consider the case of reliability analysis for a small number of intervals in subset. The research [15] is proposed to use the extended belief and plausible functions based on the generalized Dirichlet model as a type of robust models. The upper and the lower bound of the non-failure probability can be written as:

$$\underline{P}(A|c, s) = \frac{N \cdot Bel(A)}{N + s} = \chi Bel(A) \text{ and } \overline{P}(A|c, s) = \frac{N \cdot Pl(A) + s}{N + s} = 1 - \chi [1 - Pl(A)], \quad (8)$$

where N is a number of tests (measurements); s is a parameter that characterizes the measure of uncertainty; $\chi = (1 + s/N)^{-1}$, $\chi \in [0; 1]$. Some recommendations for assigning the s parameter are given in the paper [21].

In a simplified form, the expressions for reliability based on the robust Dirichlet model and the above approach can be written as:

$$\left[\underline{P}; \bar{P} \right] = \left[\chi \underline{P}; 1 - \chi \underline{Q} \right]. \tag{9}$$

In accordance with research [15], the values of the expectation bounds of an interval random variable X also can be found by the equations:

$$\underline{E}X = \int_{\Omega} \omega d\bar{F}(\omega|c, s) = (N + s)^{-1} \left(s \cdot \Omega_* + \sum_{i=1}^n c_i \inf A_i \right),$$

$$\bar{E}X = \int_{\Omega} \omega dF(\omega|c, s) = (N + s)^{-1} \left(s \cdot \Omega^* + \sum_{i=1}^n c_i \sup A_i \right).$$

For more information on this issue, see [14].

3. Results and Discussion

P-box approaches can be successfully applied in practical problems of reliability analysis. The random variable values were generated by the PTC MathCAD program with statistical parameters: expected value $m_X = 300$ MPa and standard deviation $S_X = 15$ MPa. The obtained values are the result of a numerical experiment to assess the steel strength of some structural element. The following values were obtained from data generation results: $X \in \{303.58; 289.73; 275.78; 321.17; 314.57; 282.66; 302.16; 325.46\}$ MPa. Fig. 2 shows the graphs of the empirical probability distribution functions $F_X^{emp}(x)$ based on 8 values and the normal probability distribution graph $F_X(x)$ if full statistical information is available.

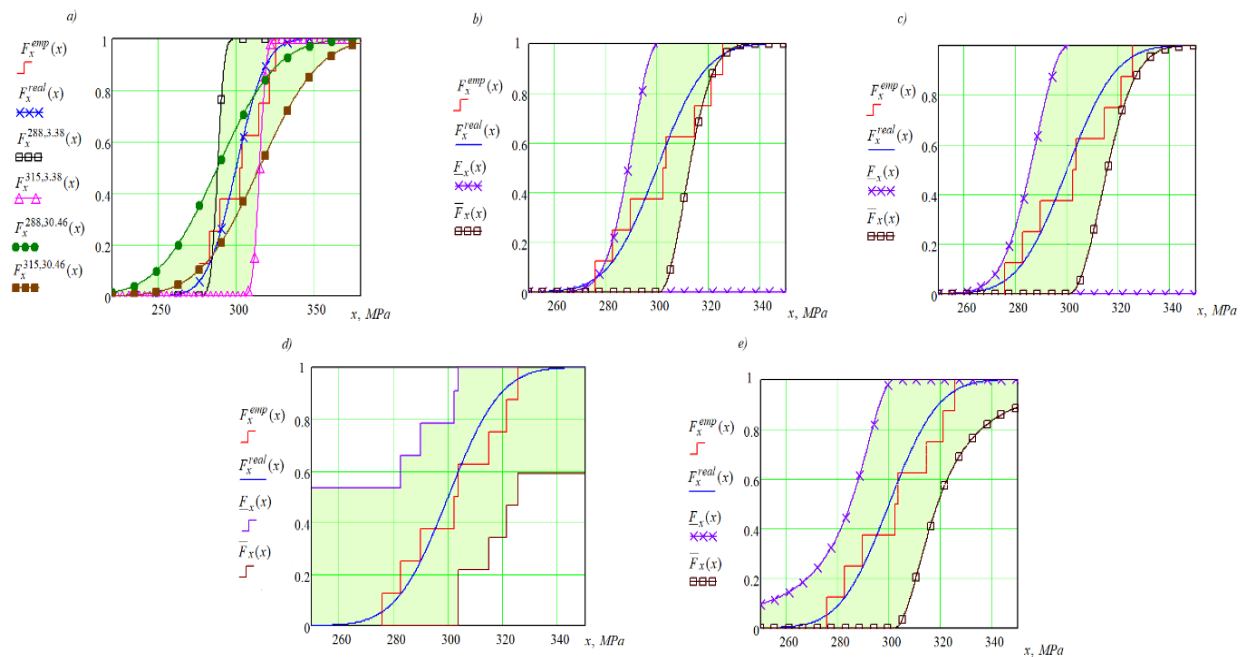


Figure 2. Different p-box cases of incomplete statistical data:
a) Combinations of normal distribution interval parameters; b) Fuzzy distribution functions with $\alpha = 0.05$; c) Fuzzy distribution functions with $\alpha = 0.15$; d) Kolmogorov-Smirnov bounds; e) Boundary distribution functions based on Chebyshev's inequality [20].

As can be seen from Fig. 2, there are various p-box approaches for modeling the incompleteness of statistical data in reliability analysis problems. Each p-block is applied depending on the quantity and quality of the initial statistical data about the random variable.

The proposed approach is considered on the example of the steel planar truss reliability analysis. The design scheme of the truss is shown in Fig. 3.

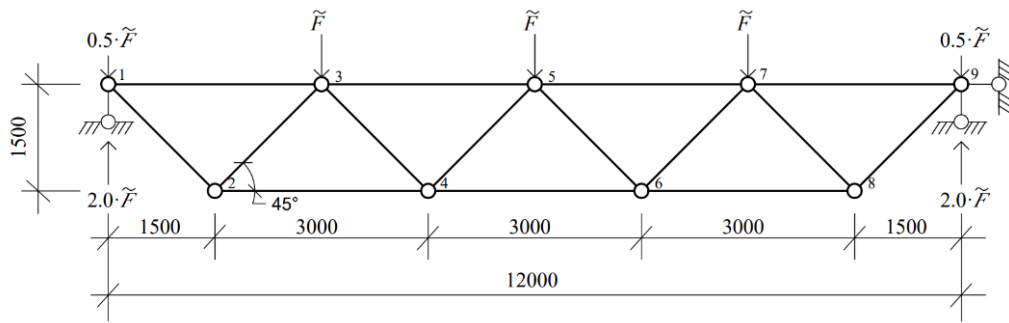


Figure 3. Planar truss design scheme.

The mathematical model of the limit state can be formed for any truss member (bar) in the form:

$$\tilde{N}_{i-j}(\tilde{F}) \leq \tilde{N}_{i-j,ult}, \quad (10)$$

where $\tilde{N}_{i-j,ult}$ is an ultimate longitudinal force for the $i-j$ truss member (bar).

The ultimate force $\tilde{N}_{i-j,ult}$ for the $i-j$ truss member can be determined by various criteria of limit states.

For example, according to the criterion of the strength of a steel truss member:

$$\tilde{N}_{i-j}(\tilde{F}) \leq \tilde{N}_{i-j,ult} = \tilde{\sigma}_{s,ult} \cdot A, \quad (11)$$

where A is a cross-sectional area of the truss member; $\tilde{\sigma}_{s,ult}$ is an ultimate stress in the steel of the truss member (random value).

Another important limit state criterion is a buckling of truss compressed members. In that case, design mathematical model can be written as: $\tilde{N}_{i-j}(\tilde{F}) \leq \tilde{N}_{i-j,ult} = \tilde{\sigma}_{s,ult} \cdot A \cdot \phi(\tilde{\sigma}_{s,ult})$, where ϕ is a buckling factor. In this research, the application of the proposed approach is presented in the case of the truss reliability analysis by the criterion of the truss member's strength using mathematical model (11).

Since the loads included in the mathematical model (11) are described by different probability distribution functions, the model (11) can be written as:

$$\tilde{N}_{i-j}(\tilde{F}_{snow}) \leq \tilde{N}_{i-j,ult} - \tilde{N}_{i-j}(\tilde{F}_{sw}), \quad (12)$$

where $\tilde{N}_{i-j}(\tilde{F}_{snow})$ is a force in $i-j$ truss member from the snow load; $\tilde{N}_{i-j}(\tilde{F}_{sw})$ is force in $i-j$ truss member from the truss and the structural cover self-weight load.

In a generalized form, inequality (12) can be written as $X \leq Y$, which is analogous to inequality (3).

Table 1. The forces in the truss members by Fig. 3.

Member	Force	Member	Force
1-2, 8-9	$\tilde{N}_{1-2} = +\frac{3 \cdot \tilde{F}}{\sqrt{2}}$	3-4, 6-7	$\tilde{N}_{3-4} = +\frac{\tilde{F}}{\sqrt{2}}$
1-3, 7-9	$\tilde{N}_{1-3} = -1.5 \cdot \tilde{F}$	3-5, 5-7	$\tilde{N}_{3-5} = -3.5 \cdot \tilde{F}$
2-3, 7-8	$\tilde{N}_{2-3} = -\frac{3 \cdot \tilde{F}}{\sqrt{2}}$	4-5, 5-6	$\tilde{N}_{4-5} = -\frac{\tilde{F}}{\sqrt{2}}$
2-4, 6-8	$\tilde{N}_{2-4} = +3 \cdot \tilde{F}$	4-6	$\tilde{N}_{4-6} = +4 \cdot \tilde{F}$

The maximum force in the truss with the design scheme according to Fig. 3 will occur in the member 4-6: $\tilde{N}_{4-6} = +4 \cdot \tilde{F}$. The mathematical model of the limit state will take the form for analyzing the reliability of this truss member:

$$\tilde{N}_{4-7}(\tilde{F}_{snow}) \leq \tilde{N}_{4-7,ult} - \tilde{N}_{4-7}(\tilde{F}_{sw}). \quad (13)$$

The force from snow load $\tilde{N}_{4-7}(\tilde{F}_{snow})$ can be described by the belief and plausibility functions in the conditions of real snow load data analysis. Data on the maximum snow cover heights of Vologda [22] will be used for reliability analysis example of the truss member (bar). The snow density on the truss surface is one of the uncertainty factors in the reliability analysis. The density of accumulated snow can vary within interval [200; 400] kg/m³, in accordance with Russian State Standard GOST 53613-2009 "Influence of environmental conditions appearing in nature on the technical products. Overall performance. Precipitation and wind". By multiplying the interval of possible snow density on the maximum snow, cover heights over the last 50 years, boundary empirical cumulative distribution functions can be constructed for the distribution of snow cover weight \tilde{S} (Fig. 4).

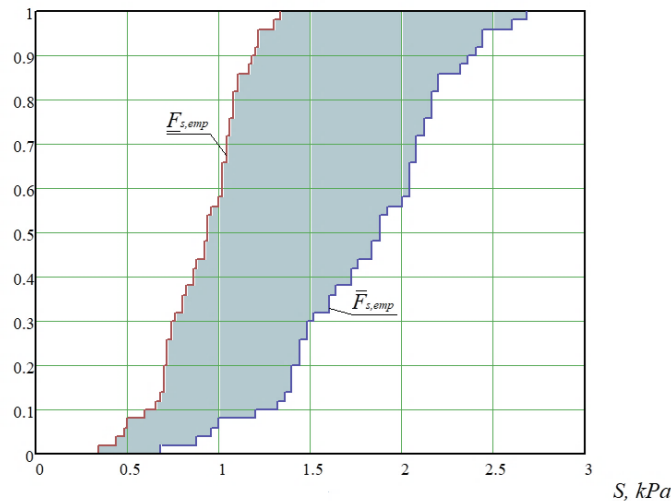


Figure 4. Boundary empirical cumulative distribution functions $\underline{F}_{s,emp}$ and $\overline{F}_{s,emp}$ for snow weight (kPa) in Vologda, Russia.

If to take the distance between the trusses 6 m for considered example, then the load area per node will be 18 m². The level part of (13) inequality can be written as:

$$\tilde{N}_{4-7}(\tilde{F}_{snow}) = \tilde{X} = 18 \cdot 4 \cdot \tilde{S} = 72 \cdot \tilde{S}. \quad (14)$$

The right part of (13) is described by the fuzzy probability distribution functions (6)-(7). There is subtraction of the fuzzy variables $\tilde{N}_{4-7,ult} = A \cdot \tilde{\sigma}_{s,ult}$ and $\tilde{N}_{4-7} = 4 \cdot \tilde{F}_{sw}$. The design parameters a_Y and b_Y can be calculated as: $a_Y = A \cdot a_{\sigma,ult} - 4 \cdot a_{F,sw}$, $b_Y = A \cdot b_{\sigma,ult} + 4 \cdot b_{F,sw}$, where $a_{\sigma,ult} = 0.5(\sigma_{s,ult,max} + \sigma_{s,ult,min})$, $b_{\sigma,ult} = 0.5(\sigma_{s,ult,max} - \sigma_{s,ult,min}) / \sqrt{-\ln \alpha}$, and $a_{F,sw} = 0.5(F_{sw,max} + F_{sw,min})$, $b_{F,sw} = 0.5(F_{sw,max} - F_{sw,min}) / \sqrt{-\ln \alpha}$. $\sigma_{s,ult,max}$, $\sigma_{s,ult,min}$ and $F_{sw,max}$, $F_{sw,min}$ are maximum and minimum values of fuzzy variables $\tilde{\sigma}_{s,ult}$ and \tilde{F}_{sw} obtained by tests and estimations.

For considered example, let the truss member 4-6 have a cross-section of a rectangular tube 100×5 mm with a cross-sectional area $A_{4-6} = 18.57 \cdot 10^{-4}$ m². Control samples of steel were tested for tensile strength. The minimum and maximum ultimate stress values during the tests are $\sigma_{s,ult,max} = 310$ MPa and $\sigma_{s,ult,min} = 290$ MPa. By collecting loads from the self-weight of the truss and the self-weight of the structural cover, the maximum and minimum values of loads in the truss node are $F_{sw,max} = 86$ kN and $F_{sw,min} = 74$ kN.

The parameters of the fuzzy probability distribution functions are $a_{\sigma,ult} = 300$ MPa, $b_{\sigma,ult} = 5.78$ MPa, $a_{F,sw} = 80$ kN, $b_{F,sw} = 3.47$ kN. Then $a_Y = 237.1$ kN; $b_Y = 24.61$ kN.

P-boxes of the random variables X and Y show at the Fig. 5.

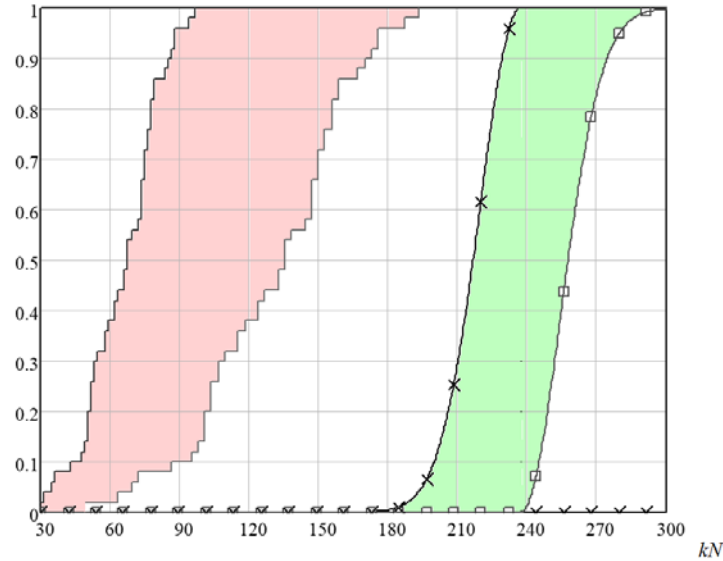


Figure 5. P-boxes of random variables X and Y.

The failure probabilities (5) are:

$$\underline{Q} = n^{-1} \cdot \sum_{i=1}^n \bar{F}_Y(x_i) \rightarrow \frac{1}{50} \cdot (50 \cdot 0) = 0,$$

$$\bar{Q} = n^{-1} \cdot \sum_{i=1}^n F_Y(\bar{x}_i) \rightarrow \frac{0.064}{50} = 0.00128.$$

These failure probability values are obtained with full confidence to experts and the complete set of interval data. To adjust the reliability value, we will introduce the uncertainty measure χ , since the number of intervals was small. We will consider the parameter χ as the confidence degree to expert estimates of a statistical subset or an assessment of the accuracy of measuring instruments or methods.

$$\text{If to take } s = 0.3, \text{ then } \chi = (1 + s/N)^{-1} \rightarrow (1 + 0.3/50)^{-1} = 0.9940.$$

The probability of non-failure is $P' = \chi \underline{P} = \chi(1 - \bar{Q}) = 0.99872 \cdot 0.99400 = 0.99272$ and $\bar{P}' = 1 - \chi \bar{Q} = 1 - 0 = 1$.

The reliability of the steel truss bar according to the steel strength [24] criterion is characterized by the interval [0.99272; 1].

The theoretical reliability value can be calculated using the FOSM (First Order Second Moment) approach by equation [16]:

$$P = \int_0^{+\infty} f_X(x) \cdot F_Y(x) dx, \quad (15)$$

where $f_X(x)$ is a probability density function (PDF) for the random variable \tilde{X} ; $F_Y(x)$ is a cumulative distribution function (CDF) for the random variable \tilde{Y} in the mathematical model (3).

The random variable \tilde{X} can be described by Gumbel distribution (or Generalized Extreme Value distribution Type-I) [22]. The random variable \tilde{Y} can be described by normal distribution in accordance with Eurocode 0 "Basis of structural design". Using following PDF and CDF [16] for the random variables \tilde{X} and \tilde{Y} , the equation (15) can be presented as:

$$P = \frac{1}{S_Y \sqrt{2\pi}} \cdot \int_0^{+\infty} \exp\left[-\exp\left(\frac{\alpha-x}{\beta}\right)\right] \cdot \exp\left[-\frac{(x-m_Y)^2}{2S_Y^2}\right] dx, \quad (16)$$

or:

$$P = 1 - \frac{1}{2\beta} \cdot \int_0^{+\infty} \exp\left[\frac{\alpha-x}{\beta} - \exp\left(\frac{\alpha-x}{\beta}\right)\right] \cdot \left[1 + \operatorname{erf}\left(\frac{x-m_Y}{\sqrt{2S_Y^2}}\right)\right] dx, \quad (17)$$

where α and β are Gumbel's distribution parameters; $\operatorname{erf}()$ is the error function.

Let $\alpha = 1.08 \text{ kPa} \cdot 72 \text{ m}^2$ and $\beta = 0.41 \text{ kPa} \cdot 72 \text{ m}^2$ by the [22] recommendations; $m_Y = 237 \text{ kN}$ and $S_Y = 25 \text{ kN}$ similarly with the a_Y and b_Y parameters above.

The result of the numerical experiment in the form of reliability 0.99354 also fell into the interval obtained within the framework of inaccurate interval and fuzzy estimates [0.99272; 1]. Therefore, the proposed method of reliability analysis can be used in engineering practice of structural reliability analysis.

Reliability intervals for other truss member can be obtained by a similar approach. The structural reliability interval for the strength of the whole truss as the structural system can be calculated [15] as:

$$\begin{cases} \underline{P} = \max\left(0, \sum_{i=1}^n \underline{P}_i - (n-1)\right), \\ \bar{P} = \min(\bar{P}_i) \end{cases}$$

where \underline{P}_i and \bar{P}_i are lower and upper bounds of non-failure probability for i -th member of the truss; n is a number members in the truss.

The table with reliability intervals for truss bars can be formed for a plane truss. Table 2 contains the example of such table.

Table 2. Reliability of planar truss elements.

Planar truss element (Fig. 1)	\underline{P}	\bar{P}
1-2	0.99420	1.00000
1-3	0.99920	1.00000
2-3	0.99420	1.00000
2-4	0.99670	1.00000
3-4	0.99750	1.00000
3-5	0.99284	0.99994
4-5	0.99750	1.00000
4-6	0.99272	1.00000
5-6	0.99750	1.00000
5-7	0.99284	0.99993
6-7	0.99750	1.00000
6-8	0.99670	1.00000
7-8	0.99420	1.00000
7-9	0.99920	1.00000
8-9	0.99420	1.00000

For statistical data in the Table 2, the following bounds can be obtained:

$$\underline{P} = \max \left(0, \sum_{i=1}^n \underline{P}_i - (n-1) \right) = 14.9370 - (15-1) = 0.9370,$$

$$\overline{P} = \min(\overline{P}_i) = 0.99993.$$

The reliability of planar truss is [0.93700; 0.99993]. If this interval is too wide to make a decision about the level of truss safety, then it needs to improve the quality of statistical information: refine probability functions of distributions, increase the number of control samples, etc.

Target values for the reliability index β for various design situations, and for reference periods of 1 year and 50 years, are indicated in Appendix C, Eurocode 0 "Basis of structural design". For example, reliability index for serviceability limit state (for reference periods of 1 year) is $\beta = 2.9$. Joint Committee on Structural Safety (JCSS) Probabilistic Model Code sets target values for the reliability index β in dependence with a comparative cost of safety measures and failure consequences. However, the reliability index should be calculated individually for each structure (and structural element) based on a value of an acceptable risk [25, 26].

4. Conclusions

1. The article proposes the method for structural reliability analysis with limited statistical information about random variables: some random variables are described by a subset of interval data and others by some fuzzy probability distribution.

2. The reliability analysis examples were considered for the steel truss by the steel strength criterion based on various approaches to reliability analysis;

3. The reliability interval [0.99272; 1] by proposed method covers the reliability values by the FOSM approach 0.99354. Thus, the proposed approach allows obtaining a more cautious reliability interval for an incomplete statistical information case.

References

1. Tucker, J.Jr. A study of the compressive strength dispersion of materials with applications. Journal of the Franklin Institute. 1927. 204. Pp. 751–781. URL: doi.org/10.1016/S0016-0032(27)92044-4
2. Kang, Y.M., Di, X. Failure Mode and Reliability Analysis of Frame Structure. 13th International Conference on Applications of Statistics and Probability in Civil Engineering (ICASP13). Seoul, South Korea. 2019. doi.org/10.22725/ICASP13.170
3. Xiang, Z., Bao, Y. An Efficient Algorithm for Structural Reliability Based on Dichotomy Method. 13th International Conference on Applications of Statistics and Probability in Civil Engineering (ICASP13). Seoul, South Korea. 2019. doi.org/10.227-25/ICASP13.012
4. Zhong, C., Wang, M., Dang, C., Ke, W. Structural reliability assessment by salp swarm algorithm–based FORM. Quality and Reliability Engineering International. 2020. Pp. 1–21. doi.org/10.1002/qre.2626
5. Maier, H.R., Lence, B.J., Tolson, B.A., Foschi, R.O. First-order reliability method for estimating reliability, vulnerability, and resilience. Water Resources Research. 2001. 37(3). Pp. 779–790. URL: https://agupubs.onlinelibrary.wiley.com/doi/pdf/10.1029/2000WR900329
6. Zhang, J., Du, X. A second-order reliability method with first-order efficiency. Journal of Mechanical Design. 2010. 132(10). Pp. 1–8. doi.org/10.1115/1.4002459
7. Proppe, C. Markov Chain Monte Carlo Simulation Methods for Structural Reliability Analysis. Procedia engineering. 2017. 199. Pp. 1122–1127. doi.org/10.1016/j.proeng.2017.09.226
8. Li, H., Nie, X. Structural reliability analysis with fuzzy random variables using error principle. Engineering Applications of Artificial Intelligence. 2018. 67. Pp. 91–99. doi.org/10.1016/j.engappai.2017.08.015
9. Savoia, M. Structural reliability analysis through fuzzy number approach, with application to stability. Computers & Structures. 2002. 80(12). Pp. 1087–1102. doi.org/10.1016/S0045-7949(02)00068-8
10. Li, L., Lu, Z. Interval optimization based line sampling method for fuzzy and random reliability analysis. Applied Mathematical Modelling. 2014. 38(13). Pp. 3124–3135. doi.org/10.1016/j.apm.2013.11.027
11. Zhang, Z., Jiang, C., Han, X., Hu, D., Yu, S. A response surface approach for structural reliability analysis using evidence theory. Advances in Engineering Software. 2014. 69. Pp. 37–45. doi.org/10.1016/j.advengsoft.2013.12.005
12. Jiang, C., Zhang, W., Wang, B., Han, X. Structural reliability analysis using a copula-function-based evidence theory model. Computers & Structures. 2014. 143. Pp. 19–31. doi.org/10.1016/j.compstruc.2014.07.007
13. Alvarez, D.A., Hurtado, J.E. An efficient method for the estimation of structural reliability intervals with random sets, dependence modeling and uncertain inputs. Computers & Structures. 2014. 142. Pp. 54–63. doi.org/10.1016/j.comp-struc.2014.07.006
14. Dempster, A.P. Upper and lower probabilities induced by a multivalued mapping. The Annals of Mathematical Statistics. 1967. 38 (2). Pp. 325–339. DOI: 10.1214/aoms/1177698950

15. Utkin, L.V. Analiz riska i prinyatiye resheniy pri nepolnoy informatsii [Risk analysis and decision making with incomplete information]. Saint-Petersburg: Nauka, 2007. 403 p. (rus)
16. Melchers, R.E., Beck, A.T. Structural reliability analysis and prediction. John Wiley & Sons, Hoboken. 2018. 497 p. DOI: 10.1002/9781119266105
17. Utkin, V.S. Calculation of the reliability of the earth foundations of buildings and structures according to the deformation criteria with limited information on the soils and loads. Magazine of Civil Engineering. 2016. 1. Pp. 4–13. DOI: 10.5862/MCE.61.1
18. Awruch, M.D.F., Gomes, H.M. A fuzzy α -cut optimization analysis for vibration control of laminated composite smart structures under uncertainties. Applied Mathematical Modelling. 2018. 54. Pp. 551–566. doi.org/10.1016/j.apm.2017.10.002
19. Fuh, C.F., Jea, R., Su, J.S. Fuzzy system reliability analysis based on level $(\lambda, 1)$ interval-valued fuzzy numbers. Information Sciences. 2014. 272. Pp. 185–197. doi.org/10.1016/j.ins.2014.02.106
20. Utkin, V.S., Utkin, L.V. Calculating the reliability of machine parts by means of truncated probability-distribution functions. Russian Engineering Research. 2012. 32. Pp. 627–630. doi.org/10.3103/S1068798X12070246
21. Bernard, J.M. Analysis of Local or Asymmetric Dependencies in Contingency Tables using the Imprecise Dirichlet Model. International Symposium on Imprecise Probabilities and Their Applications. 2003. Pp. 46–62. URL: https://www.researchgate.net/publication/221027462_Analysis_of_Local_or_Asymmetric_Dependencies_in_Contingency_Tables_using_the_Imprecise_Dirichlet_Model
22. Zolina, T.V., Sadchikov, P.N. Modelirovanie snegovoy nagruzki na pokrytie promyshlennogo zdaniya [Modeling of the Snow Load on the Roofs of Industrial Buildings]. Vestnik MGSU [Proceedings of Moscow State University of Civil Engineering]. 2016. 8. Pp. 25–33. (rus)
23. Vologda, snow cover and statistics for recent years [Online]. URL: https://climate-energy.ru/weather/spravochnik/sndp/climate_sprav-sndp_270370766.php. (reference date: 23.12.2020)
24. Abu-Saba, E.G. Design of steel structures. Chapman & Hall. Springer, Boston. 1995. 391 p. doi.org/10.1007/978-1-4615-2079-5
25. Roubos, A.A., Steenbergen, R., Schweckendiek, T., Jonkman, S.N. Risk-based target reliability indices for quay walls. Structural Safety. 2018. 75. Pp. 89–109. doi.org/10.1016/j.strusafe.2018.06.005
26. De Koker, N., Viljoen, C., Day, P.W. Risk-optimal sampling for reliability-based design. Structural Safety. 2020. 83. doi.org/10.1016/j.strusafe.2019.101896

Contacts:

Sergey Solovyev, ser6sol@yandex.ru

Anastasia Soloveva, solovevaa@vogu35.ru



DOI: 10.34910/MCE.107.5

Methodology for solving parametric optimization problems of steel structures

V.V. Yurchenko^{a*} , I.D. Peleshko^b 

^a Kyiv National University of Construction and Architecture, Kyiv, Ukraine

^b Lviv Polytechnic National University, Lviv, Ukraine

*E-mail: vitalina.yurchenko.scad@gmail.com

Keywords: optimization, steel structures, nonlinear programming, strength, buckling, stiffness, gradient projection method, finite element method, numerical algorithm

Abstract. The main research goal is the development of a numerical methodology for solving parametric optimization problems of steel structures with orientation to software implementation in a computer-aided design system. The paper introduces a new mathematical model for parametric optimization problems of steel structures. The design variable vector includes geometrical parameters of the structure (node coordinates), cross-sectional dimensions of the structural members, as well as initial pre-stressing forces introduced into the specified redundant members of the structure. The system of constraints covers load-carrying capacities constraints formulated for all design sections of structural members of the steel structure subjected to all ultimate load case combinations. The displacements constraints formulated for the specified nodes of the steel structure subjected to all serviceability load case combinations have been also included into the system of constraints. The method of the objective function gradient projection onto the active constraints surface with simultaneous correction of the constraints violations has been used for solving the parametric optimization problem. A numerical algorithm for solving the formulated parametric optimization problems of steel structures has been developed in the paper. The comparison of the optimization results of truss structures presented by the paper confirms the validity of the optimum solutions obtained using the proposed numerical methodology.

1. Introduction

Over the past 50 years, numerical optimization and the finite element method have individually made significant advances and have together been developed to make possible the emergence of structural optimization as a potential design tool. In recent years, great efforts have been also devoted to integrate optimization procedures into the CAD facilities. With these new developments, lots of computer packages are now able to solve relatively complicated industrial design problems using different structural optimization techniques [1].

Applied optimum design problems for bar structures in some cases are formulated as parametric optimization problems, namely as searching problems for unknown structural parameters, which provide an extreme value of the specified purpose function in the feasible region defined by the specified constraints [2]. In this case, structural optimization is performed by variation of the structural parameters when the structural topology, cross-section types and node type connections of the bars, the support conditions of the bar system, as well as loading patterns and load design values are prescribed and constants.

Kibkalo et al. in the paper [3] formulated a parametric optimization problem for thin-walled bar structures and considered methods to solve them. The searching for the optimum solution has been performed by varying the structural parameters providing the required load-carrying capacity of structural members and the minimum value of manufacturing costs.

Yurchenko, V.V., Peleshko, I.D. Methodology for solving parametric optimization problems of steel structures. Magazine of Civil Engineering. 2021. 107(7). Article No. 10705. DOI: 10.34910/MCE.107.5

© Yurchenko, V.V., Peleshko, I.D., 2021. Published by Peter the Great St. Petersburg Polytechnic University.



This work is licensed under a [CC BY-NC 4.0](https://creativecommons.org/licenses/by-nc/4.0/)

Alekseytsev has described the process of developing a parametrical-optimization algorithm for steel trusses in the paper [4]. Parametric optimization has been performed taking into account strength, stability and stiffness constraints formulated for all truss members. The objective function has been formulated depending on the specific manufacturing of the truss panel joints in term of the manufacturing cost calculated based on the labor costs and materials used.

Serpik et al. in the paper [5] developed an algorithm for parametric optimization of steel flat rod systems. The optimization problem has been formulated as a structural weight minimization problem taking into account strength and displacement constraints, as well as overall stability constraints. The cross-sectional dimensions of the truss members and the coordinates of the truss panel joints have been considered as design variables. The structural analysis of internal forces and displacements for considered structures has been performed using the finite element method. An iterative procedure for searching for optimum solution has been proposed in [6].

Sergeyev et al. in the paper [7] formulated a parametric optimization problem with constraints on faultless operation probability of bar structures with random defects. The weight of the bar structures has been considered as the objective function. Initial global imperfections have been considered as small independent random variables distributed according to normal distribution law, as well as buckling load value has been also considered as a random variable.

The mathematical model of the parametric optimization problem of structures includes a set of design variables, an objective function, as well as constraints, which reflect generally non-linear dependences between them [8]. If the purpose function and constraints of the mathematical model are continuously differentiable functions, as well as the search space is smooth, then the parametric optimization problems are successfully solved using gradient projection non-linear methods [9]. The gradient projection methods operate with the first derivatives or gradients only both of the objective function and constraints. The methods are based on the iterative construction of such a sequence of the approximations of design variables that provides convergence to the optimum solution (optimum values of the structural parameters) [10].

Additionally, a sensitivity analysis is a useful optional feature that could be used in scope of the numerical algorithms developed based on the gradients methods [11]. Thus, in the paper [12] Sergeyev et al. formulated a parametric optimization problem of linearly elastic space frame structures taking into account the stress and multiple natural frequency constraints. The cross-sectional parameters of structural members as well as node positions of the considered bar structures has been considered as design variables. The sensitivity analysis of multiple frequencies has been performed using analytic differentiation with respect to the design variables. The optimal design of the structure has been obtained by solving a sequence of quadratic programming problems.

Although many papers are published on the parametric optimization of steel structures, the development of a general computer program for the design and optimization of building structures according to specified design codes remains an actual task. Therefore, the main *research goal* is the development of a methodology for solving parametric optimization problems of steel structures with orientation on software implementation in a computer-aided design system.

In this paper, steel structures are considered as research object, which investigated for the searching for optimum parameters of the structural form. The following research tasks are formulated: to develop a mathematical model for parametric optimization of steel structures taking into account load-carrying capacities and stiffness constraints; to propose a numerical algorithm for parametric optimization of steel structures based on the gradient projection method; to confirm the validity of the optimum solutions obtained using the proposed methodology based on numerical examples.

2. Methods

2.1. Problem formulation for parametric optimization of steel structures

Let us consider a parametric optimization problem of a structure consisting of bar members. The problem statement can be performed taking into account the following assumptions widely used in structural mechanic problems: the material of the structure is ideal elastic; the bar structure is deformable linearly; external loadings applied to the structure are quasi-static.

Let us also formulate the following pre-conditions for calculation: cross-section types and dimensions of structural members are constant along member lengths; external loadings are applied to the structural members without eccentricities relating to the center of mass and shear center of its cross-sections; an additional restraining by stiffeners are provided in the design sections where point loads (reactions) applied with the exception of cross-section warping and local buckling of the cross-section elements; load-carrying capacity of the structural joints, splices and connections are provided by additional structural parameters do not covered by the considered parametric optimization problem.

A parametric optimization problem of the structure can be formulated as presented below: to find optimum values for geometrical parameters of the structure, member's cross-section dimensions and initial pre-stressing forces introduced into the specified redundant members of the bar system, which provide the extreme value of the determined optimality criterion and satisfy all load-carrying capacities and stiffness requirements. We assume, that the structural topology, cross-section types and node type connections of the bars, the support conditions of the bar system, as well as loading and pre-stressing patterns are prescribed and constants.

The formulated parametric optimization problem can be considered integrally using the mathematical model in the form of the non-linear programming task including an objective function, a set of independent design variables and constraints, which reflect generally non-linear dependences between them. The validity of the mathematical model can be estimated by the compliance of its structure with the design code requirements.

The parametric optimization problem of steel structures can be stated in the following mathematical terms: to find unknown structural parameters $\vec{X} = \{X_{\iota}\}^T$, $\iota = \overline{1, N_X}$ (N_X is the total number of the design variables), providing the least value of the determined objective function:

$$f^* = f(\vec{X}^*) = \min_{\vec{X} \in \mathfrak{S}} f(\vec{X}), \quad (1)$$

in a feasible region (search space) \mathfrak{S} defined by the following system of constraints:

$$\psi(\vec{X}) = \{\psi_{\kappa}(\vec{X}) = 0 \mid \kappa = \overline{1, N_{EC}}\}, \quad (2)$$

$$\phi(\vec{X}) = \{\phi_{\eta}(\vec{X}) \leq 0 \mid \eta = \overline{N_{EC} + 1, N_{IC}}\}, \quad (3)$$

where \vec{X} is the vector of the design variables (unknown structural parameters); f , ψ_{κ} , ϕ_{η} are the continuous functions of the vector argument; \vec{X}^* is the optimum solution or optimum point (the vector of optimum values of the structural parameters); f^* is the optimum value of the optimum criterion (objective function); N_{EC} is the number of constraints-equalities $\psi_{\kappa}(\vec{X})$, which define hyperplanes of the feasible solutions; N_{IC} is the number of constraints-inequalities $\phi_{\eta}(\vec{X})$, which define a feasible region in the design space \mathfrak{S} .

The vector of the design variables comprises of unknown geometrical parameters of the structure $\vec{X}_G = \{X_{G,\chi}\}^T$, $\chi = \overline{1, N_{X,G}}$, unknown cross-sectional dimensions of the structural members $\vec{X}_{CS} = \{X_{CS,\alpha}\}^T$, $\alpha = \overline{1, N_{X,CS}}$, as well as unknown initial pre-stressing forces $\vec{X}_{PS} = \{X_{PS,\beta}\}^T$, $\beta = \overline{1, N_{X,PS}}$, introduced into the specified redundant members of the structure (see Fig. 1):

$$\vec{X} = \{\vec{X}_G, \vec{X}_{CS}, \vec{X}_{PS}\}^T = \{\{X_{G,\chi}\}, \{X_{CS,\alpha}\}, \{X_{PS,\beta}\}\}^T, \quad (4)$$

where $N_{X,G}$ is the total number of unknown node coordinates of the steel structure; $N_{X,CS}$ is the total number of unknown cross-sectional dimensions of the structural members, $N_{X,PS}$ is the total number of unknown initial pre-stressing forces introduced into the specified redundant members of the bar system, $N_{X,G} + N_{X,CS} + N_{X,PS} = N_X$.

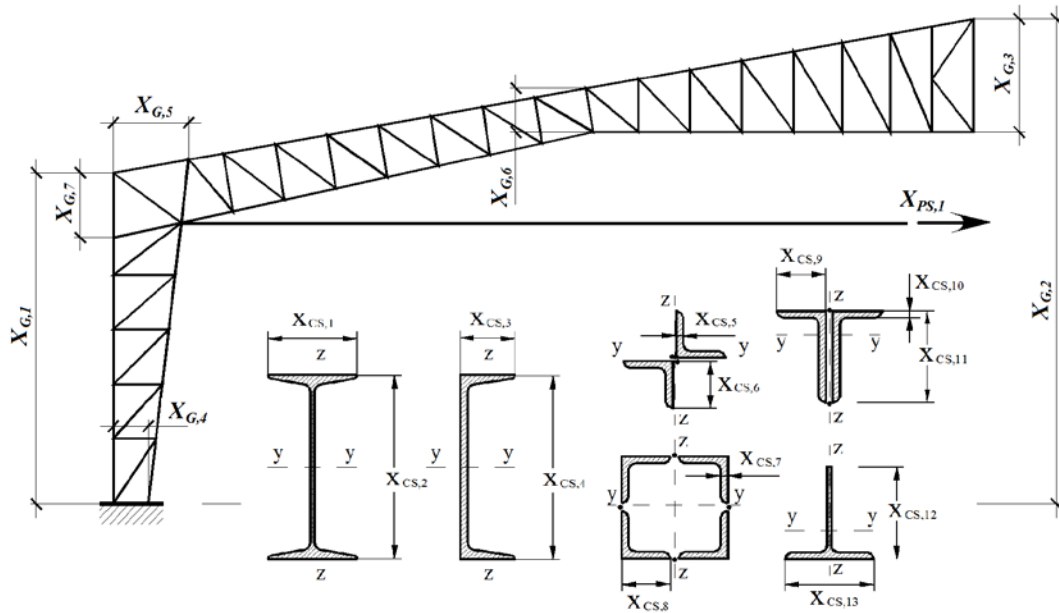


Figure 1. The unknown (variable) parameters of the structure considered as design variables.

In cases when vector of the design variables \vec{X} consists of unknown cross-sectional dimensions only:

$$\vec{X} = \vec{X}_{CS} = \{X_{CS,\alpha}\}^T, \tag{5}$$

then optimum material distribution problem Eqs. (1) – (3), Eq. (5) for the steel structure is under consideration.

The vector of the design variables \vec{X} can also consists of unknown initial pre-stressing forces

$\vec{X}_{PS} = \{X_{PS,\beta}\}^T$, $\beta = \overline{1, N_{X,PS}}$, introduced into the specified redundant members of the structure:

$$\vec{X} = \{\vec{X}_{CS}, \vec{X}_{PS}\}^T = \left\{ \{X_{CS,\alpha}\}, \{X_{PS,\beta}\} \right\}^T, \tag{6}$$

where $N_{X,CS} + N_{X,PS} = N_X$. In cases when vector of the design variables \vec{X} consists of unknown cross-sectional dimensions and unknown initial pre-stressing forces, then optimum material and internal forces distribution problem Eqs. (1) – (3), Eq. (6) for the steel structure is under consideration.

The specific technical-and-economic index (material weight, material cost, construction cost etc.) or another determined indicator can be considered as the objective function Eq. (1) taking into account the ability to formulate its analytical expression as a function of design variables \vec{X} .

Load-carrying capacities constraints (strength and stability inequalities) for all design sections of the structural members subjected to all design load combinations at the ultimate limit state as well as displacements constraints (stiffness inequalities) for the specified nodes of the bar system subjected to all design load combinations at the serviceability limit state should be included into the system of constraints Eqs. (2) – (3). Additional requirements which describe structural, technological and serviceability particularities of the considered structure can be also included into the system Eqs. (2) – (3).

The design internal forces in the structural members used in the strength and stability inequalities of the system Eqs. (2) – (3) are considered as state variables depending on design variables \vec{X} and can be calculated from the following linear equations system of the finite element method [13]:

$$\mathbf{K}(\vec{X}_G, \vec{X}_{CS}) \times \vec{z}_{ULS,k} = \vec{p}_{ULS,k}(\vec{X}_G, \vec{X}_{PS}), \quad k = \overline{1, N_{LC}^{ULS}}, \tag{1.7}$$

where $\mathbf{K}(\vec{X}_G, \vec{X}_{CS})$ is the stiffness matrix of the finite element model of the bar system, which should be formed depending on the unknown (variable) cross-sectional dimensions of the structural members \vec{X}_{CS} , as well as unknown (variable) node coordinates of the structure \vec{X}_G ; $\vec{p}_{ULS,k}(\vec{X}_G, \vec{X}_{PS})$ is the column-vector

of the node's loads for k^{th} design load combination of the ultimate limit state, which should be formed depending on unknown (variable) initial pre-stressing forces \vec{X}_{PS} , as well as unknown (variable) node coordinates of the structure \vec{X}_G ; $\vec{z}_{ULS,k}$ is the result column-vector of the node displacements for k^{th} design load combination of the ultimate limit state, $\vec{z}_{ULS,k} = \mathbf{Z}_{\text{FEM},k}^{\text{ULS}}(\vec{X}_G, \vec{X}_{CS}, \vec{X}_{PS}) = \mathbf{Z}_{\text{FEM},k}^{\text{ULS}}(\vec{X})$; N_{LC}^{ULS} is the number of the design ultimate load combinations. For each i^{th} design section of j^{th} structural member subjected to k^{th} ultimate design load combination the design internal forces (axial force, bending moments and shear forces) can be calculated depending on node displacement column-vector $\vec{z}_{ULS,k}$.

The node displacement of the bar system used in stiffness inequalities of the system Eqs. (2) – (3) are also considered as state variables depending on design variables \vec{X} and can be calculated from the following linear equations system of the finite element method [13]:

$$\mathbf{K}(\vec{X}_G, \vec{X}_{CS}) \times \vec{z}_{SLS,k} = \vec{p}_{SLS,k}(\vec{X}_G, \vec{X}_{PS}), \quad k = \overline{1, N_{LC}^{\text{SLS}}}, \quad (1.8)$$

where $\vec{p}_{SLS,k}(\vec{X}_{PS})$ is the column-vector of the node's loads for k^{th} design load combination of the serviceability limit state, which should be formed depending on unknown (variable) initial pre-stressing forces \vec{X}_{PS} , as well as unknown (variable) node coordinates of the structure \vec{X}_G ; $\vec{z}_{ULS,k}$ is the result column-vector of the node displacements for k^{th} design load combination of the serviceability limit state, $\vec{z}_{SLS,k} = \mathbf{Z}_{\text{FEM},k}^{\text{SLS}}(\vec{X}_G, \vec{X}_{CS}, \vec{X}_{PS}) = \mathbf{Z}_{\text{FEM},k}^{\text{SLS}}(\vec{X})$; N_{LC}^{SLS} is the number of the design serviceability load combinations. For each m^{th} node of the finite element model subjected to k^{th} serviceability design load combination the design vertical and horizontal displacements can be calculated depending on node displacement column-vector $\vec{z}_{SLS,k}$.

The system of constraints Eqs. (2) – (3) should cover strength and stability constraints formulated for all design sections of all structural members of the considered steel structure subjected to all design load combinations at the ultimate limit state. The following *strength constraints* should be included in the system of constraints Eqs. (2) – (3), formulated for all design sections, $\forall i = \overline{1, N_{DS}}$ (N_{DS} is the total number of the design sections in structural members), of all structural members, $\forall j = \overline{1, N_B}$ (N_B is the total number of the structural members), subjected to all ultimate load case combination, $\forall k = \overline{1, N_{LC}^{\text{ULS}}}$, namely:

- normal stresses verifications:

$$\frac{\sigma_{\max,ijk}(\vec{X})}{R_y \gamma_c} - 1 \leq 0; \quad (9)$$

- shear stresses verifications:

$$\frac{\tau_{\max,ijk}(\vec{X})}{0.58 R_y \gamma_c} - 1 \leq 0; \quad (10)$$

- as well as equivalent stresses verifications:

$$\frac{\sigma_{eqv,ijk}(\vec{X})}{1.15 R_y \gamma_c} - 1 = \frac{\sqrt{\sigma_{x,ijk}^2(\vec{X}) + 3\tau_{x,ijk}^2(\vec{X})}}{1.15 R_y \gamma_c} - 1 \leq 0, \quad (11)$$

where $\sigma_{\max,ijk}(\vec{X})$ are $\tau_{\max,ijk}(\vec{X})$ are the maximum value of the normal and shear stresses respectively caused by internal forces (axial force, bending moments and shear forces) acting in i^{th} design section of j^{th} structural member subjected to k^{th} ultimate load case combination calculated from the linear equations system of the finite element method Eq. (7); γ_c is the safety factor [14]; R_y is the design strength for steel member subjected to tension, bending and compression; $R_y \gamma_c$, $0.58 R_y \gamma_c$ and $1.15 R_y \gamma_c$ are allowable values for

normal, shear and equivalent stresses respectively [14]; $\sigma_{x,ijk}(\vec{X})$, $\tau_{x,ijk}(\vec{X})$ and $\sigma_{eqv,ijk}(\vec{X})$ are normal, shear and equivalent stresses respectively at the specified cross-section point caused by internal forces acting in i^{th} design section of j^{th} structural member subjected to k^{th} ultimate load case combination calculated from the linear equations system of the finite element method Eq. (7). The maximum value of the normal $\sigma_{\max,ijk}(\vec{X})$ and shear stresses $\tau_{\max,ijk}(\vec{X})$, as well as normal $\sigma_{x,ijk}(\vec{X})$, shear $\tau_{x,ijk}(\vec{X})$ and equivalent $\sigma_{eqv,ijk}(\vec{X})$ stresses at the specified cross-section point should be calculated depending on the variable geometrical parameters of the structure \vec{X}_G , variable initial pre-stressing forces \vec{X}_{PS} and variable cross-sectional dimensions of the structural members \vec{X}_{CS} .

All structural members can be specified into three types depending on the bending moment – axial force ratio: (i) column structural members, (ii) beam structural members and (iii) beam-column structural members. Then $N_{BCM} + N_{CM} + N_{BM} = N_B$, where N_{CM} is the total number of column structural members; N_{BM} is the total number of beam structural members; N_{BCM} is the total number of beam-column structural members.

The following *stability constraints* should be included in the system of constraints Eqs. (2) – (3), formulated for all design sections, $\forall i = \overline{1, N_{DS}}$, of the structural members subjected to all ultimate load case combination, $\forall k = \overline{1, N_{LC}^{ULS}}$, namely:

- flexural buckling verifications for all column structural members, $\forall j = \overline{1, N_{CM}}$:

$$\frac{\sigma_{\max,ijk}(\vec{X})}{\varphi_{y,j}(\vec{X}_G, \vec{X}_{CS}) R_y \gamma_c} - 1 \leq 0; \quad (12)$$

$$\frac{\sigma_{\max,ijk}(\vec{X})}{\varphi_{z,j}(\vec{X}_G, \vec{X}_{CS}) R_y \gamma_c} - 1 \leq 0; \quad (13)$$

- torsional-flexural buckling verifications for all column structural members, $\forall j = \overline{1, N_{CM}}$:

$$\frac{\sigma_{\max,ijk}(\vec{X})}{\varphi_{c,j}(\vec{X}_G, \vec{X}_{CS}) R_y \gamma_c} - 1 \leq 0; \quad (14)$$

- lateral-torsional buckling verifications for all beam structural members, $\forall j = \overline{1, N_{BM}}$:

$$\frac{\sigma_{\max,ijk}(\vec{X})}{\varphi_{b,j}(\vec{X}_G, \vec{X}_{CS}) R_y \gamma_c} - 1 \leq 0, \quad (15)$$

where $\varphi_{y,j}(\vec{X}_G, \vec{X}_{CS})$ and $\varphi_{z,j}(\vec{X}_G, \vec{X}_{CS})$ are column's stability factors corresponded to flexural buckling relative to main axes of inertia and calculated depending on the design lengths $l_{ef,y,j}$, $l_{ef,z,j}$, cross-section type and cross-section geometrical properties for the j^{th} structural member [14]; $\varphi_{c,j}(\vec{X}_G, \vec{X}_{CS})$ is the column's stability factor corresponded to torsional-flexural buckling and calculated depending on the design lengths $l_{ef,y,j}$, $l_{ef,z,j}$, $l_{ef,T,j}$, cross-section type and cross-section geometrical properties for the j^{th} structural member [14]; $\varphi_{b,j}(\vec{X}_G, \vec{X}_{CS})$ is the beam's stability factor corresponded to lateral-torsional buckling and calculated depending on the design length $l_{ef,b,j}$, cross-section type and cross-section geometrical properties for the j^{th} structural member [14]. The flexural buckling factors $\varphi_{y,j}(\vec{X}_G, \vec{X}_{CS})$ and

$\varphi_{z,j}(\vec{X}_G, \vec{X}_{CS})$, as well as torsional-flexural buckling factor $\varphi_{c,j}(\vec{X}_G, \vec{X}_{CS})$ and the lateral-torsional buckling factor $\varphi_{b,j}(\vec{X}_G, \vec{X}_{CS})$ should be calculated depending on the variable geometrical parameters of the structure \vec{X}_G and variable cross-sectional dimensions of the structural members \vec{X}_{CS} .

The following buckling verifications for beam-column structural members should also be included in the system of constraints Eqs. (2) – (3), formulated for all design sections, $\forall i = \overline{1, N_{DS}}$, of all beam-column structural members, $\forall j = \overline{1, N_{BCM}}$, subjected to all ultimate load case combination, $\forall k = \overline{1, N_{LC}^{ULS}}$, namely:

$$\frac{\sigma_{\max,ijk}(\vec{X})}{\varphi_{e,ijk}(\vec{X})R_y\gamma_c} - 1 \leq 0; \quad (16)$$

$$\frac{\sigma_{\max,ijk}(\vec{X})}{\varphi_{y,j}(\vec{X}_G, \vec{X}_{CS})c_{ijk}(\vec{X})R_y\gamma_c} - 1 \leq 0, \quad (17)$$

where $\varphi_{e,ijk}(\vec{X})$ and $c_{ijk}(\vec{X})$ are beam-column's stability factors corresponded to in-plane and out-of-plane buckling and calculated depending on the internal forces (ration of the bending moment to the axial force), as well as depending on the design lengths $l_{ef,y,j}$, $l_{ef,z,j}$, cross-section type and cross-section geometrical properties for the j^{th} structural member [14]. The beam-column's stability factors $\varphi_{e,ijk}(\vec{X})$ and $c_{ijk}(\vec{X})$ should be calculated depending on variable geometrical parameters of the structure \vec{X}_G , variable cross-sectional dimensions of the structural members \vec{X}_{CS} and variable initial pre-stressing forces \vec{X}_{PS} .

The following *local buckling constraints* should also be included into the system of constraints:

$$\frac{\bar{\lambda}_{w,j}(\vec{X}_{CS})}{\bar{\lambda}_{uw,j}(\vec{X})} - 1 \leq 0; \quad (18)$$

$$\frac{\bar{\lambda}_{f,j}(\vec{X}_{CS})}{\bar{\lambda}_{uf,j}(\vec{X})} - 1 \leq 0, \quad (19)$$

where $\bar{\lambda}_{w,j}(\vec{X}_{CS})$ and $\bar{\lambda}_{f,j}(\vec{X}_{CS})$ are the non-dimensional slenderness of the web and flange respectively of the cross-section for j^{th} structural member; $\bar{\lambda}_{uw,j}(\vec{X})$ and $\bar{\lambda}_{uf,j}(\vec{X})$ are the maximum values for corresponded non-dimensional slenderness for column, beam and beam-column structural members calculated depending on the internal forces (ration of the bending moment to the axial force), as well as depending on the design lengths $l_{ef,y,j}$, $l_{ef,z,j}$, cross-section type and cross-section geometrical properties for the j^{th} structural member [14]. The non-dimensional slenderness $\bar{\lambda}_{w,j}(\vec{X}_{CS})$ and $\bar{\lambda}_{f,j}(\vec{X}_{CS})$ should be calculated depending on the variable cross-sectional dimensions of the structural members \vec{X}_{CS} only. At the same time, the maximum values for corresponded non-dimensional slenderness $\bar{\lambda}_{uw,j}(\vec{X})$ and $\bar{\lambda}_{uf,j}(\vec{X})$ should be calculated depending on the variable geometrical parameters of the structure \vec{X}_G and variable cross-sectional dimensions of the structural members \vec{X}_{CS} and variable initial pre-stressing forces \vec{X}_{PS} .

The system of constraints Eqs. (2) – (3) should also cover the *displacements constraints* (stiffness inequalities) for the specified nodes of the considered steel structure subjected to all design load combinations

at the serviceability limit state. The following horizontal and vertical displacements constraints should be included into the system of constraints Eqs. (2) – (3), formulated for all nodes, $\forall m = \overline{1, N_N}$ (N_N is the total number of nodes in the considered steel structure), of the steel structure subjected to all serviceability load case combination, $\forall k = \overline{1, N_{LC}^{SLS}}$, namely:

$$\frac{\delta_{x,mk}(\vec{X})}{\delta_{ux,m}} - 1 \leq 0; \quad (20)$$

$$\frac{\delta_{z,mk}(\vec{X})}{\delta_{uz,m}} - 1 \leq 0, \quad (21)$$

where $\delta_{x,mk}(\vec{X})$ and $\delta_{z,mk}(\vec{X})$ are the horizontal and vertical displacements respectively for l^{th} node of the steel structure subjected to k^{th} serviceability load case combination calculated from the linear equations system of the finite element method Eq. (8); $\delta_{ux,l}$ and $\delta_{uz,l}$ are the allowable horizontal and vertical displacements for l^{th} structural node.

Additional requirements, which describe structural, technological and serviceability particularities of the considered structure, as well as constraints on the building functional volume can be also included into the system Eqs. (2) – (3). In particular these requirements can be presented in the form of constraints on lower and upper values of the design variables, $\forall l = \overline{1, N_X}$:

$$1 - \frac{X_l}{X_l^L} \leq 0; \quad (22)$$

$$\frac{X_l}{X_l^U} - 1 \leq 0, \quad (23)$$

where X_l^L and X_l^U are the lower and upper bounds for the design variable X_l ; N_X is the total number of the design variables.

2.2. An improved gradient projection method for solving the formulated parametric optimization problem

The parametric optimization problem stated as non-linear programming task by Eqs. (1) – (3) can be solved using a gradient projection method. The method of *objective function gradient projection onto the active constraints surface with simultaneous correction of the constraints violations* ensures effective searching for solution of the non-linear programming tasks occurred when optimum designing of the building structures [15, 16].

The gradient projection method operates with the first derivatives or gradients only of both the objective function Eq. (1) and constraints Eqs. (2) – (3). The method is based on the iterative construction of such sequence Eq. (24) of the approximations of the design variables $\vec{X} = \{X_l\}^T$, $l = \overline{1, N_X}$, that provides the convergence to the optimum solution (optimum values of the structural parameters):

$$\vec{X}_{t+1} = \vec{X}_t + \Delta\vec{X}_t, \quad (24)$$

where $\vec{X}_t = \{X_l\}^T$, $l = \overline{1, N_X}$ is the current approximation to the optimum solution \vec{X}^* that satisfies both constraints-equalities Eq. (1.2) and constraints-inequalities Eq. (3) with the extreme value of the objective function Eq. (1); $\Delta\vec{X}_t = \{\Delta X_l\}^T$, $l = \overline{1, N_X}$, is the increment vector for the current values of the design variables \vec{X}_t ; t is the iteration's index. The start point of the iterative searching process $\vec{X}_{t=0}$ can be assigned as engineering estimation of the admissible design of the structure.

The active constraints only of constraints system Eqs. (2) – (3) should be considered at each iteration. A set of active constraints numbers \mathbf{A} calculated for the current approximation \vec{X}_t to the optimum solution (current design of the structure) is determined as:

$$\mathbf{A} = \mathbf{\kappa} \cup \mathbf{\eta}, \quad \mathbf{\kappa} = \left\{ \kappa \mid \left| \psi_{\kappa}(\vec{X}_t) \right| \geq -\varepsilon \right\}, \quad \mathbf{\eta} = \left\{ N_{EC} + \eta \mid \phi_{\eta}(\vec{X}_t) \geq -\varepsilon \right\}. \quad (25)$$

where ε is a small positive number introduced here in order to diminish the oscillations on movement alongside of the active constraints surface.

The increment vector $\Delta\vec{X}_t$ for the current values of the design variables \vec{X}_t can be determined by the following equation:

$$\Delta\vec{X}_t = \Delta\vec{X}_{\perp}^t + \Delta\vec{X}_{\parallel}^t, \quad (26)$$

where $\Delta\vec{X}_{\perp}^t$ is the vector calculated subject to the condition of elimination the constraint's violations; $\Delta\vec{X}_{\parallel}^t$ is the vector determined taking into consideration the improvement of the objective function value. Vectors $\Delta\vec{X}_{\parallel}^t$ and $\Delta\vec{X}_{\perp}^t$ are directed parallel and perpendicularly accordingly to the subspace with the vectors basis of the linear-independent constraint's gradients, such that:

$$\left(\Delta\vec{X}_{\perp}^t \right)^T \Delta\vec{X}_{\parallel}^t = 0. \quad (27)$$

The values of the constraint's violations for the current approximation \vec{X}_t of the design variables are accumulated into the following vector:

$$\mathbf{V} = \left(\psi_{\kappa}(\vec{X}) \forall \kappa \in \mathbf{\kappa}; \phi_{\eta}(\vec{X}) \forall \eta \in \mathbf{\eta} \right).$$

Let us introduce a set \mathbf{L} , $\mathbf{L} \subseteq \mathbf{A}$, of the constraint's numbers, such that the gradients of the constraints at the current approximation \vec{X}_t to the optimum solution are linear-independent.

Component $\Delta\vec{X}_{\perp}^t$ is calculated from the equation presented below:

$$\Delta\vec{X}_{\perp}^t = [\nabla\varphi] \vec{\mu}_{\perp}, \quad (28)$$

where $[\nabla\varphi]$ is the matrix that consists of components $\frac{\partial\psi_{\kappa}}{\partial X_t}$ and $\frac{\partial\phi_{\eta}}{\partial X_t}$, here $t = \overline{1, N_X}$, $\kappa \in \mathbf{L}$, $\eta \in \mathbf{L}$; $\vec{\mu}_{\perp}$ is the column-vector that defines the design variables increment subject to the condition of elimination the constraint's violations. Vector $\vec{\mu}_{\perp}$ can be calculated as presented below.

In order to correct constraint's violations \mathbf{V} , vector $\Delta\vec{X}_{\perp}^t$ to a first approximation should also satisfy Taylor's theorem for the continuously differentiable multivariable function in the vicinity of point \vec{X}_t for each constraint from set \mathbf{L} , namely:

$$-\mathbf{V} = [\nabla\varphi]^T \Delta\vec{X}_{\perp}^t. \quad (29)$$

With substitution of Eq. (28) into Eq. (29) we obtain the system of equations to determine column-vector $\vec{\mu}_{\perp}$:

$$[\nabla\varphi]^T [\nabla\varphi] \vec{\mu}_{\perp} = -\mathbf{V}. \quad (30)$$

Component $\Delta\vec{X}_{\parallel}^t$ is determined using the following equation:

$$\Delta \vec{X}_{\parallel}^t = \xi \times \vec{p}_{\nabla f} = \xi \left(\nabla \vec{f} - [\nabla \varphi] \vec{\mu}_{\parallel} \right), \quad (31)$$

where $\nabla \vec{f}$ is the vector of the objective function gradient in the current point (current approximation of the design variables) \vec{X}_t ; $\vec{p}_{\nabla f}$ is the projection of the objective function gradient vector onto the active constraints surface in the current point \vec{X}_t ; $\vec{\mu}_{\parallel}$ is the column-vector that defines the design variable's increment subject to the improvement of the objective function value. Column-vector $\vec{\mu}_{\parallel}$ can be calculated approximately using the least-square method by the following equation:

$$[\nabla \varphi] \vec{\mu}_{\parallel} \approx \nabla \vec{f}, \quad (32)$$

or from the equation presented below:

$$[\nabla \varphi]^T [\nabla \varphi] \vec{\mu}_{\parallel} = [\nabla \varphi]^T \nabla \vec{f}, \quad (33)$$

where ξ is the step parameter, which can be calculated subject to the desired increment Δf of the purpose function on movement along the direction of the purpose function anti-gradient. The increment Δf can be assign as 5...25 % from the current value of the objective function $f(\vec{X}_t)$:

$$\Delta f = \xi (\nabla \vec{f})^T \nabla \vec{f}, \quad \xi = \frac{\Delta f}{(\nabla \vec{f})^T \nabla \vec{f}}, \quad (34)$$

where in case of minimization Eq. (1) Δf and ξ accordingly have negative values. The parameter ξ can be also calculated using the dependency presented below:

$$\xi = \frac{\Delta f}{(\vec{p}_{\nabla f})^T \nabla \vec{f}}, \quad (35)$$

that follows from the condition of attainment the desired increment of the objective function Δf on the movement along the direction of the objective function anti-gradient projection onto the active constraints surface. Step parameter ξ can be also selected as a result of numerical experiments performed for each type of the structure individually [17, 18].

Using Eqs. (28) and (31), Eq. (26) can be rewritten as presented below:

$$\Delta \vec{X}_t = [\nabla \varphi] \vec{\mu}_{\perp} + \xi \left(\nabla \vec{f} - [\nabla \varphi] \vec{\mu}_{\parallel} \right), \quad (36)$$

or

$$\Delta \vec{X}_t = \xi \nabla \vec{f} + [\nabla \varphi] (\vec{\mu}_{\perp} - \xi \vec{\mu}_{\parallel}), \quad (37)$$

where column-vectors $\vec{\mu}_{\perp}$ and $\vec{\mu}_{\parallel}$ are calculated using Eq. (30) and Eq. (32) or Eq. (33), respectively.

The linear-independent constraints of the system Eqs. (2) – (3) should be detected when constructing the matrix of the active constraints gradients $[\nabla \varphi]$ used by Eq. (30) and Eq. (32) or Eq. (33). Selection of the linear-independent constraints can be performed based on the equivalent transformations of the resolving equations of the gradient projection method using the non-degenerate transformation matrix \mathbf{H} , such that the sub-diagonal elements of the matrix $\mathbf{H}[\nabla \varphi]$ equal to zero. An orthogonal matrix of the elementary mapping (Householder's transformation) [19] has been used to select linear-independent constraints of the system Eqs. (2) – (3) as well as to form triangular structure of the nonzero elements of matrix $\mathbf{H}[\nabla \varphi]$ [15].

Using Householder's transformations described above triangular structure of the nonzero elements of matrix $\mathbf{H}[\nabla\varphi]$ is formed step-by-step. Besides, Eq. (30) and Eq. (32) can be rewritten as follow:

$$([\nabla\varphi]^T \mathbf{H}^T)(\mathbf{H}[\nabla\varphi])\bar{\mu}_\perp = -\mathbf{V}; \tag{38}$$

$$\mathbf{H}[\nabla\varphi]\bar{\mu}_\parallel \approx \mathbf{H}\nabla\bar{f}. \tag{39}$$

Equivalent Householder transformations of the resolving equations Eqs. (38), (39) have been proposed by the paper [15]. They increase numerical efficiency of the algorithm developed based on the considered method.

In order to calculate column-vectors $\bar{\mu}_\perp$ and $\bar{\mu}_\parallel$, it is required only to perform forward and backward substitutions in Eq. (38) and Eq. (39).

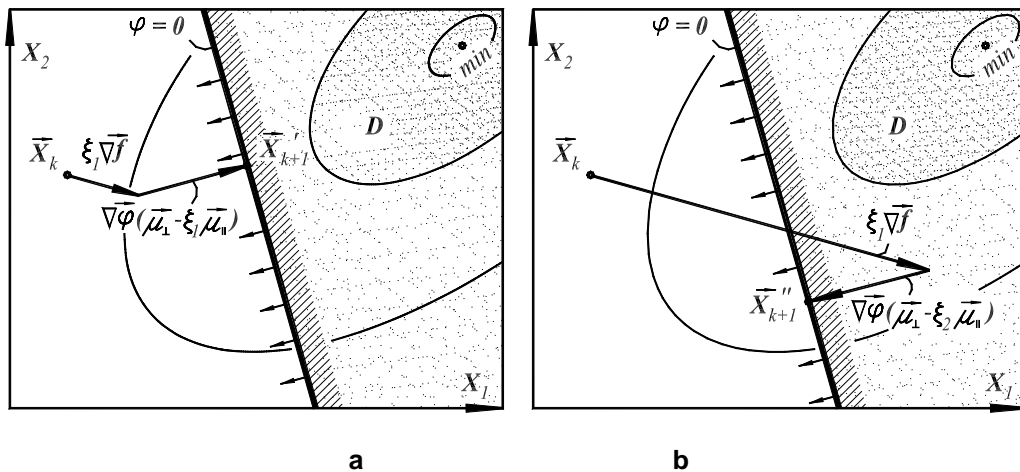


Figure 2. The selection of the constraints-inequalities:

$$\mathbf{a} - \mu_{\perp h} - \xi_1 \times \mu_{\parallel h} < 0; \quad \mathbf{b} - \mu_{\perp h} - \xi_2 \times \mu_{\parallel h} > 0.$$

To accelerate the convergence of the minimization algorithm presented above, h^{th} columns should be excluded from matrix $\mathbf{H}[\nabla\varphi]$. These columns correspond to those constraints from Eq. (3), for which the following inequality satisfies:

$$\mu_{\perp h} - \xi \times \mu_{\parallel h} > 0. \tag{40}$$

Actually, when $\mu_{\perp h} - \xi \times \mu_{\parallel h} > 0$, then the return onto the active constraints surface from the feasible region \mathfrak{S} is performed with simultaneous degradation of the objective function value (see Fig. 2, b). At the same time, in case of $\mu_{\perp h} - \xi \times \mu_{\parallel h} < 0$, both the improvement of the objective function value and the return from the inadmissible region onto the active constraints surface are performed (see Fig. 2, a).

When excluding h^{th} columns from matrix $\mathbf{H}[\nabla\varphi]$ corresponded to those constraints for which Eq. (40) is satisfied, the matrix $(\mathbf{H}[\nabla\varphi])_{red}$ with a broken (non-triangular) structure of the non-zero elements is obtained. The set \mathbf{L} of the linear-independent active constraints numbers transforms into the set \mathbf{L}_{red} respectively. At the same time, the vector of the constraint's violations \mathbf{V} reduced into the vector \mathbf{V}_{red} accordingly. In order to restore the triangular structure of the matrix $(\mathbf{H}[\nabla\varphi])_{red}$ with zero sub-diagonal elements, Givens transformations (Givens rotations) [19] can be used.

Considering Givens transformations, Eq. (38) and Eq. (39) for column-vectors $(\bar{\mu}_\perp)_{red}$ and $(\bar{\mu}_\parallel)_{red}$ can be rewritten as:

$$\left([\nabla\varphi]^T \mathbf{H}^T\right)_{red} \mathbf{G}^T \mathbf{G} (\mathbf{H}[\nabla\varphi])_{red} (\vec{\mu}_{\perp})_{red} = -\mathbf{V}_{red}; \quad (41)$$

$$\mathbf{G} (\mathbf{H}[\nabla\varphi])_{red} (\vec{\mu}_{\parallel})_{red} \approx \mathbf{G} \mathbf{H} \nabla f. \quad (42)$$

Equivalent transformations of the resolving equations Eqs. (41), (42) using Givens rotations (transformations with matrix \mathbf{G}) ensure acceleration of the iterative searching process Eq. (24) in those cases when Eq. (40) takes into account due to decreasing the amount of calculations [15].

The main resolving equation of the gradient method Eq. (36) and Eq. (37) can be rewritten as presented below:

$$\Delta \vec{X}_t = (\mathbf{H}[\nabla\varphi])_{red} (\vec{\mu}_{\perp})_{red} + \xi \left(\nabla f - (\mathbf{H}[\nabla\varphi])_{red} (\vec{\mu}_{\parallel})_{red} \right) \quad (43)$$

or

$$\Delta \vec{X}_t = \xi \nabla f + (\mathbf{H}[\nabla\varphi])_{red} \left((\vec{\mu}_{\perp})_{red} - \xi (\vec{\mu}_{\parallel})_{red} \right). \quad (44)$$

It should be noted that the lengths of the gradient vectors for the objective function Eq. (1), as well as for constraints Eqs. (2) – (3), remain as they were in scope of the proposed equivalent transformations ensuring the dependability of the optimization algorithm [15].

The determination the convergence criterion is the final question when using the iterative searching for the optimum point Eq. (24) described above. Considering the geometrical content of the gradient steepest descent method, we can assume that at the permissible point \vec{X}_t the component of the increment vector $\Delta \vec{X}_{\parallel}^t$ for the design variables should be vanish, $\Delta \vec{X}_{\parallel}^t \rightarrow 0$, in case of approximation to the optimum solution of the non-linear programming task presented by Eqs. (1) – (5). So, the following convergence criterion of the iterative procedure Eq. (24) can be assigned:

$$\left\| \Delta \vec{X}_{\parallel}^k \right\| = \sqrt{\sum_{i=1}^{N_X} \left(\Delta X_{\parallel,i}^k \right)^2} < \varepsilon_1, \quad (45)$$

where ε_1 is a small positive number. In the paper [15] the convergence criteria for the iterative procedure Eq. (24) has been presented in detail.

2.3. A parametric optimization algorithm based on the gradient projection method

Let present the following numerical algorithm to solve the parametric optimization problem for steel structures formulated above

Step 1. Describing an initial design (a set of design variables) and initial data for structural optimization.

The design variable vector $\vec{X}_k = \left(\vec{X}_G, \vec{X}_{CS}, \vec{X}_{PS} \right)_k^T$ should be specified, where k is the iteration index, $k = 0$. The structural topology, cross-section types and node type connections of the bars, the support conditions of the bar system, as well as loading and pre-stressing patterns, load case combinations and load design values are prescribed and constants.

Initial data for optimization of the considered steel structure are design strength for steel member R_y , safety factor γ_c , factors to define flexural design lengths $l_{ef,y,j}$, $l_{ef,z,j}$ and flexural-torsional design length $l_{ef,T,j}$ for all column structural members; factor to define lateral-torsional design length $l_{ef,b,j}$ for all beam structural members; allowable values for horizontal and vertical displacements $\delta_{ux,l}$ and $\delta_{uz,l}$ of the specified nodes of the considered steel structure; lower \vec{X}^L and upper \vec{X}^U bounds for the design variables; as well as specified objective function $f(\vec{X}_k)$.

Step 2. Calculation of the geometrical and design lengths for all structural members.

The geometrical lengths l_j of all structural members are calculated based on the node coordinates of the considered steel structure. The latter depend on the unknown (variable) geometrical parameters of the structure \vec{X}_G . The design lengths $l_{ef,y,j}$, $l_{ef,z,j}$ and $l_{ef,T,j}$ of all column and beam-column structural members are calculated using calculated geometrical lengths l_j and initial data relating to the design length factors. The latter are constant during the iteration process presented below. Variation of the geometrical lengths l_j and corresponded design lengths $l_{ef,y,j}$, $l_{ef,z,j}$ and $l_{ef,T,j}$ on the further iterations should be performed based on the current values of the variable (unknown) parameters \vec{X}_G of the geometrical scheme.

Step 3. Calculation of the cross-section dimensions and geometrical properties for all design cross-sections.

Geometrical properties of the design cross-sections (areas, moments of inertia, elastic section moments, radiuses of inertia, etc.), as well as non-dimensional slenderness for cross-section elements (webs and flanges) $\bar{\lambda}_{w,j}(\vec{X}_{CS})$ and $\bar{\lambda}_{f,j}(\vec{X}_{CS})$ should be calculated depending on the current values of the unknown (variable) cross-section dimensions \vec{X}_{CS} .

Step 4. Linear structural analysis of the considered steel structure.

For each m^{th} node of the finite element model subjected to k^{th} serviceability load case combination the displacements and rotations, as well as the design horizontal $\delta_{x,mk}(\vec{X})$ and vertical $\delta_{z,lk}(\vec{X})$ displacements can be calculated using the linear equations system of the finite element method Eq. (8).

For each i^{th} design section of j^{th} structural member subjected to k^{th} ultimate load case combination the design internal forces can be calculated using the linear equations system of the finite element method Eq. (7).

Step 5. Calculation of the state variables (stresses, buckling factors, allowable non-dimensional slenderness etc.).

The maximum value of the normal $\sigma_{\max,ijk}(\vec{X})$ and shear stresses $\tau_{\max,ijk}(\vec{X})$, as well as normal $\sigma_{x,ijk}(\vec{X})$, shear $\tau_{x,ijk}(\vec{X})$ and equivalent $\sigma_{eqv,ijk}(\vec{X})$ stresses at the specified cross-section point should be calculated depending on the internal forces (axial force, bending moments and shear forces) acting in i^{th} design section of j^{th} structural member subjected to k^{th} ultimate load case combination as presented by the design code.

The flexural buckling factors $\varphi_{y,j}(\vec{X}_G, \vec{X}_{CS})$, $\varphi_{z,j}(\vec{X}_G, \vec{X}_{CS})$, torsional-flexural buckling factor $\varphi_{c,j}(\vec{X}_G, \vec{X}_{CS})$ for column structural members, as well as the lateral-torsional buckling factor $\varphi_{b,j}(\vec{X}_G, \vec{X}_{CS})$ for beam structural members should be calculated depending on the corresponded design lengths, cross-section type and cross-section geometrical properties for the structural members according to the design code [14]. The stability factors $\varphi_{e,ijk}(\vec{X})$ and $c_{ijk}(\vec{X})$ for beam-column structural members should be calculated depending on the ration of the bending moment to the axial force, as well as depending on the corresponded design lengths, cross-section type and cross-section geometrical properties for the structural members according to the design code [14].

The maximum values for corresponded non-dimensional slenderness $\bar{\lambda}_{uw,j}(\vec{X})$ and $\bar{\lambda}_{uf,j}(\vec{X})$ for column, beam and beam-column structural members should be calculated depending on the internal forces (ration of the bending moment to the axial force), as well as depending on the design lengths $l_{ef,y,j}$, $l_{ef,z,j}$, cross-section type and cross-section geometrical properties for the j^{th} structural member [14].

Step 6. Verifications of the constraints and construction the set of active constraints numbers **A**.

Verification of the constraints Eqs. (9) – (17) should be performed for all ultimate load case combinations and all design cross-sections of all structural members. Verification of the constraints Eqs. (20) – (21) should be also conducted for all serviceability load case combinations and all design structural nodes. Additional requirements Eqs. (22) – (23) in the form of constraints on lower and upper values of the design variables, as well as local buckling constraints Eqs. (18) – (19) should also be verified. Set of active constraints numbers \mathbf{A} calculated for the current approximation \vec{X}_k should be constructed according to Eq. (25).

Step 7. Calculation of the current objective function value $f(\vec{X}_k)$, objective function gradient $\nabla f(\vec{X}_k)$ and determination of the desired decrement of the objective function value $\Delta f(\vec{X}_k)$.

The objective function gradient $\nabla f(\vec{X}_k)$ can be calculated by the numerical differentiation with respect to the design variables using the finite difference approximation. The desired decrement of the objective function value $\Delta f(\vec{X}_k)$ can be assigned as 5...25 % from the current objective function value $f(\vec{X}_k)$.

Step 8. Construction of the constraint's violations vector \mathbf{V} and the matrix of the active constraint's gradients $[\nabla \varphi]$. The vector of the values of the constraint's violations \mathbf{V} and the matrix of the constraint's gradients $[\nabla \varphi]$ are constructed for active constraints only according to the set of active constraints numbers \mathbf{A} .

Step 9. Construction the matrix of active linear-independent constraint's gradients with triangular structure. The set of linear-independent constraint's numbers \mathbf{L} and the matrix of active linear-independent constraint's gradients $\mathbf{H}[\nabla \varphi]$ with triangular structure are constructed according to the algorithm presented by the paper [15].

Step 10. Step parameter ξ calculation. Step parameter ξ should be calculated according to Eq. (33) or Eq. (34) and can be modified on the further iterations depending on convergence of the iterative process Eq. (24).

Step 11. Calculation the column-vectors $\vec{\mu}_\perp$ and $\vec{\mu}_\parallel$ which define the design variables increment subject to the condition of elimination the constraint's violations and subject to the improvement of the objective function value. The vectors $\vec{\mu}_\perp$ and $\vec{\mu}_\parallel$ can be calculated using Eq. (42) and Eq. (43) respectively.

If some h^{th} component of the column-vectors $\vec{\mu}_\perp$ and $\vec{\mu}_\parallel$ satisfies Eq. (35), the corresponded constraint gradient $\nabla \varphi_h$ should be excluded from the matrix $[\nabla \varphi]$, and corresponded violations V_h should be excluded from the vector \mathbf{V} , as well as the return to step 9 has to be conducted. In contrary case transition to the step 11 should be performed.

Step 12. Calculation the increment vector for the current design variables and determination the improved approximation to the optimum solution. The increment vector $\Delta \vec{X}_k$ for the current design variables values \vec{X}_k should be calculated according to Eq. (43) or Eq. (44). The improved approximation \vec{X}_{k+1} to the optimum solution should be determined according to Eq. (24).

Step 13. Stop criteria verification of iterative searching for the optimum solution. If all constraints Eqs. (9) – (23) are satisfied with appropriate accuracy, as well as inequality Eq. (45) or one of the stop criteria described by the paper [15] is also satisfied, then transition to the step 13 should be performed. In contrary case return to the step 1 should be conducted with $k \leftarrow k + 1$.

Step 14. Discretization the optimum solution \vec{X}_k obtained in the continuum space of the design variables.

Step 15. Optimum parameters of the structure is \vec{X}_k with optimum value of the objective function $f(\vec{X}_k)$.

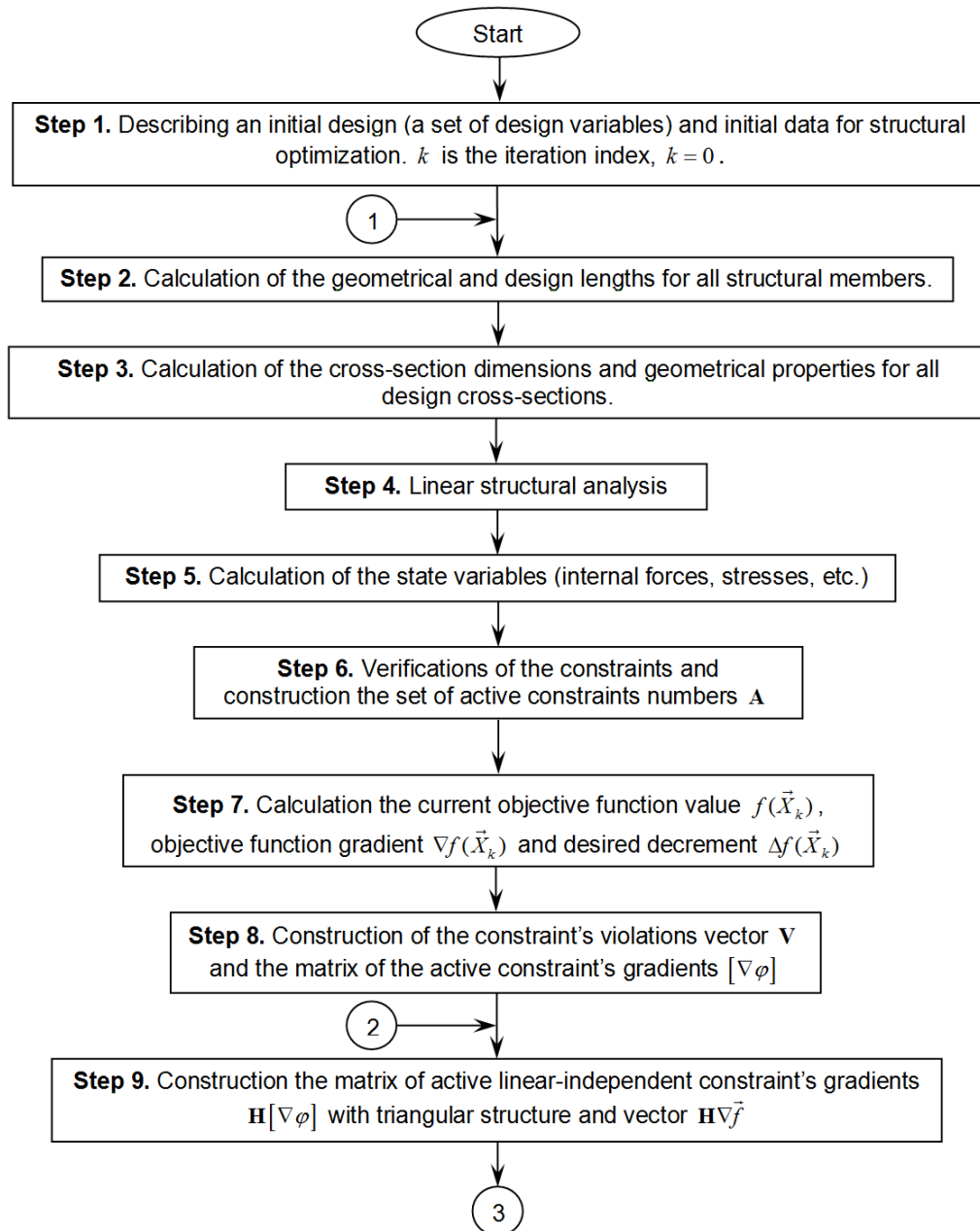


Figure 3. The flow chart for structural optimization according to the searching technique based on the gradient projection method.

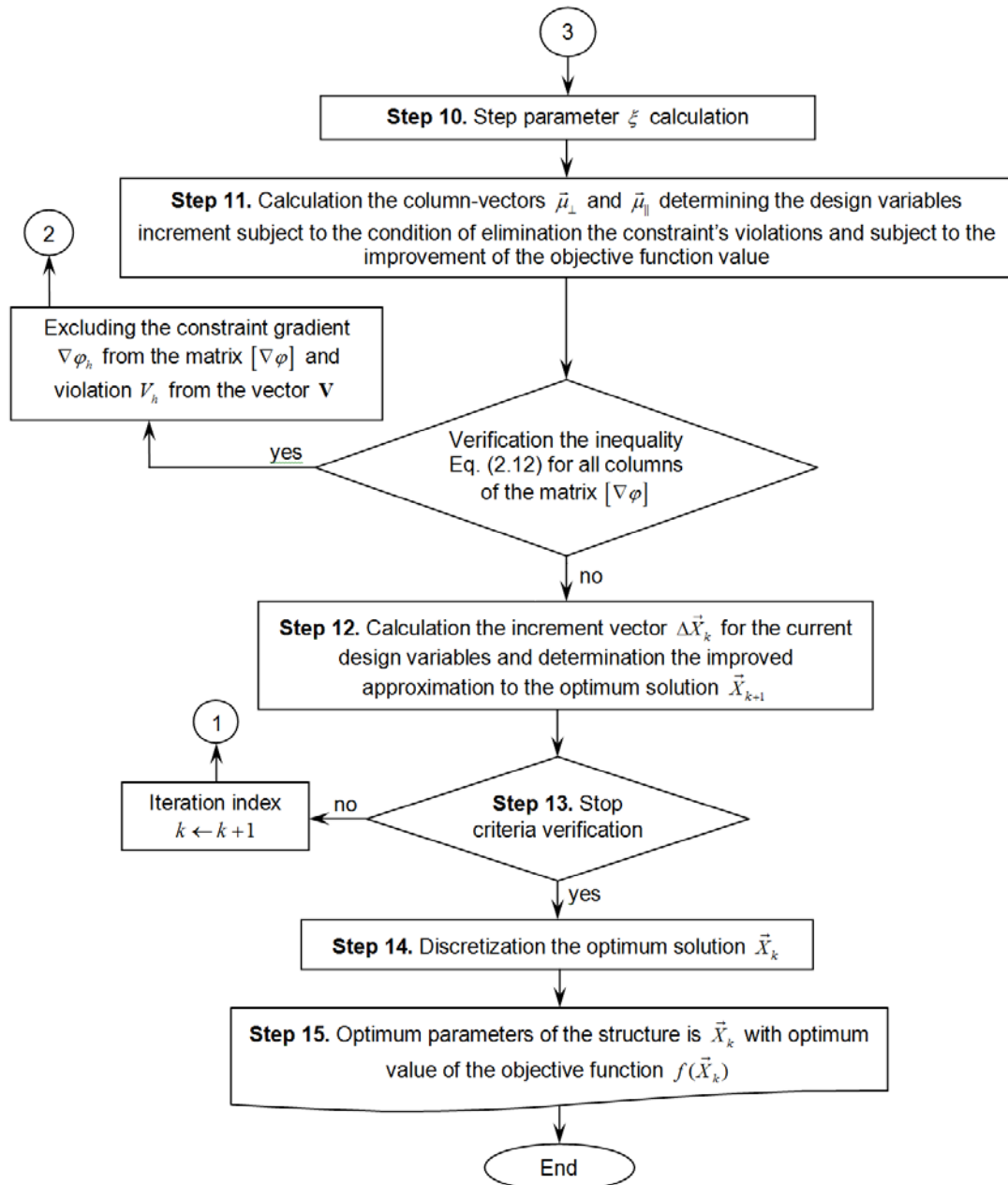


Figure 4. (continuation). The flow chart for structural optimization according to the searching technique based on the gradient projection method.

Fig. 4 presents the flow chart for structural optimization according to the searching technique describing by the gradient projection method considered above.

3. Results and Discussion

A parametric optimization methodology presented above has been realized in software OptCAD [10]. This software provides solutions to a wide range of problems, namely: (i) linear static analysis of bar structures; (ii) verification of the load-bearing capacity of the structural members according to specified design code; (iii) searching for values of the structural parameters when structure complies with design code requirements and designer's criterions; (iv) parametric optimization of the steel bar structures by the determined criterion.

In order to estimate an efficiency of the new methods or algorithms, a comparison with alternative methods or algorithms presented by other authors using different optimization techniques should be performed. Criteria to implement such comparison are described, e.g. by Haug & Arora [17] and Crowder et al. [20]. Many of these criteria, such as robustness, amount of functions calculations, requirements to the computer memory, numbers of iterations etc. cannot be used due to lack of corresponded information in the technical literature. Therefore, an efficiency estimation of the proposed methodology for solving parametric optimization problems presented above will be based on the comparison of the optimization results obtained using the proposed numerical algorithm, as well as of the results presented by the literature and widely used

for testing. The initial data and mathematical models of the parametric optimization problems considered below were assumed as the same as described in the literature.

3.1. Geometry and cross-sectional optimization of a 19-bar cantilever truss

Fig. 5 shows a 19-bar cantilever truss designed for the vertical loads $P = 10$ kN. Table 1 presents initial data for truss optimum design. There were no lower and upper bounds for the cross section areas for all truss members.

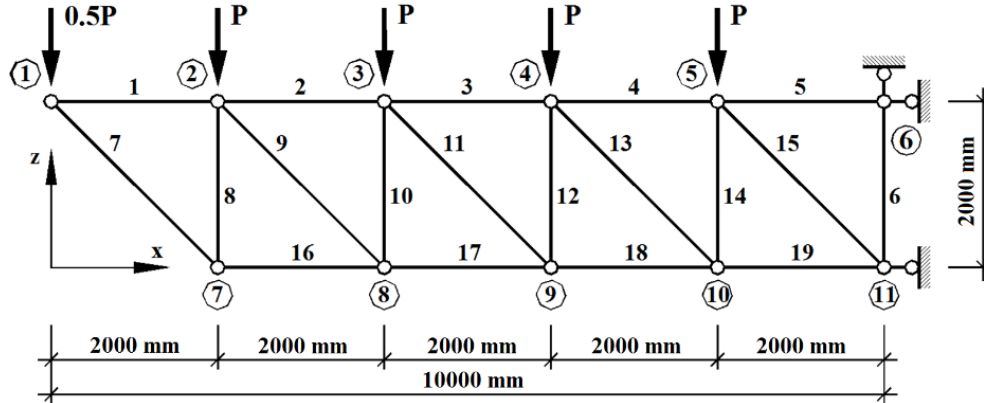


Figure 5. Design scheme of the 19-bar cantilever truss.

Table 1. Initial data for optimization of the truss.

Unit weight of the truss material	$9.81 \cdot 10^4$ kN/m ³
Modulus of elasticity	$2 \cdot 10^5$ MPa
The allowable normal stresses σ_{\max} in tension and compression	300 MPa
The allowable displacement δ_{\max} in the vertical direction for 11 th node	50 mm

Truss weight minimization has been considered as the objective function. The geometry and cross-sectional optimization problem has been formulated as searching for optimum values of the vertical coordinates z_i for all nodes of the truss lower chord, as well as for optimum value of the cross sectional area A for all truss members. Variable unknown cross-sectional area A for all truss members as well as unknown vertical coordinates z_i for all truss lower chord nodes, $\vec{X} = (A, z_i)^T$, $i = \overline{7, 11}$, were considered as design variables. The system of constraints included the normal stress constraints formulated for all truss members depending on axial forces and allowable value of the normal stresses σ_{\max} . The following displacement constraints have been also formulated for all node coordinates z_i of the truss lower chord (see Fig. 5):

$$z_i^{start} - \delta_{\max} \leq z_i \leq z_i^{start} + H - \varepsilon; \forall i = \overline{7, \dots, 11},$$

where H is the height of the truss panel, $H = 200$ cm; δ_{\max} is the maximum allowable vertical displacement for all truss nodes of the lower chord, $\delta_{\max} = 50$ mm; z_i^{start} is an initial coordinate of the truss lower chord i th node; ε is a the small positive number, $\varepsilon = 10^{-7}$. The considered optimization problem dimensions were 6 design variables and 29 constraints.

Fig. 6, a presents the optimum values for vertical coordinates of the truss lower chord. The optimum cross sectional area for all truss members is $A_{opt} = 4.0626$ cm². The optimum structural weight for the considered 19-bar cantilever truss is $G_{opt} = 139.634$ kg. There were six active constraints in the optimum point, namely normal stress constraints for the 5th, 6th, 17th, 18th, 19th truss members, as well as displacement constraint for the 11th truss node. The considered geometry and cross-sectional optimization problem for 19-bar cantilever truss has been solved by Czarnecki [21, 22]. He obtained optimal structural weight 187.945 kg.

The next geometry and cross-sectional optimization problem has been formulated as searching for optimum values of the horizontal x_i and vertical coordinates z_i for all nodes of the truss lower chord, as well

as for optimum value of the cross sectional area A for all truss members. Variable unknown cross-sectional area A for all truss members, as well as unknown horizontal x_i and vertical z_i coordinates for all truss lower chord nodes, $\vec{X} = (A, x_i, z_i)^T$, $i = \overline{7,11}$, were considered as design variables. The system of constraints included the normal stress constraints formulated for all truss members depending on axial forces and allowable value of the normal stresses σ_{\max} . The following displacement constraints have been also formulated for all nodes of the truss lower chord:

$$-1 - \frac{x_i}{x_i^{\text{start}} - L + \varepsilon} \leq 0; \quad \frac{z_i}{z_i^{\text{start}} + L - \varepsilon} - 1 \leq 0; \quad \forall i = 7 \dots 10;$$

$$-1 - \frac{z_i}{z_i^{\text{start}} - \delta_{\max}} \leq 0; \quad \frac{z_i}{z_i^{\text{start}} + H - \varepsilon} - 1 \leq 0; \quad \forall i = 7 \dots 11,$$

where L is the length of the truss panel, $L = 200$ cm. The considered optimization problem dimensions were 10 design variables and 37 constraints.

Fig. 6, b presents the optimum design values for vertical and horizontal coordinates of the truss lower chord. The optimum cross sectional area for all truss members is $A_{\text{opt}} = 4.0626$ cm². The optimum structural weight for the considered 19-bar cantilever truss is $G_{\text{opt}} = 131.11$ kg. There were eight active constraints in the optimum point, namely the normal stresses constraints formulated for the 2nd, 3rd, 4th, 5th, 7th, 16th and 19th truss members, as well as displacement constraint formulated for 11th node. The considered geometry and cross-sectional optimization problems for 19-bar cantilever truss has been solved by Czarnecki [21, 22]. He obtained optimal structural weight 178.842 kg.

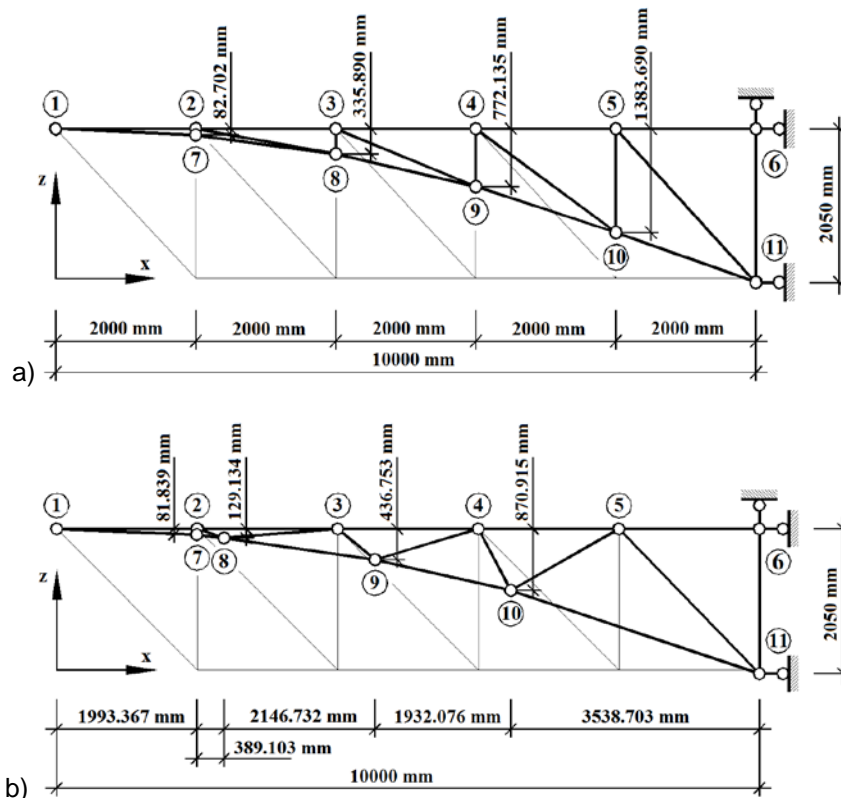


Figure 6. Optimum coordinates values for all nodes of the 19-bar cantilever truss lower chord:
a – when vertical coordinates are considered as design variable only;
b – when both vertical and horizontal coordinates are considered as design variable.

The comparison of the optimization results presented by the paper confirms the validity of the optimum solutions obtained using the proposed optimization methodology. For those design cases when the purpose function and constraints of the mathematical model are continuously differentiable functions, as well as the search space is smooth, a gradient projection method provides better optimum results comparing to the genetic algorithms.

3.2. Cross-sectional optimization of a 41-bar roof truss

Fig. 7 shows a 41-bar roof truss designed for the vertical loads $P = 4\text{ton} = 39.24\text{ kN}$ applied to the upper truss chord and $1.5P = 6\text{ ton} = 58.86\text{ kN}$ applied to the lower truss chord. A parametric optimization problem for the roof truss by the criterion of the material volume minimization has been solved by I-Cheng [23] using a genetic algorithm. He obtained the optimum volume 0.121689 m^3 for the considered roof truss.

Initial data (see Table 2) and mathematical model of the 41-bar truss optimization problem are assumed as the same as described in the paper [23]. Cross-sectional areas for 21 stiffness types of the roof truss structural members are considered as the design variables, $\bar{X} = (A_i)^T, i = \overline{1, 21}$ (see Fig. 7). Cross-sectional areas of the truss members assumed to be varying discretely starting from 2 cm^2 until and including 64 cm^2 with step 2 cm^2 . The system of constraints includes normal stresses verifications for all truss members, as well as vertical displacement constraint for truss node a . Optimization problem dimensions are 21 design variables, 80 constraints.

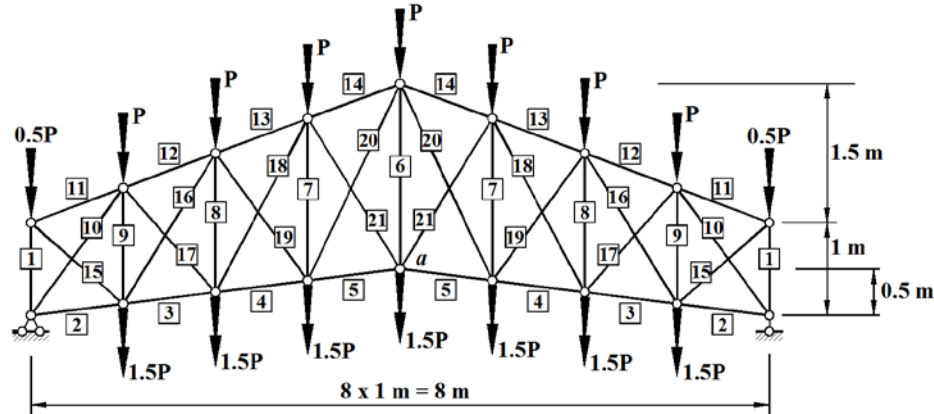


Figure 7. Design scheme of the 41-bar roof truss with stiffness types numbers.

Table 2. Initial data for optimization of the truss.

Modulus of elasticity	$2.06 \cdot 10^5\text{ MPa}$
The allowable normal stresses in tension and compression	122.625 MPa
The allowable value for the vertical displacement of the roof truss node a	6 mm

The parametric optimization problem for optimum cross-section areas of the 41-bar roof truss has been solved in the continuum space of the design variables using the improved gradient projection method described above. Table 3 presents the optimization result for the considered 41-bar roof truss. The optimum volume for the optimum truss solution is $V_{opt}^{cont} = 0.109\text{ m}^3$. The optimum solution has been validated by the convergence of the optimization algorithm in the same point subjected to the different start approximations to the design variables. The optimum solution for the roof truss obtained in the continuum space of the design variables has been further discretized. The optimum volume for the optimum truss solution in discrete space of the design variables is $V_{opt}^{disc} = 0.119\text{ m}^3$ (see Table 3).

Table 3. Optimization results for the 41-bar roof truss.

Stiffness types numbers	Optimum values for cross-section areas of the truss members [cm^2] depending on space of the design variables		Stiffness types numbers	Optimum values for cross-section areas of the truss members [cm^2] depending on space of the design variables	
	in continuum space	in discrete space		in continuum space	in discrete space
1	17.8208	18	11	14.3494	16
2	15.6555	16	12	40.1982	42
3	36.3758	38	13	52.7656	54
4	48.2494	50	14	56.8969	58
5	54.5526	56	15	17.8746	18
6	40.5101	42	16	13.0426	14
7	2.0000	2	17	12.9413	14
8	2.0000	2	18	5.4713	6
9	2.0000	2	19	6.4781	8
10	26.3752	28	20	2.9064	4
			21	2.0000	2

Truss volume [m³]	0.108997	0.118635
-------------------------------------	-----------------	-----------------

The comparison of the optimization results presented by the paper confirms the validity of the optimum solutions obtained using the proposed optimization methodology. Start values of the design variables have no influence on the optimum solution of the considered non-linear optimization problem confirming in such way accuracy and validity of the optimum solutions obtained using the proposed numerical algorithm developed based on the presented gradient projection method. For those design cases when the purpose function and constraints of the mathematical model are continuously differentiable functions, as well as the search space is smooth, a gradient projection method provides better optimum results comparing to the genetic algorithms.

4. Conclusion

The results of the presented study can be formulated as follow:

1. A new mathematical model for parametric optimization problems of steel structures has been proposed by the paper. The design variable vector includes geometrical parameters of the structure (node coordinates), cross-sectional dimensions of the structural members, as well as initial pre-stressing forces introduced into the specified redundant members of the structure has been formulated by the paper. The system of constraints covers load-carrying capacities constraints for all design sections of structural members subjected to all ultimate load case combinations, as well as displacements constraints for the specified nodes of the structure subjected to all serviceability load case combinations.

2. The method of the objective function gradient projection onto the active constraints surface with simultaneous correction of the constraints violations has been used to solve the formulated parametric optimization problem for steel structures.

3. A numerical algorithm for solving the formulated parametric optimization problems of steel structures based on the gradient projection method has been developed.

4. In order to estimate an efficiency of the proposed numerical algorithm, a comparison of the obtained optimization results with the results presented by the literature and widely used for testing has been performed. Good correlation of obtained results with the results of the other authors confirms the validity of the optimum solutions calculated using the proposed numerical algorithm.

5. It has been shown, that for those design cases when the purpose function and constraints of the mathematical model are continuously differentiable functions, as well as the search space is smooth, a gradient projection method provides better optimum results comparing to the genetic algorithms.

References

- Degertekin, S.O., Lamberti, L. Sizing, layout and topology design optimization of truss structures using the Jaya algorithm. *Applied soft computing*. 2018. Vol. 70. Pp. 903–928. DOI: 10.1016/j.asoc.2017.10.001
- Alpatov, V. The task of multi-criteria optimization of metal frame structures. *MATEC Web of Conferences*. 2017. No. 117. No. 00007. DOI: 10.1051/mateconf/201711700007
- Kibkalo, A., Lebedeva, M., Volkov, M. Methods of parametric optimization of thin-walled structures and parameters which influence on it. *MATEC Web of Conferences*. 2016. No. 53. No. 01051. DOI: 10.1051/mateconf/20165301051
- Alekseytsev, A.V. Evolutionary optimization of steel trusses with the nodal joints of rods. *Magazine of Civil Engineering*. 2013. No. 40(5). Pp. 28–37. (rus). DOI: 10.5862/MCE.40.3
- Serpik, I.N., Alekseytsev, A.V., Balabin, P.Yu., Kurchenko, N.S. Flat rod systems: optimization with overall stability control. *Magazine of Civil Engineering*. 2017. No. 76(8). Pp. 181–192. DOI: 10.18720/MCE.76.16
- Serpik, I.N., Alekseytsev, A.V. Optimization of frame structures with possibility of emergency actions. *Magazine of Civil Engineering*. 2013. No. 44(9). Pp. 23–29. (rus). DOI: 10.5862/MCE.44.3
- Sergeyev, O.A., Kiselev, V.G., Sergeyeva, S.A. Overall instability and optimization of bar structures with random defects in case of constraints on faultless operation probability. *Magazine of Civil Engineering*. 2013. No. 44(9). Pp. 30–41. (rus). DOI: 10.5862/MCE.44.4
- Permyakov, V.O., Yurchenko, V.V., Peleshko, I.D. An optimum structural computer-aided design using hybrid genetic algorithm. *Proceeding of the International Conference "Progress in Steel, Composite and Aluminium Structures"*. Taylor & Francis Group. London, 2006. Pp. 819–826.
- Perelmutter, A.V., Yurchenko, V.V. Parametric optimization of steel shell towers of high-power wind turbines. *Procedia Engineering*. 2013. No. 57. Pp. 895–905. DOI: 10.1016/j.proeng.2013.04.114
- Yurchenko, V.V., Peleshko, I.D., Beliaev, N.A. Parametric optimization of steel truss with hollow structural members based on update gradient method. *Proceedings of International Conference "Design, Fabrication and Economy of Metal Structures"*. Springer Berlin Heidelberg, 2013. Pp. 103–109. DOI: 10.1007/978-3-642-36691-8_16
- Kuci, E., Henrotte, F., Duysinx, P., Geuzaine, C. Design sensitivity analysis for shape optimization based on the Lie derivative. *Computer methods in applied mechanics and engineering*. 2017. Vol. 317. Pp. 702–722. DOI: 10.1016/j.cma.2016.12.036
- Sergeyev, O.A., Kiselev, V.G., Sergeyeva, S.A. Optimal design of 3D frame structures taking into account the stress and multiple natural frequency constraints. *Magazine of Civil Engineering*. 2016. No. 61(1). Pp. 74–81. DOI: 10.5862/MCE.61.7
- Huebner, K.H., Dewhurst, D.L., Smith, D.E., Byrom, T.G. *The finite element method for engineers*. 4th ed. John Wiley & Sons, 2001. 744 p.

14. SP 16.13330.2017, Steel structures. Moscow: Minstroy, 2017. 140 p. (rus)
15. Yurchenko, V.V., Peleshko, I.D. Improved gradient projection method for parametric optimisation of bar structures. Magazine of Civil Engineering. 2020. 98(6). Article No. 9812. DOI: 10.18720/MCE.98.12
16. Koshkin, V.L., Serpak, I.O. Optimal design of flexible rod structural members. Strength of materials. 1993. No. 25. Pp. 834–840. DOI: 10.1007/BF00780267
17. Haug, E.J., Arora, J.S. Applied optimal design: mechanical and structural systems. John Wiley & Sons, 1979. 520 p.
18. Reklaitis, G.V., Ravindran, A., Ragsdell, K.M. Engineering optimization. Methods and applications. Wiley, 2006. 688 p.
19. Wilkinson, J.H., Reinsch, C. Handbook for Automatic Computation. Volume II: Linear Algebra. Heidelberg New York Springer-Verlag Berlin. 1971. 441 p. DOI: 10.1137/1014116
20. Crowder, N.P., Denbo, R.S., Mulvey, J.M. Reporting computational experiments in mathematical programming. Mathematical Programming. 1978. Vol. 15. Pp. 316–329.
21. Czarnecki, S. Optimal structural design using a genetic algorithm. Theoretical Foundations of Civil Engineering. 1999. VII. Pp. 201–210.
22. Czarnecki, S. Multithreaded genetic program in truss shape optimization. Theoretical Foundations of Civil Engineering. 2000. VIII. Pp. 556–560.
23. I-Cheng, Y. Hybrid genetic algorithms for optimization of truss structures. Computer-aided civil and infrastructure engineering. 1999. No. 14. Pp. 199–206.

Contacts:

Vitalina Yurchenko, vitalina.yurchenko.scad@gmail.com

Ivan Peleshko, ipeleshko@hotmail.com



DOI: 10.34910/MCE.107.6

Algorithm of correcting bimoments in calculations of thin-walled bar systems

I.N. Serpik* , **R.O. Shkolyarenko**

Bryansk State University of Engineering and Technology, Bryansk, Russia

**E-mail: inserpik@gmail.com*

Keywords: frames, thin-walled bars, restrained torsion, bimoments, bar connection nodes, finite element method, iterative process

Abstract. An algorithm developed for enhancing the accuracy of the calculation of frames formed by thin-walled open-section bars is presented. The existing bar models for analysis of frame systems consisting of open-section bars subjected to restrained torsion require improvement. Some authors have shown that the traditional premise of a balance of bimoments at the junction of such bars may be violated in many cases. The methodology described in this article is formulated on the condition that the disbalance on bimoments in connecting nodes of rods reinforced with transversal ribs can be taken into account on the basis of the eccentric moments transfer on the bar junctions. An approach based on the Lagrange variational principle to the construction of equations of finite element analysis while taking into account such disbalances is proposed. Herewith, some additional nodal bimoments are introduced. They allow us to correct the solution of the problem and do not affect the global stiffness matrix of the finite element system. A presented rapidly converging iterative process makes it possible to estimate the values of such bimoments. The performance of the suggested methodology has been illustrated via an example of the calculation of frames made of I-beams and U-beams. The comparison of the results of bimoments definition using the developed bar calculation schemes and shell models have shown that the suggested algorithm allows describing the disbalance of bimoments in bar connection nodes to a fairly high degree of precision for practical goals. This result may have significant importance for improving computer modelling of deformations of the thin-walled open-section bar structures.

1. Introduction

Calculations of thin-walled bars and bar systems while taking into account torsion can be performed efficiently using shell models [1–3] or three-dimensional analysis [4]. However, the implementation of such approaches for real constructions, especially for carrying out multivariant calculations is often associated with fairly lengthy computational process working hours. Using bar design models is more promising for engineering practice.

It should be noted that the modern regulatory requirements for steel structures (Russian State Standard SP 16.13330.2017 "Steel Structures. Updated revision of SNiP II-23-81*") stipulates consideration of bimoments when determining normal stresses in bar cross sections. First of all, this factor can be significant for thin-walled open-section bars if there is restrained warping of cross sections during torsion. Theories of calculating thin-walled bars while taking into account restrained torsion within a one-dimensional approach are described in sufficient detail in scientific literature. The best known theory is the shear theory by A.A. Umansky, the shearless theory by V.Z. Vlasov, and the semi-shear theory by V.I. Slivker [5–7]. Much attention was also paid to the development of bar finite elements for thin-walled bars based on models of various types [8–26].

Several approaches to taking into account restrained torsion using the finite-element method based on bar models are presented in [8]. For the shearless theory, a double-node open-section finite element has been considered with approximation of rotation angle using Hermite cubic polynomials. For the semi-shear theory,

Serpik, I.N., Shkolyarenko, R.O. Algorithm of correcting bimoments in calculations of thin-walled bar systems. Magazine of Civil Engineering. 2021. 107(7). Article No. 10706. DOI: 10.34910/MCE.107.6

© Serpik, I.N., Shkolyarenko, R.O., 2021. Published by Peter the Great St. Petersburg Polytechnic University.



This work is licensed under a [CC BY-NC 4.0](https://creativecommons.org/licenses/by-nc/4.0/)

some stiffness matrices of open- and closed-section thin-walled bar finite elements have been constructed for three models of description of rotation angles and measures of warping of cross sections: linear approximations of rotation angle and measure of warping in a double-node finite element, quadratic approximation of rotation angle and linear approximation of measure of warping in a three-node finite element, quadratic approximations of rotation angle, and measure of warping for a three-node finite element. In [9] precision of finite-element analysis has been studied using the shearless and semi-shear theories for thin-walled open-section bars. A double-node finite element constructed within the shearless theory with cubic approximation of rotation angle and offset of the line along which the approximation of longitudinal displacements was performed is considered during analysis of deformations of plate-and-bar systems in [10]. In [11] an issue of calculation has been elaborated using a finite-element method for thin-walled open-section curved bars.

Different variants of thin-walled open-section finite elements have been constructed using analytical solutions of differential equations [13, 14, 19, 20]. In [21] an approach has been considered for implementation of the shearless theory in finite-element analysis using a double-bar finite element. By introduction of the main and dummy bar, a possibility is ensured to set the seventh degree of freedom in the node, which allows taking into account the restrained torsion within the existing software systems which traditionally use six degrees of freedom in a node.

However, the frame calculation methodology taking into account the strain warping needs to be further developed. The most widely used supposition is that presented in [6], concerning the balance of bimoments and the equality of measures of warping at bar junctions. The analysis on this basis of flat-space frames made of open-section bars [27, 28] was considered. However, [29, 30] note that such conditions are often violated, and bar interaction behavior depends significantly on their connection design. This problem can be fundamentally solved using a combined approach, where bar finite elements are introduced outside the junction node zone, and the junction strains are described using shell finite elements [31]. At the same time, the structural designs are complicated significantly in this case.

In [32–34] the regularity of the transfer of internal force factors in bar connection nodes equipped with transversal ribs has been studied in respect to disbalance of bimoments. It has been noted that such disbalance can be taken into account based on the consideration of eccentric moments transfer in the bar junctions. In [34] a step-by-step scheme for accounting of this phenomenon has been introduced within the finite element method by changing position of auxiliary linking elements between the bars. Fairly high precision of this methodology has been illustrated by an example of calculation of thin-walled structures consisting of two and three channel bars. At the same time, this approach supposes re-forming the matrix of a system of resulting equations during each iterative process step.

The aim of this work is the development of a rapidly converging, iterative scheme for accounting of physical prerequisites of [32–34] by introducing some additional nodal bimoments which do not influence the global stiffness matrix of the finite element method and do not require any changes of positions of auxiliary connection links.

2. Methods

2.1. Definition of the bimoment relationship condition

Let us consider a linearly elastic frame made of thin-walled open-section bars equipped with transversal ribs. We will assume that the frame bar has a longitudinally uniform cross-section and can be generally subjected to tension-compression, cross bending in two principal planes, and restrained torsion. Let us deem Vlasov's restrained torsion theory to be true for bars. We will discretise the object using thin-walled bar finite elements placing nodal points in the bending centers of their extreme cross sections. Herewith, we initially form bar system S , where thin-walled bars T are located between nodes U of the finite-element model, and the external load is reduced to such nodes. In system S bars T can be directly pairwise connected on nodes U or using stiff inserts D (Fig. 1). Let us assume that measures of warping cross sections are transferred through such inserts without any changes. The potential energy for bar T (Fig. 2) can be written as

$$\begin{aligned} \Pi = & \frac{1}{2} \int_0^l \left(N \varepsilon_x + M_x \chi_x + M_y \chi_y + M_\theta \theta + B_\omega \frac{d\theta}{dx} \right) dx - \\ & - \sum_{i=1}^2 \left(R_{xi} u_i + R_{yi} v_i + R_{zi} w_i + m_{xi} \phi_{xi} + m_{yi} \phi_{yi} + m_{zi} \phi_{zi} + B_{\omega i} \theta_i \right), \end{aligned} \quad (1)$$

where l is the bar length,

N is a longitudinal force,

$\varepsilon_x = \frac{\partial u}{\partial x}$ is the strain per unit of length along axis Ox ,

u is the cross section center-of-gravity displacement vector projection on axis Ox ,

M_y, M_z are the bending moments in relation to the main central axes Oy, Oz of cross section,

$\chi_y = \frac{d^2 w}{dx^2}, \chi_z = \frac{d^2 v}{dx^2}$ are the bar bending strains in relation to axes Oy and Oz ,

w, v are the cross section center of bending displacement vector projections on axes Oz and Oy ,

M_θ is a pure torsion moment,

$\theta = d\phi_x/dx$ is a measure of warping,

ϕ_x is the cross section rotation angle relative to axis Ox ,

B_ω is a bimoment,

R_{xi} is the force acting on the bar along axis Ox in cross section from node i ($i = 1, 2$),

u_i, v_i, w_i are the values u, v, w in node i ,

R_{yi}, R_{zi} are the forces applied to the bar from node i in the center of bending P_i of cross section H_i ,

$m_{xi}, m_{yi}, m_{zi}, B_{\omega i}$ are the axial moments and a bimoment acting on the bar from node i ,

$\phi_{xi}, \phi_{yi}, \phi_{zi}$ are the cross section H_i rotation angles relative to axes Ox, Oy, Oz ,

θ_i is the measure of warping for node i .

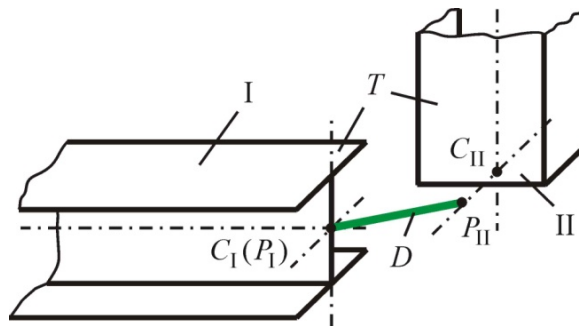


Figure 1. Example of introduction of a stiff insert D between nodes of thin-walled bars I and II : C_I, C_{II}, P_I, P_{II} are respectively centers of gravity and centers of bending of cross sections of bars to be joined.

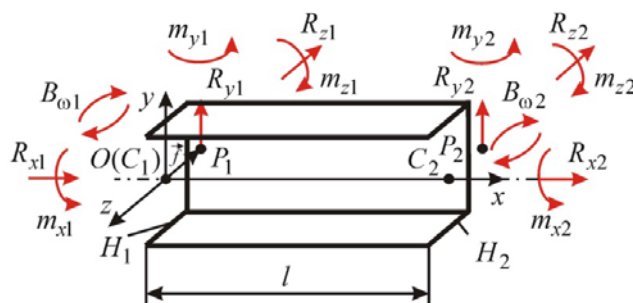


Figure 2. Bar T of system S by the example of a channel section: H_1, H_2 are the nodal cross sections with centers of gravity C_1, C_2 and bending centers P_1, P_2 ; \vec{f} is a vector connecting the cross section center of gravity and center of bending.

Let us present the bimoment of node i as

$$B_{\omega i} = B_{\omega}(m_{yi}) + B_{\omega}(m_{zi}) + \tilde{B}_{\omega i} + B_{R\omega i} \alpha_{Ri}, \quad (2)$$

where $B_{\omega}(m_{yi})$, $B_{\omega}(m_{zi})$ are bimoments created in such a node by moments m_{yi} , m_{zi} respectively with due allowance for the actual conditions of their application to the bar,

$\tilde{B}_{\omega i}$ is a bimoment which we will treat as one conditioned via transfer of bimoments from neighboring bars,

$B_{R\omega i}$ is an external bimoment applied in cross section H_i ,

α_{Ri} is the relative share of the bimoment $B_{R\omega i}$ taken up by the finite element.

For example, as shown by calculations [33], for I-section (Fig. 3a), connected with some bar L through flange Π , moment m_{yi} from such a bar will be actually transferred in the plane spaced from plane $C_i xz$ approximately at distance $d = 0.6h_{\alpha}$, where h_{α} is half the distance between the middle planes of the flanges. Let us introduce a self-balanced system of force couples acting in plane $C_i xz$ with moments m_A , m_B provided $|m_A| = |m_B| = |m_{yi}|$. Herewith, moment m_A bends the bar, and the self-balanced system of moments m_{yi} , m_B will be treated as a bimoment $B_{\omega}(m_{yi})$, the modulus of which

$$|B_{\omega}(m_{yi})| = |m_{yi}| d. \quad (3)$$

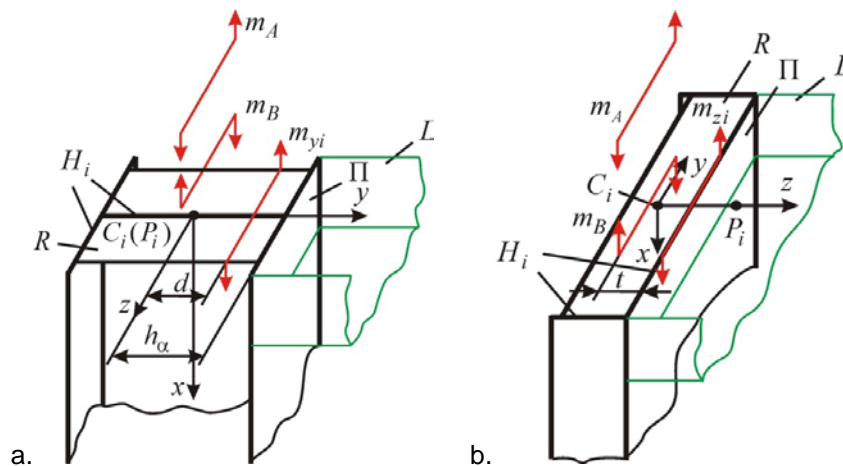


Figure 3. Transfer of a moment to I-section (a) and channel section (b): R are the transversal ribs.

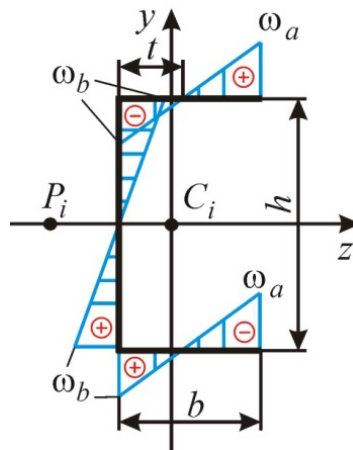


Figure 4. Principal sectorial coordinates for a channel section.

For channel section (Fig. 3b) during transfer of moment m_{zi} through the channel web Π it can be approximately assumed that it acts in the middle plane of this web [34]. Let us consider moments m_A, m_B , which are equal in absolute value to moment $|m_{zi}|$ and which are in the plane parallel to plane $C_i xy$ and spaced from the middle plane of the channel web Π by distance t . This distance corresponds to the position of points with zero values of principal sectorial coordinates [6] shown in Fig. 4, where ω_a, ω_b are coordinates depending on the dimensions of the cross section.

Then we get

$$|B_\omega(m_{zi})| = |m_{zi}|t. \quad (4)$$

According to the researches of [33, 34], we assume that in system S at the junction of two or more bars T connected directly on nodes U or using inserts D the following relationship on bimoments is fulfilled:

$$\sum_{k=1}^{k_0} (\tilde{B}_{\omega i(k)} + B_{R\omega i(k)})^* = 0, \quad (5)$$

where k_0 is the number of bars to be connected,

$\tilde{B}_{\omega i(k)}, B_{R\omega i(k)}$ are magnitudes $\tilde{B}_{\omega i}, B_{R\omega i}$ for bar k in the connecting node,

$()^*$ is a designation indicating that the signs of the bimoments in brackets are adjusted according to Fig. 5.

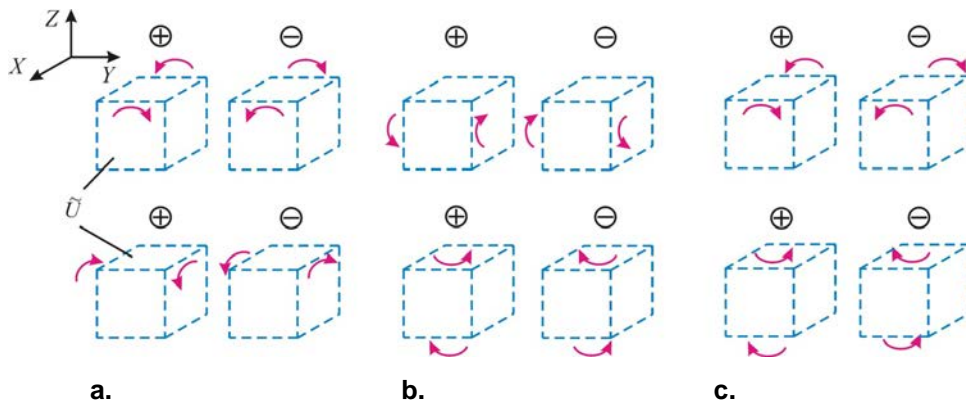


Figure 5. Sign rules for bimoments in terms of their action on connecting nodes \tilde{U} when applied relative to axes X и Y (a), Y и Z (b), and X и Z (c).

2.2. Forming the finite-element model and iterative problem solution process

Let us discretise the bar system S using the concept of the finite element method within the displacement method based on approximations used in [8, 10]. We will consider the next scheme of the description of displacements in the bar finite element of bar T (see Fig. 2). Let us represent the vector of generalised strains of the finite element as follows:

$$\{\varepsilon_e\} = \left\{ \varepsilon_x \quad \chi_y \quad \chi_z \quad \theta \quad \frac{\partial \theta}{\partial x} \right\}^T. \quad (6)$$

Vector of generalised stresses corresponding to vector $\{\varepsilon\}$

$$\{\sigma_e\} = \left\{ N \quad M_y \quad M_z \quad M_\theta \quad B_\omega \right\}^T. \quad (7)$$

Let us set down the vector of generalised displacements of finite element node i as

$$\{\delta_i\} = \left\{ u_i \quad v_i \quad w_i \quad \phi_{xi} \quad \phi_{yi} \quad \phi_{zi} \quad \theta_i \right\}^T \quad (i = 1, 2). \quad (8)$$

Taking into account Equations (6) and (7), let us represent the finite element elasticity matrix $[D_e]$ determined by relationship $\{\sigma_e\} = [D_e]\{\varepsilon_e\}$ [35] as follows:

$$[D_e] = \text{diag}\{EA \quad EI_y \quad EI_z \quad GI_t \quad EI_\omega\}, \quad (9)$$

where E, G are material elasticity modulus and shear modulus,

A is the bar cross section area,

I_y and I_z are the cross-sectional moments of inertia relative to axes Cy and Cz ,

I_t is the geometrical stiffness factor for pure torsion,

I_ω is the principal sectorial moment of inertia.

Let us approximate displacement u along axis Ox using linear law, and displacements v, w and rotation angle ϕ_x using third-degree polynomials. We represent the vector of nodal displacement of the finite element as

$$\{\delta_e\} = \left\{ \begin{matrix} \{\delta_1\} \\ \{\delta_2\} \end{matrix} \right\}. \quad (10)$$

Then taking into account Equations (6), (8), and (10), let us report the finite element strain matrix $[B_e]$ determined by expression $\{\varepsilon_e\} = [B_e]\{\delta_e\}$ [35] in terms of

$$[B_e] = [[B_{e1}] \quad [B_{e2}]], \quad (11)$$

where

$$[B_{e1}] = \begin{bmatrix} -\frac{1}{l} & 0 & 0 & 0 & 0 & 0 & 0 \\ 0 & 0 & \frac{6}{l^2} - \frac{12x}{l^3} & 0 & -\frac{4}{l} + \frac{6x}{l^2} & 0 & 0 \\ 0 & \frac{6}{l^2} - \frac{12x}{l^3} & 0 & 0 & 0 & \frac{4}{l} - \frac{6x}{l^2} & 0 \\ 0 & 0 & 0 & -\frac{6x}{l^2} + \frac{6x^2}{l^3} & 0 & 0 & 1 - \frac{4x}{l} + \frac{3x^2}{l^2} \\ 0 & 0 & 0 & -\frac{6}{l^2} + \frac{12x}{l^3} & 0 & 0 & -\frac{4}{l} + \frac{6x}{l^2} \end{bmatrix},$$

$$[B_{e2}] = \begin{bmatrix} \frac{1}{l} & 0 & 0 & 0 & 0 & 0 & 0 \\ 0 & 0 & -\frac{6}{l^2} + \frac{12x}{l^3} & 0 & -\frac{2}{l} + \frac{6x}{l^2} & 0 & 0 \\ 0 & -\frac{6}{l^2} + \frac{12x}{l^3} & 0 & 0 & 0 & \frac{2}{l} - \frac{6x}{l^2} & 0 \\ 0 & 0 & 0 & \frac{6x}{l^2} - \frac{6x^2}{l^3} & 0 & 0 & -\frac{2x}{l} + \frac{3x^2}{l^2} \\ 0 & 0 & 0 & \frac{6}{l^2} - \frac{12x}{l^3} & 0 & 0 & -\frac{2}{l} + \frac{6x}{l^2} \end{bmatrix}.$$

Let us calculate the finite element stiffness matrix using numerical integration based on Gaussian quadrature on three points. In such a case, if an auxiliary variable $\zeta = 2(x-l/2)/l$ is used, it can be set down as

$$[K_e] = \frac{l}{2} \sum_{j=1}^3 \psi_j [B_e(\zeta_j)]^T [D_e] [B_e(\zeta_j)], \quad (12)$$

where $\psi_1 = \psi_3 = 5/9$, $\psi_2 = 8/9$, $\zeta_1 = -\zeta_3 = \sqrt{0.6}$, $\zeta_2 = 0$ are coefficients and coordinates of Gaussian integration points.

When a finite element system is formed, one should transfer to nodal points in bending centers P_i . Let us note the correctness of the equality

$$u_i = u_{P_i} + \phi_{zi} f_y - \phi_{yi} f_z, \quad (13)$$

where u_{P_i} is the projection of the displacement vector of cross section H_i bending center on axis Ox ;

f_y , f_z are the projections of vector \vec{f} on axes Oy and Oz (see Fig. 2).

Taking into account Equations (8) and (13), let us express vector $\{\delta_i\}$ through vector $\{\delta_{P_i}\}$ of generalized displacements for node in the point P_i :

$$\{\delta_i\} = [\Delta] \{\delta_{P_i}\}, \quad (14)$$

where

$$[\Delta] = \begin{bmatrix} 1 & 0 & 0 & 0 & -f_z & f_y & 0 \\ 0 & 1 & 0 & 0 & 0 & 0 & 0 \\ 0 & 0 & 1 & 0 & 0 & 0 & 0 \\ 0 & 0 & 0 & 1 & 0 & 0 & 0 \\ 0 & 0 & 0 & 0 & 1 & 0 & 0 \\ 0 & 0 & 0 & 0 & 0 & 1 & 0 \\ 0 & 0 & 0 & 0 & 0 & 0 & 1 \end{bmatrix},$$

$$\{\delta_{P_i}\} = \{u_{P_i} \quad v_i \quad w_i \quad \phi_{xi} \quad \phi_{yi} \quad \phi_{zi} \quad \theta_i\}^T \quad (i=1, 2).$$

Then the finite element stiffness matrix for nodal points in bending centers will be determined by relationship

$$[K_{Pe}] = [\Omega]^{-1} [K_e] [\Omega], \quad (15)$$

where matrix

$$[\Omega] = \begin{bmatrix} [\Delta] & 0 \\ 0 & [\Delta] \end{bmatrix}.$$

Taking into account Equations (1), (2), (10), (14), and (15), the system of equations for the finite element formed on the basis of the variational principle of Lagrange can be represented as follows:

$$([\mathbf{K}_{Pe}] \{\delta_{Pe}\})^* = ([\Omega]^{-1} \{Q_e\} + \{R_{BM}\} + \{R_e\})^*, \quad (16)$$

where $\{\delta_{Pe}\}$ is the finite element displacement vector for nodes in points P_i :

$$\{\delta_{Pe}\} = \left\{ \left\{ \delta_{P1} \right\} \right\},$$

$$\{Q_e\} = \left\{ R_{x1} \quad R_{y1} \quad R_{z1} \quad m_{x1} \quad m_{y1} \quad m_{z1} \quad \tilde{B}_{\omega 1} \quad R_{y2} \quad R_{y2} \quad R_{y2} \quad m_{x2} \quad m_{x2} \quad m_{z2} \quad \tilde{B}_{\omega 2} \right\}^T,$$

$$\{R_{BM}\} = \left\{ 0 \quad 0 \quad 0 \quad 0 \quad 0 \quad 0 \quad B_{M\omega 1} \quad 0 \quad 0 \quad 0 \quad 0 \quad 0 \quad 0 \quad B_{M\omega 2} \right\}^T,$$

$$B_{M\omega i} = B_{\omega}(m_{yi}) + B_{\omega}(m_{zi}) \quad (i = 1, 2),$$

$\{R_e\}$ is the vector of parts of external nodal forces applied in cross sections H_1, H_2 .

Taking into account relationships (5) and (16) let us set down the system of linear algebraic equations for the finite-element model of bar system as

$$([K]\{\delta\})^* = (\{R_{BM}\} + \{R\})^*, \quad (17)$$

where $[K]$ is the global stiffness matrix,

$\{\delta\}$ is a vector of nodal displacement of the finite-element model,

$\{R_{BM}\}$ is a vector formed on the basis of bimoments $B_{\omega}(m_{yi})$ and $B_{\omega}(m_{zi})$,

$\{R\}$ is a vector of external generalized nodal forces.

Let us introduce the following iterative process for solution the system of Equations (17):

$$[K]\{\delta\}^{(s)} = \{R\} + \{R_{BM}\}^{(s-1)} \quad (s = 1, 2, \dots), \quad (18)$$

where s is an iteration number,

$\{R_{BM}\}^{(s-1)}$ is the vector $\{R_{BM}\}$ obtained from the results of iteration $s-1$ with $\{R_{BM}\}^{(0)} = 0$.

As shown by calculations, iterative process (18) usually practically converges on highest values of internal force factors in 3 to 6 iterations. In the first iteration one can perform LU decomposition [36] the matrix of system of equations. Then contribution of subsequent iterations into the overall labor intensity of the solution of the problem will be insignificant.

3. Results and Discussion

Let us provide the results of the calculations using the suggested methodology for two examples. In example 1 a steel deformable system formed by bars I and II was considered (Fig. 6). Bar I is made of I-section No. 20B1 according to Russian State Standard GOST R 57837-2017, bar 2 is made of channel section No. 10P according to Russian State Standard GOST 8240-97. The bars have transversal ribs R. The system has rigid fixing H and loading with force couple with moment M . This object was calculated using a shell finite element model (Fig. 7) in the finite element analysis program Autodesk NEi Nastran (license of Federal State Budget Educational Institution of Higher Education "Bryansk State Engineering Technological University", No. PR-05918596) and using a bar model (Fig. 8). 6450 quadrangular shell-type finite elements and 10 thin-walled bar finite elements were considered, respectively. Further refinement of both meshes did not lead in any significant changes of the calculation results. Fig. 9 illustrates a diagram of bimoments in bars obtained using a shell model. Fig. 10 and 11 illustrate bimoments calculated using the considered bar finite element without adjustment on bimoments and with implementation of the iterative process (18). Here the signs of bimoments correspond to local coordinate systems $x_i y_i z_i$ ($i = I, II$) for the beams (see Fig. 6). For the shell model, during calculation of bimoments according to Fig. 4 and 12 an approximate relationship was used

$$B_{\omega} = \sum_{j=1}^n \sigma_j t_j l_j \omega_j, \quad (19)$$

where n is the number of finite elements separated by the cross section in question into line segments Λ_j of its middle surfaces,

σ_j is the membrane stress for this cross section in finite element j averaged on line segment Λ_j ,

t_j is the thickness of finite element j ,

l_j is the length of line segment Λ_j ,

ω_j is the principal sectorial coordinate of the center of this line segment.

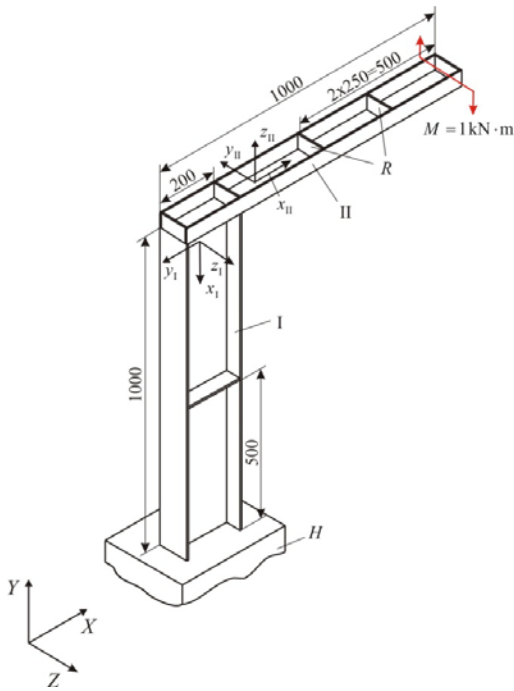


Figure 6. Double-bar system.

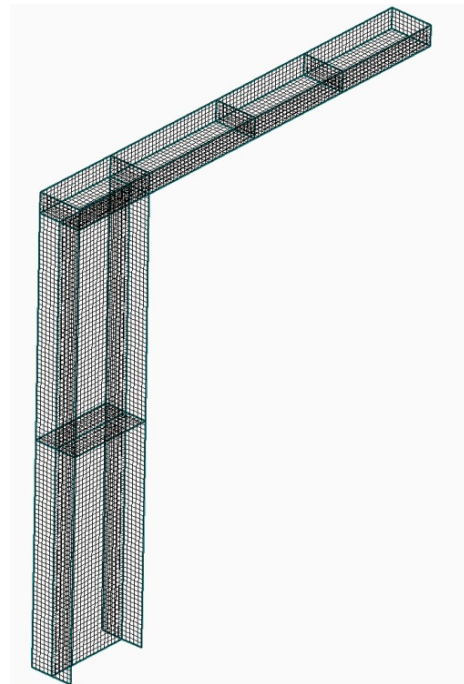


Figure 7. System of shell finite elements for example 1.

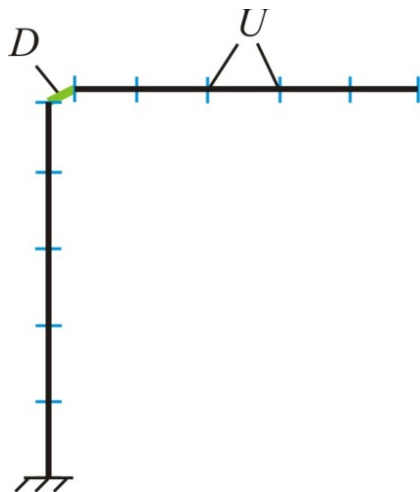


Figure 8. Splitting of example 1 object into bar finite elements: U are the finite element nodes.

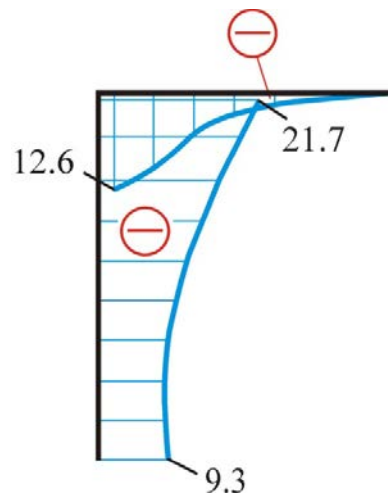


Figure 9. Diagram of bimoments according to calculation results in Autodesk NEi Nastran ($N \cdot m^2$).

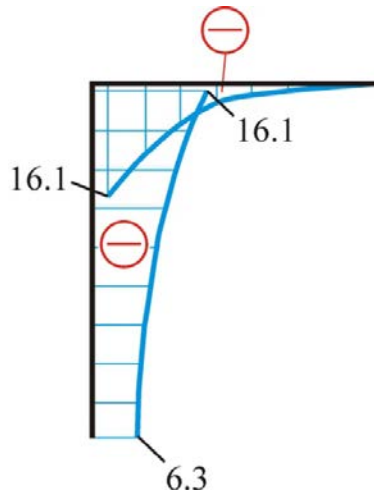


Figure 10. Bimoment calculation results for bar model without considering the disturbance on bimoments (N·m²).

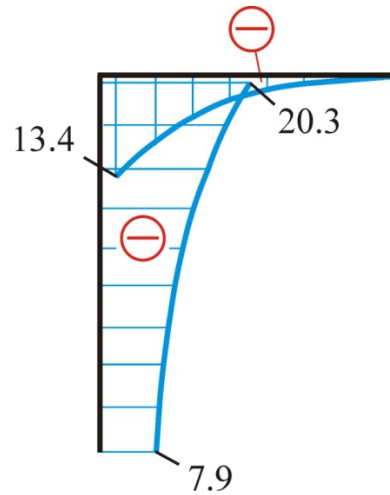


Figure 11. Diagram of bimoments obtained upon introduction of correcting nodal bimoments (N·m²).

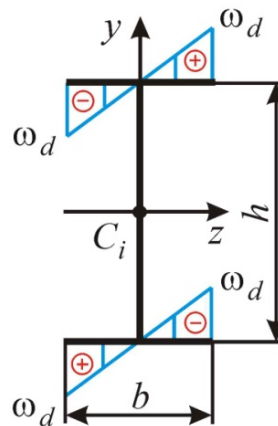


Figure 12. Principal sectorial coordinates for I-section: ω_d is a value depending on the dimensions of the cross section.

Fig. 9–11 show that on the maximum absolute value of bimoment in I-section the result obtained in the bar model without implementation of iterative process (18) is different from the shell model by 26 %, and on bimoment in channel section by 28 %. When the correcting bimoments were used, the respective discrepancies amounted only 6.5 % and 6.3 %. Fig. 13 illustrates the graphs of the behavior of these bimoments during the iterative process. It shows that the convergence on them is actually achieved in 3 iterations.

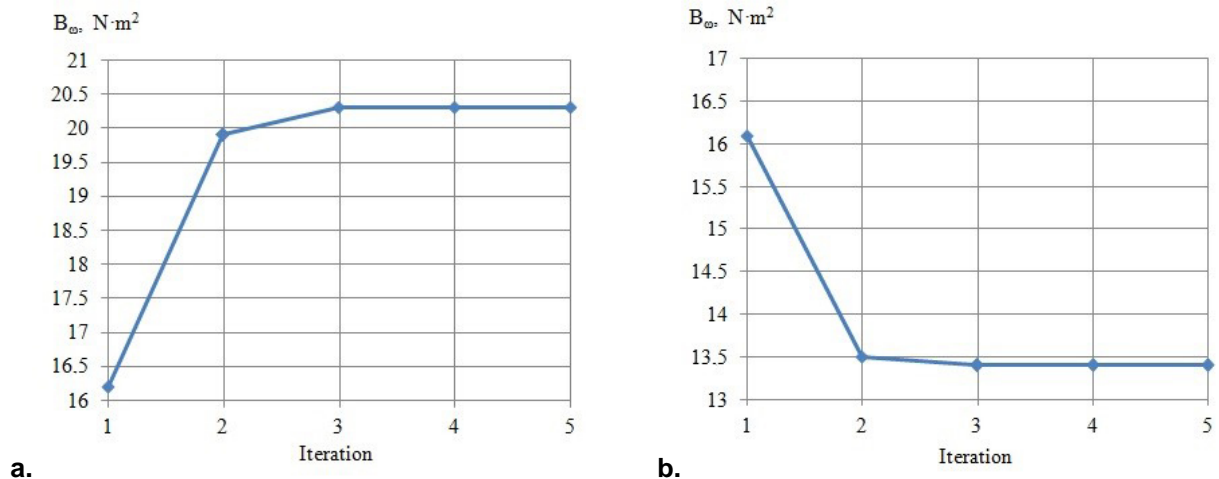


Figure 13. Bimoments in example 1 for the joined node in I-section (a) and channel section (b) depending on the iteration number.

In example 2 the steel frame (Fig. 14) is calculated. Its columns are channel sections, and the cross bar is I-section. The dimensions of cross sections are assumed to be the same as for the dimensionally identical sections in example 1. The bars are reinforced with transversal ribs R . The columns are fixed rigidly at the bottom in supports H . The system is loaded with moments M_1, M_2, M_3 , concentrated forces F_1, F_2, F_3 , acting in the median planes of the channel webs, and distributed load q , acting in the main vertical plane of the crossbar.

The calculation results were compared using shell and bar models. For the shell scheme (Fig. 15) 31,850 finite elements were used. When the bar model was formed, 92 thin-walled bar finite elements were introduced. By analogy with example 1, the results of the calculation of bimoments using Autodesk NEi Nastran are provided in Fig. 16. The bimoments obtained for the bar model based on iterative adjustment are shown in Fig. 17. The signs of bimoments in these diagrams were assumed in accordance with the position of the local coordinate axes shown in Fig. 14. Comparing Fig. 16 and 17 one can conclude that in terms of the bimoment value maximum for joined nodes, the result obtained using the suggested methodology is different from the shell model by 6.6 %, and in terms of the maximum value of bimoment in the columns, by 5.2 %. The bimoment values calculated in the iterative process for joined node A are shown in Fig. 18, where it is clear that in terms of these magnitudes, the convergence was actually achieved in 4 to 6 iterations.

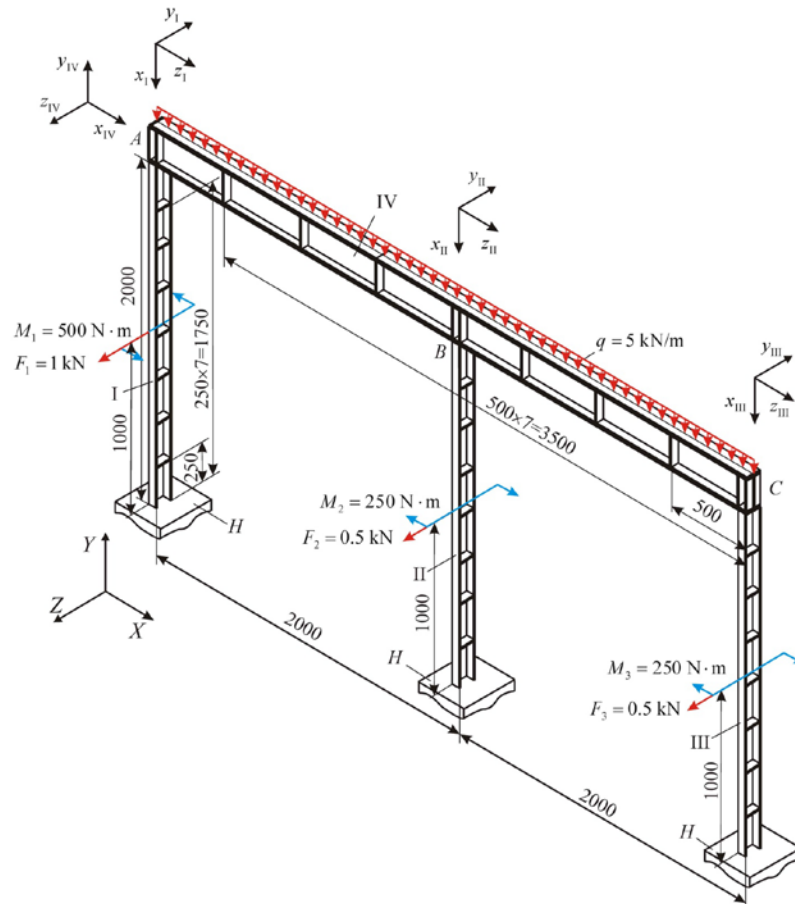


Figure 14. Double-span frame: I, II, III are the structurally identical columns; IV is the cross bar; A, B, C are the bar connection nodes.

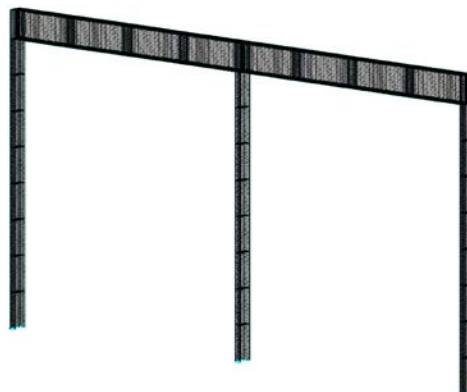


Figure 15. System of shell finite elements for example 2.

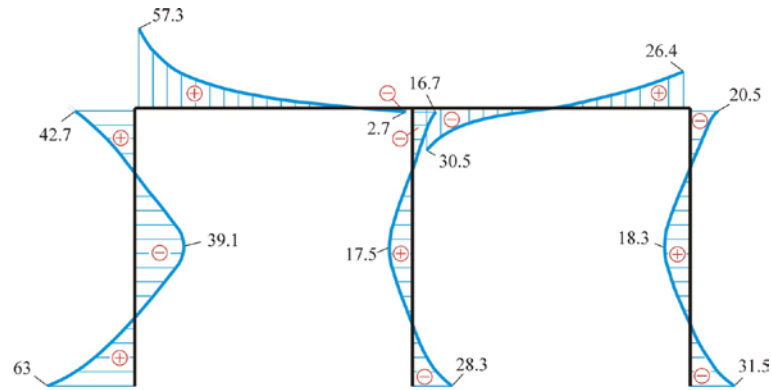


Figure 16. The results of bimoments calculation based on the shell model (N·m²).

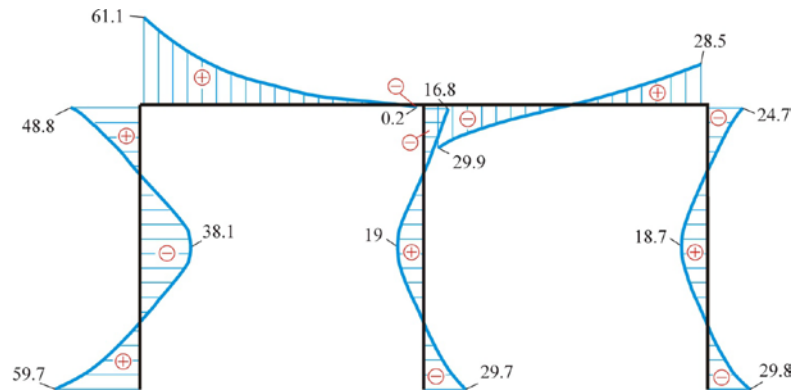


Figure 17. The results of bimoments calculation using a correcting iterative scheme in the bar model (N·m²).

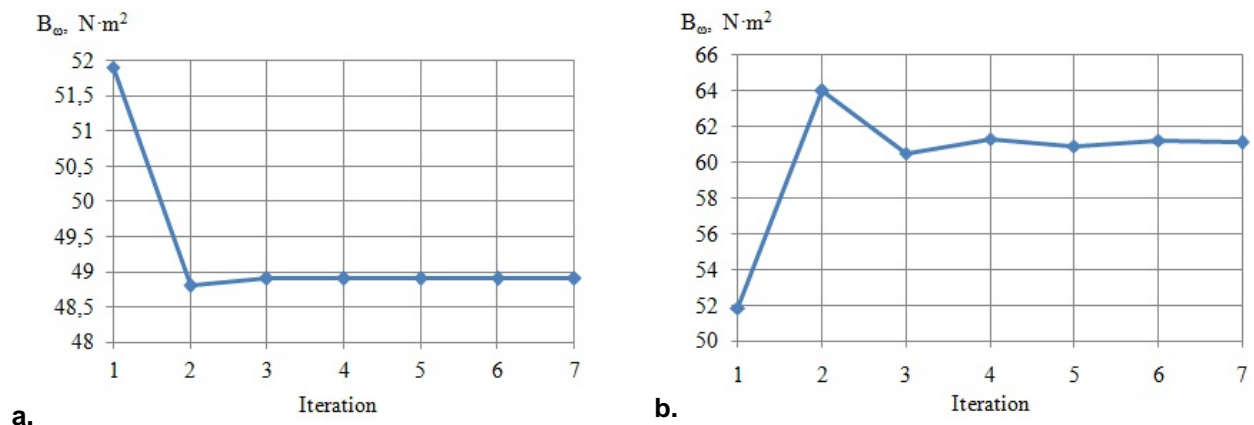


Figure 18. The change of bimoments of node A for column (a) and cross bar (b) in the iterative process.

It should be noted that in the structures where the bar connection nodes have significant reinforcement, including that using inclined ribs, some additional disturbances in terms of bimoments may appear. At the same time, such disturbance types may appear also in some straight bars if there are any design factors determining the local restrained warplings [5]. In such cases, in addition to the suggested approach, both for frames and individual bars, it is necessary to introduce into the design model some stiffening elements resistant to the bimoment transfer. According to [33, 34], when using only transversal ribs with thickness in accordance with the requirements of Russian State Standard SP 16.13330.2017, such additional disturbances are insignificant. At the same time, as follows from results of the presented work, when the bar models are used, taking into account the disbalance on bimoments in bar connection nodes caused by moment transfer behavior can increase the calculation precision significantly.

4. Conclusions

1. An algorithm of correcting bimoments has been developed. It allows taking into account the disbalance on bimoments in joined nodes of frames which are generated via open-section bars equipped with transversal ribs based on a rapidly converging iterative process. In this calculation scheme, the same matrix

of system of equations is used during each iteration. It determines the main labor intensity of the calculation process for execution of the first iteration.

2. Strains of each bar are simulated within V.Z. Vlasov's shearless theory. Based on the approach of V.V. Lalin and V.A. Rybakov, stiffness matrices have been constructed for double-node bar finite elements in which the cross section rotation angles are described using cubic law.

3. Using the variational principle of Lagrange and taking into account the conditions of the moment transfer at bar junctions, the finite element method resulting system of equations is formed. It includes the global stiffness matrix constructed in the supposition of the bimoment balance in the bar connection nodes, and on the right hand side of the equations, the correcting bimoments are included. They are determined during iterations.

4. The results are provided for finite element method calculation on bimoment values for two frames using shell models and the suggested algorithm. When corrective bimoments were used, the iterative process practically converged in 3 to 6 iterations. Herewith, the deviation of the calculation results in the presented bar models as compared with the shell schemes amounted to no more than 7 % of the maximum absolute bimoment values.

5. Acknowledgement

The reported study was funded by RFBR according to the research project No. 18-08-00567.

References

- Gordeeva, A.O., Vatin, N.I. Raschetnaya konechno-elementnaya model' kholodnognutogo perforirovannogo tonkostennogo sterzhnya v programmno-vychislitel'nom komplekse SCAD Office [Finite element calculation model of thin-walled cold-formed profile in software package SCAD Office]. Magazine of Civil Engineering. 2011. 21(3). Pp. 36–46. (rus). DOI: 10.18720/MCE.21.2
- Kvaternik, S., Turkalj, G., Lanc, D. Analysis of flexure, torsion and buckling of thin-walled frames with a focus on the joint warping behaviour. Transactions of FAMENA. 2018. 41(4). Pp. 1–10. DOI: 10.21278/TOF.41401
- Tusnina, O.A. Finite element analysis of crane secondary truss. Magazine of Civil Engineering. 2018. 77(1). Pp. 68–89. DOI: 10.18720/MCE.77.7
- Bernardo, L.F.A., Taborda, C.S.B., Andrade, J.M.A. Ultimate torsional behaviour of axially restrained RC beams. Computers and Concrete. 2015. 16(1). Pp. 67–97. DOI: 10.12989/cac.2015.16.1.067
- Vlasov, V.Z. Tonkostennyye uprugiyie sterzhni [Thin-walled elastic rods]. Gosudarstvennoye izdatel'stvo fiziko-matematicheskoy literatury. Moscow, 1959. 568 p. (rus)
- Bychkov, D.V. Stroitel'naya mekhanika sterzhnevyykh tonkostennykh konstruksiy [Structural mechanics of rod thin-walled structures] / D.V. Bychkov. Gosudarstvennoye izdatel'stvo literatury po stroitel'stvu, arkhitekture i stroitel'nym materialam. Moscow, 1962. 476 p. (rus)
- Slivker, V.I. Stroitel'naya mekhanika. Variatsionnyye osnovy [Structural mechanics. Variational bases]. Izdatel'stvo Assotsiatsii stroitel'nykh vuzov. Moscow, 2005. 736 p. (rus)
- Lalin, V.V., Rybakov, V.A. Konechnyye elementy dlya rascheta ograzhdayushchikh konstruksiy iz tonkostennykh profilyev [The finite elements for design of building walling made of thin-walled beams]. Magazine of Civil Engineering. 2011. 26(8). Pp. 69–80. (rus). DOI: 10.5862/MCE.26.11
- Lalin, V.V., Rybakov, V.A., Morozov, S.A. Issledovaniye konechnykh elementov dlya rascheta tonkostennykh sterzhnevyykh sistem [The finite elements research for calculation of thin-walled bar systems]. Magazine of Civil Engineering. 2012. 27(1). Pp. 53–73. (rus). DOI: 10.5862/MCE.27.7
- Serpik, I.N., Shvyryaev, M.V. Finite element modeling of operation for thin-walled open cross section bars to analyze plate-rod systems. Russian Aeronautics. 2017. No. 60. Pp. 34–43. DOI: 10.3103/S1068799817010068
- Serazutdinov, M.N., Ubaydulloyev, M.N., Sagdatullin, M.K. Variatsionnyy metod rascheta napryazhenno-deformirovannogo sostoyaniya tonkostennogo sterzhnya otkrytogo profilya [Variational method for calculating the stress-strain state of a thin-walled open-profile rod]. Vestnik Kazanskogo Tekhnologicheskogo Universiteta. 2014. 17(8). Pp. 255–259. (rus)
- Rybakov, V.A., Gamayunova, O.S. Napryazhenno-deformirovannoye sostoyaniye elementov karkasnykh sooruzheniy iz tonkostennykh sterzhney [The stress-strain state of frame constructions' elements from thin-walled cores]. Construction of Unique Buildings and Structures. 2013. 12(7). Pp. 79–123. (rus). DOI: 10.18720/CUBS.12.10
- Tusnin, A. Finite element for calculation of structures made of thin-walled open profile rods. Procedia Engineering. 2016. No. 150. Pp. 1673–1679. DOI: 10.1016/j.proeng.2016.07.149
- Tusnin, A.R. Konechnyy element dlya chislennogo rascheta konstruksiy iz tonkostennykh sterzhney otkrytogo profilya [Finite element for numeric computation of structures of thin walled open profile bars]. Metal Constructions. 2009. 15(1). Pp. 73–78. (rus)
- Gotluru, B.P., Schafer, B.W., Pekoz, T. Torsion in thin-walled cold-formed steel beams. Thin-Walled Structures. 2000. 37(2). Pp. 127–145. DOI: 10.1016/S0263-8231(00)00011-2
- Yoon, K., Lee, P.-S. Modeling the warping displacements for discontinuously varying arbitrary cross-section beams. Computers and Structures. 2014. No. 131. Pp. 56–69. DOI: 10.1016/j.compstruc.2013.10.013
- Panasenko, N.N., Yuzikov, V.P., Sinel'shchikov, A.V. Konechno-elementnaya model' prostranstvennykh konstruksiy iz tonkostennykh sterzhney otkrytogo profilya [Finite element model of the spatial constructions from thin-walled open section rods]. In 2 parts. Part 2. Vestnik AGTU. Ser.: Morskaya tekhnika i tekhnologiya. 2015. No. 2. Pp. 116–128.
- Musat, S.D., Epureanu, B.I. Study of warping torsion of thin-walled beams with closed cross-section using macroelements. Communications in Numerical Methods in Engineering. 1996. 12(12). Pp. 873–884. DOI: 10.1002/(SICI)1099-0887(199612)12:12<8-73::AID-CNM27>3.0.CO;2-E

19. Banić, D., Turkalj, G., Brnić, J. Finite element stress analysis of elastic beams under non-uniform torsion. Transactions of FAMENA. 2016. 40(2). Pp. 71–82. DOI: 10.21278/TOF.40206
20. Qi, H., Wang, Z., Zhang, Z. An efficient finite element for restrained torsion of thin-walled beams including the effect of warping and shear deformation. IOP Conf. Series: Earth and Environmental Science. 2019. 233(3). Pp. 032029. DOI: 10.1088/1755-1315/23-3/3/032029
21. Perelmuter, A.V., Slivker, V.I. Raschetnyye modeli sooruzheniy i vozmozhnost' ikh analiza [Design models of structures and the possibility of their analysis]. DMK Press. Moscow, 2011. 736 p. (rus)
22. Chen, C.H., Zhu, Y.F., Yao, Y., Huang, Y. The finite element model research of the pre-twisted thin-walled beam. Structural Engineering and Mechanics. 2016. 57(3). Pp. 389–402. DOI: 10.12989/sem.2016.57.3.389
23. Manta, D., Gonçalves, R. A geometrically exact Kirchhoff beam finite element with torsion warping. Proceedings of the 8th International Conference on Thin-Walled Structures (ICTWS 2018). Lisbon, Portugal. 2018. [Online]. System requirements: AdobeAcrobatReader. URL: https://research.unl.pt/ws/portalfiles/portal/5801579/A_geometrically_exact_Kirchhoff_beam_finite_element_with_torsion_warping.pdf (date of application: 19.02.2020)
24. Lalin, V.V., Rybakov, V.A., Diakov, S.F., Kudinov, V.V., Orlova, E.S. The semi-shear theory of V.I. Slivker for the stability problems of thin-walled bars. Magazine of Civil Engineering. 2019. 87(3). Pp. 66–79. DOI: 10.18720/MCE.87.6
25. Lalin, V., Rybakov, V., Sergey, A. The finite elements for design of frame of thin-walled beams // Applied Mechanics and Materials. 2014. No. 578–579. Pp. 858–863. DOI: 10.4028/www.scientific.net/AMM.578-579.858
26. Vatin, N.I., Rybakov, V.A. Raschet metallokonstruktsiy: sed'maya stepen' svobody [An Analysis of metal structures: the seventh degree of freedom]. StroyPROFIL'. 2007. 56(2). Pp. 60–63. (rus)
27. Yurchenko, V.V. Proyektirovaniye karkasov zdaniy iz tonkostennykh kholodnognutykh profiley v srede «SCAD Office» [Designing of steel frameworks from thin-walled cold-formed profiles in SCAD Office]. Magazine of Civil Engineering. 2010. 18(8). Pp. 38–46. (rus). DOI: 10.18720/MCE.18.7
28. Aleksandrov, A.V., Osokin, A.V., Aleksandrov, A.A. Razvitiye metoda konechnykh elementov dlya sistem tonkostennykh pryamolineynykh i krivolineynykh sterzhney [Development of the finite element method for systems of thin-walled straight and curved rods]. Academia. Architecture and Construction. 2006. No. 4. Pp. 57–61. (rus)
29. Perelmuter, A.V., Yurchenko, V.V. O raschete prostranstvennykh konstruktsiy iz tonkostennykh sterzhney otkrytogo profilya [On calculation of the spatial structures of thin-walled open section] // Structural Mechanics and Analysis of Constructions. 2012. 245(6). Pp. 18–25. (rus)
30. Atavin, I.V., Melnikov, B.E., Semenov, A.S., Chernysheva, N.V., Yakovleva, E.L. Influence of stiffness of node on stability and strength of thin-walled structure. Magazine of Civil Engineering. 2018. 80(4). Pp. 48–61. DOI: 10.18720/MCE.80.5
31. Chernov, S.A. Konechnyy element sterzhnya korobchatogo secheniya s uzlamy po konturu secheniya [The finite element of the box-section rod with nodes along the section contour]. Avtomatizatsiya i sovremennyye tekhnologii. 2014. No. 2. Pp. 9–13. (rus)
32. Serpik, I.N., Shkolyarenko, R.O., Shvyryayev, M.V. Konechno-elementnoye modelirovaniye raboty sistem sterzhney dvutavrovogo profilya s uchedom stesennogo krucheniya [Finite-element modeling of the operation of I-beam rod systems taking into account constrained torsion]. Integratsiya, partnerstvo i innovatsii v stroitel'noy nauke i obrazovanii: Sbornik materialov mezhdunarodnoy nauchnoy konferentsii [Integration, partnership and innovation in building science and education: Proceedings of the international scientific conference]. Moscow: Izdatel'stvo MGSU, 2016. Pp. 287–292. (rus)
33. Serpik, I., Shkolyarenko, R. Refinement of the accounting methodology of bi-moments transfer at the junctions of the I-section bars. IOP Conference Series: Materials Science and Engineering. 2019. 365(4). Pp. 042011. DOI: 10.1088/1757-899X/365/4/042011
34. Serpik, I.N., Shkolyarenko, R.O. Raschet sistem tonkostennykh sterzhney korytoobraznogo profilya s uchedom stesennogo krucheniya [Calculation of thin-walled systems of channel bars taking into account the restrained torsion]. Stroitel'stvo i rekonstruktsiya. 2018. 78(4). Pp. 31–41. (rus)
35. Zienkiewicz, O.C., Taylor, R.L., Fox, D. The Finite Element Method for Solid and Structural Mechanics. Elsevier. Oxford, 2014. 672 p.
36. Meyer, C.D. Matrix Analysis and Applied Linear Algebra. SIAM. Philadelphia, 2000. 718 p.

Contacts:

Igor Serpik, inserpik@gmail.com

Roman Shkolyarenko, shkroman130@mail.ru



DOI: 10.34910/MCE.107.7

Arbitrary quadrangular finite element for plates with shear deformations

Yu.Ya. Tyukalov 

Vyatka State University, Kirov, Russian Federation

E-mail: yutvgu@mail.ru

Keywords: finite element method, flexible plates, shear deformations, approximation of moments, arbitrary quadrangular finite element

Abstract. An arbitrary quadrangular bending finite element based on a piecewise constant approximation of moments is proposed. The solution is based on the principles of minimum additional energy and possible displacements. The finite element allows you to consider the shear deformation, regardless of the ratio of the plate thickness to its sizes. The effect of locking in the calculation of thin plates is absent. Comparison of the results of the oblique plates calculation, annular and round plates with analytical solutions and calculation results for other programs was done. The comparison shows good accuracy in determining displacements and moments. Crushing the finite elements mesh makes the displacement values tend to exact values from above. To assess the influence of the finite element shape, the square plate calculations were made. To model the square plate, quadrangular elements were used, obtained from rectangular ones by changing the slope of one side. At the same time, the calculating accuracy of the displacements and moments decreased slightly. The proposed finite element is easy to implement. The problem solution did not require a numerical integration or the mapping of the quadrangular region to the rectangular one. The necessary expressions were obtained analytically.

1. Introduction

Bendable plates are widely used as load-bearing structures of buildings and structures for various purposes. A lot of scientific literature has been devoted to the development of various types of finite elements for bendable plates [1–2]. To date, software systems use a wide range of finite elements for bendable plates, developed on the basis of displacement approximations and using the Lagrange's functional. Despite this, the development of new types of finite elements continues. In particular, papers [3–4] are devoted to new finite elements for the calculation of thin plates, developed on the basis of the general theory of elasticity.

Bendable plate calculation which consider shear deformations requires the use of finite elements based on various shear theories. In [5], the equations of the theory of elasticity are directly applied to allow shear deformations, and in [6–7] the Mindline-Reissner theory of plates is used. In contrast to the classical Kirchhoff's theory, in the Reissner's theory, rotation angles and vertical displacements are considered as independent variables, which allows one to lower the maximum order of derivatives in the strain energy functional and makes it possible to use first-order functions for displacements approximations. Direct use of the Reissner theory for constructing of finite elements leads to the "jamming" effect, which consists in the impossibility of using these finite elements to calculate thin plates. The "jamming" effect allows to use these finite elements only for thick plates. In [8], the new finite element is proposed, constructed on the basis of the Reissner plate theory, but suitable for calculating thin plates. To calculate a certain class of plates, there are analytical methods which use trigonometric series for the representation of the differential equation solutions of plate bend [9–10]. This approach allows us to obtain solutions with the necessary

Tyukalov, Yu.Ya. Arbitrary quadrangular finite element for plates with shear deformations. Magazine of Civil Engineering. 2021. 107(7). Article No. 10707. DOI: 10.34910/MCE.107.7

© Tyukalov, Yu.Ya., 2021. Published by Peter the Great St. Petersburg Polytechnic University.



This work is licensed under a CC BY-NC 4.0

accuracy for plates of a certain shape. In particular, such method is used to calculate periodic oscillations of square plates [11].

The emergence of new composite materials for plates led to the appearance of new finite elements types based on various shear theories [12–13]. For such plates the Galerkin's method is used to construct triangular and quadrangular finite elements according to the Reissner–Mindline theory of plates in [13]. In [14], the first-order shift theory was used, and displacements along the cross section vary linearly. Tasks of calculating various structures, including plates, which consider contact interaction with the base, are importance. In [15], on the basis of the finite-element contact model and the step-by-step analysis method, a numerical algorithm was developed, that allows simultaneous integration of the motion equations and the implementation of contact conditions with Coulomb friction.

For the calculation of the plates, in addition to the Lagrange functional, mixed and hybrid functionals are used [16–17]. The use of such formulations makes it possible to simplify the account of shear deformations due to the use of transverse forces and moments as unknowns, in addition to displacements. But such decisions require the observance of additional conditions to ensure convergence. In [18], a quadrangular finite element with seven degrees of freedom in each node was presented: three displacements of the median surface along the coordinate axes, two shear angles, and two normal rotation angles. This element allows to more accurately consider shear deformations when changing material properties in different directions. In [19], the finite element formulation free from the “locking” effect was presented for calculating plates with allowance for shear based on the modified Mindline theory. A separate class of problems is the plates stability analysis. To solve such problems, the finite element method is widely used, but analytical methods are also using. In [20], the analytical solution was obtained for stability analysis of thin rectangular plates. Such analytical solutions can also be used to test the finite element solutions.

In [21], the finite element model was proposed for calculating thin flexible plates, based on the moment's approximations. The solution was obtained by using the functional of the additional energy and the possible displacements principle. The resolving equations for rectangular and triangular finite elements was obtained. Such finite element models make it possible to get convergence of displacements from above. Similar solutions based on the stress' approximations were obtained for plane problems of the elasticity theory [22–23]. In [24], the method was proposed for considering shear deformations, based on the transverse forces' approximation and the additional energy functional. Shear displacements are determined independently of bend displacements. This approach is free from the locking effect and can be used to calculate any thickness plates. In [25], the finite element model also based on the moments approximations was proposed for calculating plates according of the Reissner theory.

Finite element solutions based on the moments (stresses) approximation allow one to obtain solutions that are alternative to solutions based on the Lagrange functional. This determines their relevance.

This paper aim is to build an arbitrary quadrangular finite element designed to calculate various thicknesses plates, based on the moments and transverse forces approximations. The solution will be based on papers [21, 24], in which only rectangular and triangular finite elements were considered. To evaluate the accuracy of the proposed finite element, test calculations and comparison of the results with analytical solutions and results obtained by other methods will be performed.

2. Methods

We will build the solution of the problem of bending thin plates to involve the moments approximations on the basis of the functional [1]:

$$\Pi^c = \frac{1}{2} \int_A \frac{12}{E \cdot t^3} \left(M_x^2 + M_y^2 - 2\nu M_x M_y + 2(1+\nu) M_{xy}^2 \right) dA, \quad (1)$$

E is the elastic modulus of the plate material; t is the plate thickness; ν is Poisson's ratio; M_x is bending moment directed along the X axis; M_y is bending moment directed along the Y axis; M_{xy} is torque. We write the functional (1) in the standard matrix form:

$$\Pi^c = \frac{1}{2} \int_A \mathbf{M}_s^T \mathbf{E}^{-1} \mathbf{M}_s dA. \quad (2)$$

The following notations are introduced in expression (2):

$$\mathbf{M}_s = \begin{Bmatrix} M_x \\ M_y \\ M_{xy} \end{Bmatrix}, \quad \mathbf{E}^{-1} = \frac{12}{E \cdot t^3} \begin{bmatrix} 1 & -\nu & 0 \\ -\nu & 1 & 0 \\ 0 & 0 & 2(1+\nu) \end{bmatrix}. \quad (3)$$

We introduce the notations for unknown nodal moments $M_{x,i}, M_{y,i}, M_{xy,i}$ and for the nodal moments vector of an arbitrary quadrangular finite element

$$\mathbf{M}_k^T = (M_{x,1} \ M_{y,1} \ M_{xy,1} \ M_{x,2} \ M_{y,2} \ M_{xy,2} \ M_{x,3} \ M_{y,3} \ M_{xy,3} \ M_{x,4} \ M_{y,4} \ M_{xy,4}). \quad (4)$$

In the finite element region, we will approximate the moments fields by piecewise constant functions (Fig. 1) [21, 24].

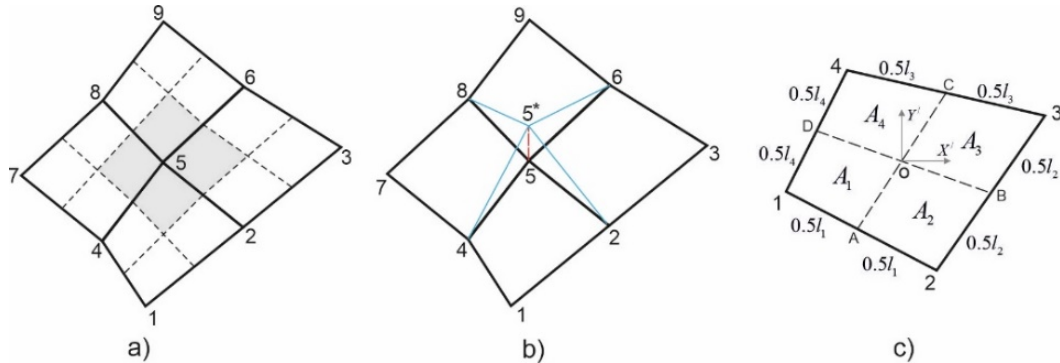


Figure 1. An arbitrary quadrangular finite element: a) dashed lines go through the midpoints of sides and divide the finite elements into regions with constant moments; b) the possible displacement of the node; c) the nodes local numbers and the coordinate system for the finite element.

To simplify the expressions recording, we introduce auxiliary stair-step functions:

$$\psi_i(x, y) = \begin{cases} 1, & (x, y) \in A_i \\ 0, & (x, y) \notin A_i \end{cases}. \quad (5)$$

And introduce the corresponding diagonal matrices

$$\Psi_i = \begin{bmatrix} \psi_i & & \\ & \psi_i & \\ & & \psi_i \end{bmatrix}. \quad (6)$$

Then the moments approximations matrix in the finite element region will have simple form:

$$\mathbf{Z}_k = [\Psi_1 \ \Psi_2 \ \Psi_3 \ \Psi_4]. \quad (7)$$

We get

$$\mathbf{M}_s = \mathbf{Z}_k \mathbf{M}_k. \quad (8)$$

Using (8), we will express the additional strain energy of the finite element in the following form:

$$\Pi_k^c = \frac{1}{2} \int_{A_k} \mathbf{M}_k^T (\mathbf{Z}_k^T \mathbf{E}^{-1} \mathbf{Z}_k) \mathbf{M}_k dA. \quad (9)$$

We introduce the notation for the local flexibility matrix of the finite element:

$$\mathbf{D}_k = \int_{A_k} \mathbf{Z}_k^T \mathbf{E}^{-1} \mathbf{Z}_k dA. \quad (10)$$

Note that the matrix \mathbf{D}_k is calculated analytically and has simple block-diagonal form:

$$\mathbf{D}_k = \begin{bmatrix} A_1 \mathbf{E}^{-1} & & & \\ & A_2 \mathbf{E}^{-1} & & \\ & & A_3 \mathbf{E}^{-1} & \\ & & & A_4 \mathbf{E}^{-1} \end{bmatrix}, \quad (11)$$

$A_1 \div A_4$ are the areas of the finite element parts in which the moments are constant (Fig. 1).

From the flexibility matrices of finite elements, the global flexibility matrix \mathbf{D} is formed, and from vectors \mathbf{M}_k the global nodes moments vector \mathbf{M} . Using the introduced notation, we obtain the following expression of functional (2):

$$\Pi^c = \frac{1}{2} \mathbf{M}^T \mathbf{D} \mathbf{M}. \quad (12)$$

It is important that the matrix \mathbf{D} is block-diagonal and consists of square matrices measuring 3 by 3. Therefore, the matrix \mathbf{D} is easily analytically reversible. This circumstance greatly simplifies the construction of the problem solution.

In accordance with the principle of additional energy minimum, the moments fields must satisfy the equilibrium equations and static boundary conditions. To ensure the moments fields equilibrium, we compose the grid nodes equilibrium equations using the possible displacements principle [21, 24].

Fig. 1b shows the possible displacement of the node and the finite elements adjoined to it. To approximate vertical displacements in the finite element region, which are caused by the possible displacement of node i , we will use the following function:

$$\delta w_i(x, y) = a_{1,i} + a_{2,i}x + a_{3,i}y + a_{4,i}xy, \quad i = 1 \div 4, \quad (13)$$

x, y are point coordinates in the local coordinate system of finite element XY' (Fig. 1c). To determine the parameters $a_{j,i}$ included in the expression for the approximating functions (13), it is necessary to form the following matrix:

$$\mathbf{B} = \begin{bmatrix} 1 & x_1 & y_1 & x_1 y_1 \\ 1 & x_2 & y_2 & x_2 y_2 \\ 1 & x_3 & y_3 & x_3 y_3 \\ 1 & x_4 & y_4 & x_4 y_4 \end{bmatrix}, \quad (14)$$

x_i, y_i are coordinates of node i of the finite element. If the possible displacement of node is taken equal to unity, then the parameters $a_{j,i}$ are elements of the inverse matrix \mathbf{B}^{-1} :

$$\mathbf{B}^{-1} = \begin{bmatrix} a_{1,1} & a_{1,2} & a_{1,3} & a_{1,4} \\ a_{2,1} & a_{2,2} & a_{2,3} & a_{2,4} \\ a_{3,1} & a_{3,2} & a_{3,3} & a_{3,4} \\ a_{4,1} & a_{4,2} & a_{4,3} & a_{4,4} \end{bmatrix}. \quad (15)$$

Each column of the matrix \mathbf{B}^{-1} contains the parameters of approximating functions for possible displacement of one finite element node.

The principle of possible displacements can be written as follows:

$$\delta U_i + \delta V_i = 0. \quad (16)$$

δU_i is the internal forces work of the finite elements adjoined to the node i ; δV_i is the external forces potential due to possible displacements. For one finite element k , the internal forces work, in the general case, is written as follows:

$$\delta U_i^k = \int_{A^k} \left(M_x \frac{\partial^2(\delta w_i)}{\partial x^2} + M_y \frac{\partial^2(\delta w_i)}{\partial y^2} + M_{xy} \frac{\partial^2(\delta w_i)}{\partial x \partial y} \right) dA. \quad (17)$$

From expression (12) we obtain:

$$\delta \varphi_{xi} = \frac{\partial(\delta w_i)}{\partial x} = a_{2,i} + a_{4,i}y, \quad \delta \varphi_{yi} = \frac{\partial(\delta w_i)}{\partial y} = a_{3,i} + a_{4,i}x, \quad \delta k_{xyi} = 2 \frac{\partial^2(\delta w_i)}{\partial x \partial y} = 2a_{4,i}, \quad (18)$$

$\delta \varphi_{xi}$, $\delta \varphi_{yi}$ are the possible rotation angles along the X and Y axes, respectively; δk_{xyi} is possible torsional curvature.

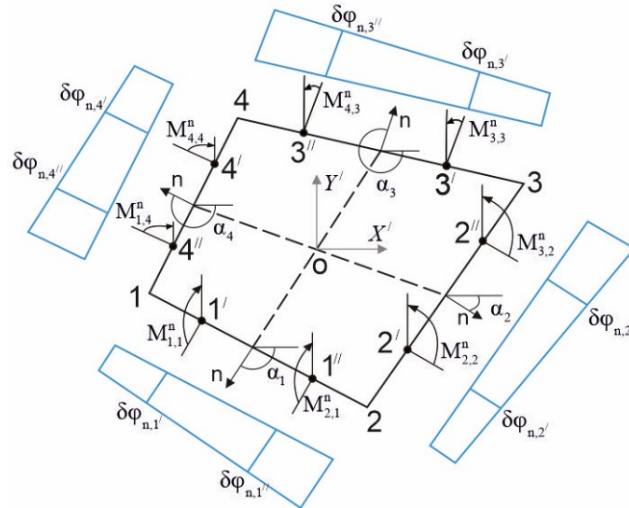


Figure 2. Graphs of the rotation angles changing along the normal to the finite element sides.

Obviously, the bending curvatures $\frac{\partial^2(\delta w_i)}{\partial x^2}$, $\frac{\partial^2(\delta w_i)}{\partial y^2}$ are equal to zero and the finite element rotates without bending. At the same time, the moments which normal to the sides of the finite element perform the work with the corresponding rotation angles. But the torques perform the work inside the finite element area. Therefore, we write the work of the finite element internal forces in the following form:

$$\delta U_i^k = \oint_{S^k} M_n \delta \varphi_n dS + \int_{A^k} M_{xy} \delta k_{xyi} dA, \quad (19)$$

M_n is the moment normal to the borders (sides) of the finite element; $\delta \varphi_n$ is the angle of the section rotation along the normal to the borders (sides) of the finite element; S^k are the finite element borders. In accordance with (18), torsion curvature is constant in the finite element region, therefore

$$\int_{A^k} M_{xy} \delta k_{xyi} dA = 2a_{4,i} (M_{xy,1}A_1 + M_{xy,2}A_2 + M_{xy,3}A_3 + M_{xy,4}A_4). \quad (20)$$

Cosines and sines of the angles indicated in Fig. 2, are calculated by the node's coordinates:

$$\begin{aligned} \cos \alpha_1 &= \frac{y_2 - y_1}{l_1}, \quad \cos \alpha_2 = \frac{y_3 - y_2}{l_2}, \quad \cos \alpha_3 = \frac{y_4 - y_3}{l_3}, \quad \cos \alpha_4 = \frac{y_1 - y_4}{l_4}, \\ \sin \alpha_1 &= \frac{x_1 - x_2}{l_1}, \quad \sin \alpha_2 = \frac{x_2 - x_3}{l_2}, \quad \sin \alpha_3 = \frac{x_3 - x_4}{l_3}, \quad \sin \alpha_4 = \frac{x_4 - x_1}{l_4}. \end{aligned} \quad (21)$$

The section rotation angle along the normal to the side k of the finite element, by the possible displacement of node i , is calculated by the following formula:

$$\delta \varphi_n = \delta \varphi_x \cos \alpha_k + \delta \varphi_y \sin \alpha_k = (a_{2,i} + a_{4,i}y) \cos \alpha_k + (a_{3,i} + a_{4,i}x) \sin \alpha_k. \quad (22)$$

The points coordinates on the finite element sides indicated in Fig. 2 are determined by the following formulas:

$$\begin{aligned}
x_{1'} &= \frac{3x_1 + x_2}{4}, x_{1''} = \frac{x_1 + 3x_2}{4}, y_{1'} = \frac{3y_1 + y_2}{4}, y_{1''} = \frac{y_1 + 3y_2}{4}, \\
x_{2'} &= \frac{3x_2 + x_3}{4}, x_{2''} = \frac{x_2 + 3x_3}{4}, y_{2'} = \frac{3y_2 + y_3}{4}, y_{2''} = \frac{y_2 + 3y_3}{4}, \\
x_{3'} &= \frac{3x_3 + x_4}{4}, x_{3''} = \frac{x_3 + 3x_4}{4}, y_{3'} = \frac{3y_3 + y_4}{4}, y_{3''} = \frac{y_3 + 3y_4}{4}, \\
x_{4'} &= \frac{3x_4 + x_1}{4}, x_{4''} = \frac{x_4 + 3x_1}{4}, y_{4'} = \frac{3y_4 + y_1}{4}, y_{4''} = \frac{y_4 + 3y_1}{4}.
\end{aligned} \tag{23}$$

Substituting the points coordinates in (22), we obtain the expressions for the rotation angles of the section, along the normal to the sides, for the points indicated in Fig. 2:

$$\begin{aligned}
\delta\varphi_{ni,j'} &= \left(a_{2,i} + a_{4,i} y_{j'} \right) \cos \alpha_j + \left(a_{3,i} + a_{4,i} x_{j'} \right) \sin \alpha_j, \\
\delta\varphi_{ni,j''} &= \left(a_{2,i} + a_{4,i} y_{j''} \right) \cos \alpha_j + \left(a_{3,i} + a_{4,i} x_{j''} \right) \sin \alpha_j, \quad i, j = 1, 2, 3, 4.
\end{aligned} \tag{24}$$

In (24), the index i denotes the node number, whose possible displacement is considered; index j denotes the side number of the finite element.

Bending moments directed along the normal to the finite element sides are calculated by the well-known formula:

$$M_n = -M_x \sin^2 \alpha_i - M_y \cos^2 \alpha_i - 2M_{xy} \sin \alpha_i \cos \alpha_i. \tag{25}$$

In (25), moments enter with a minus sign, since the moments external to the boundary opposite to the internal moments. Using (25), we calculate the normal moments values, that are constant for each half of the finite element side:

$$\begin{aligned}
M_{1,1}^n &= -M_{x,1} \sin^2 \alpha_1 - M_{y,1} \cos^2 \alpha_1 - 2M_{xy,1} \sin \alpha_1 \cos \alpha_1, \\
M_{2,1}^n &= -M_{x,2} \sin^2 \alpha_1 - M_{y,2} \cos^2 \alpha_1 - 2M_{xy,2} \sin \alpha_1 \cos \alpha_1, \\
M_{2,2}^n &= -M_{x,2} \sin^2 \alpha_2 - M_{y,2} \cos^2 \alpha_2 - 2M_{xy,2} \sin \alpha_2 \cos \alpha_2, \\
M_{3,2}^n &= -M_{x,3} \sin^2 \alpha_2 - M_{y,3} \cos^2 \alpha_2 - 2M_{xy,3} \sin \alpha_2 \cos \alpha_2, \\
M_{3,3}^n &= -M_{x,3} \sin^2 \alpha_3 - M_{y,3} \cos^2 \alpha_3 - 2M_{xy,3} \sin \alpha_3 \cos \alpha_3, \\
M_{4,3}^n &= -M_{x,4} \sin^2 \alpha_3 - M_{y,4} \cos^2 \alpha_3 - 2M_{xy,4} \sin \alpha_3 \cos \alpha_3, \\
M_{4,4}^n &= -M_{x,4} \sin^2 \alpha_4 - M_{y,4} \cos^2 \alpha_4 - 2M_{xy,4} \sin \alpha_4 \cos \alpha_4, \\
M_{1,4}^n &= -M_{x,1} \sin^2 \alpha_4 - M_{y,1} \cos^2 \alpha_4 - 2M_{xy,1} \sin \alpha_4 \cos \alpha_4.
\end{aligned} \tag{26}$$

The rotation angles along each side of the finite element vary linearly (Fig. 2), and the moments are constant on the half of each side, therefore

$$\begin{aligned}
\oint_{S^k} M_n \delta\varphi_n dS &= \frac{1}{2} (M_{1,1}^n \delta\varphi_{ni,1'} l_1 + M_{1,2}^n \delta\varphi_{ni,1''} l_1 + M_{2,2}^n \delta\varphi_{ni,2'} l_2 + M_{2,3}^n \delta\varphi_{ni,2''} l_2 + \\
&M_{3,3}^n \delta\varphi_{ni,3'} l_3 + M_{3,4}^n \delta\varphi_{ni,3''} l_3 + M_{4,4}^n \delta\varphi_{ni,4'} l_4 + M_{1,4}^n \delta\varphi_{ni,4''} l_4).
\end{aligned} \tag{27}$$

Summing up the integrals (20) and (27), we obtain the internal forces work δU_i^k of the finite element on the possible displacement of the node i . The work can be written in vector form:

$$\delta U_i^k = \mathbf{C}_i^T \mathbf{M}_k, \tag{28}$$

\mathbf{C}_i is the vector whose elements are the total coefficients from expressions (19) and (27), which are multipliers of the corresponding unknown moments. The vector \mathbf{C}_i elements will have the following expressions:

$$\mathbf{C}_i = -\frac{1}{2} \left\{ \begin{array}{l}
\delta\varphi_{ni,1}/l_1 \sin^2 \alpha_1 + \delta\varphi_{ni,4}/l_4 \sin^2 \alpha_4 \\
\delta\varphi_{ni,1}/l_1 \cos^2 \alpha_1 + \delta\varphi_{ni,4}/l_4 \cos^2 \alpha_4 \\
2\delta\varphi_{ni,1}/l_1 \sin \alpha_1 \cos \alpha_1 + 2\delta\varphi_{ni,4}/l_4 \sin \alpha_4 \cos \alpha_4 - 2A_1 a_{4,i} \\
\delta\varphi_{ni,2}/l_2 \sin^2 \alpha_2 + \delta\varphi_{ni,1}/l_1 \sin^2 \alpha_1 \\
\delta\varphi_{ni,2}/l_2 \cos^2 \alpha_2 + \delta\varphi_{ni,1}/l_1 \cos^2 \alpha_1 \\
2\delta\varphi_{ni,2}/l_2 \sin \alpha_2 \cos \alpha_2 + 2\delta\varphi_{ni,1}/l_1 \sin \alpha_1 \cos \alpha_1 - 2A_2 a_{4,i} \\
\delta\varphi_{ni,3}/l_3 \sin^2 \alpha_3 + \delta\varphi_{ni,2}/l_2 \sin^2 \alpha_2 \\
\delta\varphi_{ni,3}/l_3 \cos^2 \alpha_3 + \delta\varphi_{ni,2}/l_2 \cos^2 \alpha_2 \\
2\delta\varphi_{ni,3}/l_3 \sin \alpha_3 \cos \alpha_3 + 2\delta\varphi_{ni,2}/l_2 \sin \alpha_2 \cos \alpha_2 - 2A_3 a_{4,i} \\
\delta\varphi_{ni,4}/l_4 \sin^2 \alpha_4 + \delta\varphi_{ni,3}/l_3 \sin^2 \alpha_3 \\
\delta\varphi_{ni,4}/l_4 \cos^2 \alpha_4 + \delta\varphi_{ni,3}/l_3 \cos^2 \alpha_3 \\
2\delta\varphi_{ni,4}/l_4 \sin \alpha_4 \cos \alpha_4 + 2\delta\varphi_{ni,3}/l_3 \sin \alpha_3 \cos \alpha_3 - 2A_4 a_{4,i}
\end{array} \right\}. \quad (29)$$

After calculating the internal forces work on the possible displacements of the all finite element nodes, we obtain

$$\left\{ \begin{array}{l}
\delta U_1^k \\
\delta U_2^k \\
\delta U_3^k \\
\delta U_4^k
\end{array} \right\} = \mathbf{L}_k \mathbf{M}_k, \quad \mathbf{L}_k = \begin{bmatrix} \mathbf{C}_1^T \\ \mathbf{C}_2^T \\ \mathbf{C}_3^T \\ \mathbf{C}_4^T \end{bmatrix}. \quad (30)$$

The matrix \mathbf{L}_k consists of four rows and twelve columns. From the finite elements matrices \mathbf{L}_k , in accordance with the nodes numbering, the global matrix \mathbf{L} is formed for the entire system.

The external forces potential by the possible displacement of node i

$$\delta V_i = P_{z,i} + \sum_{\kappa=1}^m \int_{A_k} q_z \delta w_i dA = \bar{P}_{z,i}. \quad (31)$$

The integral in (31) is calculated over the area m of finite elements adjacent to node i . $P_{z,i}$ is force which is concentrated in the node; q_z is load which is distributed over the element area. For the case of a uniformly distributed load, the integral is calculated analytically. As calculations showed, without loss of accuracy, the uniformly distributed load can be replaced by concentrated nodes. Then we get

$$\delta V_i = P_{z,i} + \sum_{k=1}^m q_z A_{i,k} = \bar{P}_{z,i}, \quad (32)$$

$A_{i,k}$ is part of the finite element area adjacent to the node i (see Fig. 1). From the values $\bar{P}_{z,i}$, in accordance with the nodes numbering, the global vector of external forces \mathbf{P} is formed. In accordance with (15), we obtain the nodes equilibrium equations system

$$\mathbf{LM} + \mathbf{P} = 0. \quad (33)$$

Using the Lagrange multipliers, equations (33) are added to the functional (11).

$$\Pi^c = \frac{1}{2} \mathbf{M}^T \mathbf{D} \mathbf{M} + \mathbf{w}^T (\mathbf{L} \mathbf{M} + \mathbf{P}), \quad (34)$$

\mathbf{W} is the nodal displacements vector. To consider the static boundary conditions, it is necessary to compose additional equations and, using the Lagrange multipliers, add it to the functional (34). Then the vector will include these additional parameters. The necessary equations are given in [21, 24].

To obtain solving equations, we equate the derivatives (34) with respect to the vectors \mathbf{M} and \mathbf{w} to zero:

$$\begin{aligned} \mathbf{D} \mathbf{M} + \mathbf{L}^T \mathbf{w} &= 0, \\ \mathbf{L} \mathbf{M} + \mathbf{P} &= 0. \end{aligned} \quad (35)$$

Expressing the vector \mathbf{M} from the first equation and substituting it into the second equation, we obtain:

$$\begin{aligned} \mathbf{K} &= \mathbf{L} \mathbf{D}^{-1} \mathbf{L}^T, \\ \mathbf{K} \mathbf{w} &= \mathbf{P}, \\ \mathbf{M} &= \mathbf{D}^{-1} \mathbf{L}^T \mathbf{w}. \end{aligned} \quad (36)$$

When calculating thick plates, it is necessary consider additional shear deformations. In the framework of the proposed methodology, we can consider the shear state regardless for the bending state and use the following functional [24]:

$$\Pi^c = \frac{1}{2} \int_S \left(\frac{2k(1+\nu)}{E \cdot t} \right) (Q_x^2 + Q_y^2) dS, \quad (37)$$

$k = 6/5$ is coefficient which consider the parabolic law of the shear stresses change along the plate thickness. Q_x, Q_y are transverse forces. We introduce the notations:

$$\mathbf{Q}_s = \begin{Bmatrix} Q_x \\ Q_y \end{Bmatrix}, \quad \mathbf{E}_{sh}^{-1} = \frac{12(1+\nu)}{5E \cdot t} \begin{bmatrix} 1 & 0 \\ 0 & 1 \end{bmatrix}. \quad (38)$$

Then

$$\Pi^c = \frac{1}{2} \int_S \mathbf{Q}_s^T \mathbf{E}_{sh}^{-1} \mathbf{Q}_s dS. \quad (39)$$

We consider the case when the transverse forces are assumed constant over the finite element region. Then for one finite element we get:

$$\Pi_k^c = \frac{1}{2} \mathbf{Q}_k^T \mathbf{D}_{sh,k} \mathbf{Q}_k, \quad (40)$$

A_k is the finite element area; $\mathbf{Q}_k = \begin{Bmatrix} Q_{x,k} \\ Q_{y,k} \end{Bmatrix}$ is the finite element transverse forces vector. Then

$$\mathbf{D}_{sh,k} = A_k \mathbf{E}_{sh}^{-1}. \quad (41)$$

For whole system, we can write

$$\Pi^c = \frac{1}{2} \mathbf{Q}^T \mathbf{D}_{sh} \mathbf{Q}, \quad (42)$$

\mathbf{Q} is vector of shear forces for whole system; \mathbf{D}_{sh} is global flexible matrix of the shear for whole system.

Using the possible displacements principle, we compose the nodes equilibrium equations under shear. To approximate possible displacements under shear, we also use expression (12). As a result of the node possible displacement, the shear deformations take place in the sections:

$$\delta\gamma_{xz} = \frac{\partial(\delta w_{sh,i})}{\partial x} = a_{2,i} + a_{4,i}y, \quad \delta\gamma_{yz} = \frac{\partial(\delta w_{sh,i})}{\partial y} = a_{3,i} + a_{4,i}x. \quad (43)$$

Then the work of the internal transverse forces for the finite element k , at the possible displacement of node i , can be expressed as follows:

$$\begin{aligned} \delta U_i^k &= \int_{A_k} (\delta\gamma_{xz} Q_{x,k} + \delta\gamma_{yz} Q_{y,k}) dS = \\ &= a_{2,i} A_k Q_{x,k} + a_{3,i} A_k Q_{y,k} + Q_{x,k} a_{4,i} \int_{A_k} y dS + Q_{y,k} a_{4,i} \int_{A_k} x dS. \end{aligned} \quad (44)$$

To calculate the integrals (44), we divide the quadrangular finite element into two triangles 1-2-3 and 1-3-4 (see Fig. 1). Next, we will perform integration over each part using triangular coordinates. Then we get the following simple expression:

$$\begin{aligned} \delta U_i^k &= a_{2,i} A_k Q_{x,k} + a_{3,i} A_k Q_{y,k} + \\ &+ \frac{a_{4,i}}{3} (A_{123} (y_1 + y_2 + y_3) + A_{134} (y_1 + y_3 + y_4)) Q_{x,k} + \\ &+ \frac{a_{4,i}}{3} (A_{123} (x_1 + x_2 + x_3) + A_{134} (x_1 + x_3 + x_4)) Q_{y,k}, \end{aligned} \quad (45)$$

A_{123} , A_{134} are the areas of the triangles 1-2-3 and 1-3-4 (see Fig. 1). We write the work δU_i^k in matrix form:

$$\delta U_i^k = \mathbf{C}_{sh,i}^T \mathbf{Q}_k, \quad (46)$$

$\mathbf{C}_{sh,i}$ is a vector whose elements are coefficients from expression (45), which are multipliers of the corresponding unknown transverse forces.

$$\mathbf{C}_{sh,i} = \begin{Bmatrix} a_{2,i} A_k + \frac{a_{4,i}}{3} (A_{123} (y_1 + y_2 + y_3) + A_{134} (y_1 + y_3 + y_4)) \\ a_{3,i} A_k + \frac{a_{4,i}}{3} (A_{123} (x_1 + x_2 + x_3) + A_{134} (x_1 + x_3 + x_4)) \end{Bmatrix}. \quad (47)$$

After calculating the internal forces work on possible displacements of all nodes of finite element, we obtain

$$\begin{Bmatrix} \delta U_1^k \\ \delta U_2^k \\ \delta U_3^k \\ \delta U_4^k \end{Bmatrix} = \mathbf{L}_{sh,k} \mathbf{Q}_k, \quad \mathbf{L}_{sh,k} = \begin{bmatrix} \mathbf{C}_{sh,1}^T \\ \mathbf{C}_{sh,2}^T \\ \mathbf{C}_{sh,3}^T \\ \mathbf{C}_{sh,4}^T \end{bmatrix}. \quad (48)$$

The matrix $\mathbf{L}_{sh,k}$ consists of four rows and two columns. From the finite element matrices $\mathbf{L}_{sh,k}$, in accordance with the nodes numbering, the global matrix is formed for the whole system \mathbf{L}_{sh} .

The external forces potential is calculated by (32). The nodes equilibrium equations system under shear:

$$\mathbf{L}_{sh} \mathbf{Q} + \mathbf{P} = 0. \quad (49)$$

Including the equilibrium equations in functional (42) with the help of Lagrange multipliers, we obtain

$$\Pi^c = \frac{1}{2} \mathbf{Q}^T \mathbf{D}_{sh} \mathbf{Q} + \mathbf{w}_{sh}^T (\mathbf{L}_{sh} \mathbf{Q} + \mathbf{P}), \quad (50)$$

\mathbf{w}_{sh} is the nodal displacements vector, caused by the sections shear deformations. To obtain solving equations, we equate the derivatives (50) with respect to the vectors \mathbf{Q} and \mathbf{w}_{sh} to zero:

$$\begin{aligned} \mathbf{D}_{sh} \mathbf{Q} + \mathbf{L}_{sh}^T \mathbf{w}_{sh} &= 0, \\ \mathbf{L}_{sh} \mathbf{Q} + \mathbf{P} &= 0. \end{aligned} \quad (51)$$

Expressing the vector \mathbf{Q} from the first equation and substituting it into the second equation, we obtain:

$$\begin{aligned} \mathbf{K}_{sh} &= \mathbf{L}_{sh} \mathbf{D}_{sh}^{-1} \mathbf{L}_{sh}^T, \\ \mathbf{K}_{sh} \mathbf{w}_{sh} &= \mathbf{P}, \\ \mathbf{Q} &= \mathbf{D}_{sh}^{-1} \mathbf{L}_{sh}^T \mathbf{w}_{sh}. \end{aligned} \quad (52)$$

To consider the static boundary conditions, it is necessary to compose additional equations and, using the Lagrange multipliers, add into functional (50). Then the vector will include these additional unknowns. The necessary equations are given in [24]. Obviously, the total nodes displacements considering shear deformations are determined as the sum:

$$\mathbf{w}_{sum} = \mathbf{w} + \mathbf{w}_{sh}. \quad (53)$$

3. Results and Discussions

As mesh refinement test, we calculated of the skew plate which is supported by hinges along the contour (Fig. 3). For such plate, the finite-difference solution is given in [26]. We used parallelogram finite elements with the largest angle of 120 degrees. The plate has the following parameters: $E = 10^7 \text{ kN} / \text{m}^2$, $\mu = 0.21$, $t = 0.1\text{m}$, $q = 10\text{kN} / \text{m}^2$. The geometric dimensions are shown in Fig. 3. The calculations were performed for three finite element grids: a 6 by 10 grid, a 10 by 20 grid, and a 20 by 40 grid. In addition, for comparison, the calculations of this plate were performed according to the LIRA-SCAD program. All results are summarized in Table 1, where SFEM is the solution according to the proposed method.

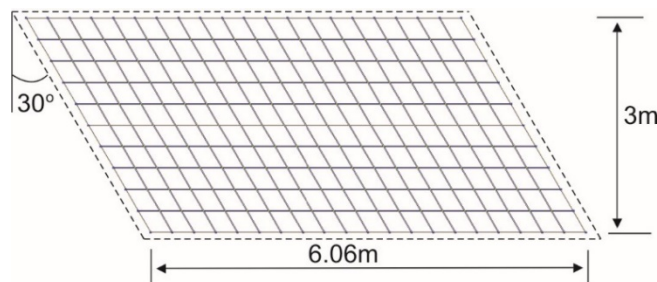


Figure 3. The skew plate with hinge supports.

Table 1. Displacements and bending moments in the plate center (Fig. 3).
Mesh refinement test.

Solution (grid)	w, mm	$M_x, \text{kN} \cdot \text{m} / \text{m}$	$M_y, \text{kN} \cdot \text{m} / \text{m}$
SFEM (6x10)	10.779	3.654	9.903
SFEM (10x20)	10.039	3.586	9.451
SFEM (20x40)	9.587	3.529	9.132
LIRA-SAPR (6x10)	9.093	3.290	8.303
LIRA-SAPR (10x20)	9.115	3.404	8.611
LIRA-SAPR (20x40)	9.149	3.449	8.731
Timoshenko [26]	9.719	–	8.712

The results in Table 1 show that the plate center displacement obtained using the proposed finite element (SFEM), when crushing the mesh tends to the exact value from above. Similar results were obtained for rectangular and triangular finite elements, also constructed on the basis of the stress approximation [22]. For the smallest grid, the obtained displacement value differs from the analytical one by 1.4 percent. The bending moments also tend to exact values from above. The value of the maximum moment, obtained on the smallest grid, is 4.8 percent more than the analytical value.

As a further example, the half-ring was calculated on the uniformly distributed load action (Fig. 6). The half-ring has a hinged support along the lines DE and DB, and clamped support along the line EA. Line

AB is the symmetry axis, therefore, at the nodes lying on this line, zero torques were taken. The following data were accepted in the calculations: $E = 10000 \text{ kN/m}^2$, $\mu = 0.3$, $t = 0.1 \text{ m}$, $q = 10 \text{ kN/m}^2$, $R = 6 \text{ m}$, $r = 3 \text{ m}$.

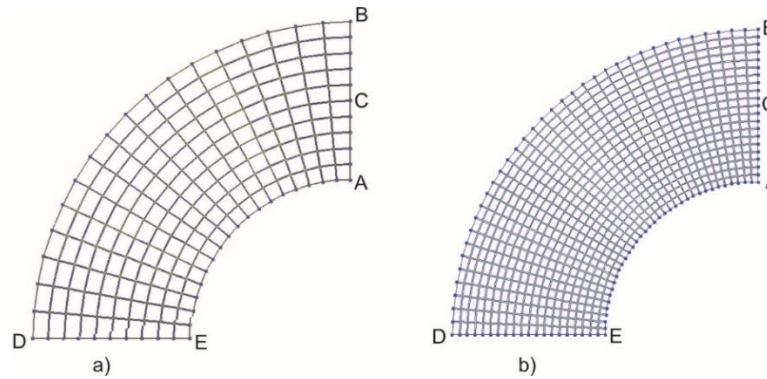


Figure 4. Finite-element meshes of the half-ring.

The obtained results were reduced to dimensionless form:

$$\bar{w} = w \frac{1000D}{qR^4}, \bar{M}_x = \frac{M_x}{qR^2}, \bar{M}_y = \frac{M_y}{qR^2}. \quad (54)$$

Table 2. Comparison of finite element results for the half-ring with the analytical solution.

Solution	\bar{w}_c	$\bar{M}_{x,A}$	$\bar{M}_{y,A}$	$\bar{M}_{x,C}$	$\bar{M}_{y,C}$	$\bar{M}_{x,B}$
SFEM (Fig. 4a)	0.374	0.0134	0.0387	-0.00460	-0.0173	-0.00226
SFEM (Fig. 4b)	0.362	0.0133	0.0396	-0.00445	-0.0169	-0.00394
LIRA-SAPR (Fig. 4a)	0.350	0.0098	0.0287	-0.00422	-0.0163	-0.00352
LIRA-SAPR (Fig. 4b)	0.348	0.0108	0.0336	-0.00434	-0.0166	-0.00291
Analytical [27]	0,358	0,0118	0,0393	-0,00439	-0,0168	-0.00234

Analysis of the results shown in Table 2, demonstrates a good accuracy of the proposed finite element. The value of the radial direction moment $\bar{M}_{y,A}$, which has the prevailing values, is very close to the analytical value. The maximum displacement obtained by the proposed method differs from the analytical value by less than one percent. The moment value in the circumferential direction is an order of magnitude smaller than the moment value in the radial direction. The proposed finite element gives a significantly greater value of this moment. It should be noted that this moment value obtained by the LIRA-SAPR program is also much greater than the analytical value. We also note that the values of another moment $\bar{M}_{x,C}$ in the circumferential direction, obtained both by the proposed method and by the LIRA-SAPR program, are close to the analytical value.

To assess the influence of the finite element shape (mesh distortion test), the square plate that have clamped support along the contour was calculated on the action of the uniformly distributed load. Figure 5 shows the finite element grid for the plates quarter. The calculations were performed for grids with angles from zero to 60 degrees.

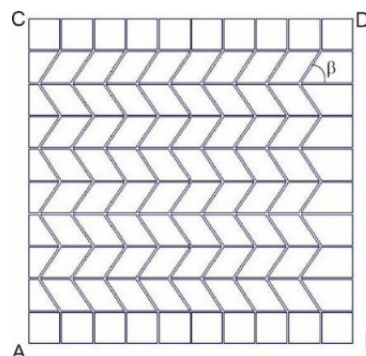


Figure 5. The finite element grid for the square plates quarter. The sides of the AC and AB are pinched; the sides of CD and BD are symmetry axes.

The following data were accepted for the plate: $E = 10000 \text{ kN} / \text{m}^2$, $\mu = 0.3$, $t = 1 \text{ m}$, $q = 10 \text{ kN} / \text{m}^2$. Table 3 shows the results of calculations of the plate without considering shear deformations. Obviously, then larger the angle β , the more distorted the finite element shape, and the more significantly the calculation results should differ from the values obtained for the grid of square finite elements ($\beta = 0$).

Table 3. Calculation results for the square plate (Fig. 5). Mesh distortion test.

β , degrees	$w_D, \text{ mm}$	$M_{x,D}, \text{ kNm} / \text{ m}$	$M_{y,D}, \text{ kNm} / \text{ m}$	$M_{y,B}, \text{ kNm} / \text{ m}$
0	18.537	8.361	8.361	-18.251
10	18.527	8.303	8.282	-18.143
20	18.516	8.230	8.184	-18.024
30	18.503	8.140	8.072	-17.901
40	18.488	8.037	7.953	-17.774
50	18.469	7.930	7.834	-17.649
60	18.446	7.823	7.723	-17.535

First of all, we note that the displacement of the plate center depends on the angle β insignificant. At $\beta = 60$ degrees, the displacement value is less than the displacement for the square grid only on 0.5 percent. The value of the moment $M_{y,B}$ in the clamped side, taken modulus, is less than the absolute value of this moment at $\beta = 0$ on 3.9 percent. The value of the moment $M_{x,D}$, at $\beta = 60$, decreases by 6.4 percent. In general, we can conclude that even with a strong distortion of the finite elements shape, when the maximum internal angle becomes equal to 150 degrees, the proposed arbitrary quadrangular finite element allows us to obtain sufficiently accurate values of displacements and moments for the square-shaped plate.

As the next test example (shear locking test), the calculations of the hinged and clamped support round plates (Fig. 6) on action of a uniformly distributed load with considering shear deformations were performed. For such plates, there are Timoshenko-Mindline analytical solutions center displacements.

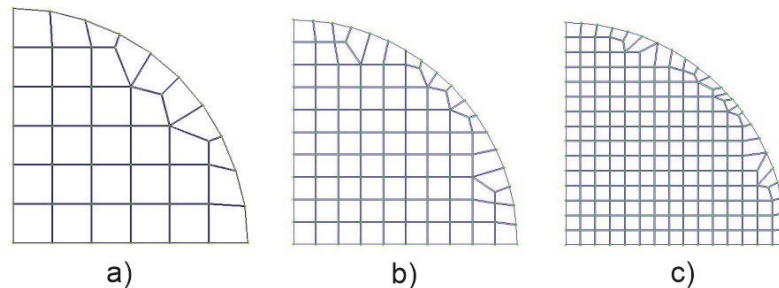


Figure 6. Finite element mesh for a quarter of the round plate.

For a hinged round plate, this Timoshenko-Mindline decision is written as follows:

$$w = \frac{qR^4}{62D} \left(\frac{5 + \mu}{1 + \mu} \right) + \frac{qR^2}{4kGt}. \quad (55)$$

For clamped round plate:

$$w = \frac{qR^4}{62D} + \frac{qR^2}{4kGt}, \quad (56)$$

R is the plate radius; t is the plate thickness; $D = \frac{Et^3}{12(1 - \mu^2)}$ is the plate cylindrical stiffness; $k = \frac{5}{6}$;

$G = \frac{E}{2(1 + \mu)}$ is shear modulus. The following parameters have been used for the plate:

$E = 10^7 \text{ kN} / \text{m}^2$, $\mu = 0.3$, $q = 10 \text{ kN} / \text{m}^2$, $R = 3 \text{ m}$. The calculation results are summarized on Table 4 and Table 5.

Table 4. The hinged round plate center displacement (Fig. 6). Shear locking test.

t, m	w, mm			
	Fig. 6a	Fig. 6b	Fig. 6c	Formula (55)
0.1	57.0493	56.4158	56.3331	56.4158
0.5	0.46989	0.46698	0.46435	0.46481
1	0.06401	0.06337	0.06339	0.06337
1.5	0.02157	0.02149	0.02142	0.02138
2	0.01064	0.01062	0.01060	0.01055

In formulas (55) and (56), the second terms, which are determined the value of displacements due to shear deformations, are the same. Note that when calculating according to the proposed method, displacements from shear deformations are determined independently of the bending state and will also be the same for the considered support options of the plates. The results in the Tables show the general tendency for the displacement values to approach the exact values from above, as well as good accuracy even for coarse grids.

Table 5. The clamped round plate center displacement (Fig. 6). Shear locking test.

t, m	w, mm			
	Fig. 6a	Fig. 6b	Fig. 6c	Formula (56)
0.1	14.3394	14.0010	13.8079	13.8908
0.5	0.12821	0.12561	0.12415	0.12461
1	0.02130	0.02102	0.02086	0.02084
1.5	0.00891	0.00885	0.00882	0.00876
2	0.00530	0.005284	0.005280	0.00524

When modeling the round plate, arbitrary quadrangular elements were used, but most of them have a square shape. But the finite elements located along the plate border have different sizes and arbitrary shapes. These elements are located near the supports, therefore, the greatest transverse forces arise in them. They will make a significant contribution to the displacements caused by the shear, and thereby determine the calculation accuracy. Thus, we note that the proposed arbitrary quadrangular finite elements allow one consider shear deformations with high accuracy and regardless of the ratio of the plate thickness to its dimensions. The shear locking effect in the calculation of thin plates is absent.

4. Conclusion

1. An arbitrary quadrangular bending finite element based on a piecewise constant approximation of moments is proposed. The solution is based on the principles of minimum additional energy and possible displacements. The finite element allows you to consider the shear deformation, regardless of the ratio of the plate thickness to its sizes. The effect of locking in the calculation of thin plates is absent.

2. There is compared the results of the oblique plates calculations, annular and round plates with analytical solutions and calculation results for other programs. The results comparison shows good accuracy in determining displacements and moments. The crushing of finite elements mesh cause the displacement values tend to exact values from above.

3. To assess the influence of the finite element shape, calculations were made for skew plate. To model the plate, quadrangular elements were used, obtained from rectangular ones by changing the slope of one side. As a result, one of the finite element internal corners varied from 90 to 150 degrees. At the same time, the calculating accuracy of the displacements and moments decreased only by 4 and 6 percent, respectively.

4. The proposed finite element is easy to implement. A numerical integration and the mapping of the quadrangular region to the rectangular one is not used to get the solution. All necessary expressions are obtained analytically.

References

1. Gallagher, R.H. Finite Element Analysis: Fundamentals. Englewood Cliffs, Prentice-Hall, 1975. 420 p.
2. Eslami, M.R. Buckling and Postbuckling of Beams, Plates and Shells. Springer. New York, 2018. 588 p.
3. Anssi, T. Karttunen, Raimo von Herten, J.N. Reddy, Jani Romanoff. Exact elasticity-based finite element for circular plates. Computers & Structures. 2017. Vol. 182. Pp. 219–226.
4. Nguyen-Xuan, H. A polygonal finite element method for plate analysis. Computers & Structures. 2017. Vol. 188. Pp. 45–62.
5. Karttunen, A.T., Herten, R., Reddy, J.N., Romanoff, J. Shear deformable plate elements based on exact elasticity solution. Computers & Structures. 2018. Vol. 200, Pp. 21–31.
6. Fallah, N. On the use of shape functions in the cell centered finite volume formulation for plate bending analysis based on Mindlin-Reissner plate theory// Computers & Structures. 2006. Vol. 84. Pp. 1664–1672.
7. Khezri, M., Gharib, M., Rasmussen, K.J.R. A unified approach to meshless analysis of thin to moderately thick plates based on a shear-locking-free Mindlin theory formulation. Thin-Walled Structures. 2018. Pp. 161–179.
8. Katili, I., Batoz, J.L., Maknun, I.J., Hamdouni, A., Millet, O. The development of DKMQ plate bending element for thick to thin shell analysis based on the Naghdi/Reissner/Mindlin shell theory. Finite Elements in Analysis and Design. 2015. Vol. 100. Pp. 12–27.
9. Mirsaidov, M.M., Abdikarimov, R.A., Vatin, N.I., Zhgutov, V.M., Khodzhaev, D.A., Normuminov, B.A. Nonlinear parametric oscillations of viscoelastic plate of variable thickness. Magazine of Civil Engineering. 2018. 82(6). Pp. 112–126. DOI: 10.18720/MCE.82.11
10. Sukhoterin, M.V., Baryshnikov, S.O., Knysh, T.P., Abdikarimov, R.A. Natural oscillations of a rectangular plates with two adjacent edges clamped. Magazine of Civil Engineering. 2018. 82(6). Pp. 81–94. DOI: 10.18720/MCE.82.8.
11. Abdikarimov, R., Khudayarov, B., Vatin, N.I. To Calculation of Rectangular Plates on Periodic Oscillations. MATEC Web of Conferences. 2018. Vol. 245. 01003.
12. Kumara, R., Lala, A., Singhb, B.N., Singhc, J. New transverse shear deformation theory for bending analysis of FGM plate under patch load. Composite Structures. 2019. Vol. 208. Pp. 91–100.
13. Duan, H., Ma, J. Continuous finite element methods for Reissner-Mindlin plate problem. Acta Mathematica Scientia. 2018. Vol. 38. Pp. 450–470.
14. Park, M., Choi, D.-H. A two-variable first-order shear deformation theory considering in-plane rotation for bending, buckling and free vibration analysis of isotropic plates. Applied Mathematical Modelling. 2018. Vol. 61. Pp. 49–71.
15. Lukashevich, A.A. Modelling of contact interaction of structures with the base under dynamic loading. Magazine of Civil Engineering. 2019. 89(5). Pp. 167–178. DOI: 10.18720/MCE.89.14
16. Lin, M., Junping, W., Xie, Ye. A hybridized formulation for the weak Galerkin mixed finite element method. Journal of Computational and Applied Mathematics. 2016. Vol. 307. Pp. 335–345.
17. Rodrigues, J.D., Natarajan, S., Ferreira, A.J.M., Carrera, E., Bordas, S.P.A. Analysis of composite plates through cell-based smoothed finite element and 4-noded mixed interpolation of tensorial components techniques. Computers & Structures. 2014. Vol. 135. Pp. 83–87.
18. Doa, T.V., Nguyenb, D.K., Ducc, N.D., Doanc, D.H., Buie, T.Q. Analysis of bi-directional functionally graded plates by FEM and a new third-order shear deformation plate theory. Thin-Walled Structures. 2017. Vol. 119. Pp. 687–699.
19. Senjanović, I., Vladimir, N., Hadžić, N. Modified Mindlin plate theory and shear locking free finite element formulation. Mechanics Research Communications. 2014. Vol. 55. Pp. 95–104.
20. Ullah, S., Zhong, Y., Zhang, J. Analytical buckling solutions of rectangular thin plates by straightforward generalized integral transform method. International Journal of Mechanical Sciences. 2019. Vol. 152. Pp. 535–544.
21. Tyukalov, Yu.Ya. Finite element models in stresses for bending plates. Magazine of Civil Engineering. 2018. 82(6). Pp. 170–190. DOI: 10.18720/MCE.82.16
22. Tyukalov, Yu.Ya. Finite element models in stresses for plane elasticity problems. Magazine of Civil Engineering. 2018. 77(1). Pp. 23–37. DOI: 10.18720/MCE.77.3
23. Tyukalov, Yu.Ya. Equilibrium finite elements for plane problems of the elasticity theory. Magazine of Civil Engineering. 2019. 91(7). Pp. 80–97. DOI: 10.18720/MCE.91.8
24. Tyukalov, Yu.Ya. Calculation method of bending plates with assuming shear deformations. Magazine of Civil Engineering. 2019. 85(1). Pp. 107–122. DOI: 10.18720/MCE.85.9
25. Tyukalov, Yu.Ya. Finite element model of Reissner's plates in stresses. Magazine of Civil Engineering. 2019. 89(5). Pp. 61–78. DOI: 10.18720/MCE.89.6
26. Timoshenko, S.P., Voinovskiy-Kruger, S. Plastiny i obolochki [Plates and shells]. Moscow: Nauka, 1966. 636 p. (rus)
27. Belkin, A.Ye., Gavryushin, S.S. Raschet plastin metodom konechnykh elementov [Finite element analysis of plates]. Moscow: MGTU, 2008. 231 p. (rus)

Contacts:

Yury Tyukalov, yutvgu@mail.ru



DOI: 10.34910/MCE.107.8

Open flow damper in effluent control system

P.G. Tarasevsky^{*,a}, V.L. Badenko^a, I.V. Goryunov^b

^a Peter the Great St. Petersburg Polytechnic University, St. Petersburg, Russia

^b Company "Elita", St. Petersburg, Russia

*E-mail: 89213886908@mail.ru

Keywords: Oil products control, water quality control, flow damper, combined heat and power station, CFD

Abstract. Nowadays, there are enterprises that use a direct-flow cooling system without treatment of used water before discharging it into a water body. Most of these enterprises use outdated equipment in the cooling system (including oil cooling systems). As a result, there is a high probability of oil products getting into the natural water body. An oil product in a stream of water can be dissolved and undissolved (emulsion). The design of the flow damper proposed in this work is part of a functioning industrial water quality control system. The flow damper is designed to register undissolved oil products in the water flow from the cooling system of a CHP plant. Measurements are conducted at the control points. The research model includes the development of a solid model of the flow damper (including the analysis of its use in a natural environment modelled by software package with the possibility of CFD analysis) and the calculation of oil particles ascent time inside the damper. The result of the study is the design of the flow damper, which ensures oil film detection in the cooling system effluents discharged into the water body.

1. Introduction

Nowadays the environmental protection issues are significant for water resources consumers [1–8], and especially for enterprises that discharge effluents into water bodies [9]. The State Duma of the Russian Federation conducts an active policy on improving the environmental situation, and in particular the state of water bodies, by increasing fines for legal entities and individuals [10].

Active consumers of water resources are combined heat power stations (CHP), which use water to cool oil-filled equipment that is part of the CHP cooling system [11]. Some CHP plants have a flow-through cooling system, where water is taken from a water body (river, lake, etc.) by a pumping station, used as cooler for equipment and finally is discharged back into the water body after passing through the circuits of cooling system. At the same time, the cooling system includes oil chillers which ensure the operation of turbine generators, feed pumps and other parts of the CHP. In this units the natural water could have a contact with industrial oil. Oil cooler is a shell and a tube or plate type heat exchanger which is pumped with water that removes heat from the oil circuit. Oil cooler maintain the set temperature of the lubricating oil that is necessary to support the set oil pressure in equipment. It should be noted, that oil chiller is subject to high depreciation and as a result, it needs repairing. Most often reasons of repairing on oil chiller occur due to several causes: corrosive destruction of heat exchange tubes, violations of the tightness of rolled joints of tubes with tube sheets, some factory defects formed during their manufacture or installation. The number of oil chillers depends on the power of the CHP and can reach several dozen. At the same time, the disruption of the operation of oil chillers can lead to serious environmental consequences, such as discharge of a large volume of oil products into the used water body, which in turn leads to serious economic consequences for enterprises.

Tarasevsky, P.G., Badenko, V.L., Goryunov, I.V. The open flow damper in effluent control system. Magazine of Civil Engineering. 2021. 107(7). Article No. 10708. DOI: 10.34910/MCE.107.8

© Tarasevsky, P.G., Badenko, V.L., Goryunov, I.V., 2021. Published by Peter the Great St. Petersburg Polytechnic University.



This work is licensed under a [CC BY-NC 4.0](https://creativecommons.org/licenses/by-nc/4.0/)

In case of using water resources without constant pollution monitoring, there is a probability of an emergency when water body will inevitably suffer and be polluted by oil products [12]. Therefore, according to the materials [13–14], CHPs with a flow-through cooling system are sources of oil products (TP-22S turbine oil [15]) entering the water body used as a source of cooling water. The discharge of oil products into a water body leads to inevitable environmental consequences [16] in the framework of pollution of both water and land resources [17].

Nowadays, for example, the Russian normative document determining the control mode of CHP's waste water is [18], according to which the sampling schedule for CHP effluents is approved by local regulatory organizations. As known, the regular oil products control in the effluents of the CHP is carried out once every few days (from three to ten). Such method excludes the possibility of oil products operational monitoring of wastewater.

Thus, it is necessary for CHP plants with a direct-flow cooling system to control oil contamination level in water which is discharged from the flow-through cooling system. In particular, the wastewater should not contain traces of industrial oil. Industrial oil serves as an intermediate heat carrier in the cooling systems of equipment and can get into water due to malfunction of heat exchangers.

Today, such technologies as digital twins and internet of things (IoT) are developed actively. In terms of Industry 4.0 technologies, using automatic monitoring of oil concentration in effluent of the CHP cooling system is strongly recommended. In future, industrial water control systems could be part of global environmental monitoring system [19–22].

The literature review has shown that the main gap in problem of prevention of water bodies pollution by CHP is development of effective monitoring of the CHP sewage water [12–14]. To ensure online monitoring of the cooling system effluent, at present, the employees of Russian company ELITA-Petersburg LLC have developed and commissioned industrial water control system that provides continuous monitoring of oil products in effluents of CHPs cooling system [23].

One of the parameters for the effluents control by this system is the control of oil films on the surface of effluents discharged into a water body at the spillway with laser oil detector. Laser technologies could be also use to create building information models [24–26].

To ensure proper control, the authors developed the element to soothe the flow.

Created damper is used in the cushion pools were effluents outfall to local water-system area. The damper is necessary for the operation of the oil detector device. This is due to the need for a water surface with an angle of inclination of waves less than 20° [27]. Otherwise, the reflected laser beam from the oil film will not fall into the receiving area of the device.

Objectives of the work are:

- design of flow damper for calming the open flow which ensures the operation of the oil film detector to notify the presence of oil products;
- modeling of damper work with program of CFD analysis;
- justification of the principles of the damper operation.

2. Materials and Methods

2.1. Oil film registration method

To date, the presence of an oil product in a fluid stream can be detected by registration of oil films on the surface of the analyzed water [27]. Instrumentally, the fixation of the presence of an oil product occurs due to the difference in reflectivity (reflection coefficients) of water and oil product. In this project Russian-made device was used to identify the presence of oil stains on the surface of the liquid (which was previously applied to control the presence of oil stains on the river Neva [28]).

This method is based on laser detection of the water surface with a laser beam directed vertically downward (wavelength – 0.65 μm) with measurement frequency < 30 s. The difference in reflection coefficients for oil products and water makes possible to detect oil films. This method allows detecting oil spots with a thickness from 0.5 microns (the more the oil thickness, the more is reflected light intensity, and as a result the registered signal is higher).

In practice, in the places where the oil film detector is installed, there are differences in elevations of water conduit structures, due to which there is a destruction of the water surface and the formation of disturbances that destroy the structure of the formed oil spots [29].

The effective functioning of the oil film detector requires ensuring the optimal flow mode of the analyzed liquid. In this mode, due to the difference in densities, emulsified particles of the oil float to the surface and form oil films. These oil films are available for detector.

Often, the essence of the structure that provides “calming” of the flow is to change the vector of the fluid velocity and its direction along the profile of the water conduit (tube), thereby eliminating the vortex movement. Usually, such structures are used in closed pipelines [30]. Also, structures are known that carry out pressure damping in open reservoirs [31]. Their significant disadvantage is the destruction of the all-liquid flow including surface. That is unacceptable in the case of the task of water quality control using the selected detector, in which it is necessary to locally provide conditions for the formation of an oil slick from emulsified oil particles in the flow with the possibility of them, by a device that performs laser beam reflection from the water surface inside the structure being developed. The main principle of operation of the designed flow damper is to reduce the speed inside it, due to the diversion of a part of the flow by perforation in the damper channels. The area with a reduced flow rate inside itself provides for the appearance of particles of emulsified oil located at the surface of the liquid, due to the difference in density of oil and water.

Thus, the basic task of the damper of soothing the flow in the water control system is: to ensure the proper residence time of the liquid inside the damper, corresponding to the time of formation of oil films from emulsified particles of oil.

The time required for the ascent of emulsified oil particles in the flow of the analyzed water depends on the rate of their ascent to the surface of the liquid due to the difference in the densities of waste water and oil product. In this study, the ascent rate is determined similarly to the principle of the design of treatment facilities for removal of oil products from the storm water sewage.

The control points, where the flow soothing damper is used is the chamber with a cross section of 6x6 m at the discharge point in the local river, see Fig. 1.

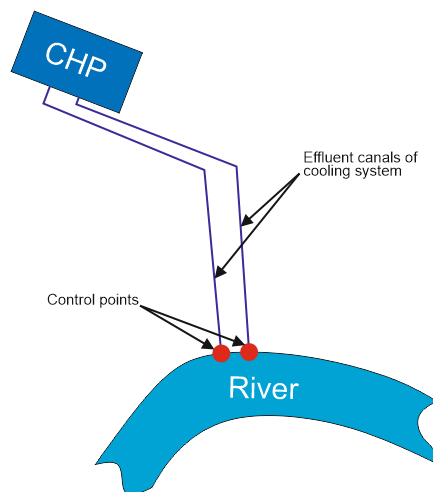


Figure 1. Placement scheme of dampers.

2.2. Basic parameters of flow soothing method

The required time within the flow inside the damper is determined by terminal ascent rate of particles of oil products according to the Stokes formula:

$$g_{em} = \frac{gd_{oil}^2(\rho_w - \rho_{oil})}{18\mu}, \quad (1)$$

where d_{oil} is diameter of oil product particle; ρ_{oil} is density of oil product (TP-22S); ρ_w is water density; μ is dynamic coefficient of water viscosity.

Ascent time is defined as the ratio of the path of a particle of oil from the flow to the water surface (l) to its rate g_{em} :

$$t = \frac{l}{g_{em}} \quad (2)$$

The ascent depth is taken as 0.05 m. Due to the difference in the densities of the oil and water, the oil products will accumulate in the upper part of the stream and weak oil concentration could be detected because the oil detector's lower level is 0.5 microns.

To calculate the ascent rate, the following parameters are defined (see Table 1):

Table 1. Data for calculating the ascent rate of oil particles.

No	Parameter	Value	Note
1	d_{oil}, μ	300	See [32]
2	$\rho_{oil}, \text{kg/m}^3$	0.87	See [15]
3	$\rho_w, \text{kg/m}^3$	1.0	See [32]
4	$\mu, \text{g/cm s}$	0.0131	See [32]

Based on (1) and the data from Table 3, the ascent rate is defined as:

$$g_{em} = 0.0049 \text{ m/s}.$$

Based on (2), the time is determined:

$$t = 10.3 \text{ s}.$$

A certain time characterizes the minimum required time for the fluid flow inside the flow damper of designed size.

The flow rate inside the damper is based on the ratio of the area of the flow damper (in perpendicular projection to the flow movement) to the perforations area inside the damper:

$$n = \frac{W_1}{W_2}. \quad (3)$$

The speed inside the damper is equal to the ratio of the estimated flow speed to the coefficient n .

$$g_2 = \frac{g_1}{n} \cdot (1 - c), \quad (4)$$

where c is the shape resistance coefficient [33].

2.3. Flow soothing damper

Based on certain parameters, a flow damper design has been developed, shown in Fig. 2.

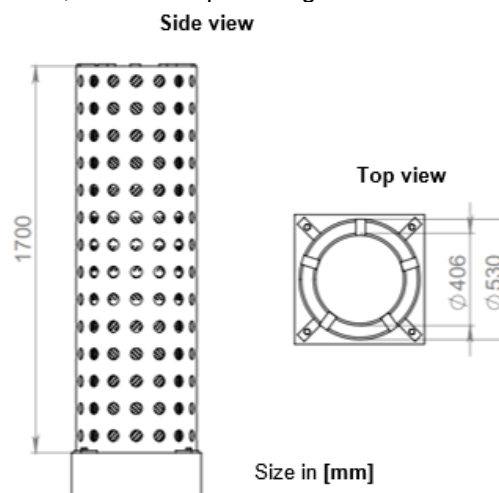


Figure 2. Flow damper device design.

The existing design of the flow damper is based on the separation of part of the fluid from the existing flow (by passing of water through the perforations) and damping the flow energy when it interacts with the damper walls by creating a large local resistance.

The device shown in Fig. 2 is constructed of two cylinders located one in the other. In this design, cylinders with radii of 406 mm and 530 mm are used, the dimensions of the cylinders are selected based on the convenience of mounting the equipment through a standard sewer manhole [34].

Due to various perforations size with a decrease in their area in the section plane to the center of the structure, a significant decrease in the flow rate is achieved.

External perforations are holes with a diameter of 50 mm, arranged in increments of 120 mm to prevent clogging of the inner part of the damper with a smaller fraction of trash shown in Fig. 3.

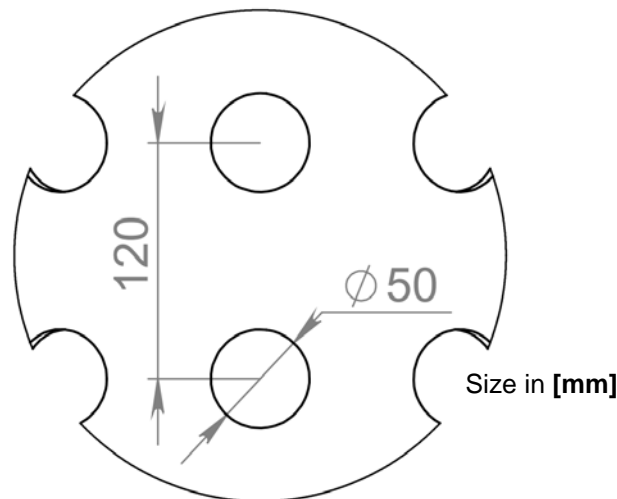


Figure 3. External punch perforations.

The internal perforation of the flow damper consists of parallel slots, 3.2 mm wide and 110 mm high, arranged at an angle of 45° with a pitch of 15 mm. Vertical perforations on inner cylinder have different directions, for more efficient quenching of flow energy, shown in Fig. 4.

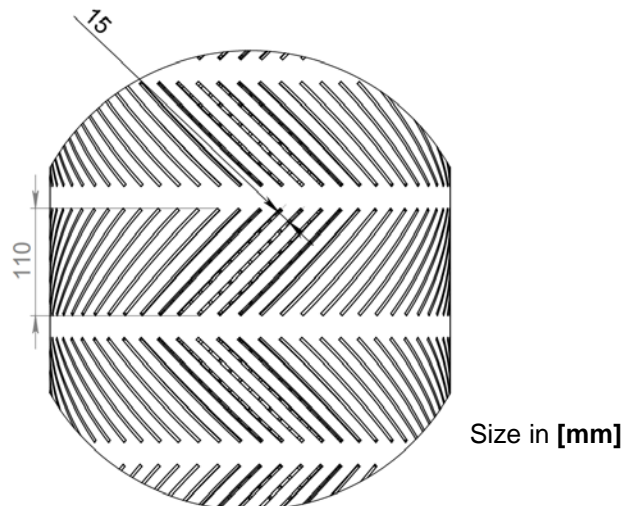


Figure 4. Perforation of the inside of the damper.

The construction is additionally equipped with a concrete load to ensure stability and resistance to the fluid flow.

3. Results and Discussion

The construction of the flow-damping device was developed with 3d-modeling software packages using computational fluid dynamics simulation packages (Solid works Flow Simulation), which makes it possible to evaluate the performance of this unit in an environment close to the actual operating conditions.

Construction designed with using dynamic simulation packages witch usually uses for solving whole host of hydraulics issues [35–40].

In our task the boundary conditions were:

- mass flow rate of liquid 16 000 m³/h;
- environmental pressure – atmospheric;
- liquid – water with a temperature of 5 °C;
- roughness:

concrete (cushion pool) – 1 mm;

damper (used steel with paint) – 0.2 mm.

Total number of cells in the grid: 131 678.

After the statement of the problem and its solution, the following results were obtained Fig. 5 shows the diagram of the water flow velocity distribution (side view).

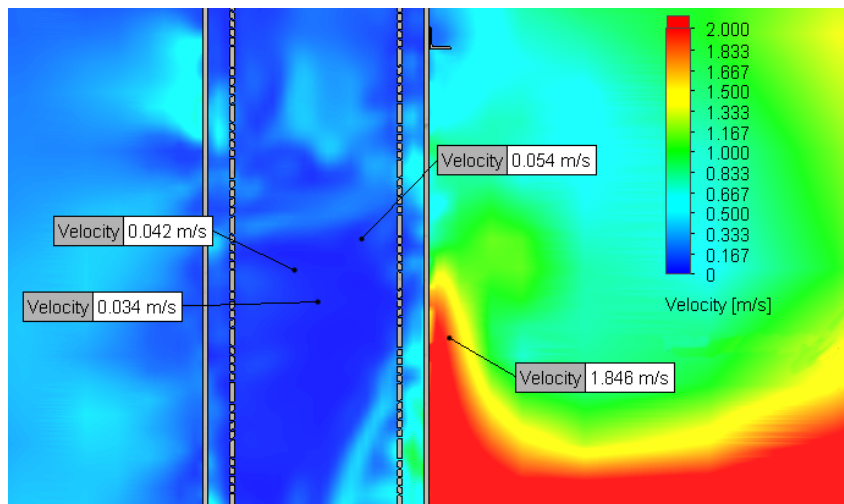


Figure 5. Velocity distribution diagram (side view).

As seen from the Fig. 5, the flow velocity inside the damper is much less than beyond its borders, so values greater than 1 m/s are observed in front of the damper. The high flow velocity outside the damper is based on a high-water flow rate (up to 16 000 m³/h) passing through the damper installation site – a stilling chamber installed at the place where the wastewater from the CHP cooling system is discharged into the local river.

In Fig. 6 a plot of the plane is presented at a distance of 1.2 m from the bottom of the chamber (at this level the flow surface was established in the problem being solved).

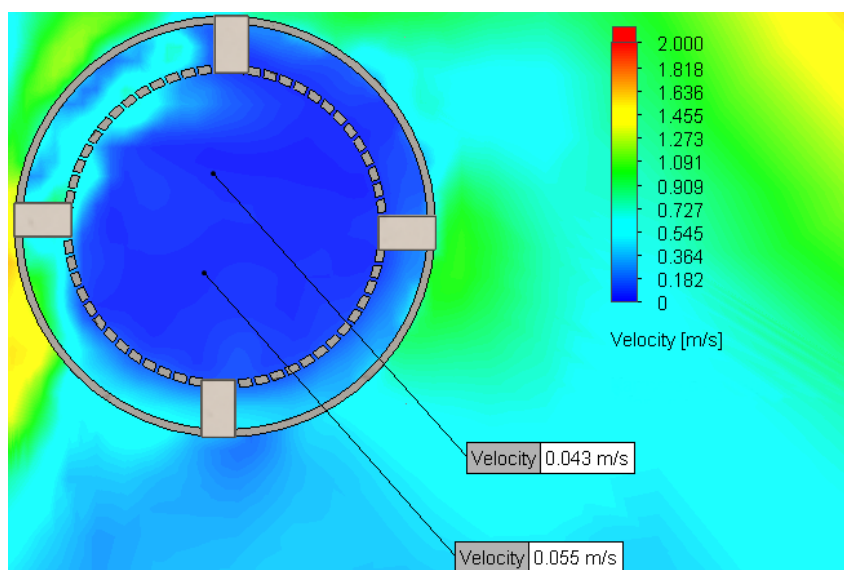


Figure 6. Velocity distribution diagram in a stream (top view).

As seen in this diagram, the velocities on the surface of the liquid are 0.034–0.055 m/s.

Fig. 7 shows a graph of the distribution of water speed along an axis passing from the center of the flow damper.

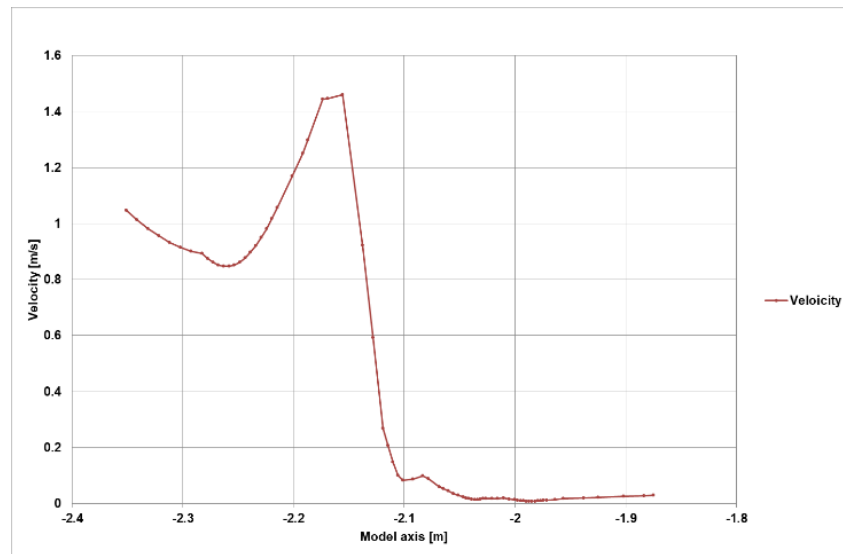


Figure 7. The graph of the distribution of speeds before the damper and inside it.

Damper's damping plate is located on points – 2.078 m and – 2.140 m and point – 1.875 m is the center of the damper.

The effectiveness of the damper is clearly visible outside speed is 0.85–1.45 m/s, while inside the damper is less than 0.1 m/s.

It should be noted that in this chamber the flow damper not only reduces the speed inside itself, but also provides a smooth surface of the liquid to reliably determine the presence of oil films on its surface. Installed opposite the spillway collector, it provides damping of the waves generated when the liquid leaks from the collector into the water intake chamber.

Considering the theoretical indicators of speed inside the damper when installing it in a chamber with a cross section of 6×6 m, we take the depth of filling of the chamber as 1.2 m (from the simulation results). By formula (3) we find the ratio of the area of the damper to the total area of perforations for a given depth of coverage of the body of the damper (at a depth of 1.2 m, 7 levels of inclined perforation are covered).

$$n = \frac{0.64}{0.076} = 8.42.$$

By the formula (4) we determine the flow rate inside the damper.

$$g_2 = \frac{0.61}{8.42} \cdot (1 - 0.46) = 0.042 \text{ m/s}.$$

At a given speed, the time spent by the particles inside the damper is:

$$t = \frac{0.530[m]}{g_2} = 12.6 \text{ s}.$$

This time of flow located inside the damper will ensure the detection of oil emulsified particles and the formation of the oil layer, visible to the device of oil films.

The theoretical value of the speed differs from the calculated one due to neglect of the following parameters:

- orientation of perforations to the direction of flow;
- surface characteristics;
- the form resistance coefficient does not take into account perforation;
- the distance from the outlet manifold to the damper (speed distribution during outflow to the pool).

Thus, in this work, the efficiency of the developed damper is graphically and computationally presented.

4. Conclusions

In order to ensure the operation of the online detector for registration of oil products in CHP effluents the method and device for calming of the water flow is proposed.

The functioning of the device is based on ensuring low speeds of fluid movement inside. As a result, in the presence of oil in wastewater, a smooth calm film of oil products is formed on the water surface. This allows to determine oil products by a detector based on laser beam reflection from the surface.

Simulation of the operation of this device under conditions close to real is considered and the theoretical basis for calculating the speed inside the flow damper is given.

The rational design of the flow damper is selected and justified by the program simulation results.

5. Acknowledgement

The research is funded by the Ministry of Science and Higher Education of the Russian Federation as part of World-class Research Center program: Advanced Digital Technologies (contract No. 075-15-2020-934 dated 17.11.2020).

References

1. Harshica, F., Hyunsu, J. Distribution of petrogenic polycyclic aromatic hydrocarbons (PAHs) in seafood following Deepwater Horizon oil spill. *Marine Pollution Bulletin*. 2019. 145. Pp. 200–207.
2. Xinran, L., Min, L. Indigenous PAH degraders along the gradient of the Yangtze Estuary of China: Relationships with pollutants and their bioremediation implications. *Marine Pollution Bulletin*, 2019. 142. Pp. 419–427.
3. Sharma, B.M., Melymuk, L., Bharat, G. Spatial gradients of polycyclic aromatic hydrocarbons (PAHs) in air, atmospheric deposition, and surface water of the Ganges River basin. *Science of the Total Environment*, 2018. 627. Pp. 1495–1504.
4. Maurice, L., López, F., Becerra, S. Drinking water quality in areas impacted by oil activities in Ecuador: Associated health risks and social perception of human exposure. *Science of the Total Environment*. 2019. 690. Pp. 1203–1217.
5. Felicia, E., Wanga, C.C., Casadob, C. Preconcentration and post-column fluorescent derivatization for the environmental water monitoring of an antihelmintic macrocyclic drug used in livestock. *Heliyon*. 2019. 5.
6. Zhenguang, Y., Jinfen, P. Seawater quality criteria derivation and ecological risk assessment for oil pollution in China. *Marine Pollution Bulletin*, 2019. 142. Pp. 25–30.
7. Lindenmayer, D.B., Lindenmayer, G.E. Likens Adaptive monitoring: a new paradigm for long-term research and monitoring *Trends Ecol. Evol.* 2009. 24. Pp. 482–486.
8. Anas, B.J., Meegahage, M.S., Evans, D.S., Jeffries, B. Wissel Scale-dependent effects of natural environmental gradients, industrial emissions and dispersal processes on zooplankton metacommunity structure: implications for the bioassessment of boreal lakes *Ecol. Indic.* 2017. 82. Pp. 484–494.
9. Kassotis, C.D., Iwanowicz, L.R., Akob, D.M. Endocrine disrupting activities of surface water associated with a West Virginia oil and gas industry wastewater disposal site. *Science of the Total Environment*. 2016. 557–558. Pp. 901–910.
10. Gosduma uzhestochila shtrafy za zagryazneniye vodnykh obyektov [State Duma increased fees for polluting water recourses] [Online]. URL: <https://tass.ru/obschestvo/6310895> (date of application: 10.11.2019).
11. Delgado, A., Herzog, H. A simple model to help understand water use at power plants. Working Paper. Cambridge, 2012. 19 p.
12. Jones, D., Gates, A. Autonomous marine environmental monitoring: Application in decommissioned oil fields. *Science of the Total Environment*. 2019. 668. Pp. 835–853.
13. Na Zhodinskoy TETs proizoshla utechka masla [Oil leak on Zhodinskoy CPH] [Online]. URL: <https://news.tut.by/accidents/28-0041> (date of application: 10.11.2019).
14. Po tekhnologicheskomu kanalu Arkhangel'skoy TETs v reku Yuras popali nefteprodukty [Petroleum products got to the Uras river from Arkhangel's CHP technological channel] [Online]. URL: <https://www.echosevera.ru/news/2016/10/31/23918.html> (date of application: 10.11.2019).
15. RD 34.43.102-96. Guidelines for Use of Petroleum-Based Turbine Oils. VTI, 1997.
16. Arephjev, N.V., Badenko, V.L. Prediction of the possible damage caused by oil products spill from the sunk ships and vessels. *Marine radioelectronics*. 2009. 1. Pp. 44–47.
17. Gordey, D.A., Terleyev, V.V. Ekologo-ekonomicheskaya otsenka tekhnologii vosstanovleniya neftezagryaznennykh pochv Sankt-Peterburga [Ecology-economical assessment of technologies of oil contaminated soil recovery in Saint-Petersburg]. XXXVIII Nedelya nauki SPBGPU [XXXVIII SPBGPU's week of science]. Trudy SPbGPU. Saint-Petersburg: Izd-vo SPbGPU, 2009. Pp. 356–357. (rus)
18. RD 153-34.0-02.405-99. Procedural Guidelines for Standardization of Discharges of Pollutants with Wastewaters from Thermal Power Stations. VTI, 2000.
19. Bevilacqua, M., Bottani, E., Ciarpica, F.E., Costantino, F., Di Donato, L., Ferraro, A., Paroncini, M. Digital Twin Reference Model Development to Prevent Operators' Risk in Process Plants. *Sustainability*. 2020. 12(3). Pp. 1088.
20. Min, Q., Lu, Y., Liu, Z., Su, C., Wang, B. Machine learning based digital twin framework for production optimization in petrochemical industry. *International Journal of Information Management*. 2019. 49. Pp. 502–519.

21. Cohen, Y., Faccio, M., Pilati, F., Yao, X. Design and management of digital manufacturing and assembly systems in the Industry 4.0 era. *International Journal of Advanced Manufacturing Technology*. 2019. 105(9). Pp. 3565–3577.
22. Rasheed, A., San, O., Kvamsdal, T. Digital twin: Values, challenges and enablers from a modeling perspective. *IEEE Access*. 2020. 8. Pp. 21980–22012.
23. Na Vyborgskoy TETs PAO «TGK-1» vvedena v opytnuyu ekspluatatsiyu sistema ekonomitoringa [Eco-monitoring system started using on Vyborgskaya CHP] [Online]. URL: <http://www.tgc1.ru/press-center/news/i/full/na-vyborgskoi-tehc-pao-tgk-1-vvedena-v-opytnuju-ehksplua/> (date of application: 10.11.2019).
24. Badenko, V., Fedotov, A., Vinogradov, K. Hybrid Algorithms of Laser Scanning Point Cloud for Topological Analysis. *Advances in Intelligent Systems and Computing*. 2019. 797. Pp. 223–234.
25. Badenko, V., Tammsaar, S., Beliaevskii, K., Fedotov, A., Vinogradov, K. Multithreading in Laser Scanning Data Processing. *Lecture Notes in Computer Science*. 2019. 11619. Pp. 289–305.
26. Badenko, V., Fedotov, A., Zotov, D., Lytkin, S., Volgin, D., Garg, R.D., Liu, M. Scan-to-BIM methodology adapted for different application. *Int. Arch. Photogramm. Remote Sens. Spatial Inf.* 2019. Pp. 1–7.
27. Opticheskiy registrator neftyanykh plenok "KRAB" [Online]. URL: <https://www.lumex.ru/catalog/krab-1.php> (date of application: 08.11.2019).
28. Yedinaya avtomatizirovannaya sistema registratsii razlivov nefteproduktov distantsionnymi opticheskimi kompleksami v akvatorii r. Neva (Sankt-Peterburg) [Union automatic system of oil stain record in Neva river (Saint-Petersburg)] URL: <http://www.npkgoi.ru/?module=articles&c=profil&b=3&a=4> (date of application: 08.12.2019).
29. Fangli, Q., Guansuo, W., Liping, Y. Modelling oil trajectories and potentially contaminated areas from the Sanchi oil spill. *Science of the Total Environment*. 2019. 685. Pp. 856–866.
30. Benhadj, R., Ouazzane, A.K. Flow conditioners design and their effects in reducing flow metering errors. *Sensor Review*. 2002. 246. Pp. 223–231.
31. Qiulin, L., Lianxia, L., Huasheng, L. Study on the Best Depth of Stilling Basin with Shallow-Water Cushion. 2018. Pp. 2081.
32. Karelin, Ya.A. Ochistka stochnykh vod neftyanykh promyslov i zavodov [Wastewater treatment of oil fields and factories]. Moscow: Stroyizdat, 1982, 184 p. (rus)
33. Bashta, T.M. Mashinostroitel'naya gidravlika: Spravochnoye posobiye [Hydraulics Engineering: A Reference Guide]. Moscow: Engineering, 1971, 672 p. (rus)
34. GOST 3634-99. Access manhole covers and storm-flow receivers for manholes. Technical requirements. CNS, 2001.
35. Babakhani Dehkordi, P., Azdarpour, A., Mohammadian, E. The hydrodynamic behavior of high viscous oil-water flow through horizontal pipe undergoing sudden expansion—CFD study and experimental validation. *Chemical Engineering Research and Design*. 2018. 139. Pp. 144–161.
36. Yuan, S., Zou, Z., Zou, L. Uncertainty quantification of hydrodynamic forces on the DTC model in shallow water waves using CFD and non-intrusive polynomial chaos method, *Ocean Engineering*, Vol. 198, 2020.
37. Harnsihacacha, A., Piyapaneeekoon, A., Kowitwarangkul, P. Physical water model and CFD studies of fluid flow in a single strand tundish. *Materials Today: Proceedings*. 2018. 5(2). Pp. 9220–9228.
38. Rauen, W.B., Binliang, L., Falconer, R. CFD and experimental model studies for water disinfection tanks with low Reynolds number flows. *Chemical Engineering Journal*. 2008. 137. Pp. 550–560.
39. Chengqian, W., Shaowei, L., Wuhua, D., Shuo, C. CFD Simulations of the Air/Water Two-phase Flow in an Annular Centrifugal Contactor. *Energy Procedia*. 2013. 39. Pp. 467–473.
40. Li, X., Shuai, Y., Zaojian, Z., Lu, Z. Uncertainty quantification of hydrodynamic forces on the DTC model in shallow water waves using CFD and non-intrusive polynomial chaos method. *Ocean Engineering*. 2020. 198.

Contacts:

Philipp Tarasevsky, 89213886908@mail.ru

Vladimir Badenko, vbadenko@gmail.com

Igor Goryunov, i.goryunov@smartwater.su



DOI: 10.34910/MCE.107.9

Flexural properties of hogweed chips reinforced cement composites

T.A. Musorina* , D.D. Zaborova , M.R. Petrichenko, O.N. Stolyarov 

Peter the Great St. Petersburg Polytechnic University, St. Petersburg, Russia

*E-mail: tamusorina@mail.ru

Keywords: concrete composites, hogweed, polypropylene fiber, mechanical properties, bending, reinforcement efficiency

Abstract. Application of natural plant additives allows improving thermal and mechanical properties of concrete composites. Environmentally friendly wood waste is gaining particular popularity. One of the promising filler types for concrete is hogweed chips. In this study, the flexural properties of two types of concrete composites reinforced with plant additive samples, including a large additive of hogweed 50 mm long and a medium additive of hogweed 25 mm long were examined. In addition, a composite sample reinforced with short polypropylene fiber was produced. Each series of concrete composite consists of three samples. A three-point bending test was conducted to determine the reinforcement efficiency of the manufactured composites. Instron 5965 (USA) unit helped determine maximum load and normal stress. The results showed that the flexural strength of composites with long additive pieces is greater than that of the other samples. The increase in flexural strength was 5% and 25% for composite made of short and long pieces, respectively. The interaction mechanism between wood additives and cement matrix in the composite was analyzed by means of optical microscopy. The surface formations were found to significantly affect the bonding properties of the concrete and the hogweed.

1. Introduction

Concrete has been a conventional material in construction for the last 150 years and its composition is permanently improved by various additives that affect its thermal and mechanical properties [1–9]. Concrete admixtures (additives) enhance the properties of concrete for applications in construction with special requirements. Concrete additives are used to achieve desired workability in case of low water-cement ratio, and to enhance setting time of concrete for long distance transportation of concrete [10–13].

Today, there are many wood additives in the market of construction and building materials. Many of available materials are environmentally friendly. Wood additives may be used in the following form: wood chips, sawdust, shavings, wood dust, ash. In addition to low density, wood materials have high strength performance. Wood is also characterized by unique physical and chemical characteristics, including low heat and sound conductivity, corrosion resistance in aggressive environments, the ability to quench vibrations, easy workability and shaping.

Using more efficient materials, an ecological approach to design is aimed at developing a comfortable building environment with lower environmental costs. The production of cement wood fiber panels contributes to the re-evaluation of industrial by-products, such as the use of waste from the wood industry [14–16]. Cheap wood fuel in the form of briquettes without the use of binding substances are widely used in the Russian market. In addition, soft waste in small quantities is used in hydrolysis production, for the manufacture of albolite (wood concrete). In albolite, cement occupies on average 10–22% and in

Musorina, T.A., Zaborova, D.D., Petrichenko, M.R., Stolyarov, O.N. Flexural properties of hogweed chips reinforced cement composites. Magazine of Civil Engineering. 2021. 107(1). Article No. 10709. DOI: 10.34910/MCE.107.9

© Musorina, T.A., Zaborova, D.D., Petrichenko, M.R., Stolyarov, O.N., 2021. Published by Peter the Great St. Petersburg Polytechnic University.



This work is licensed under a CC BY-NC 4.0

sawdust concrete up to half. This does not affect strength performance, but significantly reduces thermal protection of concrete. Wood-based concrete cannot absorb water due to lack of pores. The place of pores is occupied by wood filler. In most cases, wood is well impregnated with lime, and also tightly captured with cement, so that water cannot penetrate inside the material.

Sawdust-based concrete (structural and thermal insulation concrete), in which sawdust and sand are used as a filler, while cement and lime as a binder, also found some appropriate applications. For the production of sawdust concrete blocks, small sawdust wood without adding wood chips is used. Mixtures can be used for manufacturing unit blocks of various sizes for subsequent erection of walls of buildings, as well as for direct laying in formwork during erection of monolithic walls. There is gypsum-sawn concrete used for the construction of walls in residential, public and industrial buildings (single-story buildings of III and IV category of durability) with a relative humidity not exceeding 60% [17]. In works [18, 19], wood waste (sawdust and wood shaving) ash (WWA) of pretreated timber was added as a supplement to a concrete from 0 to 30% by weight of cement with step of 5%, while the strengths and the water absorption of the matrix were evaluated. The compressive and the flexural strengths of WWA concrete investigated ranged from 3.65 to 28.66 N/mm², with the lowest values obtained at 30% additive level of ash. When compared with the strength of reference concrete sample, the compressive and flexural strengths of WWA concrete were between 62 and 91% and 65 and 98%, respectively. It was concluded that WWA could be blended with cement without adversely affecting the strength properties of concrete.

Some researchers have conducted tests which showed promising results that wood ash can be suitably used to partially replace cement in concrete production [20, 21]. Another main advantage of wood filler addition to cementitious materials is that they are inexpensive, available in large quantities, environmentally friendly, and easy to process. Hence, incorporating the usage of wood ash as replacement for cement in blended cement is beneficial for the environmental point of view as well as producing low cost construction entity thus leading to a sustainable relationship.

To build for tomorrow, the two building methods are being combined. Hybrid structures containing both wood and concrete elements are becoming increasingly popular in contemporary architecture. In the context of the National Resource Programme "Resource Wood" (NRP 66), Swiss researchers have now developed an even more radical approach to combine wood and concrete. They are fabricating a load-bearing concrete which itself consists largely of wood. In many blends, the volume fraction of the wood is over 50 percent. Cement-bonded wood products have been around for more than a hundred years. However, previously they were used only for non-load-bearing purposes, such as insulation [22].

Cement-bonded wood composite panels are not novel products used in construction. They are available on the market since the early 1960s [23]. The results indicate that fibers reduces permeability and the infiltration rate, while reducing surface abrasion and improving freeze-thaw durability. It is also shown that the ratio between flexural and compressive strength is around 47%. For the numerical simulation [24], an eXtended Finite Element Method (XFEM) has been used to simulate the fracture process of the three-point bending panel using Abaqus software. The results of study [25] showed that increasing the amount of wood waste reduces density and slightly decreases thermal conductivity. In 1934, an innovative technology in low-rise construction – the use of wood-concrete blocks of permanent formwork in the Netherlands developed [26]. Durisol has been manufactured since the 30s by the Swiss company of the same name on special industrial production lines from machine chips, M500 Portland cement and chemical additives. The company produces wall panels, coating plates, hollow blocks (50x25x30 cm). In the construction of residential buildings up to 14 stories high in Switzerland, durisol hollow blocks are used, while the voids located vertically and horizontally are filled with concrete, which forms a concrete grid that carries a vertical load, and the durisol itself serves as thermal insulation.

A series of experiments were carried out to study the effect of wood extractives, chamotte and CaCl₂ on hydration and hardening of cement paste [27–29]. It also allowed study of the effects of these additives on mechanical and physical properties of Cement-bonded Particle Board (CBPB). The CBPB was tested for Modulus of Rupture (MOR), Internal Bond (IB), Thickness Swelling (TS) and Water Absorption (WA). The results showed that water-soluble wood extractive increases the hydration time of cement. It was observed that different amounts of chamotte and CaCl₂ in neat cement could significantly affect the setting and hardening time. Replacement of cement with 10% of CaCl₂ and 10% chamotte in boards increased the MOR and IB. It was determined that alder and poplar wood extractives increase the hydration time of cement paste and decrease the amount of compression strength of cement stone compared to control samples.

The study [30] investigates the influence of maple-wood sawdust addition on the mechanical and microstructural properties of cemented paste backfill (CPB). Mechanical properties of CPB were determined by uniaxial compressive strength (UCS) tests and microstructural changes were evaluated by mercury intrusion porosimetry (MIP), and scanning electron microscopy (SEM) analysis. Results indicate that the addition of 12.5% maple-wood sawdust (by dry mass of binder) improves the strength development

of CPB specimens at later hydration age (91 curing days). However, the UCS showed lower improvement at a higher maple-wood sawdust content of 14.5%. Furthermore, the incompatibility of some wood species with cementitious materials means that the compatibility of each wood species must be assessed individually [31].

This experimental study aims to evaluate the contribution of the High-Performance Fiber-Reinforced Cementitious Composite (HPFRCC) laminate with steel and GFRP bars to the flexural behavior of RC slabs. The experimental results were suggestive of the effect of the properties of the HPFRCC laminate, including its application procedure, steel fiber volume fraction, incorporation of longitudinal reinforcement, and the type of reinforcement (steel or GFRP bars), on the increase in the load-bearing capacity of the slab [32]. The effect of replacing aggregate with waste glass particles on the compressive strength and weight of concrete is investigated in [33]. Results indicated that replacing aggregate with glass particles of more than 30% lead to an increment in the compressive strength of concrete. The weight of concrete remains almost the same in all of the specimens. Briefly, based on the results it could be concluded that the optimum percentage for replacing aggregate with glass particles is 50%. Concrete-containing wood aggregate in percentages of 0, 15, 20, and 25 in place of crushed stone was developed with characteristic compressive strength of 25 MPa, with a mix proportion of 1:1.26:2.76 and with a water/cement ratio of .45. The compressive strength of control concrete was 31.40 MPa and that of wood aggregate concrete with 15% replacement level was 32.36 MPa that is 3.06% above the control concrete. Therefore, wood aggregate can be used in the production of concrete, and the optimum replacement was found to be 15% from all considerations [34]. In this study [35], the wood waste, wood shavings, and sawdust were tested in ratios of 2.5, 5, 10, and 20% by the weight of sand. The results showed that increasing the amount of waste hinders the workability of the sample and prolongs setting times. Furthermore, compounds with larger-sized particles, those based on wood shavings, showed a more pronounced decrease in density and produced the best thermal results. Finally, contrary to what one might expect, the wood-shavings compounds also presented better mechanical properties.

In this regard, for Russia, it is worth considering hogweed (*Heracleum mantegazzianum*) as a plant additive to concrete: it is ubiquitous and is considered a big problem. Hogweed Sosnowski is a large, herbaceous plant in the umbrella family (*Apiaceae*). The natural range is within the boundaries of the forest belt of the mountains of the Caucasus. I.P. Mandenova was first to describe this plant in 1944. In the middle of the 20th century, it was widely introduced in the fields of the European part of the USSR and Eastern Europe as a fodder culture. Due to the ability to self-sow in the late 20th century, it began to spread intensively beyond the land on which it was cultivated. All parts of the plant contain furocoumarins: substances that dramatically increase sensitivity of human or animal skin exposed to them to ultraviolet light. The toxic sap and pollen lesions of the plant can cause burns not only on contact with unprotected skin, but through clothing as well [36]. The plants of hogweed can reach heights of around 3–5 m with 1 m long leaves. People can spread the seeds by transporting the soil containing them stuck to car tires [37].

Despite all the shortcomings, there are positive examples of the use of hogweed. Scientists have proposed the use of hogweed in the manufacturing of batteries. Supercapacitors, which were used in the production of fibers from the stems of hogweed, are a kind of storage devices for energy. They are distinguished from conventional batteries by high power, long energy storage life and long service life. Researchers from NUST "MISiS" suggested that the optimal electrodes for supercapacitors are the fibers contained in the dry stems of the plant. The stems consist of a hard bark and a soft inner core, similar to a sponge, which forms a diverse porous structure. Such a design is suitable for use in carbon materials as the basis for a storage device [38, 39].

A literature review showed that dry hogweed was not used as a wood and plant additive in the world practice. Therefore, the research topic is relevant and it should be considered from the point of view of the mechanical properties of the new concrete composite. Hogweed is advisable to use as a plant additive, as in our country large areas of fields and roadsides are occupied by this plant. In dry form, it is safe (it does not emit any harmful substances) and, given the structure of the stem, it is of interest as a cheap additive. To do this, research focuses on the use of hogweed in construction as an additive to concrete.

The purpose of this work is to determine the flexural properties of concrete reinforced with various additives. To achieve this purpose, the following objectives must be achieved:

1. Manufacturing samples of concrete with various additives
2. Determination of the flexural properties of concrete composites.
3. Analysis of wood aggregate-concrete matrix interaction.

2. Methods

2.1. Manufacture of the concrete samples

In this work, four types of concrete samples were manufactured, including a reference unreinforced sample; sample of concrete composite with short polypropylene (PP) fibers, and two types of composite samples reinforced with hogweed chips of different length.

Hogweed was collected in a dry form during the wintertime (when hogweed stops blooming). At this time of the year, hogweed has an empty stem, like bamboo, and it is not poisonous. After that, the stem was cut into additives for concrete composite with a length of 25 mm and 50 mm.

Short PP fiber was selected for comparative analysis specifically, since this type of filler is most often used for the manufacture of fiber-reinforced concrete. The characteristics of the samples are listed in Table 1. The reinforcing fillers are shown in Fig. 1.

Table 1. Samples specification.

No	Reinforcement	Abbreviation	Length, mm
1	non-reinforced	Ref.	–
2	PP short fiber	PP short fiber	54
3	Hogweed chips	B-1	50
4	Hogweed chips	B-2	25

Fine-grained concrete with sand grains 2.5 mm in size was used. Plasticizer was added to concrete mixtures in order to improve workability. The amount of each constituent of the concrete is listed in Table 2. The compressive strength at the age of 28 days is at least 30 MPa. The aggregate volume fraction in the manufactured samples was approximately 2%. Composite samples were made by using the mold of 77×200×20 mm. Prior to testing, the test samples were cured for 28 d at 23°C and 95% RH. No fewer than three samples were tested for each series. Table 3 summarizes the experimental results of three-point bending tests for all specimens.

Table 2. The constituents of fine-grained concrete (kg/m³).

Cement	Sand (0–2.5 mm)	Plasticizer	Water
500	1000	10	285

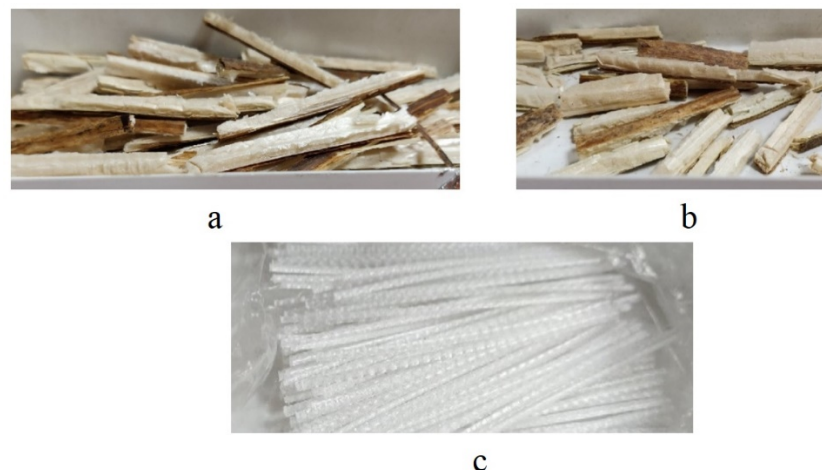


Figure 1. Types of additives: (a) large (50 mm), (b) medium (25 mm), and (c) PP short fiber (54 mm).

2.2. Flexural testing of the concrete samples

Samples of composites were subjected to a three-point bending test as shown in Fig. 2. The flexural tests were performed on an Instron 5965 universal testing machine at a span of 150 mm. The specimens were tested at a constant loading rate of 1 mm/min in a standard climate at 20°C and 65% RH. The concrete specimen is subjected to a load at its center. Specimen deflection is measured by movement of the crosshead displacement of the testing machine.

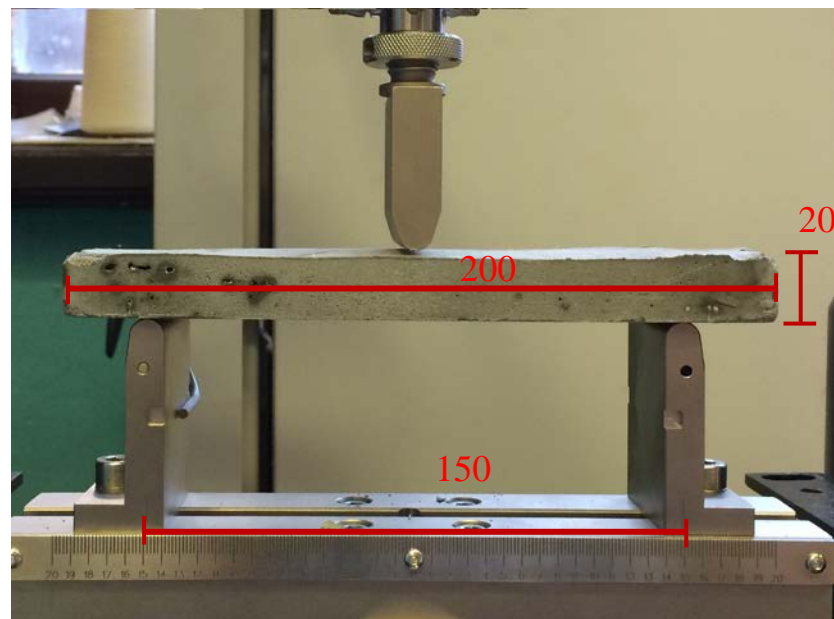


Figure 2. Three-point bending test.

From the results of the tests, the value of the flexural strength was determined as the ratio of the maximum bending moment at sample failure to the axial moment of inertia by the following equation:

$$\sigma = \frac{M_{bend}^{max}}{W_z}, \quad (1)$$

where M_{bend}^{max} is the maximum bending moment, kNm; W_z is moment of inertia, m^3 [40].

3. Results and Discussion

3.1. Flexural behavior

The results of the tests showed that the fillers used have a significant effect on the flexural performance of the concrete composites. Fig. 3 shows the flexural stress-deflection curves of the concrete composites developed in this study. The flexural behavior of the samples is very similar and does not depend on the type of reinforcing aggregates. The initial part of the stress-deflection curve is characterized by linear properties. There is a first transverse crack corresponding to the maximum peak in the curve.

There is a certain difference in both the strength and plasticity characteristics. Analyzing these results shows that the sample of cement composites reinforced with long chip pieces (B-1) has the highest flexural strength. For the other samples, this difference is less noticeable. The value of the deflection demonstrates that the additives improve the plasticity characteristics (approx. 1/3) compared to the non-reinforced sample. Further, with increasing deflection, flexural stress and the slope of the curves decrease. In other words, the reinforcing component significantly contributes to increasing the elastic modulus of the sample.

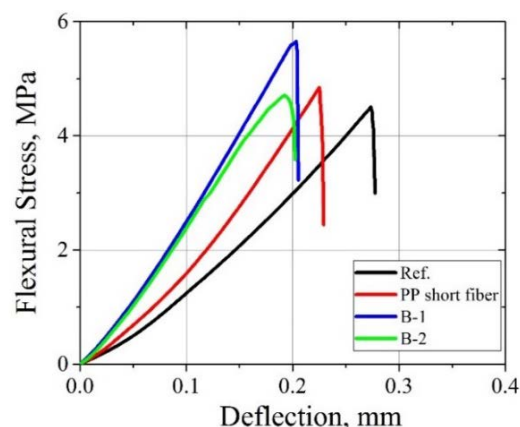
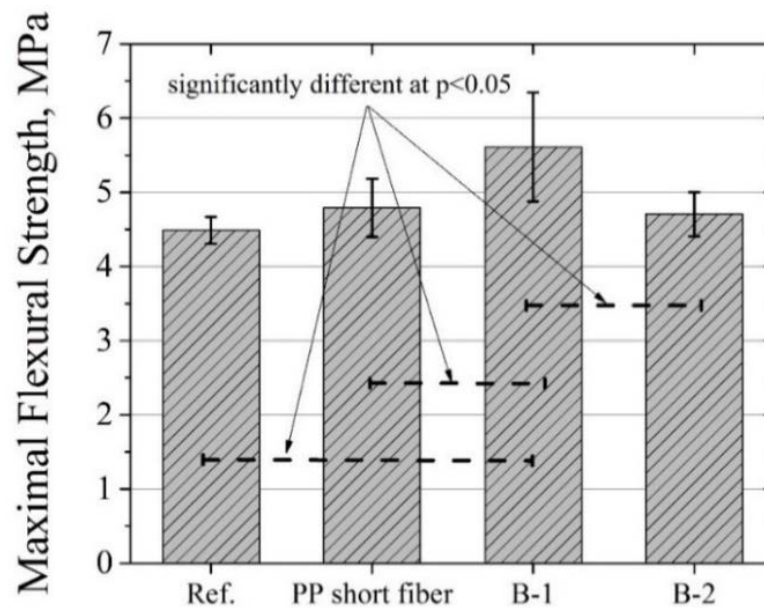


Figure 3. Stress-deflection curves of cement composites with different aggregate types.

Table 3. Test results.

Sample	b , m	h , m	l	F , N	M , Nm	W_z , m ⁴	σ , MPa	σ_{avr} , MPa	
1	B-1	0.077	0.018	0.150	592.7	22.3	3.96E-06	5.6	5.6
2	B-2	0.077	0.018	0.150	522.2	19.6	3.98E-06	4.9	4.4
3	PP	0.077	0.021	0.150	630.1	23.7	5.39E-06	4.4	4.8
4	Ref	0.077	0.024	0.150	859.7	32.4	7.19E-06	4.5	4.6
5	B-1	0.077	0.019	0.150	631.0	23.7	4.65E-06	5.1	
6	B-2	0.077	0.021	0.150	540.5	20.3	5.52E-06	3.7	
7	PP	0.077	0.020	0.150	708.4	26.6	5.15E-06	5.2	
8	Ref	0.077	0.020	0.150	600.1	22.6	5.11E-06	4.4	
9	B-1	0.077	0.016	0.150	537.6	20.2	3.29E-06	6.1	
10	B-2	0.077	0.022	0.150	719.4	27.0	5.99E-06	4.5	
11	PP	0.077	0.020	0.150	688.4	25.8	5.34E-06	4.8	
12	Ref	0.077	0.017	0.150	446.4	16.7	3.53E-06	4.8	

Another point to note when comparing the developed samples is that the flexural strength calculated according to equation (1) was selected. Fig. 4 shows the maximal flexural strength (MFS) of the developed samples. The flexural strength of the reference sample is 4.6 MPa, which is minimal among all the results obtained. The highest MFS value, 5.6 MPa, was obtained in the case of sample B-1, reinforced with 50 mm long hogweed chips. Sample with 25 mm long hogweed chips (B-2) has a bending strength of 4.4 MPa. The flexural strength of the PP short fiber sample is 4.8 MPa.

**Figure 4. Effect of the concrete filler on the flexural strength of the concrete samples.**

3.2. Reinforcement efficiency

In order to determine the reinforcement efficiency, we calculated an efficiency factor as the ratio of the MFS value to the value of the non-reinforced sample. Fig. 5 shows the reinforcement efficiency of the developed samples. The results show that a maximum increase of 25% is observed in the case of the B-1 sample. This is because the additives themselves have a large dimension and absorb a certain percentage of moisture from the mixture on contact with water. In the other two samples, the increase is not more than 5 to 7%.

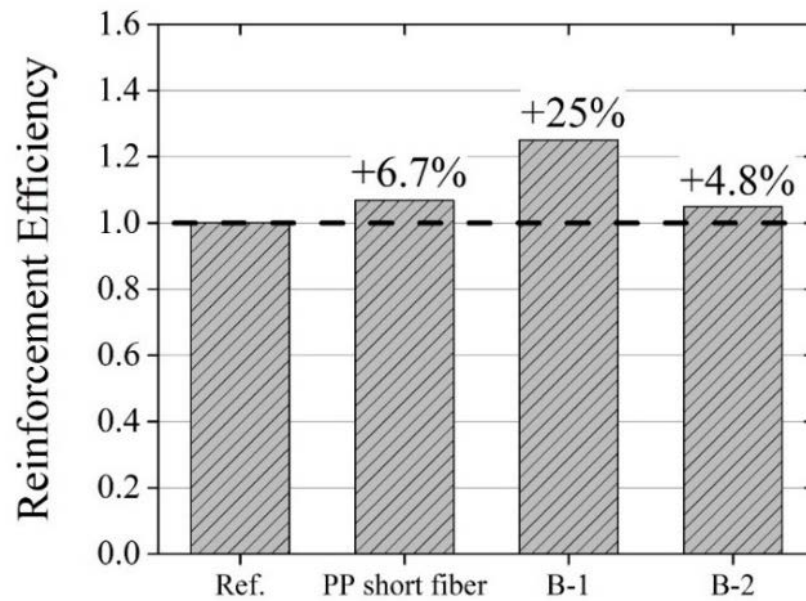


Figure 5. The percentage of effectiveness of reinforcement.

However, as shown above, this difference may not always be statistically significant. In other words, it is impossible to confirm the effect of using a particular reinforcing component. To confirm these results, it is necessary to perform a statistical analysis of pair comparison of individual samples among the series.

3.3. Statistical analysis

A series of three samples were tested for each type of concrete composite. The amount of experimental data is sufficient to identify statistics and confirm the results.

The effect of the concrete filler on the flexural properties of the concrete samples was revealed via statistical analyses. These analyses were performed by using one-way ANOVA (analysis of variance) at a significance level of 0.05. Fisher's Least Significant Difference (LSD) post hoc test was applied to determine which specific groups were significantly different from others. Table 4 summarizes the ANOVA results for the Maximal Flexural Strength analyzed in this work. For investigated characteristic, the p values are equal to 0.064, which are greater than 0.05. From these results, it can be concluded that the difference in flexural strength among the four specimens is not significantly different.

Table 4. One-way ANOVA test results.

Source	DF	Sum of squares	Mean square	F Value	P Value
Dependent variable: Maximal Flexural Strength					
Model	3	1.71913	0.57304	3.86548	0.064
Error	7	1.03773	0.14825		
Total	10	2.75685			

Fisher's (LSD) post hoc test was applied to examine the significance of the differences between average values of Maximal Flexural Strength of concrete samples. Table 5 shows the Fisher's (LSD) post hoc test results between groups of mean. Different letters indicate significant differences among groups ($p < 0.05$). The results showed that the effect of the filler type on the maximal flexural strength was significant for B-1 sample.

Table 5. Fisher's (LSD) post hoc test results.

Sample	Maximal Flexural Strength	p-value			
		Reference	PP short fiber	B-1	B-2
Reference	A		0.338	0.012	0.535
PP short fiber	A			0.049	0.816
B-1	B				0.047
B-2	A				

The same letter indicates that the difference of the means is not significantly different at the 0.05 level.

3.4. The mechanism of interaction of the hogweed chips and concrete matrix

The results obtained above indicate that the reinforcement effect when using hogweed additive is achieved only when using long pieces (50 mm). This length of the reinforcing chip may introduce some inaccuracies in the determination of flexural strength. In addition, the mechanism of interaction between the chip and the matrix in a concrete composite is unclear. One of the determining factors is the bonding of the reinforcement to the matrix in the composite. Weak adhesion may lead to a significant decrease in the mechanical properties of concrete composites. Optical microscopy analysis was performed to determine the interaction mechanism of chips and matrix in the composite. Fig. 6 shows micrographs of the surface of hogweed chips taken with a 50x magnification. As it can be seen, spherical growths like crystals form on the chip surface. This can be explained by the capillarity effect. In this case, the spherical drops on the surface are formed because of the worse wetting, the closer the shape of the particles will be to the spherical one. In the optimal case, the crystals should grow inside the aggregates, for example, in the case of alkali-resistant glass-roving, which is well wetted; or at least cover the surface evenly for better adhesion to the matrix. In this case, such formations on the surface worsen the adhesion of the concrete mixture and hogweed.



Figure 6. Sediment on the surface of hogweed.

The research in this paper differs from others in that previously dry hogweed was not used in concrete composites as wood and plant additives. But at the same time, this material also has increased mechanical properties. The flexural strengths of WWA concrete investigated ranged from 3.65 to 5.57 MPa, with the lowest values obtained at 30% additive level of ash [18]. The highest flexural strengths value, 5.6 MPa, was obtained in the case of sample B-1, reinforced with 50 mm long hogweed chips. Comparing the results with other works we can note the following: the developed samples of composites are similar in structure to those presented in [18, 19, 24, 26]; their main difference is the cheapness and availability of the filler material. It should also be noted that similar strength indicators of the developed composites were obtained by various authors in [20, 21, 25].

Table 6 shows the properties of a conventional concrete composite and a new material. The last column shows the difference between the composites

Table 6. Properties of concrete.

Properties	Unit	Values for typical concrete	Values for the new material	Difference
Density	Kg/m ³	2400	1754	-27%
Normal stress	MPa	4.6	5.6	+22%

4. Conclusions

In this paper, experimental studies have shown that the type of reinforcing aggregate has an effect on the flexural properties of concrete composites. Four types of samples were developed, including reference non-reinforced sample; concrete composite reinforced with PP short fibers; two types of concrete composites reinforced with plant additive samples, including a large additive of hogweed 50 mm long and

a medium additive of hogweed 25 mm long were examined. In addition, a series of composite samples were made from a composite sample reinforced with short polypropylene fiber of 54 mm length. Manufactured samples were tested for flexural strength at the age of 28 days. The results showed that a 50 mm long hogweed sample has the highest maximum flexural strength. However, a large-scale factor that requires larger beams to be tested may have an impact here. For the other samples, no statistically significant reinforcement effect was found. However, it should be noted that the determining factor in the application of such short reinforcement is not only the reinforcing efficiency, but also the increase in crack resistance and ductility characteristics of the concrete composite. In addition, the analysis has shown that at least the mechanical characteristics of the original concrete are preserved if another function of using the composite is assumed, for example, increased thermal conductivity.

During the experiment, the greatest increase in strength was revealed in samples with an additive of 50 mm; with the additive of hogweed 25 mm, a high increase in strength was not observed. As for recommendations: in construction, when creating a concrete composite, it is better to use a 50 mm long hogweed additive.

The research of this topic is in high demand for the following reason: the additive will not only have a positive effect on the environment (reducing the weed), but can also improve the mechanical properties of concrete and reduce the amount of cement used in the concrete composite production. Due to the reduction in density, the weight of the structure is reduced, which leads to a reduction in the load from its own weight.

In prospect, concrete composites reinforced with a dry plant additive will be studied and calculated for thermal properties.

5. Acknowledgments

Special acknowledgments are expressed to our teacher and friend Professor Mikhail Petrichenko, who passed away on 31.01.2021.

This work is supported by the Russian Science Foundation under grant 21-79-10283.

References

- Kornienko S.V., Popova E.D. «Green» construction in Russia and other countries. *Construction of Unique Buildings and Structures*. 2017. 4 (55). Pp. 67–93. DOI: 10.18720/CUBS.55.5
- Buka-Vaivade K., Sliseris J., Serdjus D., Pakrastins L., Vatin, N.I. Rational use of HPSFRC in multi-storey building. *Magazine of Civil Engineering*. 2018. 84(8). Pp. 3–14. DOI: 10.18720/MCE.84.1
- Lam T.V., Vu D.T., Dien V.K., Bulgakov B.I., Korol E.A. Properties and thermal insulation performance of lightweight concrete. *Magazine of Civil Engineering*. 2018. 84(8). Pp. 173–191. DOI: 10.18720/MCE.84.17
- Yartsev V.P., Mamontov S.A., Mamontov A.A., Savenkov D.A. The operational properties of fine-grained concrete filled with chrome leather shavings. *Modern Science: Theory, Methodology, Practice Materials of the 1st All-Russian (National) Scientific and Practical Conference*. 2019. Pp. 126-132.
- Gagarin V.G. Akhmetov V.K., Zubarev K.P. Moisture behavior calculation of single-layer enclosing structure by means of discrete-continuous method. *MATEC Web of Conferences*. 2018. 170. Pp. 03014. DOI: 10.1051/mateconf/201817003014
- Gagarin V.G. Akhmetov V.K., Zubarev K.P. Unsteady-state moisture behavior calculation for multilayer enclosing structure made of capillary-porous materials. *IOP Conference Series: Earth and Environmental Science*. 2018. 177. Pp. 012021. DOI: 10.1088/1755-1315/177/1/012021
- Gagarin V.G. Akhmetov V.K., Zubarev K.P. The moisture regime calculation of single-layered enclosing structures on the basis of the application of the discrete-continuum method. *IOP Conference Series: Materials Science and Engineering*. 2018. 456. Pp. 012105 DOI: 10.1088/1757-899X/456/1/012105
- Gumerova E., Gamayunova O., Meshcheryakova T. Energy efficiency upgrading of enclosing structures of mass housing of the Soviet Union. *Advances in Intelligent Systems and Computing*. 2017. 692. Pp. 432-439. DOI: 10.1007/978-3-319-70987-1_45
- Gamayunova O., Radaev A., Petrichenko M., Shushunova N. Energy audit and energy efficiency of modular military towns. *E3S Web of Conferences*. 2019. 110. Pp. 01088. DOI: 10.1051/e3sconf/201911001088
- Klyuev S.V., Klyuev A.V., Vatin N.I. Fiber concrete for the construction industry. *Magazine of Civil Engineering*. 2018. 84(8). Pp. 41–47. DOI: 10.18720/MCE.84.4
- Morozov V.I., Pukhareno Yu.V., Yushin A.V. The numerical investigations of double-span concrete beams strengthened with fiber reinforced plastics across the oblique section. *Materials Physics and Mechanics*. 2017. 1-2 (31). Pp. 40–43
- Kiyans A.V. Concrete with recycled polyethylene terephthalate fiber. *Magazine of Civil Engineering*. 2018. 84 (8). Pp. 109–118. DOI: 10.18720/MCE.84.11
- Kornienko S.V. A method for solving the three-dimensional problem of joint unsteady heat and moisture transfer for building envelopes. *News of higher educational institutions. Building*. 2006. 2. Pp. 108–110
- Fapohunda C., Bolatito A., Akintoye O. O. A review of the properties, structural characteristics and application potentials of concrete containing wood waste as partial replacement of one of its constituent materials. *Journal of built environment*. 2018. 1 (6). DOI: 10.2478/jbe-2018-0005
- Jorge F. C., Ferreira J., Pereira C. Wood-cement composites: a review. *Holz als Roh- und Werkstoff*. 2004. 62(5). Pp. 370-377. DOI: 10.1007/s00107-004-0501-2
- Vaishali G. Ghorpade effect of wood waste ash on the strength characteristics of concrete. *Nature Environment and Pollution Technology*. 2012. 11(1). Pp. 121-124

17. Rusina V.V., Dubrovina Yu.Yu., Chernov E.I. Concretes for walling based on waste from mechanical processing of wood. *Building materials*. 2017. 10. Pp. 32–35.
18. Udoeyo F. F., Young D. T., Inyang H.I., Oparadu E. E Potential of wood waste ash as an additive in concrete. *Journal of Materials in Civil Engineering*. 2006. 18 (4). DOI: 10.1061/(ASCE)0899-1561(2006)18:4(605)
19. Chowdhury S., Maniar A., Suganya O.M. Strength development in concrete with wood ash blended cement and use of soft computing models to predict strength parameters. *Journal of Advanced Research*. 2015. 6 (6). Pp. 907–913. DOI: 10.1016/j.jare.2014.08.006
20. Batayneh M., Marie I., Asi I. Use of selected waste materials in concrete mixes. *Waste Management*. 2007. 27(12). Pp. 1870–1876. doi:10.1016/j.wasman.2006.07.026
21. Naik T.R., Kraus R.N., Siddique R. CLSM containing mixture of coal ash and a new pozzoloanic material. *Aci Materials Journal*. 2003. 100(3). Pp. 208–215.
22. Ramega M. H., Burrige H The wood from the trees: The use of timber in construction. *Renewable and Sustainable Energy Reviews*. 2017. 68. Pp. 333–359. DOI: 10.17863/CAM.10386
23. Mengya L., Khennane A., Khelifa M., Ganaoui M. E. Structural response of cement-bonded wood composite panels as permanent formwork. *Composite Structures*. 2018. 209. Pp. 13-22. DOI: 10.1016/j.compstruct.2018.10.079
24. Li M., Khelifa M., Ganaoui M.E. Mechanical characterization of concrete containing wood shavings as aggregates. *International Journal of Sustainable Built Environment*. 2017. 2 (6). Pp 587–596. DOI.org/10.1016/j.ijbsbe.2017.12.005
25. Morales-Conde M.J., Rodríguez-Liñán C., Pedreño-Rojas M.A. Physical and mechanical properties of wood-gypsum composites from demolition material in rehabilitation works. *Construction and Building Materials*. 2016. 114. Pp. 6–14. DOI: 10.1016/j.conbuildmat.2016.03.137
26. Kuprava L. R., Nikulnikov R. S. Modern construction technologies. Durisol permanent formwork - building blocks based on natural materials. Scientific support for the development of agriculture in the context of reform. Collection of scientific papers based on the materials of the international scientific and practical conference of teaching staff. 2014. Pp. 199–202
27. Nazerian M., Gozali E., Ghalehno M. D. The influence of wood extractives and additives on the hydration kinetics of cement paste and cement-bonded particleboard. *Journal of Applied Sciences*. 2011. 11. Pp. 2186–2192.
28. Azrieda, A.R.N., Razali A.K., Izran K., Rahim S., Abdul-Aziz M. Hydration performance of cement-bonded wood composites: Compatibility assessment of six pioneer forest species. *Borneo Science*. 2010. 25. Pp. 47–57.
29. Olorunnisola A.O. Effects of particle geometry and chemical accelerator on strength properties of rattan-cement composites. *African Journal of Science and Technology*. 2007. 8. Pp. 22–27.
30. Koohestani B., Koubaa A., Belem T., Bussi ere B., Bouzahzah H. Experimental investigation of mechanical and microstructural properties of cemented paste backfill containing maple-wood filler. *Construction and Building Materials*. 2016. 121. Pp. 222–228
31. Karade S.R., Cement-bonded composites from lignocellulosic wastes. *Construction and Building Materials*. 2010. 24 (8). Pp.1323–1330.
32. Sabbaghian, M., & Kheyroddin, A. Flexural strengthening of RC one way slabs with high-performance fiber-reinforced cementitious composite laminates using steel and GFRP bar. *Engineering Structures*. 2020. 221. 111106. doi: 10.1016/j.engstruct.2020.111106
33. Dabiri, H., Sharbatdar, M. K., Kavyani, A., & Baghdadi, M. The Influence of Replacing Sand with Waste Glass Particle on the Physical and Mechanical Parameters of Concrete. *Civil Engineering Journal*. 2018. 4(7). 1646. doi: 10.28991/cej-03091101
34. Thandavamoorthy, T. S. Wood waste as coarse aggregate in the production of concrete. *European Journal of Environmental and Civil Engineering*. 2015. 20(2), 125–141. doi:10.1080/19648189.2015.1016631
35. Morales-Conde, M. J., Rubio-de-Hita, P., & P erez-G alvez, F. Composite Mortars Produced with Wood Waste from Demolition: Assessment of New Compounds with Enhanced Thermal Properties. *Journal of Materials in Civil Engineering*. 2018. 30(2). 04017273. doi:10.1061/(asce)mt.1943-5533.0002148
36. Ozerova N. A., Krivosheina M. G. Features of formation of secondary areas of hogweed *Sosnovsky* and *Mantegazzi* (*Heracleum sosnowskyi*, *H. mantegazzianum*) on the territory of Russia. *Russian journal of biological invasions*. 2018. 1. Pp. 78–87. DOI: 10.1134/S2075111718020091
37. Dalke I. V., Chadin I. F. Scientific guidelines for the drafting of the destruction of unwanted undergrowth *Sosnovsky* hogweed on the territory of rural settlement "Letka" Priluzsky District of the Komi Republic. [Online]. System requirements: pdf. URL: http://proborshevik.ru/wp-content/uploads/2017/09/Recommen_Letka_2015.pdf (date of application: 26.04.2020).
38. Dangerous wild grass will be used in batteries. [Online]. URL: https://www.eurekalert.org/pub_releases/2019-08/nuos-dwg082619.php (date of application: 26.04.2020).
39. Musorina T.A., Naumova E.A., Shonina E.V., Petrichenko M.R., Kukolev M.I. Thermotechnical properties of an energyefficient material based on a herbal supplement (dry hogweed). *Vestnik MGSU*. 2019. 12 (14). Pp. 1555–1571. DOI: 10.22227/1997-0935.2019.12.1555-1571
40. Volkova A.A., Paykov A.V., Stolyarov O.N., Semenov S.G., Melnikov B.E. Structure and properties of textile reinforced concrete. *Magazine of Civil Engineering*. 2015. 7. Pp. 50–56. DOI: 10.5862/MCE.59.5

Contacts:

Tatiana Musorina, tamusorina@mail.ru

Daria Zaborova, zaborova-dasha@mail.ru

Mikhail Petrichenko, fonpetrich@mail.ru

Oleg Stolyarov, stolyarov_on@spbstu.ru



DOI: 10.34910/MCE.107.10

Performance of structurally viable green concrete derived from natural Pozzolan and Nanosilica

M. Ibrahim^a, M. Nasir^b, S.R. Hussaini^a, S.K. Najamuddin^a, A.O. Ewebajo^{*a}

^a King Fahd University of Petroleum and Minerals, Saudi Arabia

^b Imam Abdulrahman Bin Faisal University, Saudi Arabia

*E-mail: adeoluwaewebajo@gmail.com

Keywords: alkaline-activated concrete, fresh and hardened properties, morphology and mineralogy, nanosilica, natural Pozzolan, pore structure

Abstract. The effect of admixing nanosilica on the fresh and hardened properties of natural pozzolan (NP) based alkali activated concrete (AAC) was examined. The workability, setting times, engineering properties, durability characteristics and pore structure of concrete were evaluated. In addition, the polymerization mechanism was assessed by SEM and XRD analysis. The results indicated that there was insignificant influence of nanosilica on the flow of mortar, however, the setting times of concrete were prolonged with an increase in the nanosilica content. The prominent phases evolved in XRD pattern were philipsite and anorthite which are form of C/N-A-S-H and C-(A)-S-H gel, respectively. A greater absorption of Al and Ca was observed in the mixes prepared with sizeable amount of nanosilica, which enhanced the microstructure and pore structure characterized by fewer voids (>1000 nm) and more gel pores (<10 nm). It is postulated that both the mechanical properties and durability are beneficially enhanced by the synergistic-interaction of NP-nanosilica.

1. Introduction

Ordinary Portland cement (OPC) manufacturing is an energy intensive process which contributes about 6 % to 8 % of CO₂ emissions of total greenhouse gases (GHGs) [1]. As the cement production is expected to grow steadily to meet the demand coupled with the stringent conditions being imposed by the global community to limit the GHGs emissions, the building materials research has embarked on finding low carbon footprint alternative binders to OPC [2]. Among various options available, alkali activated binder (AAB) has been extensively researched as they are synthesized utilizing industrial by-products as well as natural materials [1, 3–7]. The notable benefits of using AAB are environmental, economic and technical [6, 8, 9]. The technical benefits include high early strength and improved durability, particularly under the exposure of acid and sulfate environments [10–13].

However, the rate of strength development of AABs was found to be slow when cured at room temperature conditions and rapid at elevated temperature curing, particularly those binders synthesized by using low Ca precursor materials [14, 15]. The necessity of curing these binders at elevated temperature is to accelerate the setting in order to achieve sufficient structural strength leading to up-scale the technology to the industrial level. Hence, the synthesis of AABs that can set within the reasonable limits and gain sufficient strength when cured at room temperature conditions would certainly widen its application beyond the precast industry.

With the aim of improving the strength gain of AABs that were synthesized using low Ca precursor materials when cured at lower temperatures, researchers focused on increasing the fineness of the source materials or blending alternative industrial byproducts and natural materials to alter the chemical and

Ibrahim, M., Nasir, M., Hussaini, S.R., Najamuddin, S.K., Ewebajo, A.O. Performance of structurally viable green concrete derived from natural pozzolan and nanosilica. Magazine of Civil Engineering. 2021. 107(7). Article No. 10710. DOI: 10.34910/MCE.107.10

© Ibrahim, M., Nasir, M., Hussaini, S.R., Najamuddin, S.K., Ewebajo, A.O., 2021. Published by Peter the Great St. Petersburg Polytechnic University



This work is licensed under a CC BY-NC 4.0

mineralogical composition of the primary source materials [16, 17]. These alternative materials included; metakaolin, silica fume, rice husk ash and blast furnace slag, etc. The alternative materials that contained Ca were found to have greater influence on the fresh and hardened properties of alkali-activated concrete (AAC) [14, 18]. The setting time of AABs that were synthesized using low Ca precursor materials such as low Ca fly ash was delayed, however, inclusion of GGBFS in these mixes accelerated it [19]. This is mainly due to the availability of Ca in the GGBFS which quickly dissolves in water to form a binder. It has been reported that the final setting time of alkali activated low Ca fly ash was more than 24 hours because of slow polymerization at ambient conditions [19].

Whilst, inclusion of OPC in the mixture shortened setting time that was comparable to binder containing OPC alone [19]. Kumar et al. [20] studied the effect of adding 5 to 50 % replacement of fly ash with GGBFS on the reaction kinetics, strength development and microstructure. In another study, Temuujin et al. [16] investigated incorporation of CaO and Ca(OH)₂ on the strength development of fly ash based concrete. They observed that Ca enhanced the rate of strength development. De Silva et al. [21] partially replaced GGBFS with metakaolin. Their results revealed that the incorporation of metakaolin delayed the final setting due to delay in the heat release peak. As a result of which there was marginal reduction in the strength as well. The enhanced fresh and hardened properties of AABs that were synthesized using fly ash/GGBFS blends was attributed to the formation of C-S-H along with the polymeric gel such as C/N-A-S-H [22–24].

Recently, nanomaterials have attracted significant interest in the building materials research. The usage of these materials in the cementitious binders has the potential of manipulating the material characteristics at nano-level, thereby enhancing the micro-level properties. It is believed that the finer materials increase the rate of dissolution, consequently, improving the fresh and hardened properties of cementitious binders. The changes in the binder structure at these levels significantly improves the macro-level properties, thus, providing a new functionality to the end product [25, 26]. Several studies were carried out earlier to investigate the use of nanomaterials in the OPC-based binders [27–32].

It was reported that the engineering properties of these binders were enhanced due to the usage of nanomaterials, particularly from nanosilica. It was reported in one of the studies that the compressive strength of mortars prepared with nanosilica was more than that of mortars prepared by incorporating microsilica [27]. The increase in the mechanical strength was attributed to the enhanced pozzolanic reaction in the mixture containing nanosilica. Nazari and Riahi [33] found improvement in the mechanical properties of the concrete due to the addition of nanosilica. They posited that superior properties were attributed to the enhanced formation of C-S-H. They further noticed that the microstructure of binder at 4 % nanosilica addition was dense and uniform compared to the other mixes. The improved properties of nanosilica-based concrete are also due to the fact that it plays vital role in strengthening the interfacial zone between the aggregate and paste [34].

The AABs are formed when the precursor materials are activated in the presence of highly alkaline activators to form polymeric compounds. In the process of poly-condensation, intensive three-dimensional structural network is formed during the formation of AAB. The chain length of the network depends on the reactivity of the source material. Therefore, nanomaterials could possibly play a key role in the case of AAB formation even more than that of OPC-based binders. Firstly, by improving the reactivity of the precursor materials, secondly, by forming stable longer network of three-dimensional polymeric compounds. Taking into account the advantages of nanomaterials, they were also used as partial replacement of fly ash, in the earlier studies with a view to accelerate the polymerization process during the synthesis of AAB. Phoo-ngernkham et al. [35] investigated the usage of nano-silica and nano-alumina on the mechanical and morphological characteristics of fly ash based AAB. Elsewhere, up to 10 % nano-silica was incorporated in the AAB [36]. In their study, 6 % nano-silica was the optimum dosage in yielding improved properties [36].

In an earlier study by authors, synthesis of natural pozzolan as AAB indicated potential in extensive utilization as precursor material in developing viable structural alkali activated concrete [37]. The strength and microstructural properties of NP-based AAC were enhanced by incorporating nanosilica when the binder was cured at room and elevated temperature [38, 39]. Also, the influence of type of alkaline activators on the NP-based concrete was discussed in detail earlier by authors [40]. A detailed study was also reported earlier by authors on the influence of nanosilica on the porosity [41]. Keeping in view the enormous specific surface area of nanomaterials that could possibly enhance the properties of AABs in twofold. Firstly, by improving the polymerization products in the presence of alkaline activators that will decrease the voids in the binder structure. Secondly, by densifying microstructure by particle packing effect which enhances the pore structure of solid and maximizes the gel network. Therefore, this study aims to investigate the effect of nanosilica on the fresh and hardened properties of NP-based AAC focusing on the setting time and pore structure. The results of this study could possibly elucidate the polymerization mechanism of NP-based AAC incorporating nanosilica which would help in characterizing the pore structure and pore size distribution as well.

2. Materials and Methods

2.1. Materials

The oxide composition of natural pozzolan (NP) obtained from X-ray fluorescence (XRF) analysis is depicted in Fig. 1. The physico-chemical properties of nanosilica provided by AkzoNobel supplier are given in Table 1. Na_2SiO_3 (SS) having silica modulus of 3.3 and 14 M NaOH (SH) at a weight ratio of 2.50 was used to activate precursor materials. The granulometry of coarse aggregate (CA) used was conforming to ASTM C33 curve #8 [42] wherein 60 % of 4.75 mm, 35 % of 2.36 mm and 5 % of 1.18 mm size of aggregates were proportioned. The particle size distribution of the fine aggregates (FA) are summarized in Table 2.

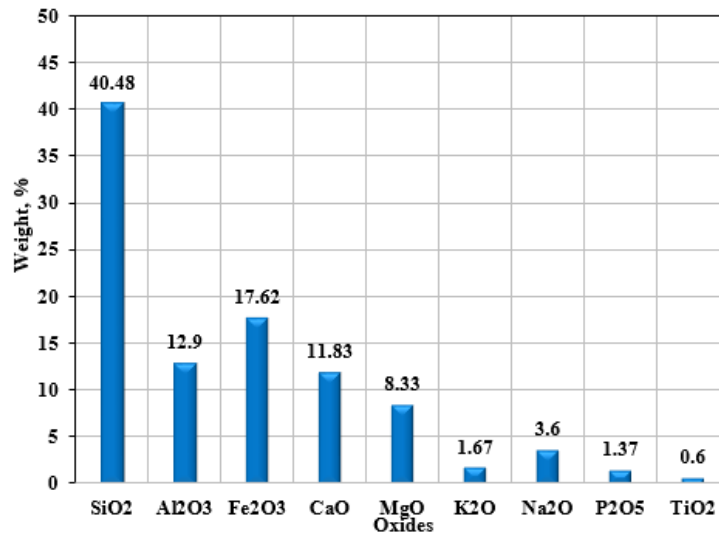


Figure 1. Oxide composition of NP by XRF.

Table 1. Physico-chemical properties of nanosilica.

Parameters	Properties
SiO ₂	99 %
Al ₂ O ₃	1.20 %
TiO ₂	0.03 %
Fe ₂ O ₃	0.01 %
pH-value	9.5
Mean Particle size	35 nm
Surface area	80 m ² /g
Solid matter content	50 %
Density	1.2–1.4 g/cm ³

Table 2. Particle size distribution of fine aggregate.

ASTM Sieve #	Size	% passing
4	4.75 mm	100
8	2.36 mm	100
16	1.18 mm	100
30	600 μm	76
50	300 μm	10
100	150 μm	4

2.2. Methods

2.2.1. Mix composition and curing

A set of five alkali-activated natural pozzolan-based mixtures were cast by admixing 0 %, 1 %, 2.5 %, 5% and 7.5 % of nanosilica. The following parameters were kept invariant: total binder content was 400 kg/m³, SS was 150 kg/m³, SH was 60 kg/m³, while FA and CA was approximately 635 kg/m³ and 1179 kg/m³, respectively [41]. Besides, a conventional concrete mix was also prepared having 370 kg/m³ of binder and

water to cement ratio of 0.45 in order to compare with AAC. AAC samples for each mix were prepared by firstly making liquid portion of the mixture by adding required quantities of SS, SH and colloidal nanosilica followed by sonication to disperse it properly. Subsequently, dry materials were introduced in the Hobart paddle mixer and mixed thoroughly. Afterwards, the alkaline solution was mixed until the substance became homogeneous. Next, the fresh concrete was filled in to the moulds in two segments and demolded after 24 hours. All the prepared specimens were cured at the ambient laboratory condition (Temp: 23 ± 2 °C and RH 50 ± 5 %) until testing.

2.2.2. Fresh properties

The workability was determined by conducting flow table test according to ASTM C1437 [43]. The setting times of concrete were determined by measuring penetration resistance in accordance with ASTM C403 [44].

2.2.3. Hardened properties

NMR relaxometry using a GeoSpec 2–75 core analyzer was used to study the pore structure of concrete. The cylindrical specimens of size 40 mm diameter and 40 mm height were utilized. Prior to the test, specimens were fully saturated under 10 MPa pressure [45, 46]. The compressive strength, flexural strength and modulus of elasticity of concrete were determined according to ASTM C109 [47], C78 [48] and C469 [49] respectively.

The water absorption and volume of permeable voids (VPV) were measured utilizing $\varnothing 75$ mm \times 150 mm high cylindrical specimens according to the procedure described in ASTM C642 [50]. Most importantly, modified rapid chloride permeability and non-steady state chloride migration coefficient were also determined in accordance with the procedure outlined by Noushini and Castel [8] and NT Build 492 [51] respectively, for all the AAC mixes along with the conventional concrete. The measurements were conducted post 28 and 90 days of ambient temperature curing.

3. Results and Discussion

3.1. Influence of nanosilica on the fresh properties of binder

The plots of penetration resistance versus elapsed time for various concrete mixes is shown in Fig. 2(a) to 2(f). For each plot, a befitting exponential curve was drawn and equation was obtained. Subsequently, the initial setting time and final setting time were computed by taking 3.5 MPa and 27.6 MPa as the penetration resistance, respectively. The alkaline activator, a liquid portion in the mixture, is the essential component in the synthesis of AABs. According to the methodology presented elsewhere to perform setting times test [52], ASTM C191 [53] was followed in which normal consistency was determined by adjusting alkaline activator content in the mixture. However, adjusting alkaline activator content in order to achieve normal consistency of the AAB in accordance with ASTM C191 [53] has been originally specified for OPC based binder, may not be appropriate to be used for AABs. This concern was also expressed by Teixeira-Pinto et al. [54]. This is particularly true because of the fact that the chemical ingredients present in the alkaline activator participate in the chemical reaction in which precursor material is transformed in to a polymeric compound such as C-A-S-H or N-A-S-H or both depending on the composition of the source materials [55, 56].

Hence, determining the setting times of AABs by utilizing concrete in accordance with ASTM C403 [44] which does not require liquid portion to be adjusted is more appropriate. It is also worth mentioning that the initial and final setting times of any binder are essentially required to plan the concreting work. Duration of initial setting is of importance that determines when the concrete is no longer be workable and prior to which consolidation and finishing works could be scheduled. Similarly, determining the final setting time of concrete is also important to know when the concrete can start to take the loads.

Table 3 summarizes the initial and final setting times of the AAC incorporating nanosilica along with the OPC based concrete. As expected, the initial and final setting times of the OPC based concrete were less compared to the AAC containing variable quantity of nanosilica. The average initial setting time was in the range of 4 h 52 min to 6 h 37 min, while, the final setting time was between 6 h 50 min and 9 h 9 min. As mentioned earlier, the penetration resistance test was conducted in the laboratory conditions (at 23 ± 2 °C and 50 ± 5 % RH). The quantity of lime (CaO) in the source material accelerates the setting of AAB as it dissolves relatively quickly compared to Si and Al [57]. Nath and Sarker [19] studied the effect of adding GGBFS on the fly ash based AAB cured in ambient conditions discovered that the GGBFS content accelerated the setting of binder. According to their results the setting of AAB prepared without GGBFS was more than 24 hours, while, 10 % addition resulted in initial and final setting times of 290 min and 540 min, respectively. The initial and final setting times of AAC synthesized without nanosilica in this study was on average 4 h 52 min and 6 h 50 min, respectively. Both the setting times were prolonged in the AAC mixtures as the NP replacement with nanosilica was increased. Similar results were observed in the previous research conducted by Gao et al. [58].

As reported in a previous study that the first step in the process of alkali activation is the dissolution of source material in to the highly alkaline solution [59]. When nanosilica is added in the mixture, due to an increase in the concentration of Si, pH of the alkaline solution drops which delays the reaction. This was also proven by the calorimetric studies carried out by Deir et al. [57] wherein high silica content delayed the heat release peak. This phenomenon has delayed the setting of NP-based binder modified with nanosilica. Another important factor which retarded the setting was the reduction in CaO content in the mixture when nanosilica was added as a replacement of NP (Fig. 1). Though the nanosilica dissolves quickly in the alkaline solution, this effectively retards the dissolution of Si and Al of the precursor material unless the high alkalinity breaks the layers to dissolve these species from the source material (Fig. 1 and Table 1). Thus, the combined influence of these factors played a role in delaying the setting times of NP-based AAC modified with nanosilica. However, the overall setting times of the AAC containing nanosilica were reasonable to be used in cast in place applications.

Table 4 shows the flow of alkali activated mortar. There was marginal increase in the flow of mortar as the quantity of nanosilica increased in the mix up to a replacement level of 2.5 %. Beyond this replacement level, the workability was slightly reduced. Apparently, there was no adverse influence on the workability of binder due to the addition of nanosilica. At higher replacement levels, decrease in the flow of mortar could be attributed to the increase in water demand because of increase in specific surface area of nano particles (Table 1). Since the flow of mortar was between the range of 140 to 200 mm in all mixture, they are characterized as plastic flow as recently reported by [18].

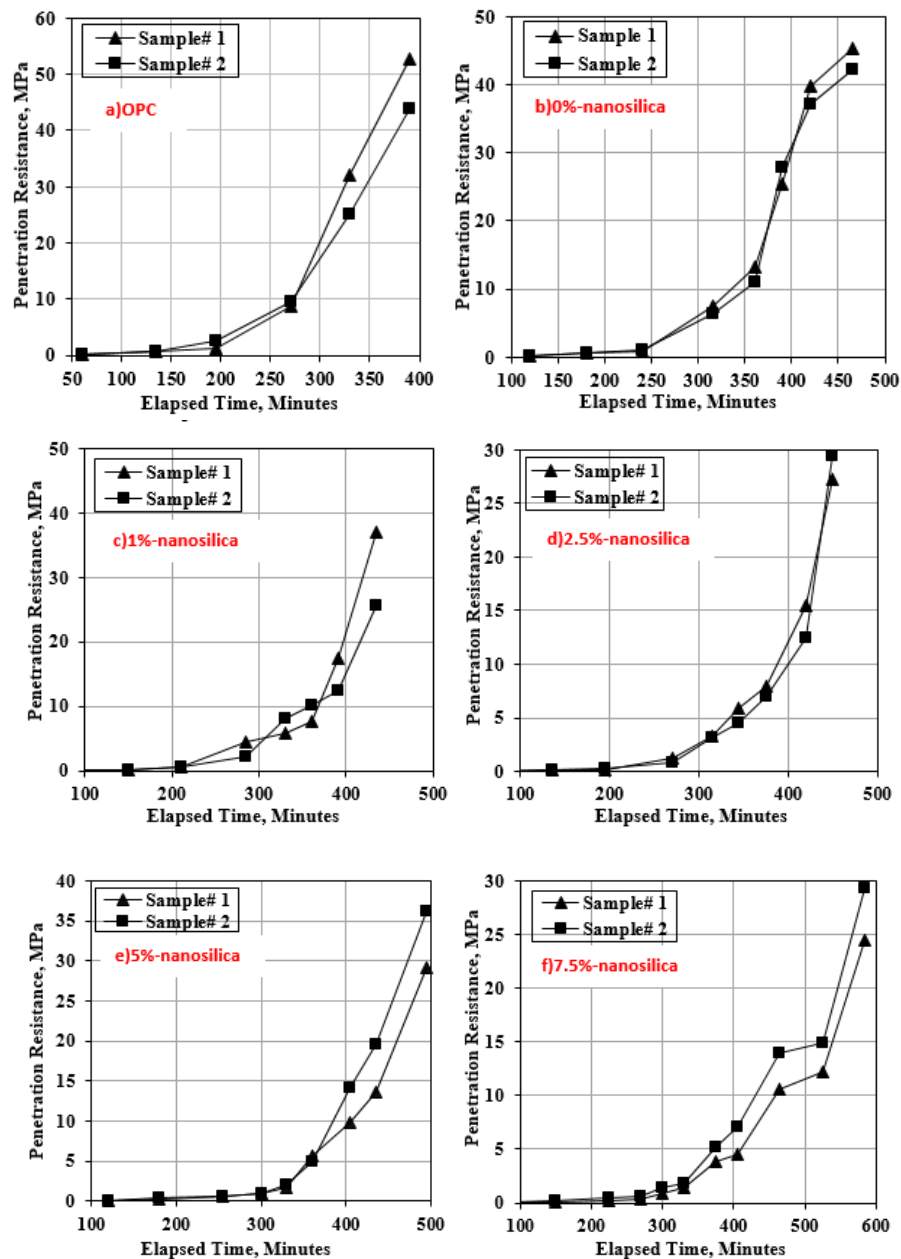


Figure 2(a-f). Penetration resistance versus elapsed time of concrete.

Table 3. Setting times of various concrete mixes.

Mix #	Sample 1		Sample 2	
	Initial setting time, min	Final setting time, min	Initial setting time, min	Final setting time, min
OPC	3 h 56 min	5 h 38 min	3 h 54 min	5 h 39 min
0 %-nanosilica	4 h 48 min	6 h 48 min	4 h 56 min	6 h 52 min
1 %-nanosilica	5 h 6 min	6 h 47 min	5 h 11 min	6 h 59 min
2.5 %-nanosilica	5 h 31 min	7 h 24 min	5 h 38 min	7 h 19 min
5 %-nanosilica	5 h 56 min	7 h 56 min	5 h 42 min	7 h 58 min
7.5 %-nanosilica	6 h 52 min	9 h 14 min	6 h 22 min	9 h 5 min

Table 4. Flow of nanosilica incorporated mortar.

Mix #	Flow of mortar, mm				
	1	2	3	4	Average
0 %-nanosilica	162	166	169	160	164
1 %-nanosilica	174	167	175	165	170
2.5 %-nanosilica	175	168	172	173	172
5 %-nanosilica	162	159	155	155	158
7.5 %-nanosilica	147	155	154	152	152

3.2. Influence of nanosilica on the hardened properties of binder

The pore structure and pore size distribution of hardened cementitious materials govern the micro- and macro-level properties of concrete. By and large the pores in the hardened cementitious materials are categorized into four types depending on the pore diameter. These are: (1) gel pores, (2) small capillary pores, (3) large capillary pores and (4) voids, respectively, having a pore diameter <10, 10 to 100, 100 to 1000 and >1000 nm [60]. The incremental porosity data obtained through the NMR relaxometry was used to calculate contributive porosity of the concrete specimens. The contributive porosity is defined as the proportion of certain category of pores with respect to the total pore volume of the solid. The contributive porosity of various concrete mixes is shown in the Fig. 3 and Fig. 4 that were cured for 28 and 90 days, respectively. The following observations were made:

- Predominantly, the pore diameter was between 1 nm and 100 μm in the various concrete mixes.
- After 28-day curing, the percentage of gel pores (diameter <10 nm) was 1.13 % in the control AAC mixture, while, they were between 2.59 % and 2.85 % in the mixes containing nanosilica.
- However, the pores having diameter >10 nm were in greater proportion in the AAC mix prepared with 0 % nanosilica in relation to the mixes having 1 to 7.5 % nanosilica.
- The extent of pores having diameter between 100 and 1000 nm were about 4 % in the 0 % nanosilica at 28 days, whereas 1.85, 1.98, 1.44 and 1.40 % in 1, 2.5, 5 and 7.5 % nanosilica, respectively.
- Further, highest of about 7 % of pores having diameter more than 1000 nm were obtained in the 0 % nanosilica, while 4.73, 5.76, 4.33, and 3.95 % in the 1, 2.5, 5 and 7.5 % nanosilica, respectively.
- The continuation of curing from 28 to 90 days, marginally reduced the gel pores (<10 nm) in all the concrete mixes, however, there was significant reduction in the volume of pores classified as voids (>1000 nm). This was particularly noticeable in the mixes prepared with increased nanosilica content.
- Besides, the percentage of pores having diameter <10 nm increased with the nanosilica quantity increment in the mix. The quantity of these pores was twice in the nanosilica modified concrete compared to the control mix at 28 days. Regardless of curing period, the range of pores having diameter in the range of 100 to 1000 nm together with >1000 nm was proportionately reduced with an increase in nanosilica content in the mixture.

Therefore, incorporation of nanosilica in the mixture resulted in higher volume of gel pores and lower voids. The total pore volume was in the range of 11.23 % to 18.35 % such that lowest was recorded in the 7.5 % nanosilica modified concrete and the highest in the reference AAC batch (Table 6). The results obtained in this research are in good agreement with results of a study by Rodríguez et al. [61], wherein an overall porosity was in the range of 6.32 % to 9.75 %. Similar trend was also noted elsewhere [62]. Shaikh et al. [63] adduced that nanosilica forms an envelope to the aggregates consequently lowering capillary pores in the

adjacent matrix. A detailed discussion about the pore structure has been reported in a recent publication of the authors [41].

The refinement of the pore structure in the case of binder prepared with nanosilica is possibly due to the enhanced polycondensation of alkaline-activated products. Evidently, as shown in the Fig. 5(a) to 5(e), the morphology of the binder tends to densify with an increase in nanosilica content in the alkali activated concrete mix. The micrograph of AAB prepared without nanosilica was relatively inhomogeneous, as shown in the Fig. 5(a). It appears to be composed of a non-uniform structure. Due to the termination of polymerization there was insufficient gel formation observed. Fig. 5(b) through 5(e) shows the micrographs of nanosilica incorporated mixes. Evidently, the matrix enhanced as the quantity of nanosilica is increased. The effect of nanosilica on the microstructure of NP-based binder has been discussed in detail in a previously published work elsewhere [39].

The products formed due to alkaline-activation included a philipsite phase that was most prominent in the XRD patterns, as shown in the Fig. 6. It is a form of C-A-S-H gel having Na in the framework [64]. Also, anorthite was detected in the XRD pattern whose structure resembles with C-A-S-H gel without Na in the framework [64]. In addition, the phases such as, C-S-H, quartz, hematite, calcite, and zeolite-Y also appeared in the spectra. These are the phases which determine the nature of the binder and are responsible for imparting skeletal strength. The crystallinity of these phases governs the physical properties of these binders. A close observation at the different XRD patterns reveals that the philipsite, anorthite, C-A-S-H and zeolite-Y peaks were sharp and wide in the case of AAB containing higher nanosilica. Mainly, the philipsite peak around 32.7° and 52° 2θ is seemingly intense and wider in the case of AAB prepared with 5 % and 7.5 % nanosilica. In addition, the concentration of the peak at 36° 2θ associated to C-A-S-H gel was strong in the case of AAB prepared with more than 2.5 % nanosilica.

The primary difference between the hydration products of OPC and AAB is that, C-S-H is formed in the case of former, while in the latter either Al or Na or both are absorbed in the C-S-H to form C-A-S-H or C/N-A-S-H [65]. It is an important gel product formed in the polymerization mechanism of AAB which is believed to be denser than that of C-S-H [65]. Due to the enormous specific surface area of nanosilica particles, reactivity may have been enhanced that promoted the polycondensation process of supplementary C-A-S-H phase in the binder structure [66, 67]. This is particularly true due to the fact that the ratio of Al/Si was high in the AAB synthesized with sizeable quantity of nanosilica according to energy dispersive spectroscopy (EDS) data discussed in detail by the authors [39].

As a result of enhanced polycondensation due to superior formation of hydration products, the mechanical properties of the AAC prepared with partially replacing NP with nanosilica were significantly improved. Table 5 summarizes compressive and flexural strength along with the modulus of elasticity of AAC.

The compressive strength of concrete was lower at 7 days in the AAC incorporating nanosilica. The greater quantity of nano-silica retarded strength development. On contrary, at later ages after 28 and 90 days, there was significant development in compressive strength noted in the 5 as well as 7.5 % nanosilica incorporated binder. However, slow strength gain in the AAC modified with 7.5 % nanosilica was noted which may possibly be attributed to embedded remnants of unreacted particles in the binder structure observed in the micrograph (Fig. 5). Also, the addition of higher quantity of silica believed to delay the heat release peak as a result of decrease in the pH [57]. It is important to indicate here that the strength gain in the nanosilica modified concrete was rather slow owing to the slow cross-linking of polymeric units [68].

It is demonstrated that the cross-linking takes place faster when the AABs are cured at elevated temperature [68]. However, curing these binders at elevated temperature could possibly solidify the gel prematurely which will discontinue the dissolution of aluminates and silicates of the precursor material in to the alkaline solution. Thereby, terminating the process of polymerization which hampers the formation of polymeric units [69, 70]. This connotes that admixing nanosilica involves slow reaction kinetics at early ages, whereas admixing more than 5 % of nanosilica negatively affects the long-term strength development.

Mixes prepared with admixing more than 2.5 % nanosilica also gained superior flexural strength. Though there was high early strength in the OPC-based concrete, it was about 60 % lower when compared with the 5 % and 7.5 % nanosilica added AAC cured for 90 days. The flexural strength of AAC incorporating nanosilica was superior to OPC-based concrete. It is to be noted that the elastic modulus of AAC of similar grades is lower compared to the conventional concrete (Table 5). The influence of nanosilica is clearly evident from the mechanical properties of AAC and an increase in the nano particles in the binder structure improved compressive strength, flexural strength and modulus of elasticity which corroborates the findings of total porosity, as demonstrated in Table 6. The total porosity was more or less proportional to the nanosilica content in the batch.

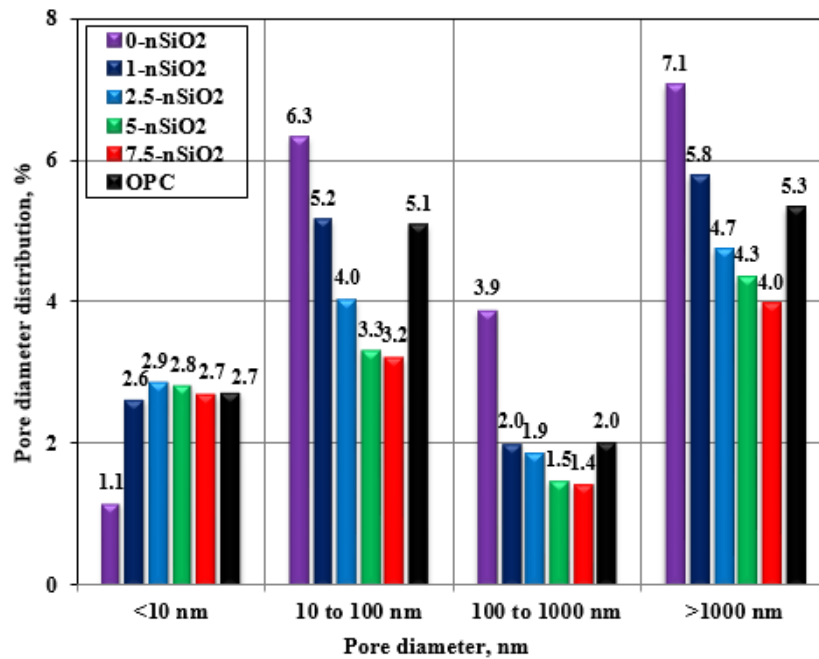


Figure 3. Contributive porosity of concrete after 28 days of curing.

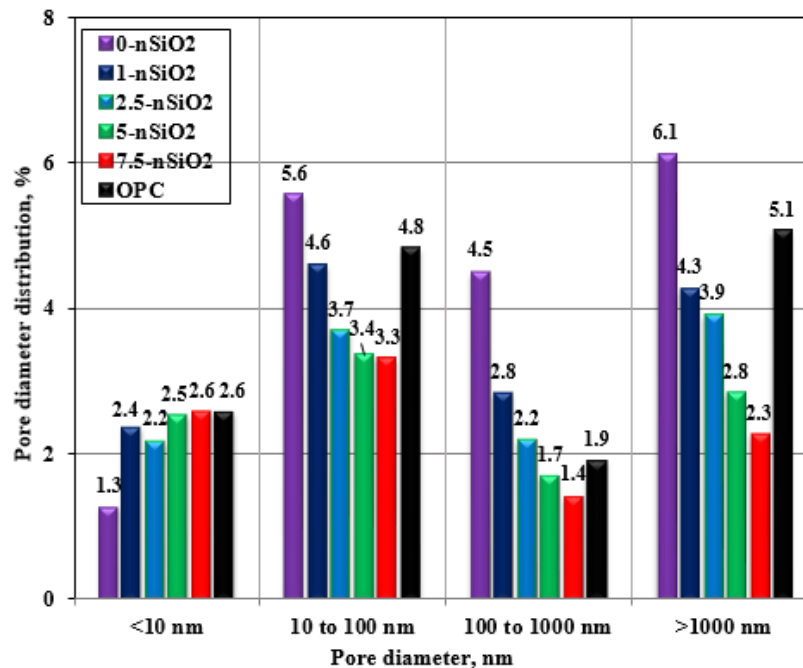


Figure 4. Contributive porosity of concrete after 90 days of curing.

Table 6. Cumulative pore volume in the concrete.

Mix #	Cumulative pore volume, %	
	28-days	90-days
OPC	15.05	14.34
0 %-nanosilica	18.35	17.43
1 %-nanosilica	15.49	14.03
2.5 %-nanosilica	13.45	11.92
5 %-nanosilica	11.86	10.39
7.5 %-nanosilica	11.23	9.53

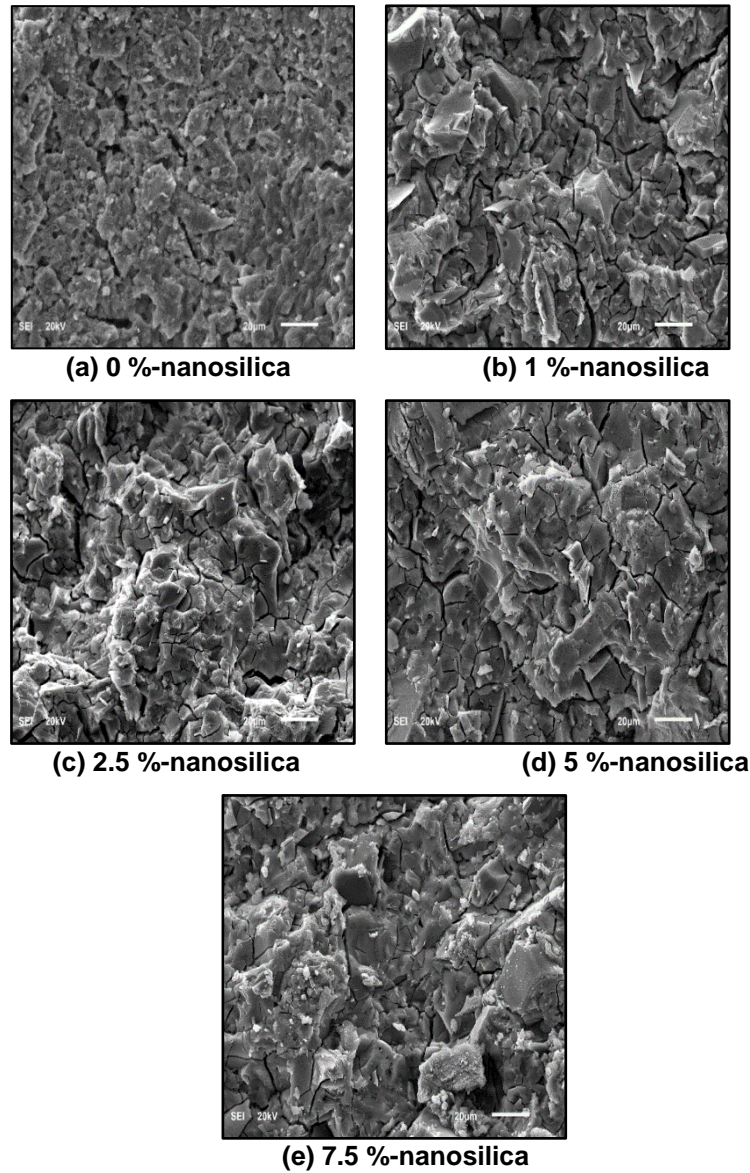


Figure 5(a-e). Micrographs of AAC incorporating nanosilica.

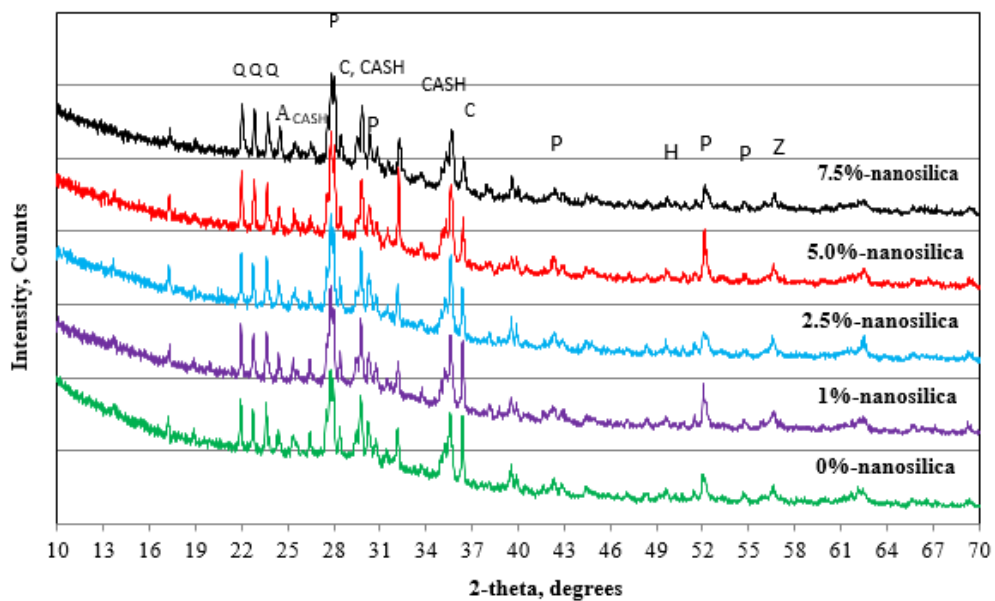


Figure 6. XRD of different AABs incorporating nanosilica. (Q:Quartz, CASH: Calcium Alumina Silicate Hydrate, P; Philipsite, C: Calcite, Z; Zeolite Y, A; Aluminosilicate, H; Hematite).

Table 5. Mechanical properties of various AAC mixes.

Mix #	Compressive strength, MPa			Flexural strength, MPa		Modulus of Elasticity, GPa	
	7d	28d	90d	28d	90d	28d	90d
OPC	24.3	35.5	36.3	4.5	4.6	24.4	25.1
0 %-nanosilica	13.8	25.5	27.9	3.9	4.9	13.8	14.5
1 %-nanosilica	14.2	28.4	31.4	4.2	5.1	15.2	15.9
2.5 %-nanosilica	11.6	29.8	36.3	4.9	5.5	16.0	18.1
5 %-nanosilica	9.4	45.0	60.6	6.2	7.5	24.0	28.7
7.5 %-nanosilica	7.8	38.0	58.8	6.1	7.6	19.4	27.0

3.3. Influence of nanosilica on the durability of concrete

The water absorption and volume of permeable voids are among the very important durability characteristics of the hardened concrete. Water absorption in the range of 3 % to 6 % is generally categorized as good concrete suitable for structural applications. The water absorption of hardened AAC prepared by combination of NP and nanosilica after 28 and 90 days of room curing is shown in Fig. 7. It decreased as the nanosilica content increased in the mix. It was in the range of 4.20 % to 5.89 % and 3.52 % to 5.15 % after 28 days and 90 days of curing, respectively. As expected, the water absorption reduced when the curing progressed from 28 days to 90 days. The maximum value of 5.12 % was recorded in the AAC mixture prepared without nanosilica, while it was about 4.85 %, 4.82 %, 3.52 % and 3.45 %, respectively, in the concrete mixes containing 1 %, 2.5 %, 5 % and 7.5 % nanosilica after 90 days of room temperature curing.

The results of volume of permeable voids are shown in Fig. 8 which appears to be following similar trend as water absorption. The volume of permeable voids tended to lower linearly with an increase in nanosilica content. The water absorption and volume of permeable voids in the OPC based concrete was more or less similar to the results obtained for the AAC prepared with lower level of nanosilica. However, the percentage of water absorption and volume of permeable voids of the AAC prepared with 5 % and 7.5 % nanosilica was considerably lower than that of the OPC concrete as well as the control alkali activated mix.

The results support the notion developed in SEM analysis (Fig 5) wherein enhancement in the microstructure was evident owing to the refinement in the pore structure attributed to the greater enrichment and intertwining of the polymeric compound in the nanosilica modified concrete (Fig. 6). These trends were reflected on the chloride permeability and migration coefficient data. There was reduction in the chloride permeability and the coefficient of chloride migration with an increase in nanosilica content, as summarized in Table 7. The chloride permeability was between 343 and 579 Coulombs in the various AAC mixes after 28 days of ambient curing, which obviously reduced with the continuation of curing up to 90 days. The lowest permeability was observed in the AAC prepared with highest nanosilica content. Similar trend was observed in the case of chloride migration coefficient. It was in the range of 6.93 to 16.68 ($\times 10^{-12}$) m^2/s in the AAC after 28 days of curing, lowest in the 7.5 % nanosilica and highest in the control AAC mix.

However, the chloride permeability was lower in the OPC concrete compared to any AAC mix investigated in this study. Nonetheless, the chloride migration coefficient in the conventional OPC concrete was comparable to the 2.5 % nanosilica mixture. When the chloride permeability was carried out using 60V potential based on ASTM C1202, the charge passed was estimated to be about 8250 Coulombs in the fly ash based AAC reported by Thomas et al. [71]. The authors have expressed concern about the heat generation in the chloride permeability cell. However, inclusion of GGBFS in the binder improved the results. A free chloride diffusion coefficient in the fly ash based binder was more than 38 ($\times 10^{-12}$) m^2/s , while between 6 and 8 ($\times 10^{-12}$) m^2/s was measured in the GGBFS modified concrete [71]. A study conducted by Ravikumar and Neithalath [72] reported a chloride migration coefficient of about 7 ($\times 10^{-12}$) m^2/s for a GGBFS content of 400 kg/m³ activated with an alkaline activator having silica modulus of 1.5. Hence, the results obtained in this study are in compliance to the results reported in the earlier studies.

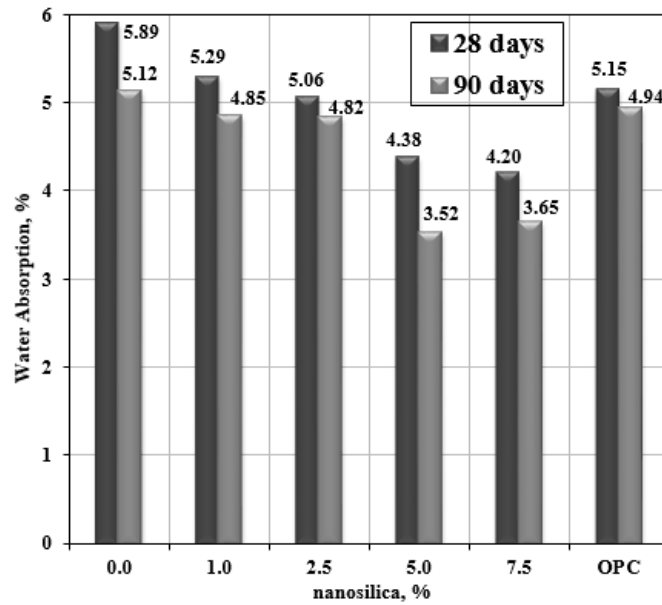


Figure 7. Water absorption of concrete.

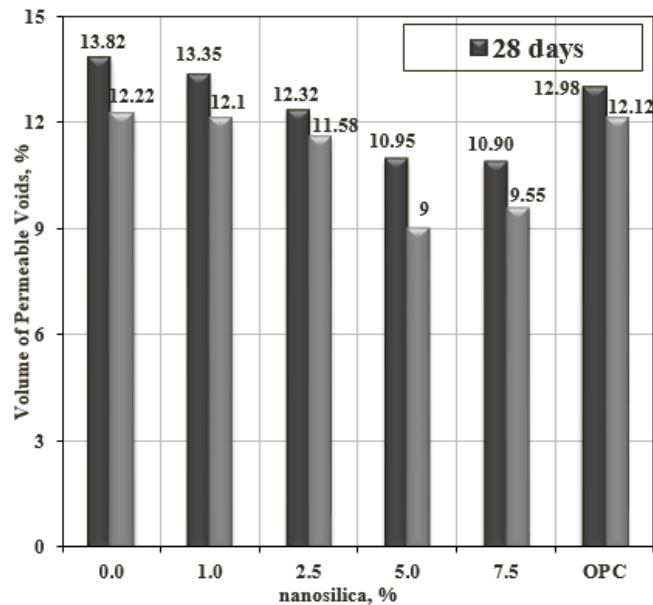


Figure 8. Volume of permeable voids of concrete.

Table 7. Chloride permeability and migration coefficients in the AAC.

Mix #	Chloride permeability, Coulombs		Chloride migration coefficient, $m^2/s (\times 10^{-12})$	
			28d	
	28d	90d	28d	90d
OPC	337	323	12.43	10.44
0 %-nanosilica	579	551	16.68	12.83
1 %-nanosilica	549	527	14.67	12.63
2.5 %-nanosilica	479	456	11.74	10.52
5 %-nanosilica	348	327	8.70	7.83
7.5 %-nanosilica	343	322	6.93	6.22

4. Conclusions

The objective of this study was to evaluate the fresh and hardened properties of natural pozzolan (NP)-based alkali activated concrete (AAC) synthesized at low temperature curing. The effect of nanosilica was studied by substituting varying nanosilica dosages up to 7.5 %. Following conclusions could be drawn:

- There was positive impact of admixing up to 2.5 % of nanosilica on the workability due to lubricating effect provided by nanosilica and thereafter the mix tend to stiffen.
- The setting times were retarded with increment in nanosilica content ascribed to the slow dissolution of Si and Al from the precursor material as well as reduction in CaO content present in NP.
- The incorporation of nanosilica significantly improved the microstructure which consequently refined the pore structure by reducing voids and increasing the gel pores. There was increased absorption of Ca and Al attributed to enhancement in the polycondensation process. The formation of philipsite whose structure is similar to C/N-A-S-H contributed to strength skeleton.
- It is postulated that the synergism of NP and up to 5 % of nanosilica significantly improves the mechanical properties, whereas up to 7.5 % nanosilica is beneficial for enhancing the durability characteristics due to both chemical as well as physical influence on the binder structure.

It is envisioned that the effect of other nano materials, such as nano-alumina in improving the pore structure of NP-based AAB may also be interesting and further add value to the literature.

5. Acknowledgment

The authors gratefully acknowledge the Center for Engineering Research (CER) of the Research Institute and Center for Integrative Petroleum Research, King Fahd University of Petroleum and Minerals, Dhahran, Saudi Arabia.

References

1. Ankur, M., Rafat, S. An overview of geopolymers derived from industrial by-products. *Constr. Build. Mater.* 2016. 127. Pp. 183–198.
2. Galishnikova, V.V., Abdo, Sh., Fawzy, A.M. Influence of silica fume on the pervious concrete with different levels of recycled aggregates. *Magazine of Civil Engineering.* 2020. 93(1). Pp. 71–82. DOI: 10.18720/MCE.93.7
3. Ryu, G.S., Lee, Y.B., Koh, K.T., Chung, Y.S. The mechanical properties of fly ash based geopolymer concrete with alkaline activators, *Constr. Build. Mater.* 2013. 47. Pp. 409–418.
4. Davidovits, J. Geopolymer chemistry and sustainable development – the poly(sialate) terminology: a very useful and simple model for the promotion and understanding of green-chemistry, in: J. Davidovits (Ed.), *Proceedings of the World Congress Geopolymer*, Saint Quentin, France, 2005. 69–73.
5. Adewumi, A.A., Ismail, M., Ariffin, M.A.M., Yusuf, M.O., Maslehuddin, M., Mohamed, H.D. Strength and microstructure of alkali-activated natural pozzolan and limestone powder mortar. *Magazine of Civil Engineering.* 2019. 92(8). Pp. 36–47. DOI: 10.18720/MCE.92.3
6. Yusuf, M.O., Megat Johari, M.A., Ahmad, Z.A., Maslehuddin, M. Strength and microstructure of alkali-activated binary blended binder containing palm oil fuel ash and ground blast-furnace slag. *Construction and Building Materials.* 2014. 52. Pp. 504–510.
7. Sharonova, O.M., Yumashev, V.V., Solovyov, L.A., Anshits, A.G. The fine high-calcium fly ash as the basis of composite cementing material. *Magazine of Civil Engineering.* 2019. 91(7). Pp. 60–72. DOI: 10.18720/MCE.91.6
8. Noushini, A., Castel, A. Performance-based criteria to assess the suitability of geopolymer concrete in marine environments using modified ASTM C1202 and ASTM C1556 methods. *Materials and Structures.* 2018. 51(146). Pp. 1–16.
9. Dvorkin, L.I. The Influence of Polyfunctional Modifier Additives on Properties of Cement-Ash Fine-Grained Concrete. *Magazine of Civil Engineering.* 2020. 93(1). Pp. 121–133. DOI: 10.18720/MCE.93.10
10. Tayeh, B.A., Al Saffar, D.M., Aadi, A.S., Almeshal, I. Sulphate resistance of cement mortar contains glass powder. *Journal of King Saud University: Engineering Sciences.* 2019.
11. Tayeh, B.A., Hasaniyah, M.W., Zeyad, A.M., Awad, M.M., Alaskar, A., Mohamed, A.M., Alyousef, R. Durability and mechanical properties of seashell partially-replaced cement. *Journal of Building Engineering.* 2020. 101328.
12. Nasir, M., Megat Johari, M.A., Maslehuddin, M., Yusuf, M.O. Sulfuric acid resistance of alkali/slag activated silico-manganese fume-based mortars. *Structural Concrete.* 2020. 2020b. Pp. 1–15. DOI: 10.1002/suco.201900543
13. Nasir, M., Megat Johari, M.A., Maslehuddin, M., Yusuf, M.O. Sulfuric acid resistance of alkali/slag activated silico-manganese fume-based mortars. *Structural Concrete.* 2020. 2020c. Pp. 1–15. DOI: 10.1002/suco.202000079
14. Nasir, M., Johari, M.A.M., Yusuf, M.O., Maslehuddin, M., Al-Harathi, M.A., Dafalla, H. Impact of Slag Content and Curing Methods on the Strength of Alkaline-Activated Silico-Manganese Fume/Blast Furnace Slag Mortars. *Arabian Journal for Science and Engineering.* 2019. 44(10). Pp. 8325–8335.
15. Nasir, M., Johari, M.A.M., Maslehuddin, M., Yusuf, M.O., Al-Harathi, M.A. Influence of heat curing period and temperature on the strength of silico-manganese fume-blast furnace slag-based alkali-activated mortar. *Construction and Building Materials.* 2020. 251. 118961.
16. Temuujin, J., Williams, R., van Riessen, A. Effect of mechanical activation of fly ash on the properties of geopolymer cured at ambient temperature. *Journal of Materials Processing Technology.* 2009. 209(12-13). Pp. 5276–5280. DOI: 10.1016/j.jmatprotec.2009.03.016

17. Somna, K., Jaturapitakkul, C., Kajitvichyanukul, P., Chindaprasirt, P. NaOH activated ground fly ash geopolymer cured at ambient temperature. *Fuel*. 2011. 90(6). 21182124. DOI: 10.1016/j.fuel.2011.01.018
18. Nasir, M., Johari, M.A.M., Yusuf, M.O., Maslehuddin, M., Al-Harthi, M.A. Synthesis of Alkali-Activated Binary Blended Silico-Manganese Fume and Ground Blast Furnace Slag Mortar. *Journal of Advanced Concrete Technology*. 2019. 17(12). Pp. 728–735.
19. Nath, P., Sarker, P.K. Effect of GGBFS on setting, workability and early strength properties of fly ash geopolymer concrete cured in ambient condition. *Construction and Building Materials*. 2014. 66. Pp. 163–171.
20. Kumar, S., Kumar, R., Mehrotra, S.P. Influence of granulated blast furnace slag on the reaction, structure and properties of fly ash based geopolymer. *Journal of Materials Science*. 2010. 45(3). Pp. 607–615. DOI: 10.1007/s10853-009-3934-5
21. De Silva, P., Sagoe-Crenstil, K., Sirivivatnanon, V. Kinetics of geopolymerization: Role of Al_2O_3 and SiO_2 . *Cement and Concrete Research*. 2007. 37(4). Pp. 512–518. DOI: 10.1016/j.cemconres.2007.01.003
22. Granizo, M.L., Alonso, S., Blanco-Varela, M.T., Palomo, A. Alkaline Activation of Metakaolin: Effect of Calcium Hydroxide in the Products of Reaction. *Journal of the American Ceramic Society*. 2002. 85(1). Pp. 225–231. DOI: 10.1111/j.1151-2916.2002.tb00070.x
23. Dombrowski, K., Buchwald, A., Weil, M. The influence of calcium content on the structure and thermal performance of fly ash based geopolymers. *Journal of Materials Science*. 2007. 42(9). Pp. 3033–3043. DOI: 10.1007/s10853-006-0532-7
24. Yip, C.K., Lukey, G.C., Provis, J.L., van Deventer, J.S.J. Effect of calcium silicate sources on geopolymerisation. *Cement and Concrete Research*. 2008. 38(4). Pp. 554–564. DOI: 10.1016/j.cemconres.2007.11.001
25. Jayapalan, A.R., Lee, B.Y., Kurtis, K.E. Can nanotechnology be 'green'? Comparing efficacy of nano and microparticles in cementitious materials. *Cement and Concrete Composites*. 2013. 36. Pp. 16–24.
26. Balaguru, P., Chong, K. Nanotechnology and Concrete: Research Opportunities. *Proceedings of ACI Session on Nanotechnology of Concrete: Recent Developments and Future Perspectives*. Denver, USA, Nov. 7, 2006.
27. Jo, B., Park, J., Tae, G., Kim, C. Characteristics of cement mortar with nano- SiO_2 particles. *Construction and Building Materials*. 2007. 21. Pp. 1351–1355.
28. Ozyildirim, C., Zegetosky, C. Exploratory Investigation of Nanomaterials to Improve Strength and Permeability of Concrete. *Journal of the Transportation Research Board*. 2010. Pp. 1–8.
29. Hosseini, P., Booshehrian, A., Farshchi, S. Influence of Nano- SiO_2 Addition on Microstructure and Mechanical Properties of Cement Mortars for Ferrocement. *Journal of the Transportation Research Board*. 2010. Pp. 15–20.
30. Belkowitz, J.S. An Investigation of Nano Silica in the Cement Hydration Process. MSc thesis. University of Denver, 2009.
31. Amiri, B., Bahari, A., Nik, A.S., Movahedi, N.S. Use of AFM technique to study the nanosilica effects in concrete mixture. *Indian Journal of Science and Technology*. 2012. 5(2). Pp. 2055–2059.
32. Polat, R., Demirboğa, R., Karagöl, F. Mechanical and physical behavior of cement paste and mortar incorporating nano-CaO. *Structural Concrete*. 2019. 20(1). Pp. 361–370.
33. Nazari, A., Riahi, S. Microstructural, thermal, physical and mechanical behavior of the self-compacting concrete containing SiO_2 nanoparticles. *Materials Science and Engineering A*. 2010. 527. Pp. 7663–7672.
34. Qing, Y., Zenan, Z., Deyu, K., Rongshen, C. Influence of nano- SiO_2 addition on properties of hardened cement paste as compared with silica fume. *Construction and Building Materials*. 2007. 21. Pp. 539–545.
35. Phoo-Ngernkham, T., Chindraprasirt, P., Sata, V., Hanjitsuwan, S., Hatanaka, S. The effect of adding nanosilica and nano- Al_2O_3 on properties of high calcium fly ash geopolymer cured at ambient temperature. *Materials and Design*. 2014. 55. Pp. 58–65.
36. Adak, D., Sarkar, S., Mandal, S. Effect of nano silica on strength and durability of fly ash based geopolymer mortar. *Construction and Building Materials*. 2014. 70. Pp. 453–459.
37. Ibrahim, M., Megat Johari, M.A., Kalimur Rahman, M., Maslehuddin, M. Effect of alkaline activators and binder content on the properties of natural pozzolan-based alkali activated concrete. *Construction and Building Materials*. 2017. 147. Pp. 648–660. DOI: 10.1016/j.conbuildmat.2017.04.163
38. Ibrahim, M., Megat Johari, M.A., Maslehuddin, M., Kalimur Rahman, M. Influence of nano- SiO_2 on the strength and microstructure of natural pozzolan based alkali activated concrete. *Construction and Building Materials*. 2018. 173. Pp. 573–585.
39. Ibrahim, M., Megat Johari, M.A., Rahman, M.K., Maslehuddin, M., Hatim, D.M. Enhancing the engineering properties and microstructure of room temperature cured alkali activated natural pozzolan based concrete utilizing nanosilica. *Construction and Building Materials*. 2018. 189. Pp. 352–365.
40. Ibrahim, M., Megat Johari, M.A., Maslehuddin, M., Kalimur Rahman, M., Salami, B.A., Hatim Dafalla, M. Influence of composition and concentration of alkaline activator on the properties of natural-pozzolan based green concrete. *Construction and Building Materials*. 2019. 201. Pp. 186–195.
41. Ibrahim, M., Megat Johari, M.A., Hussaini, S.R., Kalimur Rahman, M., Maslehuddin, M. Influence of pore structure on the properties of green concrete derived from natural pozzolan and nanosilica. *Journal of Sustainable Cement-Based Materials*. 2020. Pp. 1–26.
42. ASTM C33-10, Standard Specification for Concrete Aggregates, ASTM International, West Conshohocken, PA, 2010.
43. ASTM C1437, 2010. Standard Test Method for Flow of Hydraulic Cement Mortar, ASTM International, West Conshohocken, PA.
44. ASTM C403, 2010. Standard Test Method for Time of Setting of Concrete Mixtures by Penetration Resistance, ASTM International, West Conshohocken, PA.
45. Ji, Y.L., Sun, Z.P., Yang, X. Assessment and mechanism study of bleeding process in cement paste by 1H low-field NMR. *Construction and Building Materials*. 2015. 100. Pp. 255–261.
46. Wang, Y., Yuan, Q., Deng, D., Ye, T., Fang, L. Measuring the pore structure of cement asphalt mortar by nuclear magnetic resonance. *Construction and Building Materials*. 2017. Pp. 450–458.
47. ASTM C109, 2010, Standard Test Method for Compressive Strength of Hydraulic Cement Mortars (Using 2-in. or [50-mm] Cube Specimens), ASTM International, West Conshohocken, PA, 2010.
48. ASTM C78-10, Standard Test Method for Flexural Strength of Concrete (Using Simple Beam with Third-Point Loading), ASTM International, West Conshohocken, PA, 2010.
49. ASTM C469, 2010, Standard Test Method for Static Modulus of Elasticity and Poisson's Ratio of Concrete in Compression, ASTM International, West Conshohocken, PA, 2010.
50. ASTM C642, 2010. Standard Test Method for Density, Absorption, and Voids in Hardened Concrete, ASTM International, West Conshohocken, PA.

51. NTBUILD-492, NORDTEST METHOD: Concrete, Mortar And Cement-Based Repair Materials: Chloride Migration Coefficient From Non-Steady-State Migration Experiments. 2010.
52. Mallikarjuna Rao, G., Gunneswara Rao, T.D. Final Setting Time and Compressive Strength of Fly Ash and GGBS-Based Geopolymer Paste and Mortar. *Arabian Journal for Science and Engineering*. 2015. 40. Pp. 3067–3074.
53. ASTM C191, 2010. Standard Test Methods for Time of Setting of Hydraulic Cement by Vicat Needle, ASTM International, West Conshohocken, PA.
54. Teixeira-Pinto, A., Fernandes, P., Jalali, S. Geopolymer Manufacture and Application – Main problems when using concrete technology. *Geopolymers*. International Conference, Melbourne, 2002. Australia, Siloxo Pty. Ltd.
55. Fernández-Jiménez, A., Palomo, A. Composition and microstructure of alkali activated fly ash binder: effect of the activator. *Cement and Concrete Research*. 2005. 35(10). Pp. 1984–1992. DOI: 10.1016/j.cemconres.2005.03.003
56. Haha, M.B., Lothenbach, B., Le, S.G., Winnefeld, F. Influence of slag chemistry on the hydration of alkali-activated blast-furnace slag-Part II: Effect of Al_2O_3 . *Cement and Concrete Research*. 2012. 42(1). Pp. 74–83. DOI: 10.1016/j.cemconres.2011.05.002
57. Deir, E., Gabreziabihier, B.S., Peethamparan, S. Influence of starting material on the early age hydration kinetics, microstructure and composition of binding gel in alkali activated binder systems. *Cement and Concrete Composites*. 2014. 48. Pp. 108–117. DOI: 10.1016/j.cemconcomp.2013.11.010
58. Gao, X., Yu, Q.L., Brouwers, H.J.H. Characterization of alkali activated slag–fly ash blends containing nano-silica. *Construction and Building Materials*. 2015. 98. Pp. 397–406.
59. Duxson, P., Fernández-Jiménez, A., Provis, J.L., Lukey, G.C., Palomo, A., Van Deventer J.S.J. Geopolymer technology: the current state of the art. *Journal of Materials Science*. 2007. 42(9). Pp. 2917–2933.
60. Yokoyama, Y., Yokoi, T., Ihara, J. The effects of pore size distribution and working techniques on the absorption and water content of concrete floor slab surfaces. *Construction and Building Materials*. 2014. 50(1). Pp. 560–566.
61. Rodriguez, E.D., Bernal, S.A., Provis, J.L., Paya, J., Monzo, J.M., Borrachero, M.V. Effect of nanosilica-based activators on the performance of an alkali-activated fly ash binder. *Cement and Concrete Composites*. 2013. 35. Pp. 1–11.
62. Zuo, Y., Ye, G. Pore structure characterization of sodium hydroxide activated slag using mercury intrusion porosimetry, nitrogen adsorption, and image analysis. *Materials*. 2018. 11. 1035. DOI: 10.3390/ma11061035
63. Shaikh, F., Chavda, V., Minhaj, N., Arel, H.S. Effect of mixing methods of nano silica on properties of recycled aggregate concrete. *Structural Concrete*. 2019. 19(2). Pp. 387–399.
64. Juhuyuk, M.A., Sungchul, B.B., Celik, K.B., Yoon, S.B., Ki-Hyun, K.B., Kang, S.K.C., Paulo, J.M., Monteiro, B. Characterization of natural pozzolan-based geopolymeric binders. *Cement and Concrete Composites*. 2014. 53. Pp. 97–104.
65. Chen, W., Li, B., Li, Q., Tian, J. Effect of polyaluminum chloride on the properties and hydration of slag cement paste. *Construction and Building Materials*. 2016. 124. Pp. 1019–1027.
66. Li, Z., Wang, H., He, S., Lu, Y., Wang, M. Investigations on the preparation and mechanical properties of the nano-alumina reinforced cement composite. *Materials Letters*. 2006. 60. Pp. 356–359.
67. Barbhuiya, S., Mukherjee, S., Nikraz, H. Effects of nano- Al_2O_3 on early-age microstructural properties of cement paste. *Construction and Building Materials*. 2014. 52. Pp. 189–193.
68. Provis, J.L., van Deventer, J.S.J. *Geopolymers: structures, processing, properties and industrial applications*. Elsevier, 2009.
69. Yip, C.K., Lukey, G.C., Van Deventer, J.S.J. Coexistence of geopolymeric gel and calcium silicate hydrate at the early stage of alkali activation. *Cement and Concrete Research*. 2005. 35. Pp. 1688–1697.
70. Yip, C.K., Van Deventer, J.S.J. Microanalysis of calcium silicate hydrate gel formed within a geopolymeric binder. *Journal of Material Science* 2003. 38. Pp. 3851–3860.
71. Thomas, R.J., Ariyachandra, E., Lezama, D., Peethamparan, S. Comparison of chloride permeability methods for Alkali-Activated concrete. *Construction and Building Materials*. 2018. 165. Pp. 104–111.
72. Ravikumar, D., Neithalath, N. An electrical impedance investigation into the chloride ion transport resistance of alkali silicate powder activated slag concretes. *Cement and Concrete Research*. 2013. 44. Pp. 58–68.

Contacts:

Mohammed Ibrahim, ibrahim@kfupm.edu.sa

Muhammad Nasir, mnmuhammad@iau.edu.sa

Syed Rizwanullah Hussaini, rsyed@kfupm.edu.sa

Syed Khaja Najamuddin, sknajam@kfupm.edu.sa

Adeoluwa Ewebajo, adeoluwaewebajo@gmail.com



DOI: 10.34910/MCE.107.11

Properties of fine-grained concrete containing fly ash and bottom ash

S. Nguyen^a, Q. Thai^a, L. Ho^{*b,c} 

^a University of Transport and Communications, Hanoi, Viet Nam

^b University of Transport Technology, Hanoi, Viet Nam

^c Hiroshima University, Civil and Environmental Engineering Program, Graduate School of Advanced Science and Engineering, Hiroshima, Japan.

*E-mail: lanhhs@utt.edu.vn

Keywords: fly ash, bottom ash, fine-grained concrete, water absorption, chloride penetration, compressive strength, splitting tensile strength

Abstract. In the present paper, large amounts of bottom ash (BA) and fly ash (FA) in a Vung Ang thermal power plant in Vietnam were used to substitute crushed sand (CS) to produce fine-grained concrete. The FA content was fixed at 20 %, the BA content increased from 20 % to 50 % corresponding to the CS content decreased from 60 % to 30 %. Four mixtures of fine-grained concrete were prepared to produce concrete. It was found that the compressive and splitting tensile strengths decreased when the amount of FA and BA increased from 40 % to 70 %. The compressive and the splitting tensile strengths were comparable to those in conventional concrete containing bottom ash. The larger content of bottom ash caused higher water absorption and resulted in lower chloride resistance, which is because of the porous structure of BA. Based on the results of chloride resistance, this fine-grained concrete is classified as moderately permeable concrete. The results of this study indicated that crushed sand (fine aggregate) of fine-grained concrete can be replaced by fly ash incorporated with bottom ash up to 60 % and this fine-grained concrete can be applied for construction works as conventional concrete.

1. Introduction

Industrial wastes discharged from the thermal power plant or cement factories such as fly and bottom ashes have increased rapidly and threatened the environment. A large amount of these industrial wastes are available in many countries, especially in developing countries as Vietnam. [1–6]. It was reported that the volume of these ashes released from the thermal power plant, annually, is approximately 25 million tons, and it is expected to be 40 million tons by 2030 [7]. Bottom ash content accounts for approximately 20-25 % of the total amount of these ashes [8], and the particle size of this bottom ash has a similar size compared to that of natural fine sand i.e. river sand [2, 6, 8–11]. If these bottom and fly ashes are not used, a large area of land is needed for dumping. This also causes environmental issues like heavy metal leaching [2, 6, 8]. Therefore, authors in the field have tried to capitalize fly and bottom ash instead of partially cement and fine aggregate to benefit both economic and environmental matters [5, 12–14].

Fly ash, a by-product is known as a pozzolanic material that consists of a high amount of silica like in silica fume or rice husk ash [15–19]. Thus, fly ash has been extensively employed in the concrete field in order to enhance concrete properties in the long term such as compressive strength and chloride resistance [20–23]. On the other hand, although previous studies found that bottom ash has a low pozzolanic reaction, it does not have a negative impact on the strength development of concrete when an



appropriate amount for replacing for aggregate is used [11]. Many researchers have revealed that bottom ash could be utilized in pervious concrete or high-strength concrete, as fine aggregate [24–26].

In cement concrete, coarse aggregate takes a crucial role as a main component. However, the sources of the coarse aggregate are becoming scarce, thus, exploring a new ingredient to take the place of coarse aggregate is now essential. Natural or crushed sand has been using as a new material for replacing coarse aggregate in fine-grained concrete manufacturing (sand concrete) [3, 27, 28]. This fine-grain concrete is found to gain the same compressive strength as conventional concrete. The fine-sand concrete is considered to be fine aggregate concrete, whereas coarse aggregate is substituted by fine sand and filler material, respectively [4, 29–31]. The previous study indicated that fine-sand concrete can have comparable high compressive strength as well as durability as those of high strength concrete [4]. In addition, due to the scarcity of natural resources of river sand, researchers in the field have attempted to use fine sand, dune sand, and saline sand to replace river sand in fine-grained concrete [29, 32].

As previously discussed, bottom ash possesses a grain size, which is comparable to river sand, thus, it could be used as a new material for the replacement of fine aggregate (river sand and crushed sand). Besides, previous studies reported that bottom ash has a porous structure that could have advantages in reducing concrete shrinkage [33, 34], because of its high water absorption ability that could produce an internal curing effect [10, 35, 36]. Bottom ash has been popularly utilized in conventional concrete in many previous studies [2, 3, 6, 14, 26, 37, 38]. They found that using bottom ash could bring both positive and negative effects such as improving compressive and tensile strengths at later age, but reducing chloride resistance or increasing water absorption of concrete [2, 6, 8, 9, 26, 38]. However, to our best knowledge, the substitution of fine and coarse aggregates with a substantial amount of fly ash and bottom ash for producing fine-grained concrete has not been studied so far. Therefore, this study will firstly investigate mechanical characteristics and durability of fine-grained concrete using fly and bottom ash replaced for fine aggregate at a high level. Fly ash and bottom ash in Vung Ang thermal power plant, Vietnam is selected as a case study in this research. The mechanical characteristics are investigated through compressive and splitting tensile strengths and the durability is examined through chloride penetration and water absorption test.

2. Materials and Measurements

2.1. Materials, mixture proportion, and preparation

2.1.1. Materials

Portland cement (PC40), crushed sand (CS), fly ash (FA), bottom ash (BA) were used for producing fine-grained concrete in this study. CS was taken from Phu Ly province that meets ASTM C33 standards on particle size and other properties. FA and BA were sourced from Vung Ang thermal power plant. The chemical composition, as well as physical characteristics of cement, CS, FA, and BA, are presented in Table 1. A Superplasticizer Original Acrylic Polymers (Dynamon BT2) was used as well. The grain size distributions of fly ash, bottom ash, and crushed sand are shown in Fig. 1 and the pictures of these materials are displayed in Fig. 2.

Table 1. Chemical compositions of materials used.

Chemical composition (%)	PC40	FA	BA	Crushed sand
SiO ₂	21.49	53.9	49.59	54.88
Al ₂ O ₃	5.4	21.8	20.14	0.02
Fe ₂ O ₃	3.49	6.7	3.50	0.04
CaO	63.56	4.27	4.13	0.17
MgO	1.40	1.45	1.15	0.45
Na ₂ O	0.12	0.67	0.15	0.02
K ₂ O	0.3	3.4	3.76	0.04
LOI	0.19	6.27	1.45	1.25
Density (g/cm ³)	3.1	2.2	2.34	2.72
Mean particle size (µm)	16.1	26.9	–	–
Blaine SSA (m ² /g)	3730	–	–	–

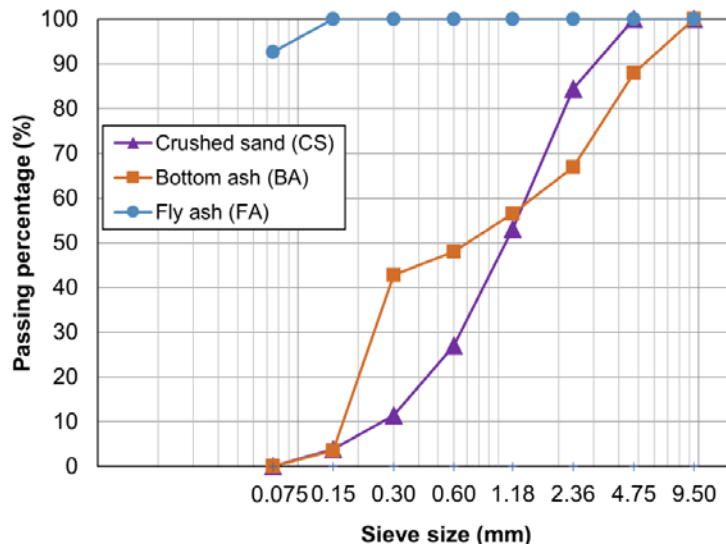


Figure 1. Distribution of particle size of crushed sand, fly ash, and bottom ash.

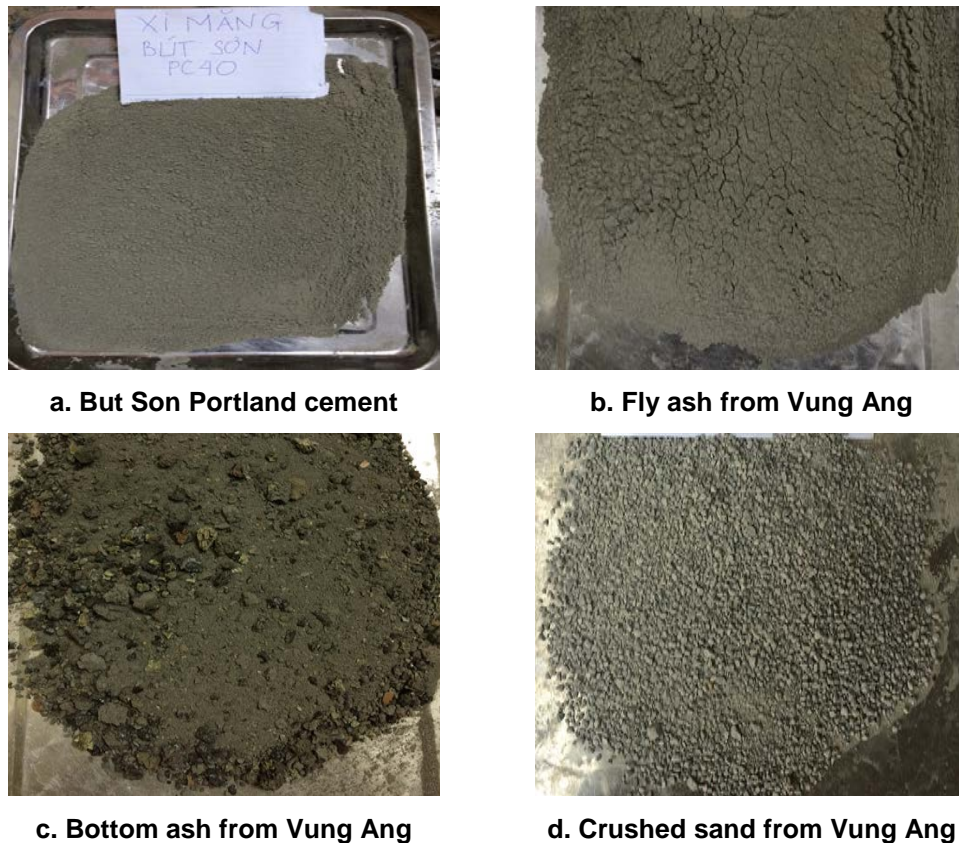


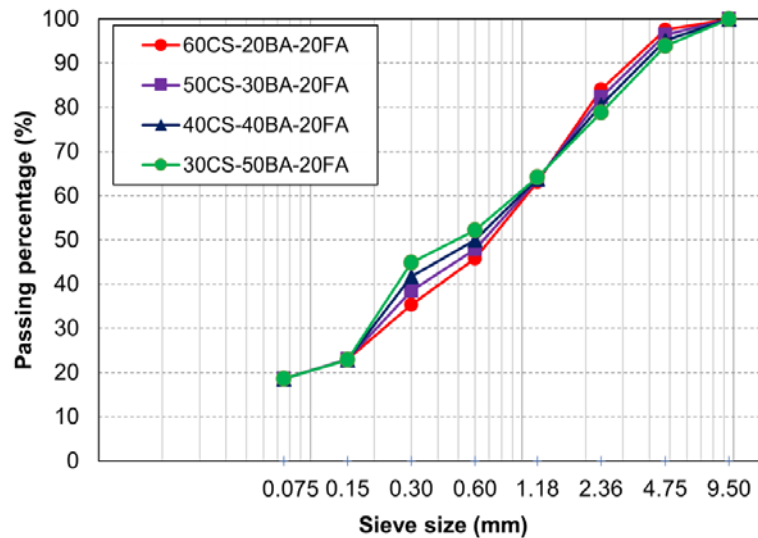
Figure 2. Materials for preparing fine-grained concrete.

2.1.2. Mixture proportions

Fine-grained concretes were prepared based on the absolute volume of the component materials [4]. The water/binder ratio was designed based on ACI 211.1 and ACI 363.2R. A consistent water/binder (w/b) ratio of 0.34 was used in all mixtures. The amount of cement was kept consistent for all mixtures (395 kg/m^3). FA and BA were adopted as a fine aggregate to partially replace the amount of crushed sand: the total amount of FA and BA ranging from 40 % to 70 % of the total weight of aggregate, whereas the amount of FA was fixed at 20 % in order to evaluate the effect of BA content to concrete properties. The amount of superplasticizer (water-reducing agent) was set constantly as 1.8 % by weight of cement. Table 2 shows the proportion of four mixtures and Fig. 3 presents the grain size distributions of all mixtures.

Table 2. Mixing proportion of fine-grained concrete.

Mixture	w/b	Water (kg/m ³)	Cement (kg/m ³)	Fly ash (kg/m ³)	Crushed sand (kg/m ³)	Bottom ash (kg/m ³)	Admixture (kg/m ³)
60CS-20BA-20FA	0.34	135	395	372	1116	372	7.11
50CS-30BA-20 FA	0.34	135	395	363	909	545	7.11
40CS-40BA-20 FA	0.34	135	395	355	710	710	7.11
30CS-50BA-20 FA	0.34	135	395	346	520	866	7.11

**Figure 3. The particle size distribution of different mixtures.**

2.1.3. Preparation and casting of specimens

A mixer is used to produce mixtures with 8 min of mixing for each mixture. Crushed sand, fly ash, bottom ash, and cement were mixed for 2 min in dry condition. After that, approximately 80 % water was added to the mixture and then they were mixed for 2 more min. Consequently, the remaining water combined with superplasticizer was supplied, and then mixed again for 4 min. The specimens used for determining compressive strength were cubed with a size of 70.7 × 70.7 × 70.7 mm, and the cylindrical specimens with a size of 150 × 300 mm were used to determine the splitting tensile strength. While the specimens used for chloride penetration and water absorption tests were also cylinders with a size of 100 × 200 mm. All specimens were cast with two layers using the vibration table, each layer was vibrated for 20 s. After compacting, the top of molds was sealed with polyethylene sheets and cured in a control room with a temperature of 20 °C. After one day, all specimens were demolded and cured in a water bath at 20 ± 2 °C up to designated ages. All tests in this study were conducted in triplicate and the mean value was used.

2.2. Testing of the specimens

2.2.1. Slump flow test

To assess the workability of fine-grained concrete, a slump flow test was conducted. The slump flow test was performed as per ASTM C143 [39]. Fig. 4 shows the measurement method of the test, in which the diameter of the circle reveals the slump value in three measurements.

**Figure 4. Example of measuring the slump flow of fine-grained concrete.**

2.2.2. Compressive strength and splitting tensile strength

To determine the compressive strength of fine-grained concrete, the compression test was conducted by referring to ASTM C39 [40, 41] for the specimens at the ages of 3, 7, and 28 days. The example of the compression test is described in Fig. 5.



Figure 5. Preparation of specimen and compression test.

The splitting tensile strength is one of the important factors, which affects properties of concrete such as controlling cracks, stiffness, bonding capacity to reinforcement, and durability. The splitting tensile strength was conducted based on ASTM C496 on specimens at 3, 7, and 28 days of curing [40, 41]. The pictures of examples of splitting tensile strength are shown in Fig. 6.



Figure 6. Example of the splitting tensile strength test.

2.2.3. Rapid chloride permeability and water absorption

The rapid chloride penetration was applied for the specimens at 28 days according to ASTM C1202-97 [42]. Fig. 7 shows the preparation and example of a chloride penetration test. The classification of chloride resistance can be referred to Table 3.

Table 3. Classification of chloride penetration value according to charge passed [42].

Charge passed (Coulomb)	Chloride ion penetration
> 4000	High
2000-4000	Moderate
1000-2000	Low
100-1000	Very low
< 100	Negligible



Fig. 7. Preparation and example of a chloride penetration test

The water absorption test was conducted as per TCVN 3113-1993 [43]. The experiment was conducted using the specimen at 28 days and an example of the preparation procedure is shown in Fig. 8. The water absorption of each specimen can be calculated by equation 1.

$$H = \frac{(m_1 - m_0) \times 100\%}{m_0}, \quad (1)$$

where: H is the water absorption of each specimen by percentage (%);

m_1 denotes the specimen under saturated condition (g);

m_0 indicates the specimen weight under the dry condition (g).



Figure 8. Soaking and drying concrete samples.

3. Results and Discussion

3.1. Workability and density of the fresh mixture

The slump flow values of different fresh mixtures are shown in Fig. 9. It can be observed that the mixture with 20 % BA (60CS-20BA-20FA) achieved the highest value compared to other mixtures. The increase in the content of bottom ash caused a reduction in the slump flow value. We can see that when the amount of BA grew up from 20 % to 50 %, the slump flow value decreased from 27 to 23 cm. This result concurs with findings in the previous studies on the conventional concrete mixture using bottom ash and rice husk ash [4, 44–46]. As reported in previous studies, bottom ash is a porous material containing meso and macro-pores inside and on the surface of particles, which helps to generate a large surface area and consequently absorb more water [44–46]. Besides, BA has a rough surface with an irregular shape, which causes high friction between particles, resulting in decreasing the slump of the fresh mixture, as indicated in previous studies [6, 8, 24, 26].

Fig. 10 presents the density of different concrete mixtures. Similar to the slump flow, the density of mixtures also reduced with an increase of BA content. This could be explained by porous structure as mentioned above and the lower specific density of BA compared to that of crushed sand as displayed in Table 1. This result is in line with the results of previous studies using BA [1, 6, 8, 24, 26]. In addition, because BA can absorb more mixing water, more and larger pores appear which causes the porous structure of concrete [8]. As a result, when a higher amount of crushed sand is replaced by BA, the unit weight of fresh concrete decreases.

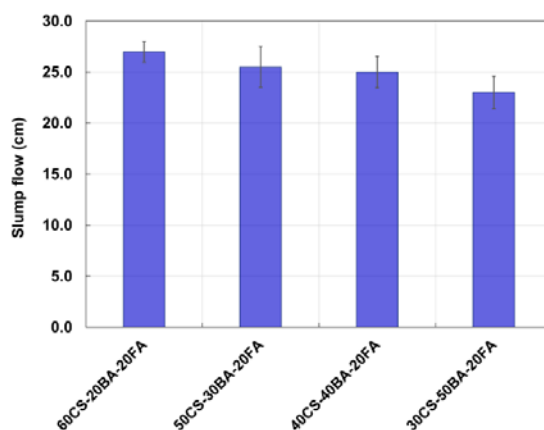


Figure 9. Slump flow of different fresh concrete mixtures.

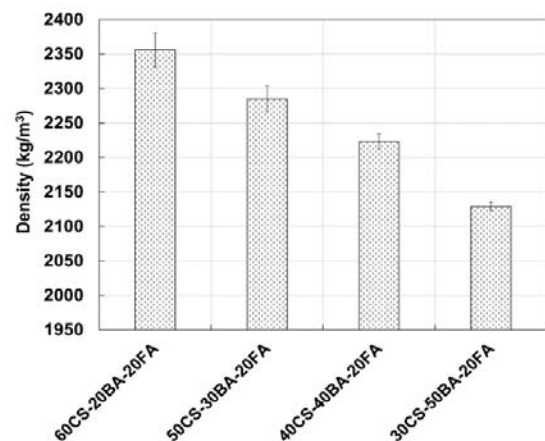


Figure 10. The unit weight of different fresh concrete mixtures.

3.2. Compressive strength and splitting tensile strength

3.2.1. Compressive strength

The compressive strength of different fine-grained concrete mixtures comprising FA and BA at 3, 7, and 28 days are presented in Fig. 11. The results imply that the compressive strength of different mixtures depends on the amount of BA in the mixture, as found in the previous study [45]. The compressive strength increased rapidly from 3 to 7 days, then slower from 7 to 28 days for all mixtures. Mixture with 20 % BA showed the highest values of compressive strength. These values were 27.0, 42.7, 52.7 MPa for the ages of 3, 7, and 28 days, respectively. The lowest values were observed for the mixture with 50 % BA. They were 14.4, 22.1, and 30.1 MPa for the age of 3, 7, and 28 days, respectively. The maximum differences of the compressive strength between the mixture containing 20 % BA and 50 % BA at 3, 7, and 28 days were 46.7 %, 48.2 %, and 42.9 %, respectively. Furthermore, when the amount of bottom ash increased, the compressive strength of concrete decreased for all curing ages, and this is consistent with results in the previous studies [24, 31, 39, 40, 43, 45, 47, 48]. The reason for lowering the compressive strength is similar to what was discussed in the previous section. Firstly, the BA particles are weaker and more porous compared to crushed sand particles [8]. Secondly, because of the larger surface area and porous structures, BA particles absorb higher amount of mixing water, which causes the increase in pore volume due to bleeding and thus lowering the density of fresh concrete. These pores reduce the bonding between aggregate and cement paste, and create a porous and weak interfacial transition zone (ITZ) between them; this resulted in the decreasing of compressive strength [8]. According to Fig. 11, we can see that at 28 days, the compressive strength achieved from is 30.1 to 52.7 MPa for all mixtures. These values of compressive strength are slightly higher than those (27.6–48.3 MPa) of conventional concrete containing bottom ash with similar cement content (ranging from 356 to 475 kg/m³) and water/cement (0.32–0.67) [49]. From these results, it can be concluded that this fine-grained concrete is probably satisfied to use in construction works like conventional concrete.

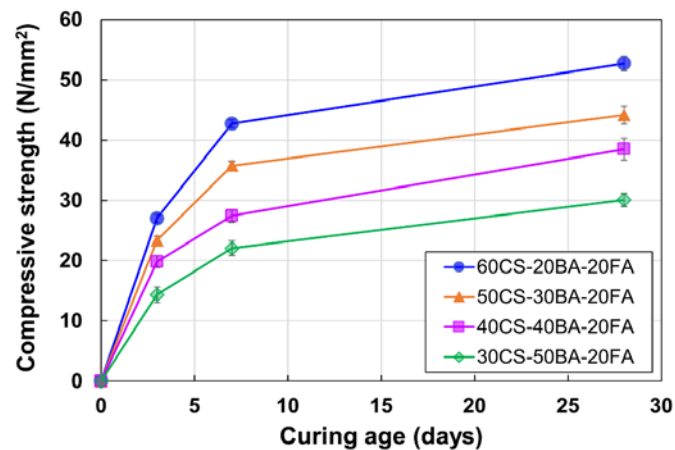


Figure 11. Compressive strength evolution of concrete until 28 days.

3.2.2. Splitting tensile strength

The splitting tensile strength of all mixtures has a similar behavior as obtained in the compressive strength as discussed previously. The splitting tensile strength increased linearly from 3 to 28 days. The highest tensile strength was observed in specimens with 20 % BA content and the lowest value was recorded in specimens with 50 % BA content. The highest values were 2.4, 3.2, and 4.3 MPa found in the mixture with 20 % BA at 3, 7, 28 days, respectively. The lowest values recorded in the mixture with 50 % BA were 1.6, 2.2, and 3.0 MPa for the ages of 3, 7, 28 days respectively. The maximum differences between the mixture containing 20 % BA and 50 % BA at 3, 7, and 28 days were 33.3 %, 31.3 %, and 30.2 %, respectively. These reduction values in the splitting tensile strength were smaller than those in the compressive strength reduction, it thus can be understood that bottom ash has less influence on the splitting tensile strength development than the compressive strength, this result is different from what has been found in the previous studies [8, 49]. This distinctive characteristic is probably attributed to the addition of water-reducing agents and material constituent (the previous study included coarse aggregate). It was indicated that the addition of this admixture could improve the splitting tensile strength [49]. Similar to the compressive, the splitting tensile strength decreased with increasing the amount of bottom ash, which agreed well with earlier studies (Fig. 12) [6, 47, 50, 51]. For example, at the age of 28 days, when the BA amount grew up from 20 % to 50 %, the splitting tensile strength decreased by approximately 30 %. This reduction was much stronger than that (ranging 2.02–15.74 %) in the previous study [6]. It was indicated that the tensile strength is mainly attributed to bonding between aggregate and cement paste [4, 52, 53].

The reduction in the tensile strength is possibly owing to the abundance of FA and BA that can cause porous micro-aggregate and increase porosity [4, 8]. These greatly weaken ITZ between aggregate and cement paste that causes the decrease of tensile strength. From Fig. 12, at 28 days, we can also observe that the splitting tensile strength ranged approximately from 3.0 to 4.3 MPa for all mixtures; this value is almost equal to those of 3.0-4.2 MPa and 3.8-4.3 MPa of self-compacting concrete and concrete comprising bottom ash with similar cement content, (ranging from 356 to 475 kg/m³) respectively in previous studies [49, 52]. It implies that the value of splitting tensile strength of this fine-grained concrete could be satisfied with the requirement of conventional concrete.

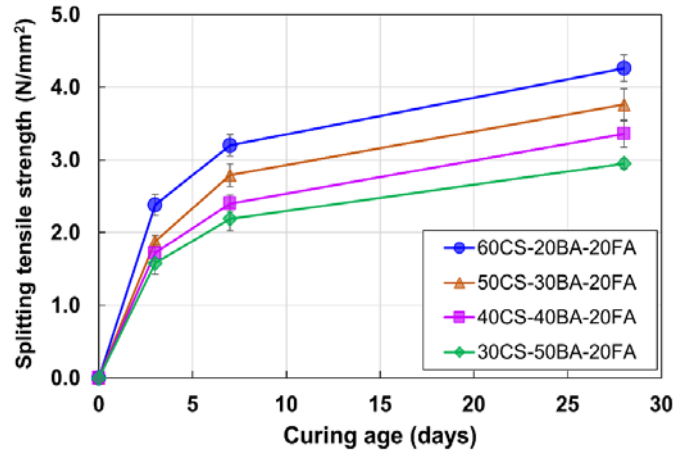


Figure 12. The tensile strength development of different mixtures.

The ratios between compressive/splitting tensile strength are shown in Fig. 13. Generally, the higher amount of FA and BA caused a lower ratio for all curing ages. At 28 days, the highest ratio was 12.4 for the mixture with 20 % BA, whereas the lowest one was 10.2 or the mixture with 50 % BA. Overall, it can be observed that the ratios were in the range of 9.1–13.4, similar to high-performance fine-grained concrete comprising rice husk ash [4] and lower than those (in range 10.5–15.2) of ordinary concrete [54]. It indicates that this fine-grained concrete containing a high amount of FA and BA can have a better splitting tensile strength in comparison with ordinary concrete with the same compressive strength. According to Le et. al [4] the high splitting tensile strength is because crushed sand used as a major aggregate can mitigate wall influence in cement paste and reduce the thickness of ITZ [44, 55].

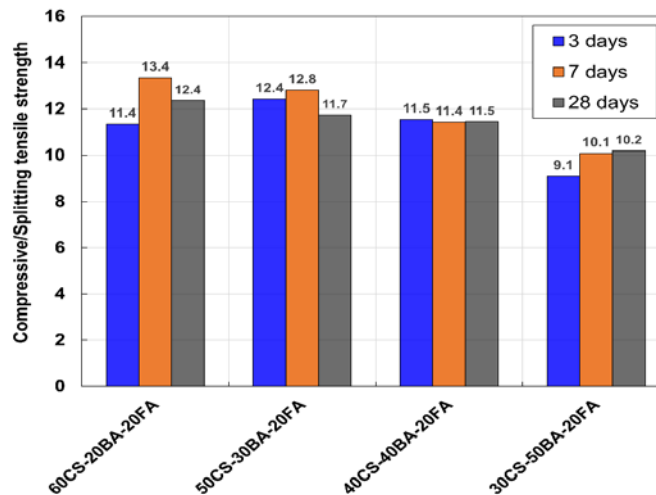


Figure 13. Ratios of compressive/splitting tensile strength.

3.3. Chloride Penetration Resistance and water absorption

3.3.1. Results of the chloride penetration test

In the marine environment, the lifecycle of reinforced concrete structures depends mainly on the degradation due to the corrosion of steel reinforcement resulted by chlorine penetration. It is generally accepted that the durability of mortar and concrete structures are governed by chloride penetration resistance. When the concentration of chloride is higher than a certain threshold, the reinforcement steel bar will be corroded [56, 57]. Thus, it is vital to discover the chloride penetration of this fine-grained concrete.

Fig. 14 shows the results of the rapid chloride test of different mixtures. The values of chloride permeability ranged from 2156 to 2430 coulombs. These values were slightly lower than those observed in

the normal concrete containing similar cement content, water/cement, and amount of water-reducing admixture (416 and 475 kg/m³ cement and water/cement ratio ranging from 0.322–0.526, and water-reducing admixture from 5.67–11.34 kg/m³), and this concrete can be classified as a moderately permeable concrete [49]. In addition, these values were smaller than those of concrete comprising bottom ash in the previous study [10, 49]. It can be observed that chloride permeability values increase when the BA content in the mixture increases from 20 % to 50 %. These results agree well with previous studies [10, 49]. Ghafoori and Bucholc [49] stated that increasing the amount of bottom ash caused increasing chloride penetration of concrete containing bottom ash. The higher chloride permeability found in the mixture with a higher amount of BA can be explained by the porous microstructure of BA and lower fresh density when the amount of bottom ash increase [8].

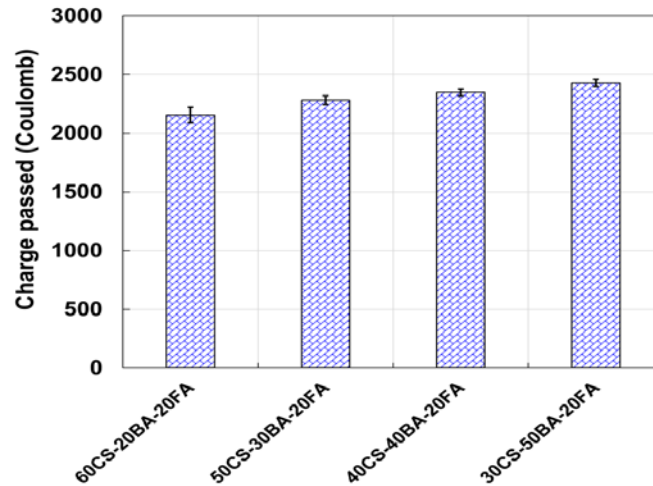


Figure 14. Chloride penetration of different mixtures at the age of 28 days.

3.3.2. Results of water permeability

The water absorption of different mixtures was conducted for the specimen at 28 days is shown in Fig. 15. From the figure, the water absorption ratio increases if the amount of BA is increased. Specifically, the absorption ratio increased from 2.0 to 3.0 % when the amount of BA increased from 20 to 50 %. In other words, the water absorption ratio increased approximately by 50% when the content of BA increased from 20 % to 50 %. This proves that the larger content of bottom ash produced the higher values of the water absorption and it is conformed with previous studies of concrete comprising bottom ash [2, 9, 47, 58]. This is the fact that owing to the porous structure of bottom ash and higher surface area, which caused a higher absorption capacity. As indicated in previous studies, concrete containing bottom ash is more porous compared to normal concrete [2, 9, 47, 58]. The structure of ITZ became porous when fine aggregate (sand) was substituted by bottom ash. Thus, the establishment of a porous structure resulted in a higher water absorption ability. Furthermore, as discussed previously, the increase in the amount of BA led to the decrease of concrete density, due to higher porosity, thus increasing water absorption ability. However, the water absorption values of this fine-grained concrete are smaller than those (4–5 %) of conventional concrete and concrete comprising bottom ash [2, 9, 47, 58]. In summary, these results of water absorption are in line with that of chloride permeability, splitting tensile and compressive strength. These findings also concur with previous studies.

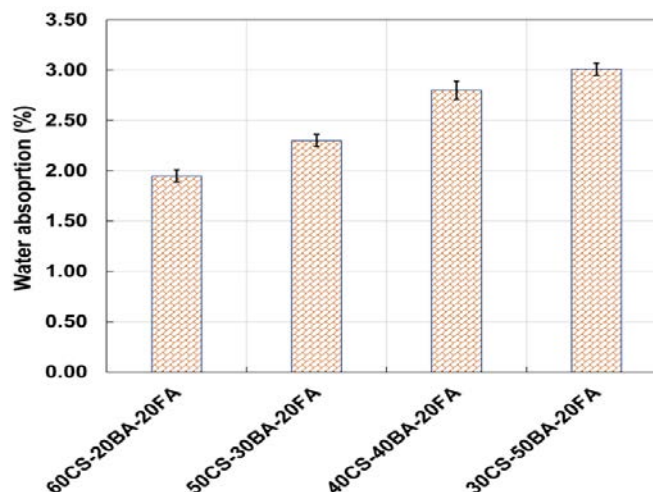


Figure 15. Water absorption of different mixtures.

4. Conclusions

In this research, we investigated mechanical characteristics and durability, namely compressive and splitting tensile strengths, chloride resistance, and water absorption of fine-grained concrete using waste material (fly and bottom ashes) to replace 30 to 60 % of fine aggregates. Some main conclusions could be derived from the experimental results:

- The compressive and splitting tensile strengths decreased with an increasing amount of bottom ash from 20 % to 50 % when the amount of fly ash fixed at 20 %. This is because of the porous structure and large surface area, which could have a high demand of water and create a large pore volume. The mixture with 20 % bottom ash had the highest compressive and splitting tensile strength, while the lowest values were observed in the mixture with 50 % bottom ash.
- The 28 day-compressive strength of this fine-grained concrete was in the range of 30.1 to 52.7 MPa and slightly larger than that of normal concrete; while the splitting tensile strength at 28 days was in the range of 3.0 to 4.3 MPa and almost similar to that of self-compacting concrete and concrete containing bottom ash with the same cement content.
- The values of chloride permeability ranged from 2156 to 2430 coulombs, and the absorption ratio ranged from 2.0 to 3.0 %. These values of chloride permeability and water absorption were almost the same or slightly higher than those of conventional concrete and concrete comprising bottom ash. Based on the results of chloride resistance, this fine-grained concrete is classified as moderately permeable concrete.
- The greater content of bottom ash addition caused the higher water absorption and resulted in the lower chloride resistance; these were caused owing to the coarse structure of bottom ash.
- The results of this study indicated that crushed sand (fine aggregate) of fine-grained concrete can be replaced by fly ash incorporated with bottom ash up to 60 %. This fine-grained concrete probably satisfies the requirement of conventional concrete in terms of mechanical properties and durability. Therefore, it is believed that this fine-grained concrete from a combination of fly and bottom ashes can be utilized for construction works in place of conventional concrete.

The findings of this study suggest that fine-grained concrete using fly ash and bottom ash replacing fine aggregate could be potentially applied for construction work instead of conventional concrete. However, this study has some limitations, for instance, only a fixed content of fly ash (20 %) and varied amounts of bottom ash ranging from 20 % to 50 % have experimented. In addition, this study mainly focused on the mechanical and durability investigation using compressive and tensile strength, chloride permeability, and water absorption. Thus, it is necessary to further investigate the amount of bottom ash replacement with 0 % and 10 % to have a consistent comparison and discussion; in which the amount of fly ash can be also a variable. The additional investigation on microstructural and physicochemical properties using thermal analysis, X-ray diffraction, scan electron microscopy, and porosity should be conducted to obtain clear evidence for explaining the influence of fly and bottom ash replacement for this fine-grained concrete.

References

1. Andrade, L.B., Rocha, J.C., Cheriaf, M. Aspects of moisture kinetics of coal bottom ash in concrete. *Cement and Concrete Research*. 2007. 37(2). Pp. 231–241. DOI: 10.1016/j.cemconres.2006.11.001
2. Singh, M., Siddique, R. Properties of concrete containing high volumes of coal bottom ash as fine aggregate. *Journal of Cleaner Production*. 2015. 91. Pp. 269–278. DOI: 10.1016/j.jclepro.2014.12.026
3. Kumar, D., Gupta, A., Ram, S. Uses of Bottom ash in the Replacement of fine aggregate for Making Concrete. *International Journal of Current Engineering and Technology*. 2014. 4(6). Pp. 3891–3895.
4. Le, H.T., Nguyen, S.T., Ludwig, H.M. A Study on High Performance Fine-Grained Concrete Containing Rice Husk Ash. *International Journal of Concrete Structures and Materials*. 2014. 8(4). Pp. 301–307. DOI: 10.1007/s40069-014-0078-z
5. Cioffi, R., Colangelo, F., Montagnaro, F., Santoro, L. Manufacture of artificial aggregate using MSWI bottom ash. *Waste Management*. 2011. 31(2). Pp. 281–288. DOI:10.1016/j.wasman.2010.05.020
6. Singh, M., Siddique, R. Effect of coal bottom ash as partial replacement of sand on workability and strength properties of concrete. *Journal of Cleaner Production*. 2016. 112. Pp. 620–630. DOI: 10.1016/j.jclepro.2015.08.001
7. The national electricity development plan for the period 2011-2020 has a vision to 2030 according to the Prime Minister's Decision No. 1028 / QD-TTg of July 21, 2011. (In Vietnamese) 2011.
8. Singh, M., Siddique, R. Effect of coal bottom ash as partial replacement of sand on properties of concrete. 72. Elsevier, 01-03-2013.
9. Singh, M., Siddique, R. Strength properties and micro-structural properties of concrete containing coal bottom ash as partial replacement of fine aggregate. *Construction and Building Materials*. 2014. 50. Pp. 246–256. DOI: 10.1016/j.conbuildmat.2013.09.026
10. Kou, S.C., Poon, C.S. Properties of concrete prepared with crushed fine stone, furnace bottom ash and fine recycled aggregate as fine aggregates. *Construction and Building Materials*. 2009. 23(8). Pp. 2877–2886. DOI: 10.1016/j.conbuildmat.2009.02.009

11. Bai, Y., Darcy, F., Basheer, P.A.M. Strength and drying shrinkage properties of concrete containing furnace bottom ash as fine aggregate. *Construction and Building Materials*. 2005. 19(9). Pp. 691–697. DOI: 10.1016/j.conbuildmat.2005.02.021
12. Saikia, N., Cornelis, G., Mertens, G., Elsen, J., Van Balen, K., Van Gerven, T., Vandecasteele, C. Assessment of Pb-slag, MSWI bottom ash and boiler and fly ash for using as a fine aggregate in cement mortar. *Journal of Hazardous Materials*. 2008. 154(1–3). Pp. 766–777. DOI: 10.1016/j.jhazmat.2007.10.093
13. Ul-Haq, E., Kunjalukkal Padmanabhan, S., Licciulli, A. Synthesis and characteristics of fly ash and bottom ash based geopolymers-A comparative study. *Ceramics International*. 2014. 40(2). Pp. 2965–2971. DOI: 10.1016/j.ceramint.2013.10.012
14. Kim, H.K. Utilization of sieved and ground coal bottom ash powders as a coarse binder in high-strength mortar to improve workability. *Construction and Building Materials*. 2015. 91. Pp. 57–64. DOI: 10.1016/j.conbuildmat.2015.05.017
15. Kiattikomol, K., Jaturapitakkul, C., Songpiriyakij, S., Chutubtim, S. A study of ground coarse fly ashes with different finenesses from various sources as pozzolanic materials. *Cement and Concrete Composites*. 2001. 23(4–5). Pp. 335–343. DOI: 10.1016/S0958-9465(01)00016-6
16. Tangpagasit, J., Cheerarot, R., Jaturapitakkul, C., Kiattikomol, K. Packing effect and pozzolanic reaction of fly ash in mortar. *Cement and Concrete Research*. 2005. 35(6). Pp. 1145–1151. DOI: 10.1016/j.cemconres.2004.09.030
17. Kocak, Y., Nas, S. The effect of using fly ash on the strength and hydration characteristics of blended cements. *Construction and Building Materials*. 2014. 73. Pp. 25–32. DOI: 10.1016/j.conbuildmat.2014.09.048
18. Nochaiya, T., Wongkeo, W., Chaipanich, A. Utilization of fly ash with silica fume and properties of Portland cement-fly ash-silica fume concrete. *Fuel*. 2010. 89(3). Pp. 768–774. DOI: 10.1016/j.fuel.2009.10.003
19. Rukzon, S., Chindaprasirt, P. Mathematical model of strength and porosity of ternary blend Portland rice husk ash and fly ash cement mortar. *Computers and Concrete*. 2008. 5(1). Pp. 75–88. DOI: 10.12989/cac.2008.5.1.075
20. Mehta, P.K., Gjrv, O.E. Properties of portland cement concrete containing fly ash and condensed silica-fume. *Cement and Concrete Research*. 1982. 12(5). Pp. 587–595. DOI: 10.1016/0008-8846(82)90019-9
21. Berndt, M.L. Properties of sustainable concrete containing fly ash, slag and recycled concrete aggregate. *Construction and Building Materials*. 2009. 23(7). Pp. 2606–2613. DOI: 10.1016/j.conbuildmat.2009.02.011
22. Khatib, J.M. Performance of self-compacting concrete containing fly ash. *Construction and Building Materials*. 2008. 22(9). Pp. 1963–1971. DOI: 10.1016/j.conbuildmat.2007.07.011
23. Thomas, M.D.A., Shehata, M.H., Shashiprakash, S.G., Hopkins, D.S., Cail, K. Use of ternary cementitious systems containing silica fume and fly ash in concrete. *Cement and Concrete Research*. 1999. 29(8). Pp. 1207–1214. DOI: 10.1016/S0008-8846(99)00096-4
24. Kim, H.K., Lee, H.K. Use of power plant bottom ash as fine and coarse aggregates in high-strength concrete. *Construction and Building Materials*. 2011. 25(2). Pp. 1115–1122. DOI: 10.1016/j.conbuildmat.2010.06.065
25. Zaetang, Y., Wongsas, A., Sata, V., Chindaprasirt, P. Use of coal ash as geopolymer binder and coarse aggregate in pervious concrete. *Construction and Building Materials*. 2015. 96. Pp. 289–295. DOI: 10.1016/j.conbuildmat.2015.08.076
26. Wongsas, A., Zaetang, Y., Sata, V., Chindaprasirt, P. Properties of lightweight fly ash geopolymer concrete containing bottom ash as aggregates. *Construction and Building Materials*. 2016. 111. Pp. 637–643. DOI: 10.1016/j.conbuildmat.2016.02.135
27. Bouziani, T., Bederina, M., Hadjoudja, M. Effect of dune sand on the properties of flowing sand-concrete (FSC). *International Journal of Concrete Structures and Materials*. 2012. 6(1). Pp. 59–64. DOI: 10.1007/s40069-012-0006-z
28. Al-Harthy, A.S., Halim, M.A., Taha, R., Al-Jabri, K.S. The properties of concrete made with fine dune sand. *Construction and Building Materials*. 2007. 21(8). Pp. 1803–1808. DOI: 10.1016/j.conbuildmat.2006.05.053
29. Mechtcherine, V., Gorges, M., Schroefl, C., Assmann, A., Brameshuber, W., Ribeiro, A.B., Cusson, D., Custdio, J., Da Silva, E.F., Ichimiya, K., Igarashi, S.I., Klemm, A., Kovler, K., De Mendona Lopes, A.N., Lura, P., Nguyen, V.T., Reinhardt, H.W., Filho, R.D.T., Weiss, J., Wyrzykowski, M., Ye, G., Zhutovsky, S. Effect of internal curing by using superabsorbent polymers (SAP) on autogenous shrinkage and other properties of a high-performance fine-grained concrete: Results of a RILEM round-robin test. *Materials and Structures/Materiaux et Constructions*. 2014. 47(3). Pp. 541–562. DOI: 10.1617/s11527-013-0078-5
30. Bederina, M., Gotteicha, M., Belhadj, B., Dheily, R.M., Khenfer, M.M., Queneudec, M. Drying shrinkage studies of wood sand concrete – Effect of different wood treatments. *Construction and Building Materials*. 2012. 36. Pp. 1066–1075. DOI: 10.1016/j.conbuildmat.2012.06.010
31. Khay, S.E.E., Neji, J., Loulizi, A. Shrinkage properties of compacted sand concrete used in pavements. *Construction and Building Materials*. 2010. 24(9). Pp. 1790–1795. DOI: 10.1016/j.conbuildmat.2010.02.008
32. Lynda Amel, C., Kadri, E.H., Sebaibi, Y., Soualhi, H. Dune sand and pumice impact on mechanical and thermal lightweight concrete properties. *Construction and Building Materials*. 2017. 133. Pp. 209–218. DOI: 10.1016/j.conbuildmat.2016.12.043
33. Collins, F., Sanjayan, J.G. Strength and shrinkage properties of alkali-activated slag concrete containing porous coarse aggregate. *Cement and Concrete Research*. 1999. 29(4). Pp. 607–610. DOI: 10.1016/S0008-8846(98)00203-8
34. Kohno, K., Okamoto, T., Isikawa, Y., Sibata, T., Mori, H. Effects of artificial lightweight aggregate on autogenous shrinkage of concrete. *Cement and Concrete Research*. 1999. 29(4). Pp. 611–614. DOI: 10.1016/S0008-8846(98)00202-6
35. Bentz, D.P., Snyder, K.A. Protected paste volume in concrete: Extension to internal curing using saturated lightweight fine aggregate. *Cement and Concrete Research*. 1999. 29(11). Pp. 1863–1867. DOI: 10.1016/S0008-8846(99)00178-7
36. Weber, S., Reinhardt, H.W. New generation of high performance concrete: Concrete with autogeneous curing. *Advanced Cement Based Materials*. 1997. 6(2). Pp. 59–68. DOI: 10.1016/S1065-7355(97)00009-6
37. Sitarz-Palczak, E., Kalembkiewicz, J., Galas, D. Comparative study on the characteristics of coal fly ash and biomass ash geopolymers. *Archives of Environmental Protection*. 2019. 45(1). Pp. 126–135. DOI: 10.24425/aep.2019.126427
38. Rafieizonooz, M., Mirza, J., Salim, M.R., Hussin, M.W., Khankhaje, E. Investigation of coal bottom ash and fly ash in concrete as replacement for sand and cement. *Construction and Building Materials*. 2016. 116. Pp. 15–24. DOI: 10.1016/j.conbuildmat.2016.04.080
39. Materials, A.S. for T. and ASTM C143, Standard Test Method for Slump of Hydraulic-Cement Concrete. Philadelphia: ASTM. 2001. URL: <https://www.astm.org/Standards/C143> (date of application: 23.05.2020).
40. ASTM. ASTM C39 Standard Test Method for Compressive Strength of Cylindrical Concrete Specimens 1. ASTM International. 2008. i. Pp. 1–7. URL: <https://www.astm.org/Standards/C39> (date of application: 23.05.2020).

41. ASTM C496. ASTM C496 / C496M-17, Standard Test Method for Splitting Tensile Strength of Cylindrical Concrete Specimens, ASTM International, West Conshohocken, PA, 2017, www.astm.org2017
42. ASTM C1202. Standard Test Method for Electrical Indication of Concrete's Ability to Resist Chloride Ion Penetration. American Society for Testing and Materials. 2012. (C). Pp. 1–8. DOI: 10.1520/C1202-12.2. URL: https://www.astm.org/Standards/C1202 (date of application: 23.05.2020).
43. TCVN, Heavyweight concrete – Method for determination of water absorption, TCVN 31131993. (1993) 1–2.
44. Van, V.T.A., Rößler, C., Bui, D.D., Ludwig, H.M. Mesoporous structure and pozzolanic reactivity of rice husk ash in cementitious system. Construction and Building Materials. 2013. 43. Pp. 208–216. DOI: 10.1016/j.conbuildmat.2013.02.004
45. Siddique, R., Aggarwal, P., Aggarwal, Y. Influence of water/powder ratio on strength properties of self-compacting concrete containing coal fly ash and bottom ash. Construction and Building Materials. 2012. 29. Pp. 73–81. DOI: 10.1016/j.conbuildmat.2011.10.035
46. Le, H.T., Ludwig, H.M. Effect of rice husk ash and other mineral admixtures on properties of self-compacting high performance concrete. Materials and Design. 2016. 89. Pp. 156–166. DOI: 10.1016/j.matdes.2015.09.120
47. Yüksel, İ., Üniversitesi, B.T. Properties of concrete containing non ground ash and slag as fine aggregate. 104(4)2007.
48. Topçu, I.B., Bilir, T. Effect of Bottom Ash as Fine Aggregate on Shrinkage Cracking of Mortars. ACI Materials Journal. 2010. 107(6). Pp. 545–553. DOI: 10.14359/51664040
49. Ghafoori, N., Bucholc, J. Investigation of lignite-based bottom ash for structural concrete. Journal of Materials in Civil Engineering. 1996. 8(3). Pp. 128–137. DOI: 10.1061/(ASCE)0899-1561(1996)8:3(128)
50. Ghafoori, N., Journal, Y.C.-M., 1998, U. Laboratory-Made RCC containing Dry Bottom Ash: Part I – Mechanical Properties. ACI Materials Journal. 1998. 95(2). DOI: 10.14359/357
51. Ghafoori, N., Cai, Y. Laboratory-made roller compacted concretes containing dry bottom ash: Part II – Long-term durability. ACI Materials Journal. 1998. 95(3). Pp. 244–251. DOI: 10.14359/368
52. Parra, C., Valcuende, M., Gómez, F. Splitting tensile strength and modulus of elasticity of self-compacting concrete. Construction and Building Materials. 2011. 25(1). Pp. 201–207. DOI: 10.1016/j.conbuildmat.2010.06.037
53. Nazari, A., Riahi, S. The effects of TiO₂ nanoparticles on physical, thermal and mechanical properties of concrete using ground granulated blast furnace slag as binder. Materials Science and Engineering A. 2011. 528(4–5). Pp. 2085–2092. DOI: 10.1016/j.msea.2010.11.070
54. Shetty, M.S. Concrete Technology–Theory and Practice, New Delhi, India, S2004.
55. Ollivier, J.P., Maso, J.C., Bourdette, B. Interfacial transition zone in concrete. 2(1) 1995.
56. Alonso, C., Andrade, C., Castellote, M., Castro, P. Chloride threshold values to depassivate reinforcing bars embedded in a standardized OPC mortar. Cement and Concrete Research. 2000. 30(7). Pp. 1047–1055. DOI: 10.1016/S0008-8846(00)00-265-9.
57. Thomas, M. Chloride thresholds in marine concrete. Cement and Concrete Research. 1996. 26(4). Pp. 513–519. DOI: 10.1016/0008-8846(96)00035-X
58. Siddique, R. Compressive strength, water absorption, sorptivity, abrasion resistance and permeability of self-compacting concrete containing coal bottom ash. Construction and Building Materials. 2013. 47. Pp. 1444–1450. DOI: 10.1016/j.conbuildmat.2013.06.081

Contacts:

Thanh Sang Nguyen, nguyenthanhsang@utc.edu.vn

Minh Quan Thai, minhquan.thai@utc.edu.vn

Lanh Si Ho, lanhs@utt.edu.vn



DOI: 10.34910/MCE.107.12

Long-term strength of polyethylene pipes with increased temperature resistance without reinforcement

A.S. Semenov , A.I. Grishchenko , V.G. Artiukh* , B.E. Melnikov

Peter the Great St. Petersburg Polytechnic University, St. Petersburg, Russia

*E-mail: artiukh@mail.ru

Keywords: polyethylene pipe, long-term hydrostatic strength, durability, elasticity, temperature, pressure, equivalent stress

Abstract. Results of long-term hydrostatic strength study of piping systems made from polyethylene with increased temperature resistance PE-RT type II of Hostalen 4731B without reinforcement are presented and discussed in this paper. The different approximations of durability curves and various equivalent stress measures are considered and compared. An analytical expression for the maximum allowable internal pressure as function of service life of pipes, temperature, geometrical parameters of pipe cross-section and material properties is given. Pipes without reinforcement with nominal outer diameters from 32 mm to 225 mm were analyzed to assess long-term hydrostatic strength using equivalent stress, provided that there is no change in mechanism of damage accumulation. This allowed us to use linear extrapolation into area of long service life. The results indicate possible use of pipes SDR7.4 in heating networks for 50 years with heat transfer fluid parameters of 95 °C and internal pressure of 1 MPa.

1. Introduction

Until recently, European public utility pipe market has traditionally been dominated by copper and galvanized steel pipes. Over past 30 years this segment has seen accelerated growth in share of pipes made from plastic. Advantage of plastics is that they are non-corrosive and resistant to many chemicals. They are flexible and easy to assemble (like “endless” pipe), hermetically sealed by fusion welding and light in weight, which facilitates their transportation and handling on site [1–6].

Typically, plastics used for production of municipal pipes are PE (polyethylene), PP-R (random copolymer of polypropylene), PB (polybutene) and to a lesser extent C-PVC (chlorinated PVC). While PP-R, PB and C-PVC have their own good high temperature properties, PE was not considered suitable for this market segment due to operating temperature limitations [7–11].

However, crosslinking of polyethylene (PE-X) allowed achieving desired long-term hydrostatic strength at high temperatures. Better flexibility and elasticity, high thermal conductivity, good economic properties and inertness provided by polyethylene have led to rapid increase in popularity of crosslinked polyethylene. At present crosslinked polyethylene is a widespread plastic material in segment of pipes for heating and water supply systems [12–17].

Recently, a promising new class of polyethylene materials (PE-RT) with significantly improved long-term high temperature strength without the need for crosslinking draws more and more attention [18–21].

Purpose of this work is to study the long-term hydrostatic strength of pipes made from polyethylene with increased temperature resistance PE-RT type II without reinforcement. The durability analysis is carried out for the following range of pipe parameters:

Semenov, A.S., Grishchenko, A.I., Artiukh, V.G., Melnikov, B.E. Long-term strength of polyethylene pipes with increased temperature resistance without reinforcement. Magazine of Civil Engineering. 2021. 107(7). Article No. 10712. DOI: 10.34910/MCE.107.12

© Semenov, A.S., Grishchenko, A.I., Artiukh, V.G., Melnikov, B.E., 2021. Published by Peter the Great St. Petersburg Polytechnic University



This work is licensed under a CC BY-NC 4.0

- working pressure in pipe (0÷2 MPa);
- temperature (50, 60, 70, 80, 90, 95, 100, 110, 115 °C);
- outer diameter of pipes (32÷225 mm);
- pipe wall thickness for SDR 7.4 (4.4÷30.8 mm); SDR 9 (3.6÷25.2 mm); SDR 11 (2.9÷20.5 mm), where SDR is the Standard Dimensions Ratio defined as the ratio of the pipe nominal outside diameter to the nominal (minimum) wall thickness.

2. Methods

2.1. Formulation of problem

Single-layer circular pipe (see Fig. 1) with inner radius R_0 , outer radius R_1 , outer diameter $d_n = 2R_1$ and wall thickness $e_n = R_1 - R_0$ is considered. Pressure p acts on the inner surface of the pipe and pressure q is applied on the outer boundary. The cylindrical coordinate system with z -axis along symmetry axis of the pipe is used.

The calculation of the equivalent stress measure, depending on geometric and loading parameters, is the aim of the boundary value problem solution. The problem has a well-known analytical solution for the stress-strain state (firstly proposed by Gabriel Lamé [22]) in the linear isothermal infinitesimal elastic formulation under assumption of isotropy of material properties.

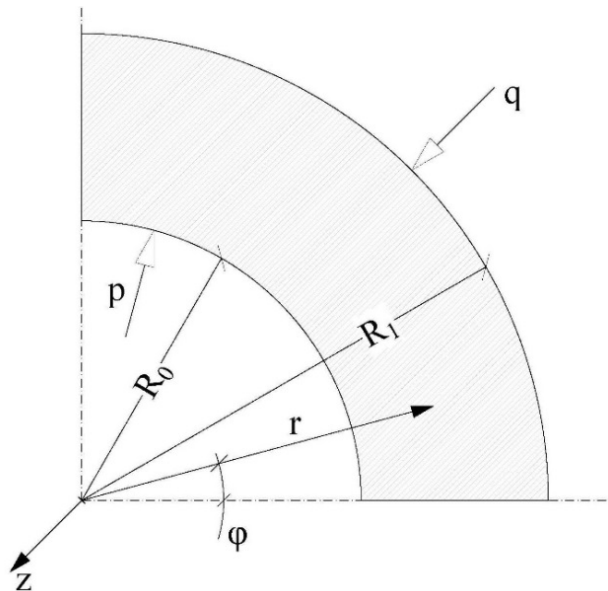


Figure 1. Schematic representation of pipe section fragment with indication of the main geometric parameters and acting loads.

2.2. Analytical solution for stress tensor components

Solution of Lamé boundary value problem [22] in linear elastic isothermal formulation in framework of hypothesis of a plane strain state when pressures acting on inner and outer surfaces of pipe are set as boundary conditions

$$\sigma_r \Big|_{r=R_0} = -p; \quad \sigma_r \Big|_{r=R_1} = -q, \quad (1)$$

has a form of following dependences of radial and circumferential stresses on applied loads, geometric parameters and distance r from axis [23]:

$$\left\{ \begin{array}{l} \sigma_r = q \frac{1}{1 - \left(\frac{R_0}{R_1}\right)^2} \left(\left(\frac{R_0}{r}\right)^2 - 1 \right) + p \frac{1}{1 - \left(\frac{R_0}{R_1}\right)^2} \left(\left(\frac{R_0}{R_1}\right)^2 - \left(\frac{R_0}{r}\right)^2 \right); \\ \sigma_\varphi = q \frac{-1}{1 - \left(\frac{R_0}{R_1}\right)^2} \left(1 + \left(\frac{R_0}{r}\right)^2 \right) + p \frac{1}{1 - \left(\frac{R_0}{R_1}\right)^2} \left(\left(\frac{R_0}{R_1}\right)^2 + \left(\frac{R_0}{r}\right)^2 \right). \end{array} \right. \quad (2)$$

The axial stress σ_z for the plane strain state case can be evaluated by the relation $\sigma_z = \nu(\sigma_r + \sigma_\varphi)$, where ν is the Poisson ratio.

In many practical applications, outer pressure is much less than internal. In this case, the influence of external pressure can be neglected and action of only internal pressure p is taken into account that leads to the simplification of relations (2) in the form:

$$\left\{ \begin{array}{l} \sigma_r = p \frac{1}{1 - \left(\frac{R_0}{R_1}\right)^2} \left(\left(\frac{R_0}{R_1}\right)^2 - \left(\frac{R_0}{r}\right)^2 \right); \\ \sigma_\varphi = p \frac{1}{1 - \left(\frac{R_0}{R_1}\right)^2} \left(\left(\frac{R_0}{R_1}\right)^2 + \left(\frac{R_0}{r}\right)^2 \right). \end{array} \right. \quad (3)$$

The typical diagrams of stress tensor components distribution along the radius within the wall thickness are shown in Fig. 2 for the PE-RT type II pipe with outer diameter 50 and wall thickness 6.9 mm.

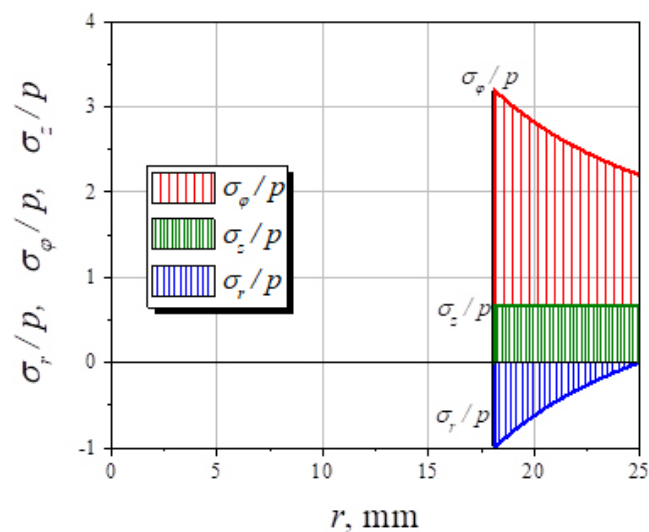


Figure 2. Example of stress tensor components distributions along the radius for the pipe with outer diameter 50 mm and wall thickness 6.9 mm.

Analysis of relations (3) allows asserting that the maximum values of circumferential stress (maximal principle stress) are realized on the inner radius

$$\max \sigma_{\varphi} = \sigma_{\varphi}(R_0) = p \frac{(R_1)^2 + (R_0)^2}{(R_1)^2 - (R_0)^2}. \quad (4)$$

It should be noted that it is possible to obtain analytical solution of the problem in viscoelastic, elastoplastic or viscoplastic formulation [24, 25]. However, numerous experiments do not demonstrate the remarkable residual strains and use of such nonlinear material models for life-time prediction will require significant increase in amount of necessary experimental data. Note also, the linear elastic solution provides conservative evaluation of stress state.

2.3. Equivalent stress measures

It is necessary to introduce equivalent stress for which formulation of strength criterion is compared with the maximum permissible value of long-term strength for analysis of strength in case of non-uniaxial stress state. Circumferential component of stress (which is always tensile and exceeds value of compressive radial component) can be considered as the maximum principal value:

$$\sigma_{eq} = \sigma_1 = \sigma_{\varphi}. \quad (5)$$

Also doubled maximum shear stress (Tresca equivalent stress) can be considered as equivalent stress

$$\sigma_{eq} = \sigma_1 - \sigma_3. \quad (6)$$

Mises stress intensity

$$\sigma_{eq} = \sqrt{\frac{1}{2} \left[(\sigma_1 - \sigma_2)^2 + (\sigma_2 - \sigma_3)^2 + (\sigma_3 - \sigma_1)^2 \right]}. \quad (7)$$

Thickness-average circumferential stress is determined by 'boiler equation'

$$\sigma_{eq} = \bar{\sigma}_{\varphi} = \frac{pR_0}{R_1 - R_0}. \quad (8)$$

Equation used in GOST 32415-2013 is approximation to the maximum principal stress, which can be obtained as a consequence of asymptotic equation (4) under assumption that the wall thickness is small:

$$\sigma_{eq} = \frac{p(R_1 + R_0)}{2(R_1 - R_0)} = \frac{p(d_n - e_n)}{2e_n} = \frac{p(SDR - 1)}{2}. \quad (9)$$

Comparison of the maximum values of equivalent stress (5)-(7) and predictions by (8) and (9) is shown in Fig. 3 for the pipe with outer diameter 50 mm and wall thickness 6.9 mm. There is 23 % difference between the minimum and maximum results.

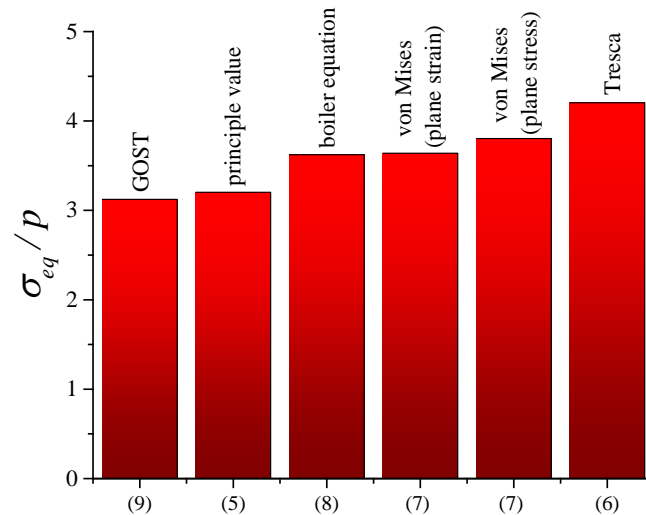


Figure 3. Comparison of equivalent stresses (5)-(9) for the pipe with outer diameter 50 mm and wall thickness 6.9 mm.

In [26, 27] results of tests of high-density polyethylene under biaxial tension are given and it is noted that when analyzing for long-term static strength at low stress levels and long durability the best prediction corresponds to the criterion of maximum principal stresses (5). At the same time, at high stress levels and short-term durability the best prognosis is provided by Mises criterion (7). Therefore, in analysis of long-term strength for long service lives the equivalent stress (5) and its simplified approximation (9) are used below.

2.4. Long-term strength curves approximation

In practice, there are various approximations of long-term strength curves [28]. In present research, the following four-term dependence of durability (time to failure) from equivalent stress and temperature originally introduced in DIN EN ISO 15875-2:2004 [29] was used for approximation of long-term strength curves of polyethylene PE-RT type II:

$$\lg(t) = A + \frac{B \lg(\sigma)}{T} + \frac{C}{T} + D \lg(\sigma), \quad (10)$$

where A , B , C and D are material constants. By transformation of (10) the more convenient for further analysis formulation with combination in one term the stress dependent expressions can be obtained:

$$\lg(t) = \left(D + \frac{B}{T} \right) \lg(\sigma) + \left(A + \frac{C}{T} \right). \quad (11)$$

Determination of coefficients of the equation (11) was carried out on the basis of minimizing following functional (according to the method of least squares):

$$L = \sum_{i=1}^n \sum_{j=1}^k \left[\left(D + \frac{B}{T_i} \right) \lg(\sigma_j) + \left(A + \frac{C}{T_i} \right) - \lg t(\sigma_j, T_i) \right]^2 \rightarrow \min. \quad (12)$$

Objective function (12) is the standard deviation. This objective function has a complex, non-linear form and a large number of local extremums. The sliding tolerance method (Nelder–Mead method [30, 31]) is used for finding a global extremum to minimize the objective function (12). Advantages of this method are ability to solve problems with both linear and nonlinear objective functions and constraints. This method does not use derivatives.

3. Results and Discussion

As a result of experimental data analysis [32] for curves of long-term strength of polyethylene of increased thermal resistance PE-RT type II of Hostalen 4731B brand approximation coefficients A , B , C

and D of equation (10) were obtained on the basis of least squares method (12). Coefficients are presented in Table 1.

Table 1. Coefficients of approximation (10) of long-term strength curve of polyethylene PE-RT type II of Hostalen 4731B.

A	-252.0882	$\lg(h)$
B	-68217.06	$K \lg(h) / \lg(\text{MPa})$
C	105350.4	$K \lg(h)$
D	136.0416	$\lg(h) / \lg(\text{MPa})$

Comparison of obtained approximations of long-term strength curves with experimental data is shown in Fig. 4, where points correspond to the experimental data, straight lines related to the calculated approximations.

Thus, equation (10) takes below given form after determining the coefficients:

$$\lg(t) = -252.0882 - \frac{68217.06}{T} \lg(\sigma) + \frac{105350.4}{T} + 136.0416 \lg(\sigma), \quad (13)$$

in which the stresses are measured in MPa, time in h, temperature in K.

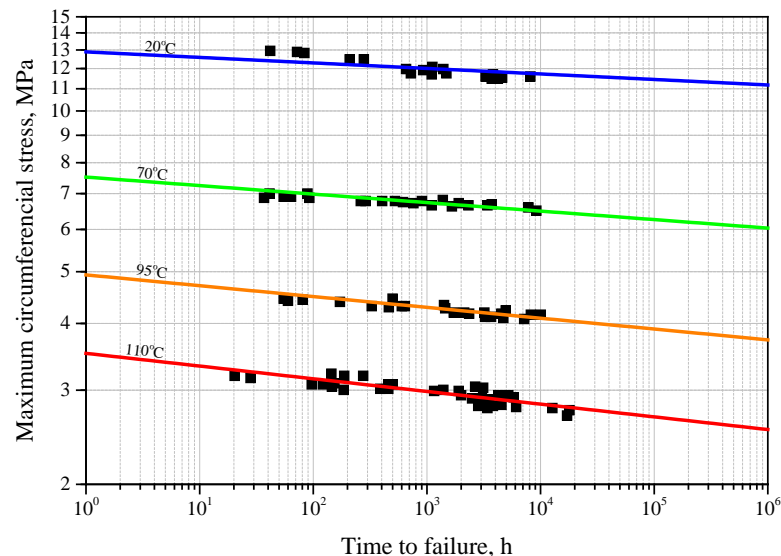


Figure 4. Curves of long-term strength based on equation (13). Experimental results are shown by points and their approximations are shown by lines.

The standard deviation for all curves in Fig. 4 is less than 1 % that confirms adequacy of choice of model and high accuracy of determining the constants.

It is important to note that introduced approximation (13) allows linear extrapolation to region of long service lives only if there is no change in damage accumulation mechanism (for example, a transition from ductile to brittle fracture mechanism or microstructural changes in material). Verification of absence of change in the mechanism of damage accumulation can be carried out experimentally.

Comparison with experimental data of alternative approaches of long-term strength approximations such as Larson-Miller equation [33]

$$\lg(t) = A + \frac{B}{T} + \frac{C}{T} \lg(\sigma) + D \lg^2(\sigma) \quad (14)$$

and Manson-Hafed equation [34]

$$\lg(t) = A + B \lg(\sigma) + C \lg^2(\sigma) + DT \quad (15)$$

demonstrated advantage (see Fig. 5) of criterion (10) in comparison with (14) and (15) which are widespread for metallic materials.

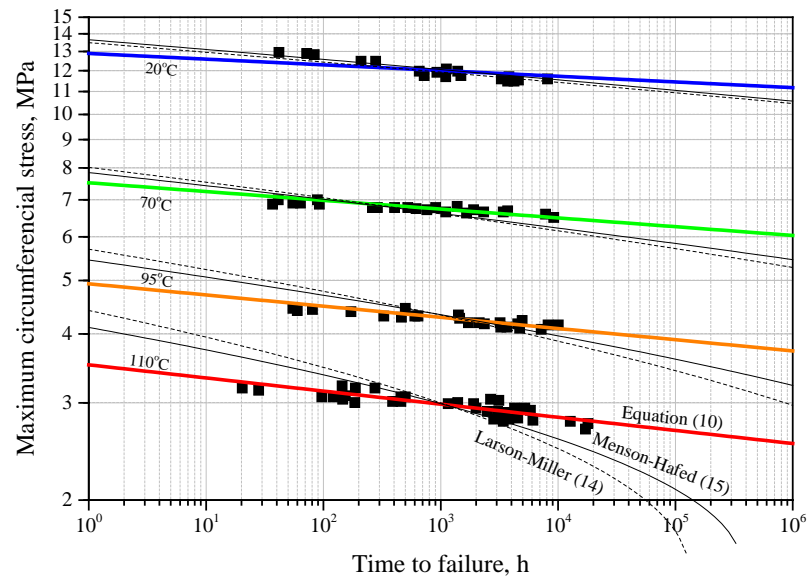


Figure 5. Comparison of experimental results with Larson-Miller approximation (14), Manson-Hafed (15) and approximation by equation (10).

Following coefficients in approximations were used (stresses are measured in MPa, time is in h, temperature is in K) for Larson-Miller criterion

$$\lg(t) = -69.0589 + \frac{28132.90}{T} + \frac{3123.772}{T} \lg(\sigma) - 8895.212 \lg^2(\sigma) \quad (16)$$

and for the criterion of Manson-Hafed

$$\lg(t) = 96.82029 + 11.10418 \lg(\sigma) - 30.12566 \lg^2(\sigma) - 0.24095T. \quad (17)$$

It should be noted that use of unified analytical approximations over entire temperature range introduces some error in analysis of specific temperatures. Example of that difference is shown in Fig. 6, which compares approximation (10) uniform for all temperatures with coefficients A , B , C and D defined by the results of experiments at $T = 20, 70, 95, 110$ °C and isothermal approximation

$$\lg(t) = F + E \cdot \lg(\sigma), \quad (18)$$

obtained on the basis of least squares method ($F = 0.677 \lg(h)$, $E = -0.01576 \lg(h)/\lg(\text{MPa})$) for set of experimental points at temperature of $T = 95$ °C. Obtained result indicates that use of approximation (10) at temperature of $T = 95$ °C for a time of more than three months provides conservative estimate with certain margin.

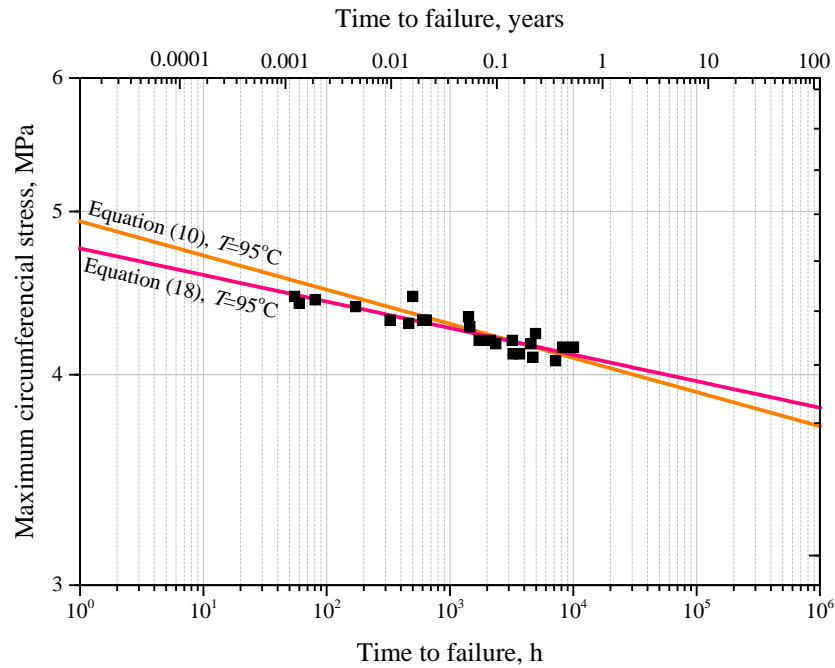


Figure 6. Comparison of approximation (10) uniform for all temperatures with approximation (18) introduced only for temperature of $T = 95\text{ }^{\circ}\text{C}$.

2.5. Long-term strength nomograms

Actual for practice nomograms «pressure-temperature-durability» were obtained for three different SDR values (see Fig. 7-9) based on the analytical solution (4) for pipe under internal pressure, equivalent stress (9) and results of approximation of long-term strength curves (13).

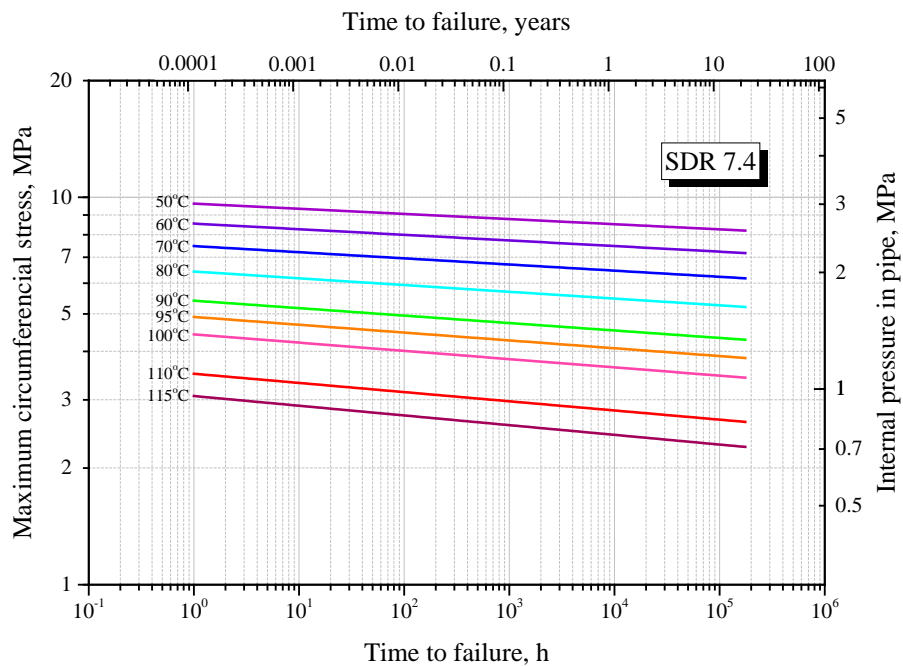


Figure 7. Long-term strength for pipes with SDR 7.4 made of polyethylene PE-RT type II of Hostalen 4731b brand.

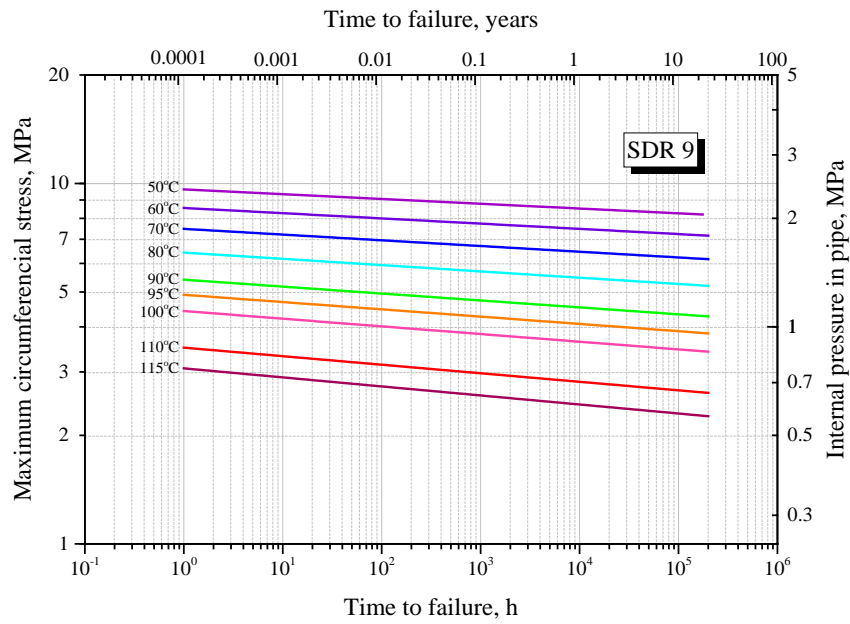


Figure 8. Long-term strength for pipes with SDR 9 made of polyethylene PE-RT type II of Hostalen 4731B brand.

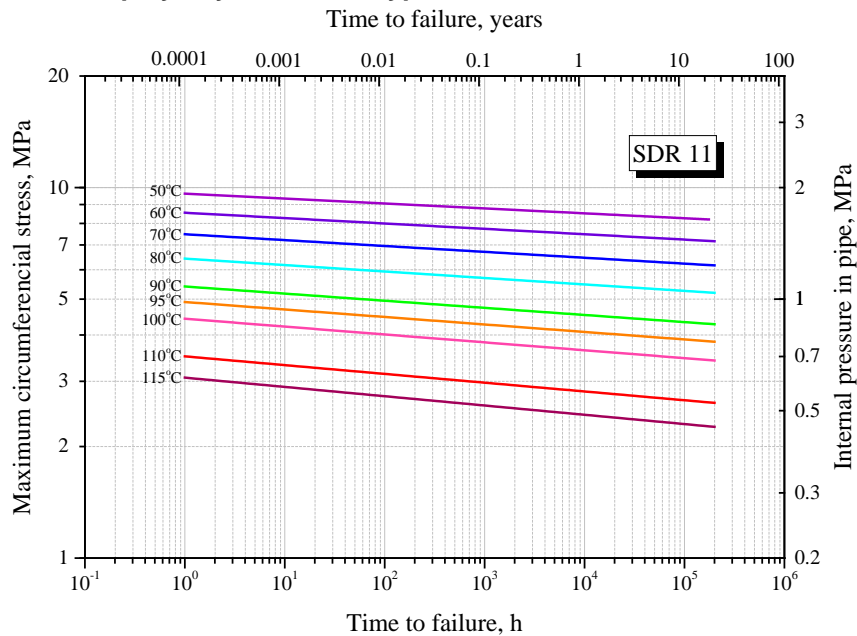


Figure 9. Long-term strength for pipes with SDR 11 made of polyethylene PE-RT type II of Hostalen 4731B brand.

With increasing SDR (decreasing relative wall thickness) the maximum allowable pressure level decreases (compare Fig. 7-9). The maximum allowable internal pressure was determined on the basis of the equation

$$p = \frac{2e_n}{d_n - e_n} \sigma_{eq} = \frac{2}{SDR - 1} \sigma_{eq} = \frac{2}{SDR - 1} 10^{\frac{\lg(t) - \left(A + \frac{C}{T}\right)}{D + \frac{B}{T}}}, \quad (19)$$

which has been obtained from the equations (9) and (10).

Long-term strength curves may slightly differ for different standard sizes of pipes with the same SDR value due to specifics of choosing nominal wall thickness from a tabulated discrete range of thicknesses in accordance with regulatory documents. As a rule, nominal wall thickness slightly differs in direction of increase from value of ratio of outer diameter to SDR that leads to conservative estimate of strength. The

durability is sensitive to variation of the wall thickness, therefore it is necessary to individually check fulfillment of strength condition for each standard size in especially critical cases.

Calculation results of the maximum allowable pressures using criterion (9) for pipes of various standard sizes SDR 7.4 made of polyethylene of increased temperature resistance PE-RT type II Hostalen 4731B brand at temperature of $T = 95\text{ }^{\circ}\text{C}$ for various service lives (from 50 years to 100 hours) are presented in Table 2.

Table 2. Maximum allowable pressure for pipes of various standard sizes (SDR 7.4) made of polyethylene PE-RT type II of Hostalen 4731B brand at temperature of $T = 95\text{ }^{\circ}\text{C}$ for various service lives.

No.	d_n , mm	e_n , mm	p , MPa			
			50 years	2 years	1 year	100 h
1	32	4.4	1.209	1.290	1.308	1.433
2	40	5.5	1.209	1.290	1.308	1.433
3	50	6.9	1.214	1.296	1.313	1.439
4	63	8.6	1.199	1.279	1.297	1.421
5	75	10.3	1.207	1.288	1.307	1.431
6	90	12.3	1.200	1.281	1.299	1.422
7	110	15.1	1.206	1.288	1.306	1.430
8	125	17.1	1.201	1.283	1.301	1.424
9	140	19.2	1.205	1.286	1.304	1.428
10	160	21.9	1.202	1.283	1.301	1.425
11	180	24.6	1.200	1.281	1.299	1.422
12	200	27.4	1.204	1.285	1.303	1.427
13	225	30.8	1.203	1.283	1.302	1.425

It can be seen from Table 2 that for all considered standard sizes at pressure of $p = 1\text{ MPa}$ condition of long-term strength is provided at heat transfer fluid temperature of $T = 95\text{ }^{\circ}\text{C}$ for service life of 50 years. The safety factor is 1.2 when using criterion (9) for all cases of standard sizes. The safety factor exceeds 1.17 when using criterion of maximum principal stresses (5).

Calculations made for verification purposes using Mises criterion (7) for plane strain state showed that in this case condition of long-term strength is also provided at pressure of $p = 1\text{ MPa}$ and heat transfer fluid temperature of $T = 95\text{ }^{\circ}\text{C}$ for service life of 50 years. At the same time, the safety factor for the considered standard sizes of pipes exceeds 1.03.

The maximum allowable pressure obtained for equivalent stress (9) for pipes of various standard sizes SDR 9 made of polyethylene of increased temperature resistance PE-RT type II of Hostalen 4731B brand at temperature of $T = 95\text{ }^{\circ}\text{C}$ for various service life (from 50 years to 100 hours) are presented in Table 3.

Table 3. Maximum allowable pressure for pipes of various standard sizes (SDR 9) made of polyethylene PE-RT type 2 of Hostalen 4731B brand at temperature of $T = 95\text{ }^{\circ}\text{C}$ for various service life.

No.	d_n , mm	e_n , mm	p , MPa			
			50 years	2 years	1 year	100 h
1	32	3.6	0.961	1.026	1.040	1.139
2	40	4.5	0.961	1.026	1.040	1.139
3	50	5.6	0.956	1.026	1.035	1.133
4	63	7.1	0.963	1.026	1.042	1.141
5	75	8.4	0.956	1.026	1.035	1.133
6	90	10.1	0.958	1.023	1.037	1.136
7	110	12.3	0.954	1.019	1.033	1.131
8	125	14	0.956	1.021	1.035	1.133
9	140	15.7	0.958	1.022	1.037	1.135
10	160	17.9	0.955	1.019	1.034	1.132
11	180	20	0.948	1.012	1.026	1.123
12	200	22.4	0.956	1.021	1.035	1.133
13	225	25.2	0.956	1.021	1.035	1.133

It can be seen from Table 3 that for all considered standard sizes at pressure of $p = 1$ MPa condition of long-term strength is provided at heat transfer fluid temperature of $T = 95$ °C for service life of 2 years. The safety factor is 1.02 when using criterion (9) for all cases of standard sizes.

All considered sizes of pipes SDR 9 withstand the pressure of 0.7 MPa for 50 years with safety factor 1.35 and the pressure of 0.6 MPa with safety factor 1.5.

Calculation results of the maximum allowable pressure using criterion (9) for pipes of various standard sizes SDR 11 made of polyethylene of increased temperature resistance PE-RT type II of Hostalen 4731B brand at temperature of $T = 95$ °C for various service life (from 50 years to 100 hours) are presented in Table 4.

Table 4. Maximum allowable pressure for pipes of various standard sizes (SDR 11) made of polyethylene PE-RT type II of Hostalen 4731B brand at temperature of $T = 95$ °C for various service life.

No.	d_n , mm	e_n , mm	p , MPa			
			50 years	2 years	1 year	100 h
1	32	2.9	0.773	0.825	0.837	0.916
2	40	3.7	0.768	0.820	0.832	0.910
3	50	4.6	0.769	0.821	0.832	0.911
4	63	5.8	0.756	0.807	0.818	0.896
5	75	6.8	0.760	0.811	0.823	0.901
6	90	8.2	0.758	0.809	0.821	0.899
7	110	10.0	0.761	0.812	0.824	0.902
8	125	11.4	0.756	0.807	0.819	0.896
9	140	12.7	0.761	0.813	0.824	0.902
10	160	14.6	0.760	0.811	0.823	0.901
11	180	16.4	0.759	0.810	0.822	0.900
12	200	18.2	0.760	0.811	0.823	0.901
13	225	20.5	0.773	0.825	0.837	0.916

It can be seen from Table 4 that for all considered standard sizes at pressure of $p = 0.6$ MPa condition of long-term strength is provided at heat transfer fluid temperature of $T = 95$ °C for service life of 50 years. The safety factor is 1.26 when using criterion (9) for all cases of standard sizes for pressure 0.6 MPa.

The safety factor 1.5 does not allow to increase pressure above 0.5 MPa for 50 years, above 0.55 MPa for 1 year and above 0.6 MPa for 100 hours for pipes of SDR 11.

The above estimates are valid for constant pressures and temperatures throughout the entire service life. In the case of realistic loading conditions with variable (piecewise constant) values, it is recommended to use the Miner's linear damage summation rule [35, 36].

4. Conclusions

1. The four-term approximation (13) of long-term hydrostatic strength curves is proposed and analyzed for polyethylene of increased temperature resistance PE-RT type II of Hostalen 4731B brand.

2. The maximum allowable internal pressure (19) is determined as a function of service life of pipes, temperature, geometrical parameters of pipe cross-section and material properties.

3. Data of proposed nomograms (Fig. 7–9) should be used to determine durability of pipes, critical pressures and safety factors for the various temperature conditions.

4. We studied pipes without reinforcement with nominal outer diameter from 32 mm to 225 mm made of polyethylene of increased temperature resistance PE-RT type II of Hostalen 4731B brand. We assessed the long-term strength using provided equivalent stress under assumption that there is no change in damage accumulation mechanism. The results obtained indicate possible use of these pipes in heating networks for 50 years with heat transfer fluid of 95 °C and working pressure of 1.0 MPa for SDR 7.4, pressure 0.8 MPa for SDR 9, pressure 0.6 MPa for SDR 11 with safety factor 1.2 in all cases.

5. Miner's relation with account of summation of damages within each interval of constancy of temperature and pressure should be used for calculating durability of pipes with changing over time levels of temperatures and pressure.

6. For validation and verification of obtained analytical results further experimental and finite element verification are required.

5. Acknowledgments

The research was funded by the Ministry of Science and Higher Education of the Russian Federation as part of the World-class Research Center program: Advanced Digital Technologies (contract No. 075-15-2020-934 dated 17.11.2020). The authors declare that there is no conflict of interest regarding the publication of this paper.

References

1. Seguela, R. On the Natural Draw Ratio of Semi-crystalline Polymers: Review of the Mechanical, Physical and Molecular Aspects. *Macromolecular Materials and Engineering*. 2007. 292(3). Pp. 235–244.
2. Artiukh, V., Mazur, V., Kukhar, V., Vershinin, V., Shulzhenko, N. Study of polymer adhesion to steel, E3S Web of Conferences. 2019. 110, 01048. <https://doi.org/10.1051/e3sconf/201911001048>.
3. Drozdov, A.D., Klitkou, R., Christiansen, J.D. Cyclic Viscoplasticity of Semicrystalline Polymers with Finite Deformations. *Mechanics of Materials*. 2013. 56. Pp. 53–64. DOI: 10.1016/j.mechmat.2012.09.005
4. Ishchenko, A., Artiukh, V., Mazur, V., Poberezhskii, S., Aleksandrovskiy, M. Experimental study of repair mixtures as glues for connecting elastomers with metals, MATEC Web of Conferences, 2019. 265, 01016. DOI: 10.1051/mateconf/201926501016
5. Pawlak, A., Galeski, A., Rozanski, A. Cavitation During Deformation of Semicrystalline Polymers. *Progress in Polymer Science*. 2014. 39(5). Pp. 921–958. DOI: 10.1016/j.progpolymsci.2013.10.007
6. Artiukh, V.G., Galikhanova, E.A., Mazur, V.M., Kargin, S.B. Energy intensity of parts made from polyurethane elastomers. *Magazine of Civil Engineering*. 2018. 81(5). Pp. 102–115. DOI: 10.18720/MCE.81.11
7. Biron, M. *Thermoplastics and Thermoplastic Composites*. Oxford, UK: Elsevier Ltd. 2014.
8. Boros, S. Long-term hydrostatic strength and design of thermoplastic piping compounds. *Journal of ASTM International*. 2011. 8(9). Pp. 57–72.
9. Pawlak, A., Krajenta, J., Galeski, A. Cavitation Phenomenon and Mechanical Properties of Partially Disentangled Polypropylene. *Polymer*. 2018. 151. Pp. 1–26. DOI: 10.1016/j.polymer.2018.07.033
10. Ultrapolymers zeigt Polyolefine mit besonderen Eigenschaften. *Österr. Kunstst. Z.* 2005. – 36(9-10). P. 221.
11. Fallatah, G., Dobbs, N., Gibson, A. Long Term Creep and Stress Rupture of Aramid Fibre. *Plastics, Rubber and Composites*. 2007. 36(9). Pp. 403–412.
12. Xiong, B., Men, Y., Lame, O., Chenal, J.-M., Seguela, R., Vigier, G. Critical Stress And Thermal Activation Of Crystal Plasticity In Polyethylene: Influence Of Crystal Microstructure And Chain Topology *Polymer*. 2017. 118. Pp. 192–200. DOI: 10.1016/j.polymer.2017.05.011
13. Humbert, S., Lame, O., Séguéla, R., Vigier, G. A Re-Examination Of The Elastic Modulus Dependence On Crystallinity In Semi-Crystalline Polymers. *Polymer*. 2011. 52(21). Pp. 4899–4909.
14. Artiukh, V.G., Karlushin, S.Yu., Sorochan, E.N. Peculiarities of Mechanical Characteristics of Contemporary Polyurethane Elastomers *Procedia Engineering*. 2015, No. 117, Pp. 938–944. DOI: 10.1016/j.proeng.2015.08.180
15. Xiong, B., Lame, O., Chenal, J.M., Seguela, R., Vigier, G., Rochas, C. In-Situ Sxrs Study and Modeling Of The Cavitation/Crystal-Shear Competition In Semi-Crystalline Polymers: Influence Of Temperature And Microstructure In Polyethylene. *Polymer*. 2013. V. 54. N. 20. Pp. 5408–5418.
16. Zhang, Y., Ben Jar, P.-Y., Nguyen, K.-C.T., Le, L.H. Characterization of Ductile Damage in Polyethylene Plate Using Ultrasonic Testing. *Polymer Testing*. 2017. 62. Pp. 51–60. DOI: 10.1016/j.polymertesting.2017.06.010
17. Xiong, B., Lame, O., Chenal, J.-M., Seguela, R., Vigier, G., Rochas, C. Temperature-Microstructure Mapping of The Initiation Of The Plastic Deformation Processes In Polyethylene Via In Situ Wxrs And Sxrs. *Macromolecules*. 2015. 48(15). Pp. 5267–5275.
18. Schramm, D. PE-RT: A New Class of Polyethylene for Industrial Pipes. 25th Int. Conference on Offshore Mechanics and Arctic Engineering. Vol. 3: Safety and Reliability; Materials Technology; Douglas Faulkner Symposium on Reliability and Ultimate Strength of Marine Structures. Hamburg, Germany, June 4-9, 2006. Paper No. OMAE2006-92266, pp. 513–521.
19. Montes, J., Castillo, Cadoux, D., Creus, J. Ageing of polyethylene at raised temperature in contact with chlorinated sanitary hot water. Part I – Chemical aspects. *Polymer Degradation and Stability*. 2012. 97(2). Pp. 149–157.
20. Detrez, F., Seguela, R., Cantournet, S. Plasticity/Damage Coupling In Semi-Crystalline Polymers Prior To Yielding: Micromechanisms and Damage Law Identification. *Polymer*. 2011. 52(9). Pp. 1998–2008.
21. Zhang, Y., Xue, S., Ben Jar, P.Y., Li, L. Quantification of Strain-Induced Damage in Semi-Crystalline Polymers: a Review. *Journal of Materials Science*. 2019. 54(1). Pp. 62–82. DOI: 10.1007/s10853-018-2859-2
22. Lamé, G. *Leçons sur la théorie mathématique de l'élasticité des corps solides*, Paris, 1852.
23. Timoshenko, S.P., Goodier, J.N. *Theory of elasticity*. McGraw-Hill. 1969. 567 p.
24. Dudnik, A.E., Chepurnenko, A.S., Nikora, N.I. Plane axisymmetric problem of thermo-viscoelasticity for a polymer cylinder. *Engineering Bulletin of Don*. 2015. No. 1, part 2.
25. Semenov, A., Melnikov, B. Interactive rheological modeling in elasto-visco-plastic finite element analysis. *Procedia Engineering*. 2016. 165. Pp. 1748–1756.
26. Greenman, A.M., Goldman, A.Ya. Long-term strength of polyethylene under conditions of biaxial tension. *Mechanics of polymers*. 1976. No. 3. Pp. 401–408.
27. Potapova, L.B., Yartsev, V.P. *Mechanics of materials under complex stress conditions*. M.: «Mechanical engineering», 2005. 209 p.
28. Kucher, N.K., Prihod'ko, R.P. Prediction of high-temperature long-term strength of materials. *Strength of Materials*. 2013. 45. Pp. 517–522. <https://doi.org/10.1007/s11223-013-9488-4>

29. DIN EN ISO 15875-2:2004. Plastics piping systems for hot and cold water installations – Crosslinked polyethylene (PE-X) – Part 2: Pipes.
30. Himmelblau, D. Applied Nonlinear Programming. McGraw-Hill, 1972. 536 p.
31. Grishchenko, A.I., Semenov, A.S. Effective methods of parameter identification for creep models with account of III stage. MATEC Web of Conferences. 2016. Vol. 53. Pp. 01043.
32. Hostalen 4731 B. Introducing a new PE-RT Type II material. Lyondell Basell // www.lyondellbasell.com.
33. Larson, F.R., Miller, J. Time–temperature relationship for rupture and creep stress // Trans. ASME. 1952. 74(5). Pp. 765–775.
34. Manson, S.S., Haferd, A.M. A linear time–temperature relation for extrapolation of creep and stress rupture data. NASA TN 2890. 1953.
35. DIN EN ISO 13760:1998. Plastics pipes for conveyance of fluids under pressure – Miner’s rule – Calculation method for cumulative damage.
36. Petrakov, G.P. The service life of plastic pipe in the polyurethane foam insulation, used for heating system. Magazine of Civil Engineering. 2012. No. 3. Pp. 54–62.

Contacts:

Artem Semenov, Semenov.Artem@googlemail.com

Alexey Grishchenko, gai-gr@yandex.ru

Viktor Artiukh, artiukh@mail.ru

Boris Melnikov, kafedra@ksm.spbstu.ru



DOI: 10.34910/MCE.107.13

Self-healing in cementitious composite containing bacteria and protective polymers at various temperatures

H. Schreiberova , T. Trtik , R. Chylik , Z. Prosek , K. Seps , J. Fladr , P. Bily* ,
A. Kohoutkova 

Czech Technical University, Prague, Czech Republic

*E-mail: petr.bily@fsv.cvut.cz

Keywords: self-healing concrete; bacteria; cracks; PVA; superabsorbent polymers (SAP); freeze, low temperature

Abstract. Autonomous sealing of cracks in concrete through bacteria-induced calcification has become a topic of great concern in the last two decades. This paper is focused on two main issues of the so-called bio-based self-healing concrete, i.e. protection of the bacterial spores embedded in the cementitious matrix and behavior of the material at low temperatures. The second aspect is particularly important as the impact of the conditions corresponding to real outside environment was rarely investigated before. An investigation of the influence of temperatures below the freezing point is a unique extension of the current state of the art. In the current study, as a form of protection, superabsorbent polymers (SAP) powder and 16 % polyvinyl alcohol (PVA) water solution are applied. The performed mechanical tests showed pronounced negative impact of the PVA addition on both tensile and compressive strength (a decrease of 56 % and 79 %, respectively), while the SAP negatively affected only the compressive strength (a drop of 30 %). In our study, the composite containing SAP reached even slightly higher tensile strength compared to the control (around 7 % increase). The healing action was observed on cracked cementitious composites beams at ideal (i.e. room) temperature, low temperature (10 °C), and after exposure to freeze cycles (−5 to 0 °C). After 28-day immersion in water at the ideal temperature, the series containing SAP and bacterial spores (BAC_SAP) showed the most pronounced healing – the value of the average maximum healed crack width (Δw_{\max}) reached 219 μm . In the case of preliminary freeze cycling, the BAC_SAP also reached the highest values. At low temperatures, the positive impact of SAP seems to be inhibited as Δw_{\max} is the highest in the control series. In all of the applied conditions, insufficient crack-sealing was detectable in the samples containing PVA. Thus, the SAP proved to be applicable for the protection of bacterial spores at ideal temperatures; however, more research concerning its mechanism in cementitious composite at lower temperatures is needed.

1. Introduction

1.1 State of the art

The reduction in the durability of concrete structures is closely related to the presence of cracks in their cover layer. Cracks accelerate the transport processes in the porous structure of concrete, thus making the material more susceptible to degradation (such as chloride corrosion, carbonation, etc.). Conveniently, concrete is known for its so-called autogenous crack sealing [1], in which the formed damages are gradually (completely, or at least partially) sealed. However, this complex phenomenon is influenced by a large

Schreiberova, H., Trtik, T., Chylik, R., Prosek, Z., Seps, K., Fladr, J., Bily, P., Kohoutkova, A. Self-healing in cementitious composite containing bacteria and protective polymers at various temperatures. Magazine of Civil Engineering. 2021. 107(7). Article No. 10713. DOI: 10.34910/MCE.107.13

© Schreiberova, H., Trtik, T., Chylik, R., Prosek, Z., Seps, K., Fladr, J., Bily, P., Kohoutkova, A., 2021. Published by Peter the Great St. Petersburg Polytechnic University



This work is licensed under a CC BY-NC 4.0

number of factors, and it cannot be easily quantified. Thus, it is not possible to completely rely on this natural behavior and regular manual inspections and repairs of the cracked surfaces must be undertaken.

However, this natural ability of cementitious materials has inspired researchers worldwide to the idea of "self-healing" concretes – cementitious materials which could autonomously detect and repair its cracks. In the 19th century, the ability of certain microorganisms, specifically bacteria, to produce calcium carbonate (the so-called biocalcification process) was discovered [2]. Based on this knowledge, in 2008, Jonkers introduced self-healing concrete with a biological agent [3]. In this novelty material, calcite-producing bacteria is in its inactive form of spores embedded together with necessary organic compounds into the concrete matrix. After a crack occurs, the spores close to the crack surfaces are activated by the penetrating moisture and organic compounds. The now active bacteria then metabolize and convert the mineral precursor compounds to calcium carbonate (CaCO_3), which gradually seals the crack.

Pilot studies proved the idea of self-healing biological concrete to be promising, but subsequent research highlighted several potential drawbacks. Although the applied bacteria is sporulated, experiments showed that the number of viable bacterial spores significantly decreases after approx. 7 days from casting [4]. It is generally believed that this reduction is caused by the crystalline pressures in the aging concrete. To overcome this limitation, researchers have been suggesting and investigating numerous methods of the bacteria protection: e.g. lightweight aggregates (LWA) [5–8], silica gel and polyurethane [9], standard and pH-responsive hydrogels [10, 11], melamine-based microcapsules [12], or the so called "Activated Compact Denitrifying Cores" (ACDC) particles [13].

Another problematic factor of the self-healing bio-based concrete is its potential dependence on temperature. The majority of studies was performed under optimal and stable conditions, i.e. at room temperature (around 22 °C) with a sufficient water supply. However, the average monthly temperature in the Central European region, for example, exceeds 15 °C only three times a year [14], while the average cultivation temperature for the most commonly used bacteria is up to 30 °C [15]. Thus, the presented in-vitro results may not be repeatable under more realistic outside conditions.

Only a few studies addressed this issue. Palin et al. [16] reported that cracks in cementitious composite containing a bacterial self-healing agent reduced their permeability by 95 % in the case of 0.4 mm wide cracks and by 93 % in the case of 0.6 mm wide cracks, when immersed in artificial seawater at 8 °C for 56 days. In contrast, a field study carried out by Paine et al. [17] did not report such optimistic results. In this study, a series of reinforced concrete wall panels were prepared partially with an addition of coated expanded perlite with immobilized bacteria. The panels were cracked and situated at their planned location – as a conventional retaining wall structure at highway. After 7 months, no complete crack healing could be observed, and bacterial calcite precipitation could not be precisely distinguished from the autogenous healing. As relative humidity stayed rather high throughout the experiment, researchers identified the low temperature (mostly below 15 °C) as one of the possible causes.

In the study presented in this paper, both of the aforementioned issues – the protection of bacterial spores in concrete matrix and application of the material under non-ideal conditions – are addressed. As the protective agents, two types of polymers are applied – superabsorbent polymer (SAP) powder and polyvinyl alcohol (PVA) in the form of a water solution.

The SAP powder (a material characterized by a striking absorption capacity up to hundred times its own weight) has already been investigated as an admixture for concrete, inter alia, to enhance the natural self-healing mechanisms [18, 19]. In our case, the function of SAP is twofold. It is believed that the swollen SAP particles (or voids after their drainage) could ensure enough space for bacteria to survive, and, at the same time, serve as a reservoir for the moisture needed for the bacteria metabolic activity. SAP has already been successfully applied to a similar purpose by Kua et al. [20], where the combination of SAP, biochar and bacteria led to closure of cracks up to 800 μm and higher recovery of mechanical properties compared to non-bacterial samples.

There is no mention in the existing literature of the application of PVA water solution in self-healing bio-based concrete. Although several studies have already evaluated its effect on mechanical properties, reduced water absorption or increased acid resistance of cementitious composites [21–24]. In this study, it is expected that the polymer could form a protective layer around the spores, while the increased porosity (according to previous research) would provide additional protective space for the bacterial spores.

1.2 Object of the study

The paper deals with the application and comparison of two polymer-based protective agents (SAP powder and PVA water solution) in cementitious composite containing bacteria and nutrient organic compounds. The influence of the applied protective agents on the material's properties (specifically on consistency and strengths) was determined via cement-flow table test, three-point bending, and

compression test. Further, the self-healing was observed on cracked specimens, which were exposed for 28 days to various conditions (room temperature, low temperature, and freeze cycles). The healing efficiency was determined based on visual investigations using high-resolution photography, 3D scanning microscopy, and dynamic modulus recovery.

1.3 Research motivation and need for research

The presented study expands the existing research by an application of two protective agents (SAP and PVA) into the bio-based self-healing concrete. Further, the main motivation of the study was to provide a unique comparison of the material's crack-sealing potential in non-optimal in-vitro conditions. As the literature review has shown, only a limited number of studies has focused on the bio-based self-healing applicability at low temperatures, and no records of its behavior after exposition to temperatures below zero were found. Thus, this paper provides a valuable insight into the proposed material's applicability, as well as it indicates the issues on which the future research should focus on.

1.4 Aims and tasks of the study

The aims and tasks of the presented experimental study were:

- To determine the material characteristics of the proposed cement composite containing SAP and PVA protective agents.
- To evaluate the impacts of the applied protective agents on the material's crack-sealing potential.
- To describe and compare the crack-sealing potential under various conditions (room vs. low temperature).
- To determine the impact of freeze cycles on the crack-sealing, thus, to determine the survival and subsequent viability of the embedded bacterial spores.

2. Materials and methods

2.1. Materials

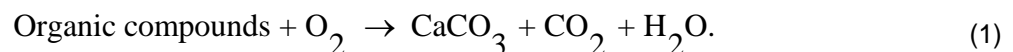
Ordinary Portland cement CEM I 42.5 R conforming to the standard EN 197-1 obtained from Závod Mokrý, Czech Republic was used for all of the series in the study. Fine aggregates with maximum grain size 1.0 mm and medium aggregates with maximum grain size 2.0 mm, both obtained from Provodínské písky a.s., Czech Republic, were applied.

For the mix preparation, distilled water was used in all cases for the sake of improved reproducibility of the experiment. Especially in the case of the SAP addition, the ionic composition of the applied mixing water may affect the results significantly. As demonstrated in our preliminary research [25], the absorption capacity of the applied SAP can reach up to 1.6 times higher values in distilled water than in tap water available in the laboratory location (Dejvice, Prague, Czech Republic).

2.2. The bacterial healing agent

Alkaliphilic and alkalitolerant, aerobic endospore-forming bacteria *Bacillus pseudofirmus* was used in this study. The bacterium (LMG 17944) was obtained from Belgian Coordinated Collections of Microorganisms (BCCM). The culture and sporulation media were prepared according to the BCCM prescriptions.

The calcium carbonate precipitation, thus the targeted crack-sealing, is achieved in the case of *Bacillus pseudofirmus* through degradation of organic compounds according to the following reaction [4]:



It follows that it is crucial to provide the organic compounds (calcium source and metabolic activator) externally, as they are not present in the concrete mix itself. In this study, the nutrients necessary for the calcite production by the bacteria were selected based on the existing literature and own preliminary testing [26]. Yeast extract obtained from Carl Roth GmbH + Co. KG, Germany was used as a metabolic activator. Calcium lactate, $\text{C}_6\text{H}_{10}\text{CaO}_6 \cdot 5\text{H}_2\text{O}$, purity ε 98 %, obtained from Carl Roth GmbH + Co. KG, Germany, was applied as a calcium source.

2.3. The protective agents

Powdered dry SAP (a cross-linked acrylamide/acrylic acid copolymer, potassium salt obtained from Evonik Industries AG, Germany) and 16 % PVA aqueous solution (consisting of 13 % polyvinyl alcohol and 4 % polyvinyl acetate, obtained from FISHEMA s.r.o., Czech Republic) were applied as protective admixtures.

2.4. Mix design, mixing, specimens, and curing

In Table 1, mix compositions of the prepared series are shown. All of the series (including control) contained the same amount of Portland cement, fine and medium aggregates, and nutrients necessary for the biocalcification. Based on the existing literature [4, 27, 28] and own experiments [26], calcium lactate in a dosage of 3.0 % of cement weight was chosen as the calcium source. Yeast extract was applied in a dosage of 0.45 % of cement weight. Although some suggested a maximal value of 0.85 % [12], our preliminary investigations indicated an unacceptable drastic drop in the compressive strength [26].

Generally, the base value of the water/cement ratio (w/c) was 0.5. In the case of SAP series, the w/c was slightly increased (additional 15 g of distilled water per 1 g of SAP based on our previous research [25]) in order to compensate for the liquid uptake by SAP, while preserving the paste flowability. On the contrary, the amount of mixing water in the PVA series was reduced by the amount of water present in the 16 % PVA water solution. Thus, the overall w/c ratio would correspond to the w/c = 0.5.

SAP was applied at a dose of 0.5 % cement weight, 16 % aqueous PVA solution at a dose corresponding to 1 % PVA cement weight. The bacteria were applied in the form of spores (their preparation described elsewhere [30]), which were thoroughly dispersed in the corresponding amount of mixing water (BAC and BAC_SAP) or the PVA aqueous solution (BAC_PVA). The final concentration of colony-forming units (CFU) per 1 ml of the mixing water (including the amount in the PVA solution) was around 8×10^6 .

Table 1. Composition of the mixtures (values in [kg/m³]).

Compound	CTRL [kg/m ³]	CTRL_SAP [kg/m ³]	CTRL_PVA [kg/m ³]	BAC [kg/m ³]	BAC_SAP [kg/m ³]	BAC_PVA [kg/m ³]
Portland cem.	586	586	586	586	586	586
Distilled water	293	337	262	293	337	262
Medium agg.	440	440	440	440	440	440
Fine agg.	1319	1319	1319	1319	1319	1319
SAP	no	2.93	no	no	2.93	no
16 % PVA	no	no	36,63	no	no	36.63
Calcium lactate	17.58	17.58	17.58	17.58	17.58	17.58
Yeast extract	2.64	2.64	2.64	2.64	2.64	2.64
Bacteria [CFU/ml]	no	no	no	8×10^6	8×10^6	8×10^6

The mixing procedure was kept identical in all cases. Yeast extract was homogenized with cement prior to mixing and calcium lactate was dissolved in mixing water. In the case of SAP and PVA series, both of the polymers were applied alongside cement and mixed prior to the aggregate and water addition.

From the prepared mixes, two types of specimens were prepared – specimens for mechanical testing and specimens for crack-sealing investigations. All of the specimens were prepared in triplicates for each mix design and testing method. Both of the types were casted in $40 \times 40 \times 160$ mm³ steel molds, thoroughly vibrated using a vibrating table. In the case of the specimens intended for the crack-sealing, around 20 profiled steel wires were placed in the middle of the span, approx. 1 cm from the mold top (Fig. 1) in order to ensure the stability of the crack widths.

The molds were then left at room temperature covered with plastic foil for 24 hours to harden. Thereafter, all of the specimens were unmolded and placed in a climate chamber with temperature 24 °C and relative humidity up to 95 % for 28 days. After the end of the curing period, dimensions of the specimens were thoroughly measured, and the samples were weighed.



Figure 1. Preparation of the samples with steel wires for the controlled crack creation.

2.5. Controlled cracking

In order to estimate the healing capacity of the proposed combinations of bacteria and protective methods, the prepared reinforced samples were cracked after the end of the curing period. The cracks were introduced through three-point bending using a calibrated electric loading machine. The loading rate was controlled manually and operatively altered to avoid complete destruction of the sample. The procedure layout is displayed in Fig. 2.

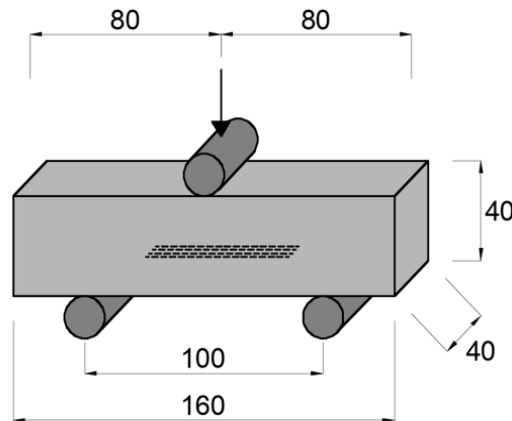


Figure 2. A layout of the crack creation through 3-point bending test.

2.6. Methodology

As already mentioned in the Introduction, the impact of the variety of conditions which may occur in real outside environment is generally neglected in the studies dealing with the bio-based self-healing concrete. To address the issue in this paper, the samples were subjected to three different conditions: ideal, low temperature and temperatures below the freezing point.

The ideal environment (25 ± 2 °C) served as the reference. This value also more or less corresponds to the highest reachable average month temperatures in the place of our research – the Central Europe region. To inspect the healing potential in the ideal conditions, the cracked samples were placed into separate plastic containers filled with tap water and left at the given temperature for 28 days. All of the series were exhibited to the ideal conditions in order to obtain a complete overview of each material's healing capacity. Thus, the contribution of bacteria and each protective method to the healing process could be determined.

The temperature of 10 °C was chosen for the investigation at low temperatures. In the place of our research, Czech Republic, the long-term air temperature normal (1981-2010) reaches and exceeds this value from May to August, i.e. in 5 months of the year, according to the data from the Czech Hydrometeorological Institute. In the case of sufficient crack sealing at this temperature, the self-healing could potentially take place for a large part of the year, thus the material could be declared applicable in the Central European region. In order to inspect this hypothesis, identically as in the ideal conditions, the cracked samples were submerged in water in plastic containers. The containers were then placed in a climate chamber with a controlled temperature of 10 °C for 28 days. In this case, only specimens with bacteria and protective polymers (i.e. BAC_SAP and BAC_PVA) and control (CTRL) were used.

An investigation of the impact of temperatures below the freezing point on the self-healing ability is a unique extension of the current state of the art. Although the crack sealing due to the metabolic activity of bacteria at freezing temperatures is not expected, it is crucial to answer the question, whether the bacteria immobilized in the cementitious material/protective polymer can withstand these conditions and restore its activity once the temperature raises. To simulate the freezing conditions, the cracked samples, prior to any water submersion, were placed into a freeze-thaw chamber. Through air flow, the temperature was precisely and gradually varied from 0 °C to -5 °C. The time of one cycle was 24 hours (Fig. 3). The samples were left at the chamber for 14 days (i.e. 14 cycles).

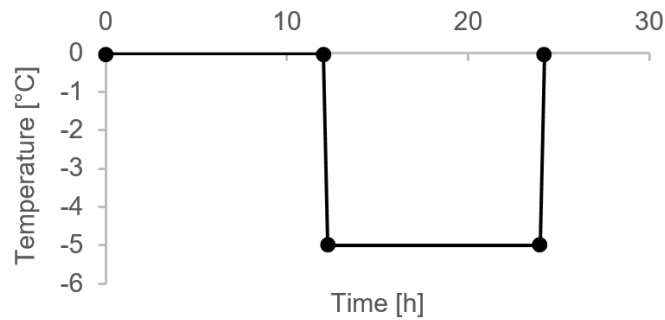


Figure 3. The temperature course of one freezing cycle.

Although such conditions do not necessarily correspond completely to reality, they are sufficiently testing a range of frequently occurring values in a relatively short test time. After the below-zero temperature cycles in the chamber, the samples were taken out and placed into water-filled containers in ideal conditions (as described above) for 28 days. As in the previous case, only specimens with protective polymers (i.e. BAC_SAP and BAC_PVA) and control (CTRL) were used.

2.7. Test methods

The main goal of this paper is to identify the properties of the proposed bacteria-polymer cementitious composites and determine their crack-sealing ability under various conditions. To obtain the information about the prepared materials, a series of mechanical and rheological tests were performed. The crack sealing potential was inspected through visual investigations and dynamic modulus recovery.

2.7.1. Consistency and mechanical tests

In order to determine the consistency of the prepared fresh cementitious composites, prior to the specimen casting, part of each paste was taken and submitted to a cement flow table test (i.e. determination of the spreading diameter). The procedure was performed according to the relevant standard [29]. Consistency was evaluated for the non-bacterial series as bacteria itself, based on the literature, was not expected to influence the property to a noticeable extent.

After the end of the curing period (i.e. 28 days from casting), the unreinforced prismatic specimens ($40 \times 40 \times 160 \text{ mm}^3$) were submitted to a three-point bending test. Subsequently, a compression test was run on the halves left after the bending. In both cases, the specimens loading was run in a deflection-controlled mode using a calibrated electric loading machine. Deflection and loading force values were recorded and analyzed using software (SMAPS). The procedures were performed according to the relevant standard [32]. As well as in the case of consistency measurements, the mechanical properties were determined only on the non-bacterial series.

2.7.2. Visual inspections of the crack healing efficiency

One of the key tasks of this paper is to determine the crack sealing efficiency of the proposed cementitious bacteria-polymer composites in various conditions. In this study, the maximum sealed crack width was selected as the basic indicator of the self-healing potential. Through this value, the extent of the crack sealing can be easily compared through the individual series without the need for uniformed damages. The average maximum healed crack width (Δw_{\max}) was determined as

$$\Delta w_{\max} = \frac{\sum w_{\max}}{n}, \quad (2)$$

where w_{\max} is the maximum crack width that was sealed in each specimen and n is the number of specimens in each series.

In order to document the development of the crack sealing, all of the cracked reinforced specimens were subjected to high-resolution photography at the beginning of the healing period, and after 28 days in the respective environment. To obtain further information about the crack-closure, selected specimens were also additionally scanned with a 3D scanning optical microscope.

2.7.3. Dynamic Young's modulus recovery

The crack-sealing in the bio-based concrete primarily aims to the extension of the structure's durability, thus improvement of the material's water-tightness through reduction of the crack area. However, recovery of mechanical properties would surely be a welcome side effect. Furthermore, the information

about the changed properties may appropriately supplement the information obtained from the visual assessments.

In this paper, the dynamic modulus was measured on all of the reinforced specimens before the cracking, after the cracking and after the healing period. For the quantity evaluation, the Resonance Frequency dynamic methodology was applied.

The Resonance Frequency dynamic method is a non-destructive test for determination of dynamic modulus (E_d) based on the responses obtained from a vibrating signal induced in the specimen. The resonance frequency of the specimen, which produces the maximum amplitude of vibration, is then used to calculate the corresponding E_d value [31]. For the evaluation, the Brüel & Kjaer assembly (measurement station type 3560-B-120, type 4519-003 acceleration transducers, an 8206 impact hammer type, and a computer) was used as described elsewhere [32].

The dynamic Young's modulus was evaluated based on the longitudinal natural frequency of the samples as

$$E_{d,l} = \frac{4lmf_l^2}{bt}, \quad (3)$$

where $E_{d,l}$ is the dynamic Young's modulus [Pa], l is the sample length [m], m is the sample mass [kg], f_l is the basic longitudinal natural frequency of the sample [Hz], b is the sample thickness [m], and t is the sample height [m] [32].

3. Results

3.1. Consistency

The comparison (Tab. 2) between the spreading of the control mix (CTRL) and mix containing SAP (CTRL_SAP) shows that the applied amount of extra mixing water (15 g distilled water per 1 g SAP) leads to a paste with consistency almost identical to the control one. Thus, the SAP liquid uptake in this specific mix design is close to the "extra mixing water" value which was applied. However, it must not be forgotten that due to the extreme sensitivity of the SAP absorption to the ionic composition of the soaking solution, the results might vary greatly with different w/c ratio or nutritive additions (calcium lactate and yeast extract), see our previous study [25].

The addition of PVA water solution led to appreciably more flowable paste compared to the control (Tab. 2). This result contradicts with the majority of studies where the PVA addition generally caused increased viscosity but reduced consistency [23]. However, the studies dealing with the water-soluble cementitious composites frequently use much lower w/c ratios (close to 0.3) [22, 33]. Thus, the results cannot be compared directly as the overall water content might influence the PVA behavior in the material greatly.

Table 2. The results of the flowability test – the initial spreading diameter and final spreading diameter after the dropping.

Mix type	Initial spreading	Final spreading
	[mm]	[mm]
CTRL	80	160
CTRL_SAP	80	159
CTRL_PVA	125	183

3.2. Tensile and compressive strength

The mechanical tests revealed several important aspects of the cementitious composite with polymer additions applied in this study. The mean values of the measured quantities are shown in Fig. 3. Firstly, the proposed dosage of the nutritive compounds (3 % wt. of cement of calcium lactate and 0.45 % wt. of cement of yeast extract) proved to be suitable as the compressive and tensile strength reached sufficiently high values (mean values 39.4 MPa and 6.4 MPa, respectively).

The series CTRL_SAP evinced satisfactory behavior in tension. Its tensile strength reached slightly higher values compared to the control mix (the mean value about 7 % greater). On the other hand, the applied alterations of the mix caused rather significant drop in the compressive strength. The mean value of the compressive strength was about 30 % lower compared to the control.

The addition of 1 % wt. of cement of PVA (in the form of 16 % water solution) in the series CTRL_PVA resulted in a drastically weaker material in both cases. The tensile strength reached only 44 % of the control mix strength, the compressive strength as low as 21 %. This finding contradicts with the results presented elsewhere as generally, the compressive strength decreased similarly as in our case, but the tensile strengths tended to be improved [21, 32].

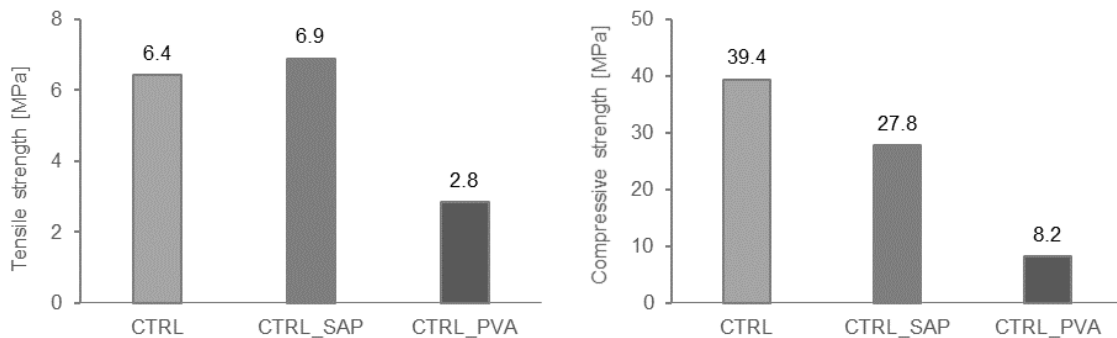


Figure 4. The mean values of tensile (left) and compressive (right) strengths of the non-bacterial mixes obtained through the mechanical tests.

3.3. Visual inspections of the crack healing efficiency

In this work, we sought to establish the applicability of the proposed bio-based self-healing concrete in other than ideal in-vitro conditions, thus extending the scope of the majority of earlier studies. In Fig. 5, for the sake of completeness, all values of the average maximum sealed crack width (Δw_{\max}) that could be identified in each series are summarized.

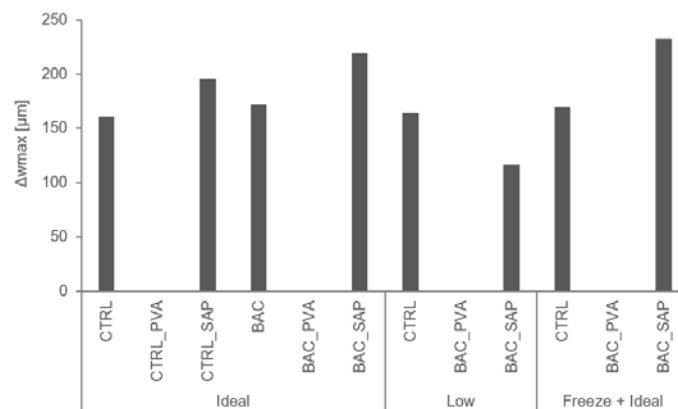


Figure 5. An overview of the average maximum healed crack widths (Δw_{\max}) in each series.

3.3.1. Healing at ideal temperature

The widest range of the cement composite mix designs was subjected to the healing in ideal conditions (i.e. room temperatures as described in the Methodology section). In general, the data suggest that detectable crack-sealing took place in all of the prepared series except the ones containing liquid PVA (Fig. 5). Further, in Fig. 6 and Fig. 7, a selection of the high-resolution photography results is provided.

In the reference series (CTRL), the value of Δw_{\max} reached 161 μm . As in the CTRL series no enhancement of the self-healing capacity was applied, this value can be considered achievable through the natural autogenous crack-sealing ability of the cementitious material in this study.

A slightly higher value (172 μm) was recorded when bacterial spores without any protection (BAC) were incorporated into the cementitious composite. This would indicate that in this study, the natural autogenous crack-sealing potential could be increased by the bacteria-driven CaCO_3 precipitation by around 7 %.

In the ideal conditions, the widest crack parts were sealed in the case of the SAP addition. In the composite with SAP alone (CTRL_SAP), the Δw_{\max} increased to 195 μm . When a combination of SAP and bacterial spores was applied (BAC_SAP), the Δw_{\max} reached as high as 219 μm . These results would indicate the overall positive impact of the SAP addition to the self-healing mechanisms as mentioned in the Introduction.

Furthermore, the difference between the series with only SAP and SAP-bacteria combination was higher (around 12 %) compared to the difference between the reference series (CTRL) and series containing the unprotected bacteria (BAC). Thus, these results may suggest the possible SAP protective potential as it seems to improve the biocalcification process itself.

In this study, as mentioned previously, the self-healing potential of PVA-based cement composite series (CTRL_PVA and BAC_PVA) showed to be completely disappointing as no crack-sealing was detectable in the case of the liquid PVA addition. This result is somewhat surprising, as the PVA presence seems to not only inhibit the biocalcification, but also the natural autogenous self-healing.

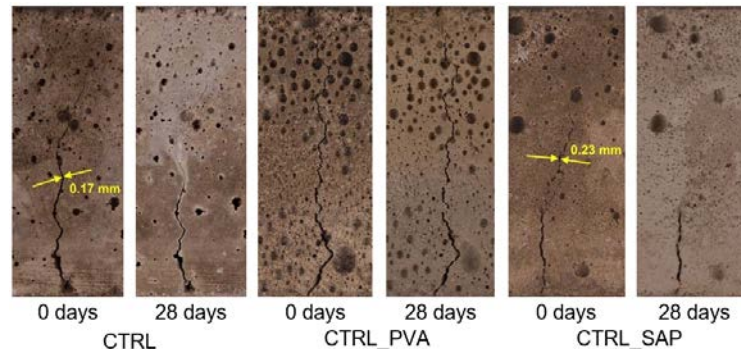


Figure 6. High-resolution photography before (0 days) and after the healing period (28 days) in ideal conditions of the non-bacterial samples. The maximum healed crack width on the individual samples is marked.

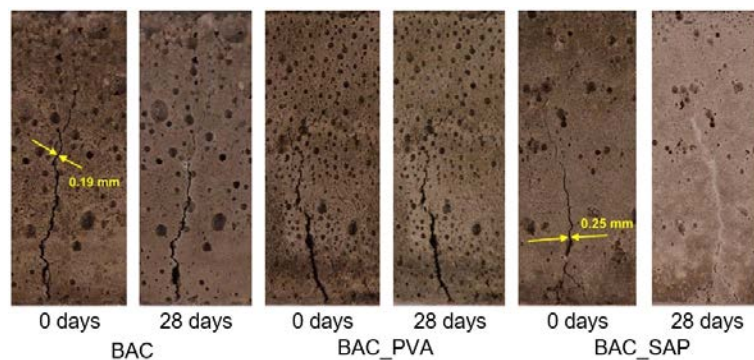


Figure 7. High-resolution photography before (0 days) and after the healing period (28 days) in ideal conditions of the bacterial samples. The maximum healed crack width on the individual samples is marked.

In Fig. 8, details of selected cracked specimens after the healing period are presented. The images are in line with the previous findings. In the case of BAC and BAC_SAP, the cracks are almost completely sealed with white crystalline precipitates. In the cracked BAC_PVA specimen, some formation of the precipitates can be also seen on the crack surfaces; however, closing of the crack was not achieved.

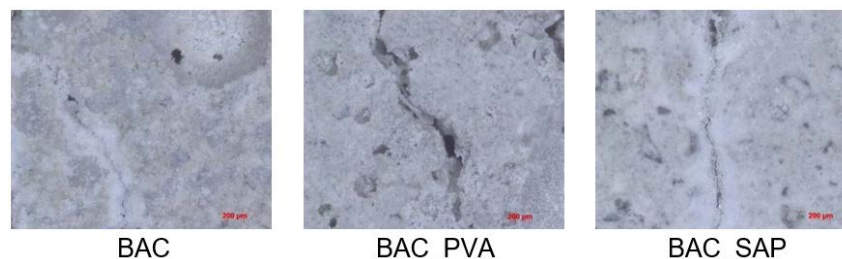


Figure 8. Images obtained using a 3D scanning microscope.

3.3.2. Healing at low temperature

As outlined in the Introduction, the problematic functionality of the bio-based self-healing concrete at lower temperatures was frequently mentioned in earlier studies. In our case, the findings are in line with the pessimistic presumptions (see Fig. 5 for complete overview and Fig. 9 for selected cracks).

In the 10 °C environment, the autogenous crack-sealing detected in the case of CTRL did not noticeably differ from the values achieved in the ideal conditions ($\Delta w_{\max} = 165 \mu\text{m}$). Interestingly, in the

BAC_SAP series, the Δw_{\max} dropped to 117 μm . Thus, it seems that not only the bacteria-driven biocalcification was limited at low temperatures as expected, but also the results indicate that the positive impact of SAP to the self-healing may be inhibited by the temperature as well. Further, it seems that the SAP at low temperatures possibly even limits the natural autogenous crack-sealing capacity as the Δw_{\max} was even lower by 30 % compared to the control series.

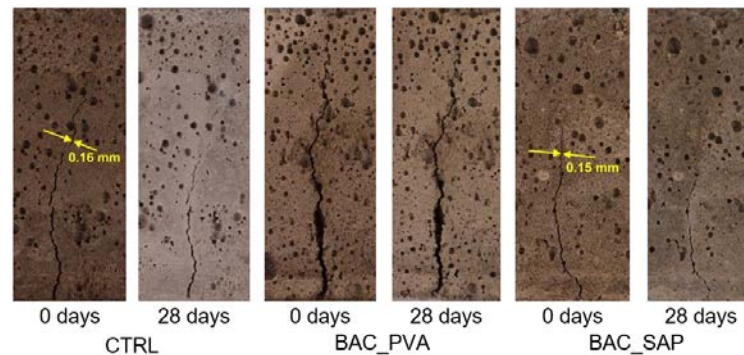


Figure 9. High-resolution photography before (0 days) and after the healing period (28 days) at low temperature of the bacterial (BAC_PVA and BAC_SAP) and non-bacterial (CTRL) samples. The maximum healed crack width on the individual samples is marked.

3.3.3. Healing at ideal temperature after exposure to freeze cycles

In the place of our research (Central European region), sub-zero temperatures are common in the winter season. Thus, as outlined in the Introduction, the regain of metabolic activity of bacteria incorporated in the cementitious matrix is a crucial factor affecting the bio-based self-healing concrete applicability in our climate zone.

In this study, the experiment involving freeze cycling followed by a healing period at room temperature (see Methodology section) yielded interesting results. In Fig. 5, a complete overview of the Δw_{\max} is shown and in Fig. 10, a selection of the high-resolution photography of the cracked specimens exhibited to the respective environment is provided.

From Fig. 5 it can be seen that, interestingly, the Δw_{\max} reached in both CTRL and BAC_SAP even slightly higher values compared to the series without the freeze treatment (170 and 233 μm , respectively). However, the difference between the two mentioned series remained almost identical in both of the environments i.e. around 35 % increase in the case of BAC_SAP. Thus, the bacteria viability was not negatively affected by the freezing cycles, possibly thanks to the SAP that served as a sufficient protective method.

Consistently with the previous results, even after the freeze treatment, no crack-sealing could be observed in the series containing liquid PVA as illustrated in Fig. 5 and Fig. 10.

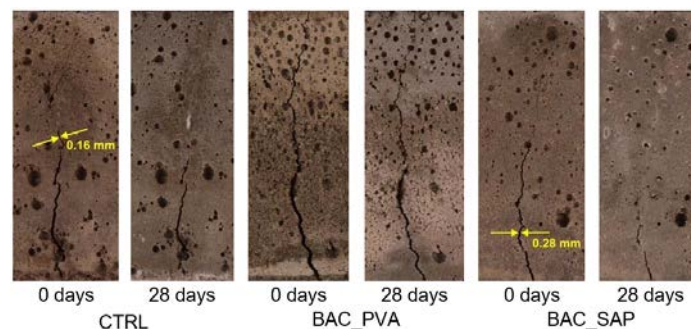


Figure 10. High-resolution photography before (0 days) and after the freeze cycles and healing period (28 days) in ideal conditions of the bacterial (BAC_PVA and BAC_SAP) and non-bacterial (CTRL) samples. The maximum healed crack width on the individual samples is marked.

3.4. Dynamic Young's modulus recovery

In order to detect possible recovery of mechanical properties (namely dynamic modulus of elasticity E_d) caused by the crack-sealing, the non-destructive resonance frequency dynamic method was applied on the reinforced specimens in this study. In Fig. 11, the mean values of $E_{d,1}$ evaluated from longitudinal

vibration measured on the specimens before cracking can be seen. These values more or less correspond to the tendencies noticeable from the mechanical tests – the addition of PVA generally caused drop of the monitored quantity, whereas the SAP series values were around the control values. After the controlled cracking, the value of $E_{d,l}$ in all of the series was zero as expected.

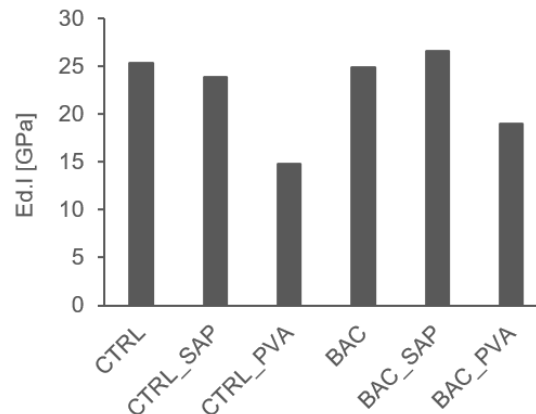


Figure 11. The mean values of the dynamic modulus of elasticity E_d measured on the uncracked specimens.

Measurements after the end of the healing period were far from complete as it was possible to detect the longitudinal frequency only for a fraction of the samples; for the rest $E_{d,l}$ remained zero. Overview of all the successfully measured samples is given in Table 2. Provided that the measurement of the longitudinal frequency could be accomplished only if the filling of the crack was sufficiently rigid and solid, the data would suggest that the combination of bacteria and SAP leads to the most reliable crack-sealing as the majority of measurable samples was from the BAC_SAP series in all of the temperature conditions. Further, the recovery rate (healed/uncracked specimen) seemed to be consistently the highest in the case of BAC_SAP series (as much as 51 %).

Table 2. Values of E_d measured on uncracked specimens, after cracking, and after the healing period. Recovery represents the ratio Healed to Uncracked values.

Environment	Specimen n.	E_d [GPa]			Recovery [%]
		Uncracked	Cracked	Healed	
Ideal	CTRL 1.3	26	0	9	35
	CTRL_SAP 1.1	23	0	5	23
	BAC 1.1	25	0	8	32
	BAC 1.2	25	0	10	38
	BAC 1.3	24	0	6	25
	BAC_PVA 1.1	19	0	6	33
	BAC_SAP 1.1	27	0	10	39
	BAC_SAP 1.2	27	0	10	38
	BAC_SAP 1.3	26	0	13	51
	BAC_SAP 1.3	26	0	13	51
Freeze	CTRL 3.1	27	0	8	31
	BAC_SAP 3.1	27	0	9	34
	BAC_SAP 3.2	27	0	6	22
Low	BAC_SAP 2.2	26	0	7	27

4. Discussion

In this paper, two different compositions of the bio-based self-healing concrete were proposed and investigated. Firstly, the materials characteristics of the proposed cementitious composites were determined. The flowability table test showed that when enriching the bio-based cement composite with SAP, a dose of extra mixing water (15 g distilled water per 1 g SAP) ensures preservation of the paste workability. The test further revealed that addition of PVA (1 % wt. of cement) leads to a more flowable paste compared to the control.

The performed mechanical tests provided information about the strengths of the proposed cement composites. According to the 3-point bending test, the addition of 0.5 % wt. of cement of SAP and extra

mixing water lead to improvement of the material's tensile strength. On the other hand, the addition of liquid PVA caused a significant drop of the tensile strength. The compressive test showed that the cement composite containing SAP in the applied dosage is a slightly weaker material in compression compared to the control. In the case of PVA application, similarly to the tensile strength, the compressive strength was lowered dramatically compared to the reference in our study.

The main aim of this paper was to provide comparison of the crack-sealing potential of the bio-based self-healing concrete containing SAP/PVA in other than ideal conditions. First of all, however, it should be noted that the overall efficiency of the crack closure in this experiment is generally lower compared to the values reported elsewhere. In our case, the maximum healed cracked width was around 300 μm (BAC_SAP), whereas other studies described sealing of cracks with widths up to 400-700 μm [5, 8, 20]. However, we must take into consideration that even scattering of the autogenous crack-sealing itself throughout the studies is considerable. This phenomenon shows how complex it is to quantify the material's efficiency, as it is influenced by a large number of, in most cases, volatile factors (such as mix design, w/c ratio, state of the applied bacteria, possibly the cement chemistry etc.).

At the ideal temperature, the visual investigations indicated that SAP may increase the natural autogenous crack-sealing capacity as the observed value Δw_{max} was around 20 % higher than control. This finding is in line with the results presented elsewhere [18, 19]. Further the SAP presence seemed to improve the biocalcification efficiency based on the visual inspections – the Δw_{max} of bacteria-SAP composite reached around 35 % higher value compared to control. This conclusion was also presented in an earlier study [20]. The investigation of dynamic modulus recovery indicated similar tendencies at the ideal temperature. The majority of the cracked specimens in which the value $E_{d,l}$ could be measured belonged to the BAC_SAP series.

Further research should be focused on the bacteria-SAP combination in conditions with a lower/inconsistent water supply. In this environment, the positive impact of SAP on autogenous crack-sealing and biocalcification might be even more pronounced as the SAP absorption capacity could ensure the needed moisture for both of the self-healing mechanisms.

Interestingly, in our study, the SAP had a slight negative impact on the self-healing at 10 °C based on the visual investigation. Although it is possible to assume that the biocalcification process was completely inhibited at this temperature, the SAP sample showed even worse results than the control. However, this finding completely contradicts with the dynamic modulus measurements as $E_{d,l}$ could be recorded only on the specimen containing bacteria and SAP.

As to the knowledge of the authors, this experiment is first of its own kind, and the mechanisms of the polymer's functionality in the cement composite at low temperatures are unknown. However, the finding provides an interesting indicator of what the future research should be focused on in terms of the SAP impact on the autogenous self-healing.

Unique results were obtained by research of the self-healing in the proposed materials after freeze cycles. In the case of SAP-bacteria composite, the visual inspections showed that the exposure to temperatures below zero did not result in any decrease in the crack-sealing capacity. After 28 days of healing in ideal conditions, the detectable crack-sealing was similar (or even higher) to the series non-treated by the freeze cycling. Similar results were indicated by the dynamic modulus recovery measurements as, again, the majority of successfully measured specimens were from the BAC_SAP series.

In our study, the impact of liquid PVA to the self-healing was disastrous in all of the healing environments. Not only it seems to inhibit the biocalcification process, but also not even any noticeable autogenous crack-sealing occurred in any of the monitored samples. The mechanism behind the negative impact is yet to be discovered as no records of its application in self-healing concrete was found in the existing literature. A possible explanation could lay in a decreased level of cement hydration caused by the polymer. This would also correspond with the results of mechanical characteristics as both the tensile and compressive strength were significantly lower compared to the control. However, further research dealing with this issue would be needed.

5. Conclusions

In the current study, the combination of bacteria *Bacillus pseudofirmus*, nutritional compounds, and SAP or PVA was applied in cement composite in order to evaluate the biologically enhanced material's self-healing potential in various healing conditions. The following conclusions can be drawn based on the current experimental investigation:

- SAP in all probability has a positive impact on the natural autogenous crack-sealing;

- In this paper, the SAP addition seemed to improve the biocalcification process, thus the bacteria driven crack-sealing;
- The SAP functionality might be limited at lower temperatures; however, more research on the exact mechanism is needed;
- The efficiency of the proposed self-healing cement composite containing the combination of SAP and bacterial healing agent did not seem to be affected by the freeze cycles;
- The application of liquid PVA turned out to be unsuitable from the point of view of both material characteristics and self-healing efficiency.

6. Acknowledgement

This paper was prepared thanks to the support of the science foundation of the Czech Republic (GAČR), project "Self-healing of cementitious composites by bacteria-induced calcification" (no. 18-15697S) and project "Durability of concrete structure and assessment of its life cycle" (SGS19/149/OHK1/3T/11).

References

1. Neville, A.M., Brooks, J.J. Properties of concrete. 5th edn. Pearson Education Ltd. Harlow, England, 2011. 442 p.
2. Ehrlich, H.L., Newman, D.K. Ehrlich's Geomicrobiology. 6th edn. CRC Press. Boca Raton, Florida, USA, 2016. 635 p.
3. Jonkers, H., Schlangen, E. Development of a bacteria-based self healing concrete. Tailor Made Concrete Structures. Amsterdam, 2008. Pp. 109–115. DOI: 10.1201/9781439828410
4. Jonkers, H.M., Thijssen, A., Muyzer, G., Copuroglu, O., Schlangen, E. Application of bacteria as self-healing agent for the development of sustainable concrete. Ecological Engineering. 2010. 36(2). Pp. 230–235. DOI: 10.1016/j.ecoleng.2008.12.036
5. Alghamri, R., Kanellopoulos, A., Al-Tabbaa, A. Impregnation and encapsulation of lightweight aggregates for self-healing concrete. Construction and Building Materials. 2016. 124. Pp. 910–921. DOI: 10.1016/j.conbuildmat.2016.07.143
6. Tziviloglou, E., Wiktor, V., Jonkers, H.M., Schlangen, E. Bacteria-based self-healing concrete to increase liquid tightness of cracks. Construction and Building Materials. 2016. 122. Pp. 118–125. DOI: 10.1016/j.conbuildmat.2016.06.080
7. Chen, H., Qian, C., Huang, H. Self-healing cementitious materials based on bacteria and nutrients immobilized respectively. Construction and Building Materials. 2016. 126. Pp. 297–303. DOI: 10.1016/j.conbuildmat.2016.09.023
8. Wiktor, V., Jonkers, H.M. Quantification of crack-healing in novel bacteria-based self-healing concrete. Cement and Concrete Composites. 2011. 33(7). Pp. 763–770. DOI: 10.1016/j.cemconcomp.2011.03.012
9. Wang, J., Van Tittelboom, K., De Belie, N., Verstraete, W. Use of silica gel or polyurethane immobilized bacteria for self-healing concrete. Construction and Building Materials. 2012. 26 (1). Pp. 532–540. DOI: 10.1016/j.conbuildmat.2011.06.054
10. Wang, J.Y., Snoeck, D., Van Vlierberghe, S., Verstraete, W., De Belie, N. Application of hydrogel encapsulated carbonate precipitating bacteria for approaching a realistic self-healing in concrete Construction and Building Materials. 2014. 68. Pp. 110–119. DOI: 10.1016/j.conbuildmat.2014.06.018
11. Wang, J., Mignon, A., Trensou, G., Van Vlierberghe, S., Boon, N., De Belie, N. Screening of pH-responsive Hydrogels for Concrete Crack Self-sealing Microorganisms-cementitious materials interactions: final conference of RILEM TC 253-MCI. Toulouse. 2018. Pp. 405–412.
12. Wang, J.Y., Soens, H., Verstraete, W., De Belie, N. Self-healing concrete by use of microencapsulated bacterial spores. Cement and Concrete Research. 2014. 56. Pp. 139–152. DOI: 10.1016/j.cemconres.2013.11.009
13. Ersan, Y.C., Boon, N., De Belie, N. Granules with activated compact denitrifying core (ACDC) for self-healing concrete with corrosion protection functionality. Microorganisms-cementitious materials interactions: final conference of RILEM TC 253-MCI. Toulouse. 2018. Pp. 475–484.
14. Territorial Air Temperatures. Historical Data of Czech Hydrometeorological Institute. [Online]. URL: <https://intranet.chmi.cz/historicka-data/pocasi/uzemni-teploty?!=en>
15. Bacillus pseudofirmus. [Online]. URL: <https://bacdiv.dsmz.de/pdf.php?id=1110&doi=10.13145/bacdiv1110.20170829.2>
16. Palin, D., Wiktor, V., Jonkers, H.M. A bacteria-based self-healing cementitious composite for application in low-temperature marine environments. Biomimetics. 2017. 2 (3). Article no. 13. DOI: 10.3390/biomimetics2030013
17. Paine, K., Sharma, T., Alazhari, M., Heath, A., Cooper, R. Application and performance of bacteria-based self-healing concrete. Microorganisms-cementitious materials interactions: final conference of RILEM TC 253-MCI. Toulouse. 2018. Pp. 387–394.
18. Snoeck, D., Van Vlierberghe, S., Steuperaert, S., Dubruel, P., De Belie, N. Self-healing cementitious materials by the combination of microfibrils and superabsorbent polymers. Journal of Intelligent Material Systems and Structures. 2012. 25 (1). Pp. 13–24. DOI: 10.1177/1045389X12438623
19. Snoeck, D. Superabsorbent polymers to seal and heal cracks in cementitious materials. RILEM Technical Letters. 2018. 3. Pp. 32–38. DOI: 10.21809/rilemtechlett.2018.64
20. Gupta, S., Kua, H.W., Pang, S.D. Healing cement mortar by immobilization of bacteria in biochar: An integrated approach of self-healing and carbon sequestration. Cement and Concrete Composites. 2018. 86. Pp. 238–254. DOI: 10.1016/j.cemconcomp.2017.11.015
21. Pique, T.M., Vazquez, A. Control of hydration rate of polymer modified cements by the addition of organically modified montmorillonites. Cement and Concrete Composites. 2013. 37 (1). Pp. 54–60. DOI: 10.1016/j.cemconcomp.2012.12.006
22. Viswanath, P., Thachil, E.T. Properties of polyvinyl alcohol cement pastes. Materials and Structures. 2008. 41(1). Pp. 123–130. DOI: 10.1617/s11527-007-9224-2
23. Knapen, E., Van Gemert, D. Cement hydration and microstructure formation in the presence of water-soluble polymers. Cement and Concrete Research. 2009. 39 (1). Pp. 6–13. DOI: 10.1016/j.cemconres.2008.10.003

24. Topič, J., Prošek, Z., Indrová, K., Plachý, T., Nežerka, V., Kopecký, L., et al. Effect of PVA modification on the properties of cement composites. *Acta Polytechnica*. 2015. 55 (1). Pp. 64–75. DOI: 10.14311/AP.2015.55.0064
25. Schreiberová, H., Fládr, J., Trtík, T., Chylik, R., Bílý, P. An investigation of the compatibility of different approaches to self-healing concrete: The superabsorbent polymers and microbially induced calcite precipitation. *IOP Conference Series: Materials Science and Engineering*. 2019. 596. Article no. 012039. DOI: 10.1088/1757-899X/596/1/012039
26. Schreiberová, H., Bílý, P., Fládr, J., Šeps, K., Chylik, R., Trtík, T. Impact of the self-healing agent composition on material characteristics of bio-based self-healing concrete. *Case Studies in Construction Materials*. 2019. 11. Article no. e00250. DOI: 10.1016/j.cscm.2019.e00250
27. Luo, M., Qian, C. Influences of bacteria-based self-healing agents on cementitious materials hydration kinetics and compressive strength. *Construction and Building Materials*. 2016. 121. Pp. 659–663. DOI: 10.1016/j.conbuildmat.2016.06.075
28. Chen, C.-C., Cucolloto, M., Balac, M. Evaluation of effect of nutrients, calcium precursors, and bacteria on mechanical properties of mortar specimens. *Microorganisms-cementitious materials interactions: final conference of RILEM TC 253-MCI*. Toulouse. 2018. Pp. 455–463.
29. ČSN EN 1015-3 Methods of test for mortar for masonry – Part 3: Determination of consistence of fresh mortar (by flow table). Czech Standardization Agency. Prague, 2020. 12 p.
30. Schreiberová, H., Bílý, P., Ryparová, P. Applicability of bio-based self-healing concrete in Central European conditions: A preliminary study. *Microorganisms-cementitious materials interactions: final conference of RILEM TC 253-MCI*. Toulouse. 2018. Pp. 501–510.
31. Marques, A.I., Morais, J., Morais, P., Rosario Veiga, M., Santos, C., Candeias, P., Ferreira, J.G. Modulus of elasticity of mortars: Static and dynamic analyses. *Construction and Building Materials*. 2020. 232. Article no. 117216. DOI: 10.1016/j.conbuildmat.2019.117216
32. ČSN EN 12390-5 Testing hardened concrete – Part 5: Flexural strength of test specimens. Czech Standardization Agency. Prague, 2000. 12 p.
33. Singh, N.B., Rai, S. Effect of polyvinyl alcohol on the hydration of cement with rice husk ash. *Cement and Concrete Research*. 2001. 31(2). Pp. 239–243. DOI: 10.1016/S0008-8846(00)00475-0

Contacts:

Hana Schreiberova, schreiberova@fsv.cvut.cz

Tomas Trtik, trtik@fsv.cvut.cz

Roman Chylik, chylik@fsv.cvut.cz

Zdenek Prosek, prosek@fsv.cvut.cz

Karel Seps, seps@fsv.cvut.cz

Josef Fladr, fladr@fsv.cvut.cz

Petr Bily, petr.bily@fsv.cvut.cz

Alena Kohoutkova, kohout@fsv.cvut.cz



DOI: 10.34910/MCE.107.14

Isotropic damage model to simulate failure in reinforced concrete beam

W.A. Al-Kutti^a , T.C. Chernykh^b 

^a Imam Abdulrahman bin Faisal University, Dammam, Saudi Arabia

^b South Ural State University, Chelyabinsk, Russia

*E-mail: wasalem@iau.edu.sa

Keywords: concrete model, isotropic damage, flexural loading, finite element analysis

Abstract. This study investigates the possibility of simulating the behavior of reinforced concrete (RC) beams subjected to flexure using a simplified elasto-isotropic damage. The phenomenological damage concept was used to evaluate stress-induced damage. The influence of the damage on elastic stiffness was used to evaluate mechanical performance with respect to material degradation. RC beams damaged in flexure with 40 %, 60 %, 75 %, and 90 % of ultimate flexural loading were modeled using the COMSOL Multi-physics finite element package to simulate mechanical performance of RC concrete beams. The proposed elasto-damage model predicted the ultimate load of the RC beams with 1 % estimated error. The proposed model showed similar ability to predict the axial strain for the reinforcement steel as the maximum strain in tensile reinforcement. The accuracy of these results were compared with other constitutive models for concrete such as elasto-plastic damage model reported in literature. The outcome of this research paper provides engineers with a simplified approach for analyzing the behavior of RC beams subjected to flexural loading using elasto-damage model.

1. Introduction

Damage mechanics refer to constitutive models characterized by diminished stiffness or a reduction of the secant modulus. Kachanov [1] introduced the concept for use in creep-related models and then later adapted it to describe the progressive failure of metals and composites and to model the behavior of the materials under fatigue. Damage models are used to describe the strain-softening behavior of concrete.

Researchers have developed damage models of varying degrees of sophistication to model damage on material such as concrete [2–21]. Two main approaches have been proposed in how the stiffness degradation to be modeled. Some researchers [3–14] have used elastic and plastic analysis coupled with damage variables representing the reduction in the stiffness. Others [15–20] coupled damage with the elastic analysis.

Besides, several mechanical loading on concrete have been modeled using elastic and plastic analysis coupled with damage. Sun et al. [4] studied the damage evolution and the plasticity development in concrete materials subjected to freeze-thaw and proposed a cohesion reduction parameter to improve the accuracy of previous damage constitutive models for concrete materials. Similar approach was used by Sarikaya and Erkmen [5] in which plastic-damage model for concrete under compression was modeled. Javanmardi and Maheri [6] developed a new algorithm for predicting crack initiation and growth direction in 3D solid concrete using anisotropic damage-plasticity model. In the study, three benchmark problems solved using the proposed algorithm were compared with experimental data and those of other numerical simulations. Javanmardi and Maheri [6] concluded that the proposed anisotropic damage-plasticity model predicted well the crack development and the numerical results match well with the experimental results previously reported in the literature.

Al-Kutti, W.A., Chernykh, T.C. An isotropic damage model to simulate failure in reinforced concrete beam. Magazine of Civil Engineering. 2021. 107(7). Article No. 10714. DOI: 10.34910/MCE.107.14

© Al-Kutti, W.A., Chernykh, T.C., 2021. Published by Peter the Great St. Petersburg Polytechnic University



This work is licensed under a CC BY-NC 4.0

In a comprehensive study, Benin et al. [7] proposed a methodology for identification of mechanical characteristics of the nonlinear material model for concrete. Benin et al. [7] investigated the damage accumulation under monotonous and cyclic loading. The material parameter identification procedure of elastic-plastic-damage concrete model was proposed and validated. In recent study, Bilal et al. [8] proposed a new plastic damage model for concrete with a novel stress decomposition to account for shear induced damage. In their model, a thermodynamic approach was used to derive the constitutive model.

For the elasto-damage model, Labadi and Hannachi [15] proposed a new damage criterion defined as an equivalent strain norm and reported that simple isotropic damage model coupled with the nonlinear elastic deformation can predict accurately the mechanical behavior of concrete. Similar study was conducted by Tao and Phillips [16] where they presented a concrete model based on the elasto-damage model for concrete subjected to bi-axial loading. The numerical and matched well with the experimental results.

Although the above researchers concluded on the suitability of using the elastic and plastic analysis coupled with damage in concrete compared with the elasto-damage model, several others [15–20] debate that the elasto-damage model can predict well the behavior of concrete with less complexity and minimum convergence problem associated in the elasto-plastic damage models. The primary objective of this study is to explore the possibility to simulate the failure of RC beams in flexural using isotropic damage parameters based on an elastic-damage constitutive model. To achieve objective, finite element analysis was conducted using COMSOL FE package and an experimental program was developed to verify the numerical results. The outcome of this research paper will provide more experimental and numerical studies on the suitability of using elasto-damage model on simulation the failure of RC beams subjected to flexural loading.

Amongst the numerous studies modeling damage Mazars et al. [2] first evaluated the influence of damage on the material responsiveness of concrete and evaluated how degradation affected the elastic stiffness of the material. This was then used to model a scalar damage parameter (d). Their research quantified this relationship as:

$$\sigma = E\varepsilon \quad (1)$$

$$E = (1 - d)E_o \quad (2)$$

where E_o and E are the secant (undamaged) and (damaged) modulus, and d is a scalar damage variable. Taher et al. [3] developed an elasto-damage model for concrete using a constitutive law proposed by Popovics [22] for stress-total strain relationship of plain concrete subjected to uniaxial tensile and compressive stress in the form of:

$$\frac{\sigma}{\sigma_u} = \frac{m \left(\frac{\varepsilon}{\varepsilon_u} \right)}{m - 1 + \left(\frac{\varepsilon}{\varepsilon_u} \right)^m} \quad (3)$$

where σ_u and ε_u are peak stress and strain, respectively, and m is a parameter dependent on σ_u . Using equation [3], a relationship between the moduli and damage variable could be obtained as shown in Fig. 1 as the following:

$$E = \frac{\sigma}{\varepsilon} = \frac{m \frac{\sigma_u}{\varepsilon_u}}{m - 1 + \left(\frac{\varepsilon}{\varepsilon_u} \right)^m} \quad (4)$$

$$E_o = E(\varepsilon = 0) = \frac{m\sigma_u}{(m - 1)\varepsilon_u} \quad (5)$$

The scalar damage becomes:

$$d_c = 1 - \frac{E}{E_c} = 1 - \frac{m_c - 1}{m_c - 1 + \left(\frac{\varepsilon_x}{\varepsilon_u}\right)^{m_c}} \text{ for } \varepsilon_x < 0 \text{ (Compression)} \quad (6)$$

$$d_t = 1 - \frac{E}{E_t} = 1 - \frac{m_t - 1}{m_t - 1 + \left(\frac{\varepsilon_x}{\varepsilon_u}\right)^{m_t}} \text{ for } \varepsilon_x < 0 \text{ (Tension)} \quad (7)$$

Where, E_c and E_t are the undamaged secant moduli representing compressive and tensile in units of MPa, respectively. m_c and m_t are the material parameters for compression and tensile induced damage respectively, and ε_x is the total strain in mm/mm.

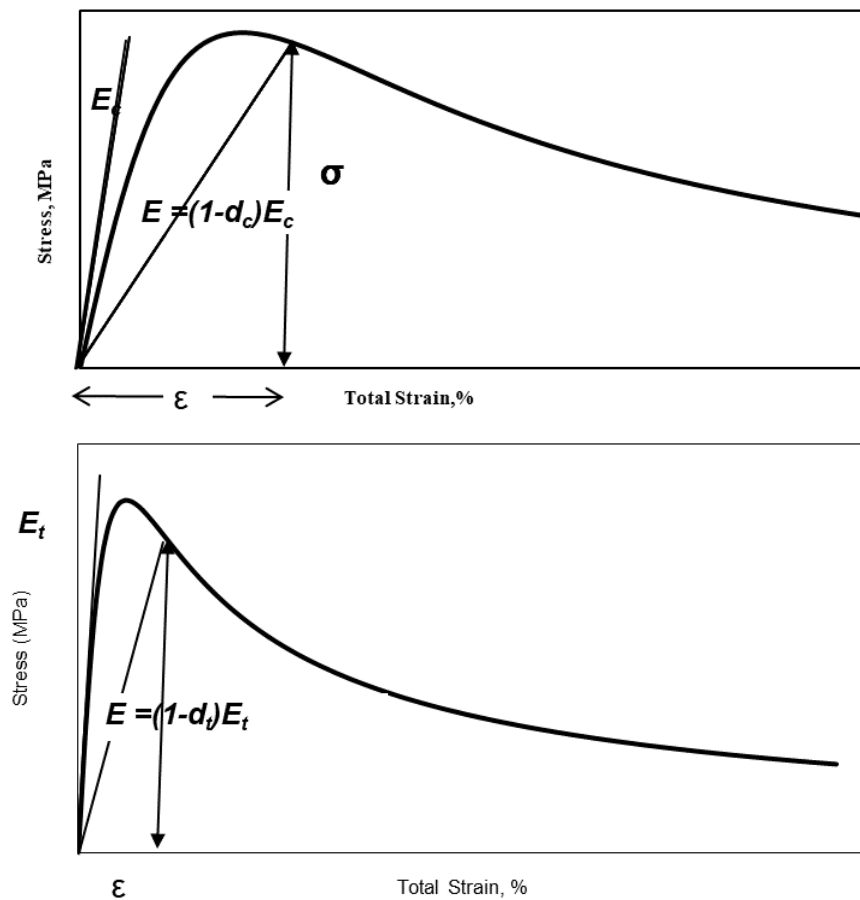


Figure 1. The relationship between scalar damage and uniaxial tensile/compressive stress-total strain curve.

2. Methods

2.1. Testing plan

To achieve the objectives of this study, different concrete samples including reinforced concrete (RC) beams and concrete cylinders were used. Four levels of mechanical loading were applied on the concrete samples as a percentage of the compressive strength of the concrete after 28 days of curing. Using the experimental results, numerical simulation of the mechanical loading leading to damage, would be achieved.

2.2. Cement, aggregates and mix design

ASTM C 150 Type I Portland cement was utilized in all the concrete mixes. Limestone coarse aggregate was used along with dune sand as fine aggregates. The specific gravity and absorption of the coarse and fine aggregates are shown in Table 1. The fine and coarse aggregates were combined such that the coarse aggregate constituted 62 % of total aggregates. The grading of coarse aggregates was

selected conforming to ASTM C 33 and is shown in Table 2. Potable water was used for casting and curing all the concrete specimens and the water to cement ratio was 0.40. Details of the mix ingredients are shown in Table 3.

Table 1. Absorption and Specific Gravity of the Coarse and Fine Aggregates.

Aggregate	Absorption (%)	Bulk Specific Gravity
Coarse Aggregate	2.5	2.54
Fine aggregate	0.5	2.64

Table 2. Grading of Coarse Aggregates.

SIZE (in)	% Retained	Cumulative (% Retained)	Cumulative (% Passing)
¾	0	0	100
½	35	35	65
3/8	35	70	30
3/16	20	90	10
3/32	10	100	0

Table 3. Mixes Ingredients.

Concrete Type	Cement Content (kg/m ³)	w/c	Admixture (kg/m ³)	Aggregate (kg/m ³)
OPC	480	0.40	3.25 (Conplast SP-440)	1725

2.3. Specimens

In this study, the experimental program consists of the following parameters: Ordinary Portland Concrete (**OPC**) and five levels of mechanical loading leading to damage applied on the concrete beams and cylinders as a percentage of compressive strength of concrete after 28 days of curing. The following concrete specimens were cast from each concrete mix:

- (i) 10 reinforced concrete (RC) beams (150 × 150 × 1200 mm) for determining the effect of mechanical damage. Fig. 2 shows the cross-section details of the RC beams. Strain gauges were placed to monitor the mechanical behavior of the RC beams when subjected to the four-point flexural test as shown in Fig. 3.
- (ii) 6 cylindrical concrete specimens (76 × 150 mm) for the determination of compressive strength.

2.4. Curing

After casting, the RC concrete beams were covered with a wet towel for 24 hours and cured in the laboratory under dry conditions for one month. The cylindrical concrete specimens were demolded and cured in water tanks for 28 days.

2.5. Laboratory Tests

The following tests assessed the mechanical properties in damaged and undamaged concrete:

2.5.1 Compressive strength

Concrete specimens were tested for compressive strength after 28 days of water curing. The specimens were capped with a sulfur compound. Prior to capping, the diameter and height of the specimens were measured. The capped specimens were then placed in a compression testing machine (3000 kN capacity). The compressive strength was determined according to ASTM C 39.

2.5.2 Flexural Test

After the beams cured for 28 days under dry laboratory conditions, two RC beams as shown in Figure 4 were loaded by a four point's flexural loading test to failure to determine the ultimate bending moment capacity. During loading, the strain in the reinforcement bars at the bottom of the RC beams was monitored as well as the strain in concrete in the compressive zone. Besides, the deflection at the mid span of the beams was measured using linear variable differential transformers (LVDT). To create mechanical induced

damage, eight RC beams were loaded at 40 %, 60 %, 75 % and 90 % of the ultimate loading capacity of the beams.

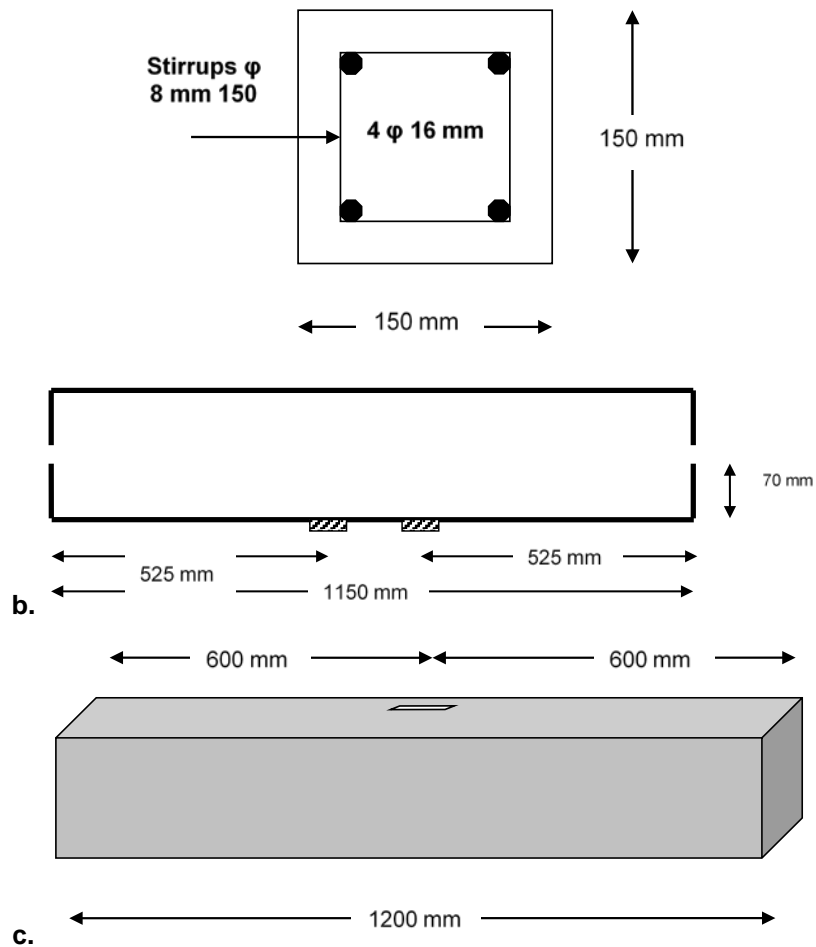


Figure 2. (a) RC beam cross section details, (b) Arrangement for strain gauges in reinforcement bars, (c) Arrangement of strain gauge in concrete.

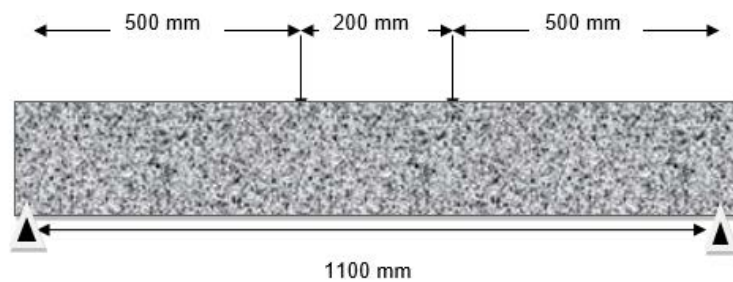


Figure 3. Four-point flexural loading.



Figure 4. Measurements of the strains in reinforcing bars and the deflection at mid span using data logger.

3. Results and Discussion:

3.1. Mechanical Behavior

The results of for the mid span deflection, strain in the reinforcement at mid span all, cracking load and maximum load are mentioned in Table 4 and Fig. 5 through 10. From Fig. 5 through 10, it can be observed that the elastic zone ended at the first cracking loads which were varied between 6.5 to 8 kN with an average of 7.5 kN for all levels of loading. Besides. These results match well with the cracking load calculated using the ACI approach [23] where it was found to be about 7 kN. However, the ACI approach shows higher stiffened behavior than the experimental results after the cracking load.

Table 4. Details of Cracking and Maximum Flexural Loading, Mid Span deflection and Strains in Reinforcement for Damaged RC Beams.

RC Beams	First Crack Load, P_{cr} (kN)	Maximum Load, P (kN)	Mid Span Deflection (mm)	Strain in Reinforcement Steel at Mid Span (μm)
B40	7.5	38	2.5	1500
B60	6.5	62	4.5	2350
B75	7.5	75	5.5	2600
B90	7.5	84	7.0	3400
B100	8	98	9.0	3750

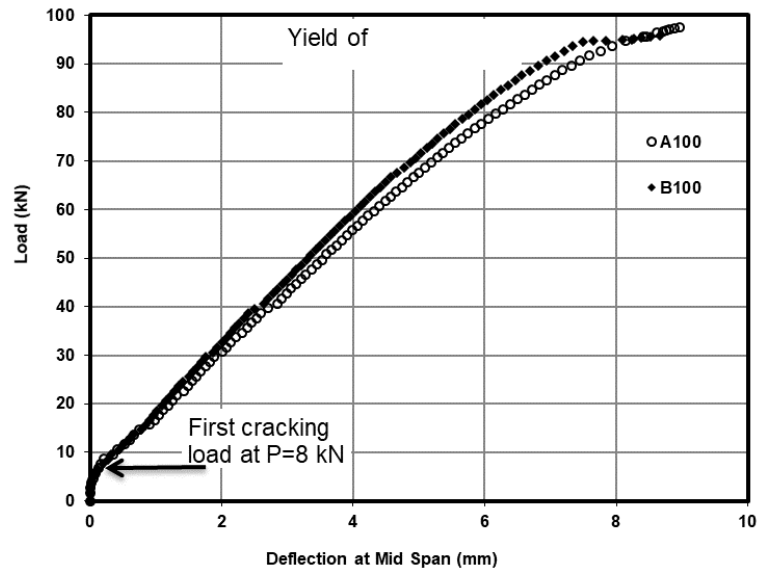


Figure 5. Load – mid span deflection curve for A100 and B100 beams.

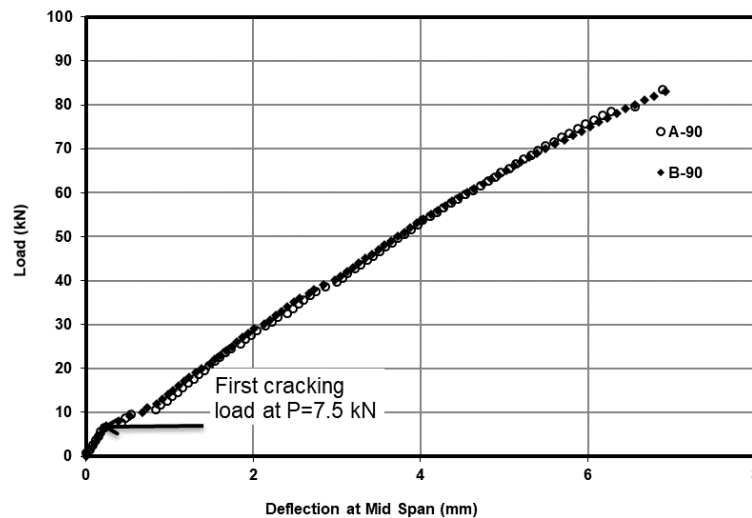


Figure 6. Load – mid span deflection curve for A90 and B90 beams.

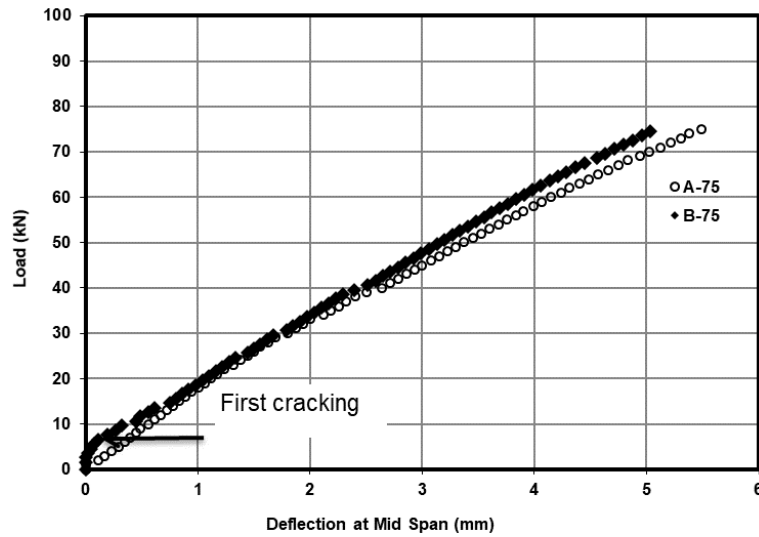


Figure 7. Load – mid span deflection curve for A75 and B75 beams.

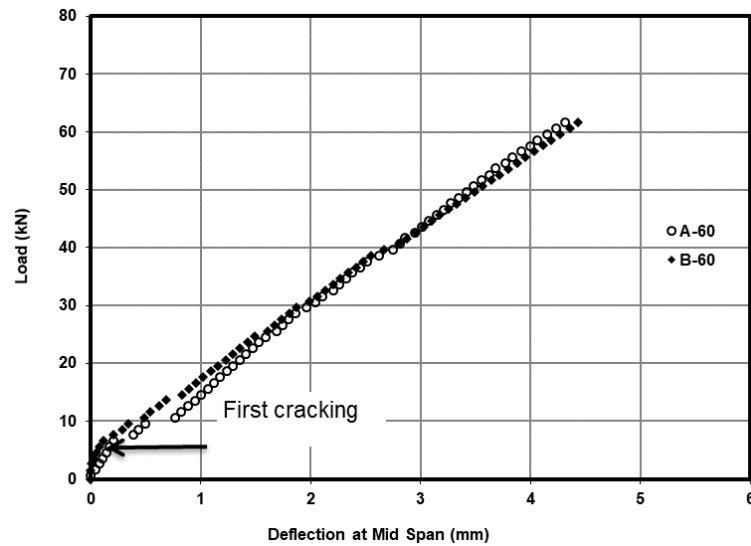


Figure 8. Load – mid span deflection curve for A60 and B60 beams.

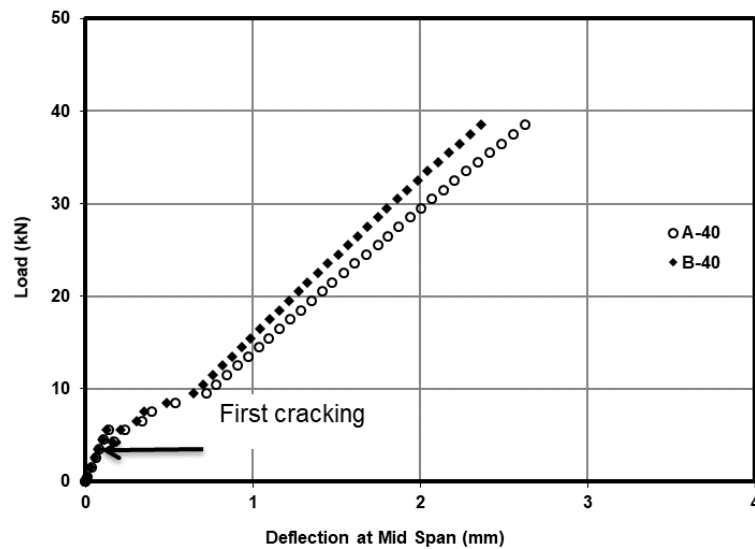


Figure 9. Load – mid span deflection curve for A40 and B40 beams.

The experimental results of the reinforcement axial strain vs. mid span deflection up to failure loading is presented in Fig. 11. The axial strain measurements were monitored at the maximum moment zone about 500 mm from the support and was found to be about 3500 μm at the maximum mid-span deflection of about 9 mm. which indicating the yielding of the reinforcement steel. The cracking map of the RC Beams

at the failure loading is presented in Fig. 12. The maximum cracking depth was found to be about 90 mm. The calculated value of z , based on ACI approach [23], was found to be about 92.4 mm from bottom of the beam which indicates a very close results between the experimental and the ACI approach [23].

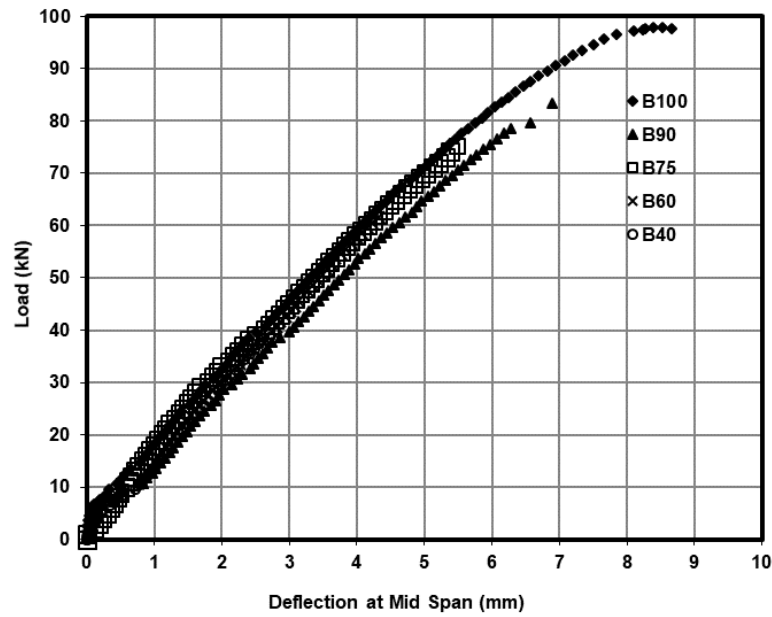


Figure 10. Load – mid span deflection curve for 40 %, 60 %, 75 %, 90 % and 100 % loading.

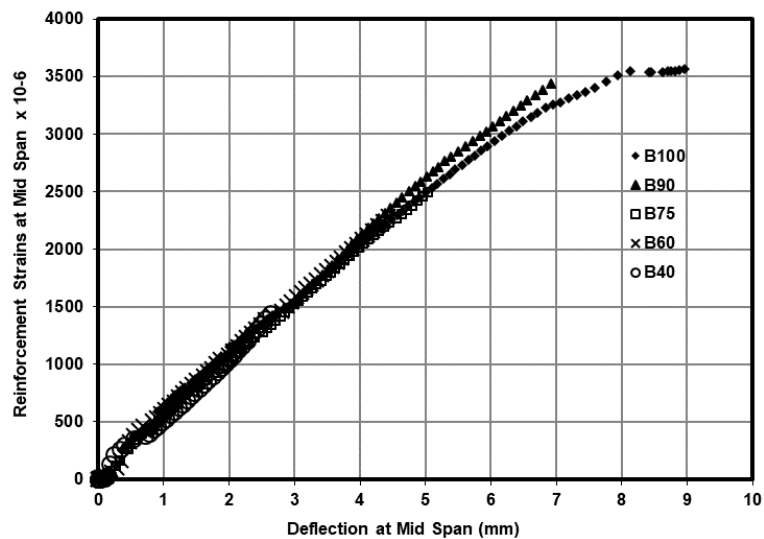


Figure 11. Strain in reinforcement vs mid span deflection curve for 40%, 60%, 75%, 90% and 100% loading.

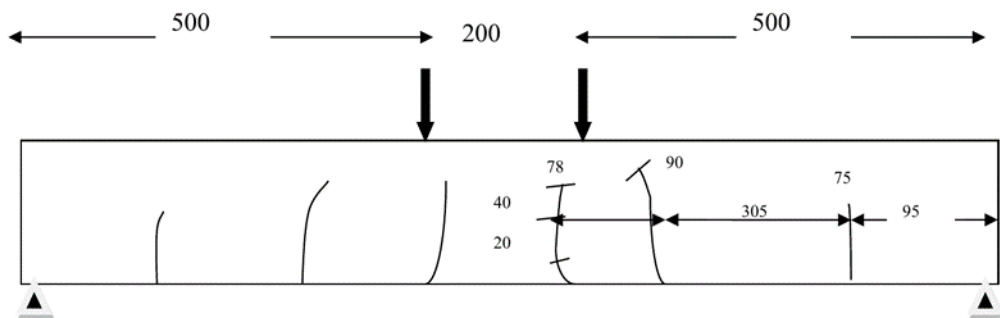


Figure 12. Cracking map of up to 100% loading.

3.2. COMSOL Simulation Steps

COMSOL finite element software [24] was used to simulate flexural behavior of RC using Scalar Damage Parameter as described in equations [1] to [7]. The Drucker-Prager yield criterion was first used to simulate the mechanical behavior of the RC beams in which the Drucker-Prager yield criterion was formulated as

$$f(I, \sqrt{J}) = \sqrt{J} + \alpha I = k \quad (8)$$

Where, $I = \sigma_{kk}$ is the hydrostatic component of the stress tensor, $J = \frac{1}{2} S_{ij} S_{ji}$ is the deviatoric stress tensor invariant, α and k are materials constants which can be related to the friction angle (φ) and cohesion (c) of the Mohr-Coulomb criterion. For plane stress, the relation between the parameters are as follows:

$$\alpha = \frac{\sin \varphi}{\sqrt{3}} \quad k = \frac{2}{\sqrt{3}} c \cos \varphi \quad (9)$$

By the calibration of the experimental $P-\Delta$ curve as shown in Fig. 6 through 10, the cohesion c and the friction angle φ were estimated by parametric study and using COMSOL model. Fig. 13 shows the finite element for the RC beams including boundary conditions of the RC beams. The steel reinforcement was modeled as a plate representing the area of reinforcement in the beam with the same thickness of the concrete section. Von Mises material model was used for the steel reinforcement in which E_s and F_{ys} was 19000 MPa and 560 MPa, respectively. A flow chart for steps required is presented in Fig. 14. Tables 5 shows the parameters used in the COMSOL model.

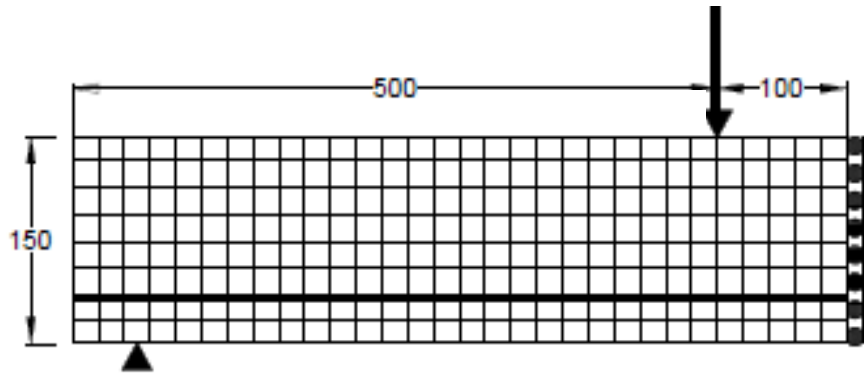


Figure 13. Finite Element Modeling of the RC Beams Subjected to Flexural Loading.

Table 5. COMSOL model parameters.

COMSOL Commands	COMSOL Expression/Parameters	Value
Constants	m_t	1.46
	m_c	3.45
	c	4.8 MPa
	φ	53o
	f_{cr}	4 MPa
	f_u	50 Mpa
	ε_{cr}	1.55e-4
	ε_u	2.3e-3
	F_{ys}	560 Mpa
	α	2.39
	β	15.6

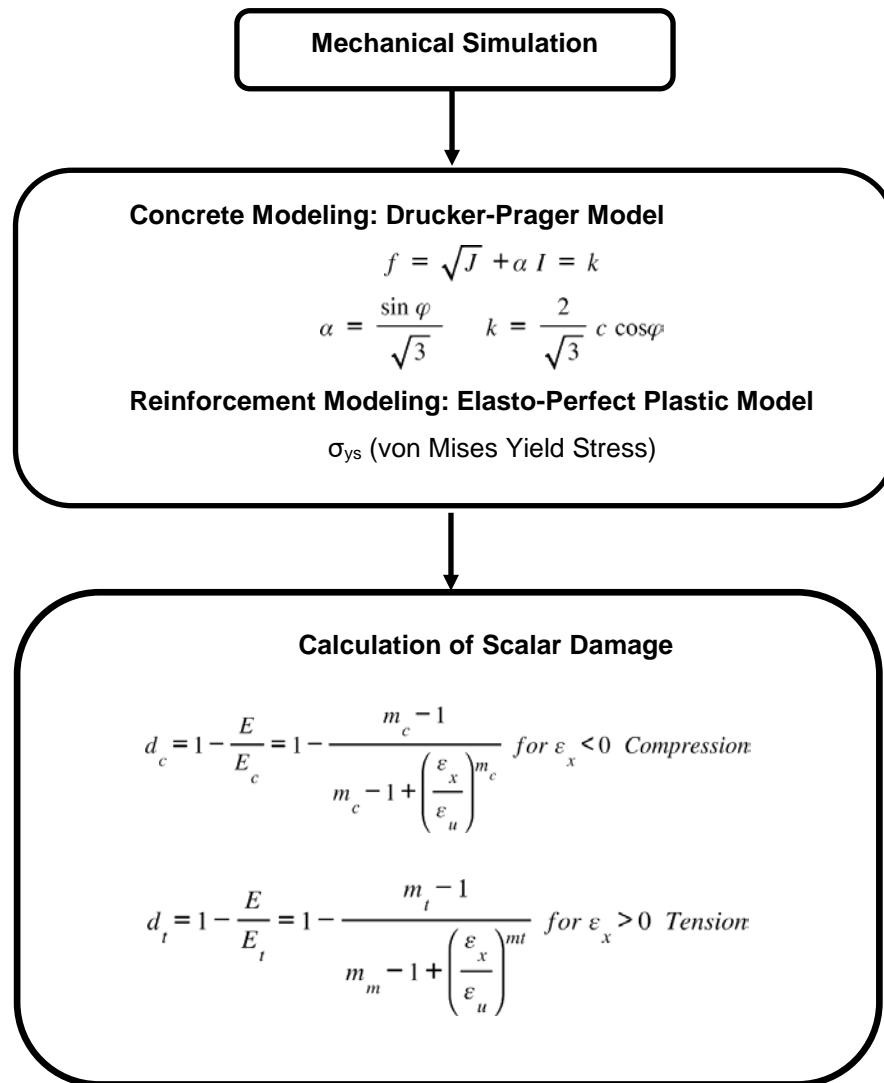


Figure 14. Flow chart for the simulation of mechanical damage in RC beams.

3.3. COMSOL Simulation of Mechanical Behavior

3.3.1 Load-deflection curves and Reinforcement Axial Strain

A comparison between the numerical simulation and ACI [23]/experimental results for load-deflection curve is shown in Fig. 15. COMSOL solution has predicted a cracking load at about 7.25 kN which match well the ACI [23] and the average experimental cracking load which were found to be about 7 and 7.5 kN, respectively. This result indicated that the proposed numerical model can predict the cracking load with about 3.5 % error. As the model is assuming full bond between the reinforcement and the concrete, it can be noticed from Fig. 15 that the COMSOL solution tends to provide more stiffened behavior similar to ACI calculation [23]. However, the COMOSL predicted an ultimate load with 94 kN compared to 95 kN achieved in the experimental flexural tests with 1 % error. The COMSOL model showed similar ability to predict the axial strain for the reinforcement steel and from Fig. 16, it can be noticed that the COMSOL maximum strain in tensile reinforcement was found to be 3500 μm at the maximum mid-span deflection of about 7.5 mm these results match well with the experimental results. The accuracy of these results were compared with other constitutive models for concrete such as the concrete damage-plasticity (CDP) model which have been recently investigated by Abdulsamee et al. [25]. Using CDP model ABAQUS package, Abdulsamee et al. [25] have reported an 4 % and 1 % error in estimating the crack and ultimate loads in RC beams, respectively. These results match well with elastic- damage model used in this study. Others such as Mohammed et al. [26] reported up to 7 % error in predicting the ultimate load when using models based on the classical orthotropic smeared crack formulation and crack band model [26].

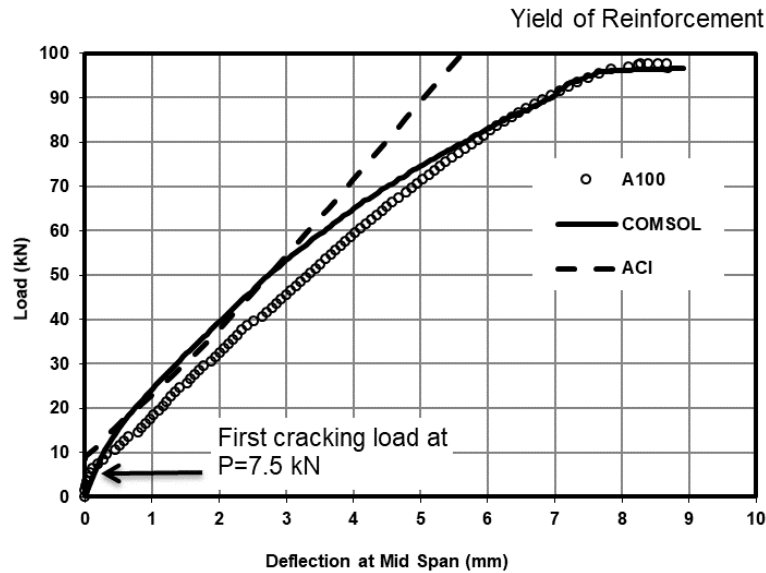


Figure 15. Comparison between Numerical Simulation ACI/ Experimental Results for load- deflection curve.

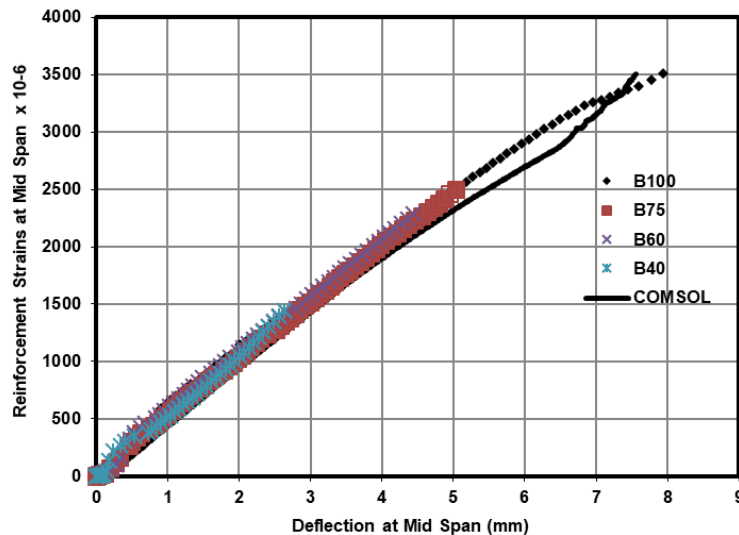


Figure 16. Comparison between Numerical Simulation ACI/ Experimental Results for Reinforcement Axial Strain.

3.3.2 Normal Stress S_x

To verify the ability of the COMSOL model to simulate the mechanical behavior of the RC beams, two-dimensional stress and strain results were plotted. Fig. 17 demonstrates the normal stress distribution (S_x) along the RC beam subjected to 90 % of ultimate flexural loading. As expected, at this level of flexural loading which approached the failure load of the beam, the maximum compressive stress was about 50 MPa and the tensile stress in the reinforcement was about 560 MPa which means that the reinforcement reached its yielding state. More details could be observed in Fig. 18, where the normal stress distribution (S_x) along the cross section of the RC beam is presented, and it can be noted that the compressive zone is fixed at 60 mm from the top of the RC beam.

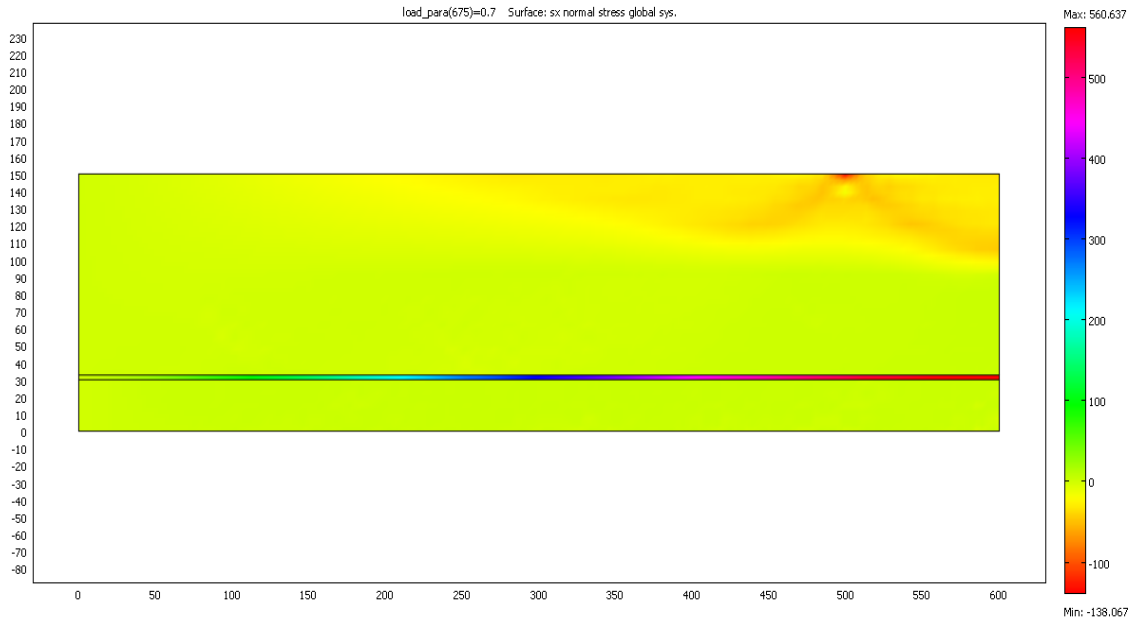


Figure 17. Normal Stress (S_x) for B90.

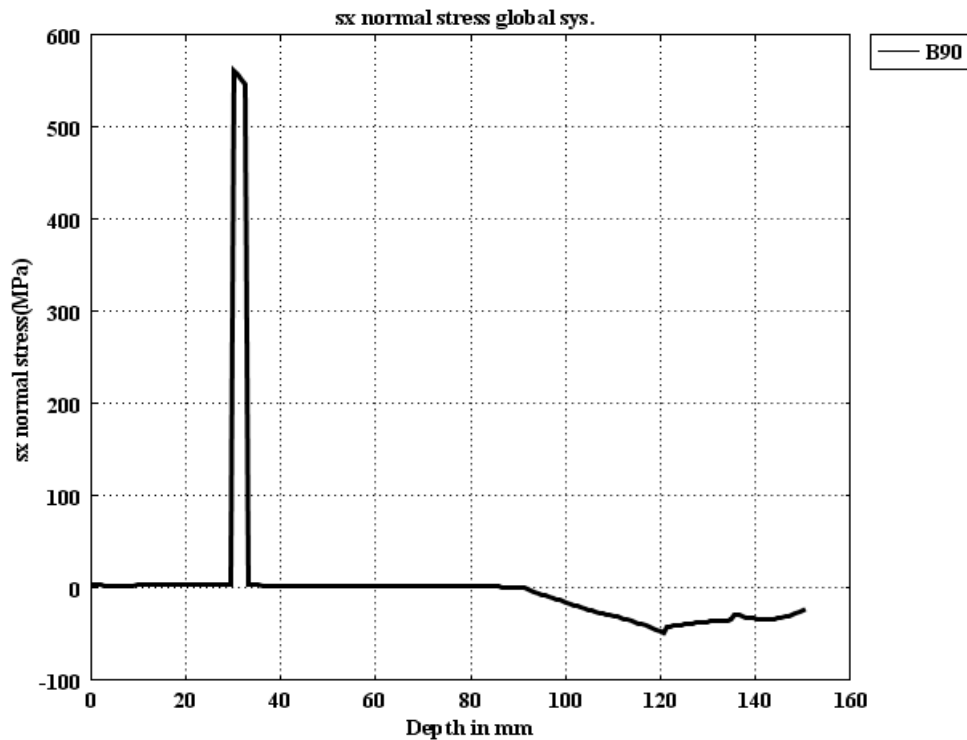


Figure 18. Normal Stress (S_x) Distribution at Constant Moment Zone ($x = 550$ mm from Support for B90).

3.3.3 Normal Strain ϵ_x

Two-dimensional simulation using the COMSOL model was conducted for normal strain (ϵ_x) and the results were plotted as in Fig. 19 & 20. When the RC beam loaded up to 90 % of its flexural loading, the normal strain in the compressive zone in the concrete approached a value of 3.5×10^{-3} as shown in Fig. 19 and 20, which is very close to the ultimate concrete values suggested by ACI. The normal strain in the reinforcement increases as more flexural load applied on the RC beam and reached a value of 3×10^{-3} which matches well with the experimental results for the normal strain in the reinforcement at 90 % of flexural loading which was about 3.5×10^{-3} as shown in Fig. 11. The accuracy of the prediction for the strains using the scalar model was reported by Stéphanie et al. [27] where they concluded that the scalar damage model provides accurate prediction for the structural behavior in concrete elements when failure is mainly due to uniaxial extension.

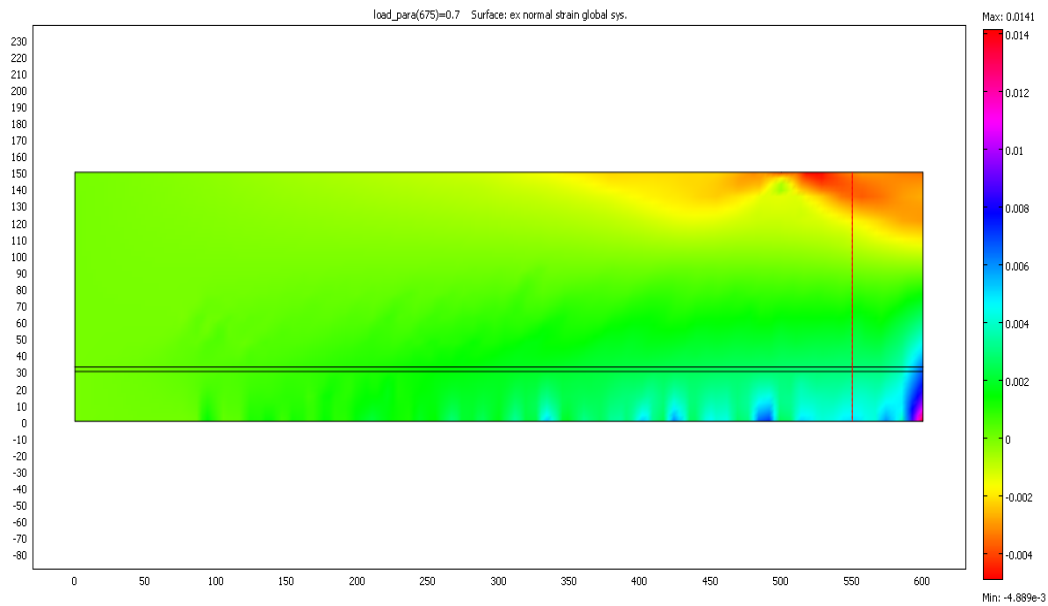


Figure 19. Normal Strain ϵ_x for B90.

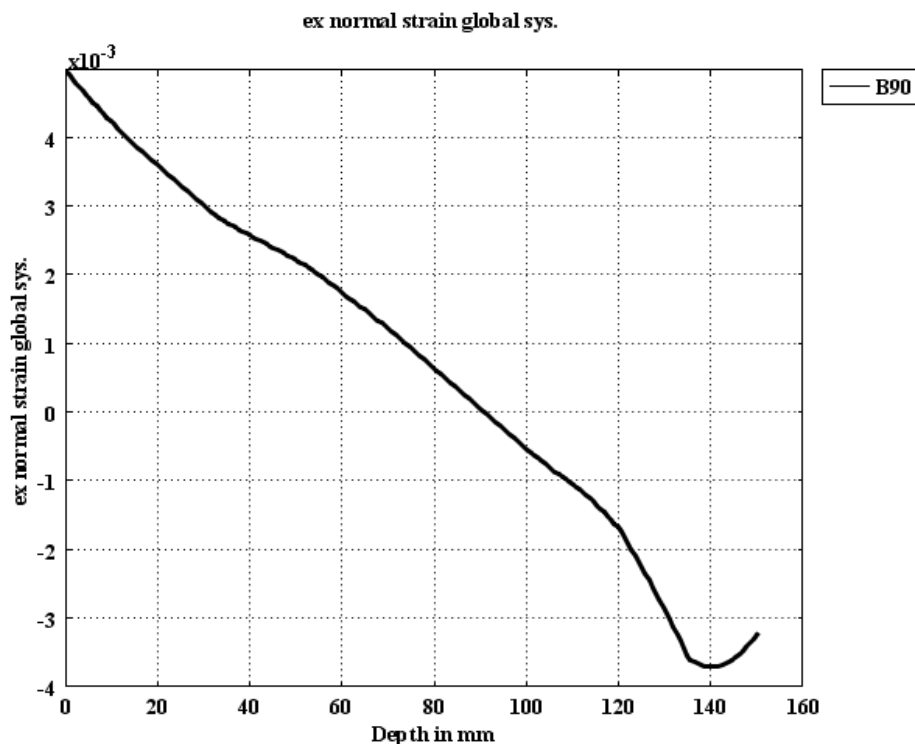


Figure 20. Normal Strain ϵ_x Distribution at Constant Moment Zone ($x = 550$ mm from Support for B90).

3.3.4 COMSOL Simulation of Mechanical Damage

The two-dimensional damage distribution at 90% and failure loading for half of the reinforced concrete beam span ($L/2 = 600$ mm) are shown in Fig. 21 and 22. Fig. 21 shows the damage distribution in the RC beam subjected to 90% of its ultimate flexural loading. From Fig. 21, it can be observed that a significant increase in compressive damage of about 0.90 was developed under point loading and these values decreased to 0.65 at the constant moment zone. When observing the tensile zone, it can be noted that there was more development in tensile damage especially towards the support because of the increase of the tensile stress with the increase of the applied flexural loading and the depth of the damage which increased up to 90 mm from the region between 150 mm from the support up to the mid span of the RC beam. At failure load, the compressive damage increased up to 0.90 with a depth of 50 mm while the damage in the tensile zone was up to 0.90 at a 90 mm depth from the bottom of the RC beam which indicates the development of a full crack in the RC beam at failure as shown in Fig. 22.

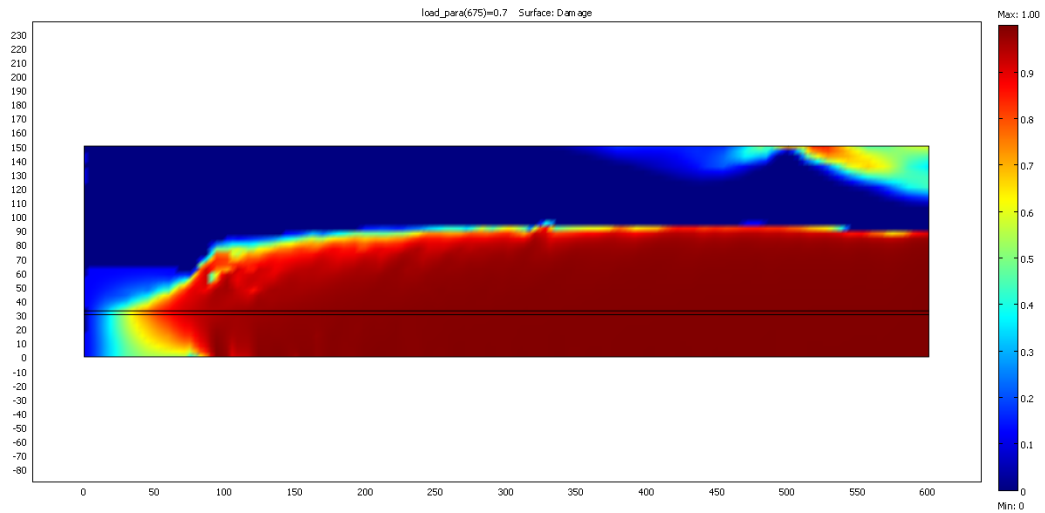


Figure 21. Scalar Damage d at 90 % Loading Beam B90.

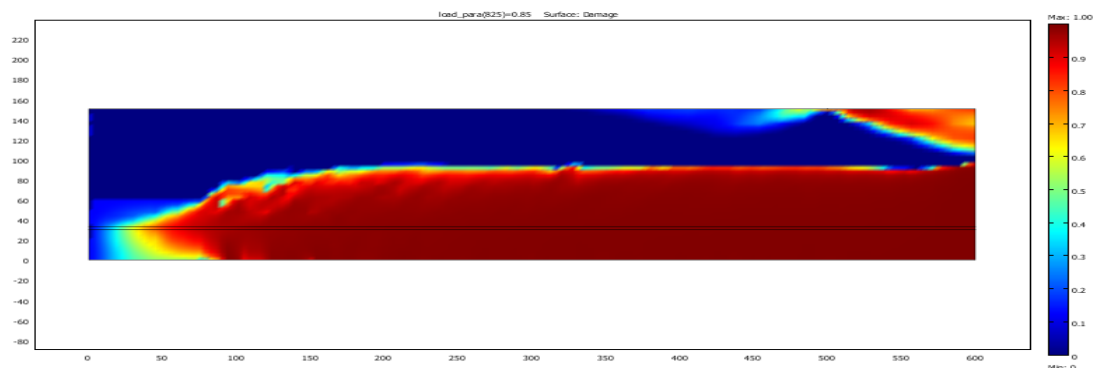


Figure 22. Scalar Damage d at Failure Loading.

More details about the development of mechanical damage along the cross section of the RC beam is shown in Fig. 23, where the scalar damage d was plotted along the cross section at the constant moment zone. From Fig. 23, it can be noted that at the constant moment zone, the tensile damage is more than 0.90 up to a depth of 80 mm for all damaged RC beams due to higher tensile stress in this region. Besides, the compressive damage was initiated when the RC beams were subjected to 75 % of their ultimate flexural loading and this indicates that the compressive damage propagated at lower rates compared with the tensile damage due to the fact that the concrete sustained more compressive stress than tensile damage.

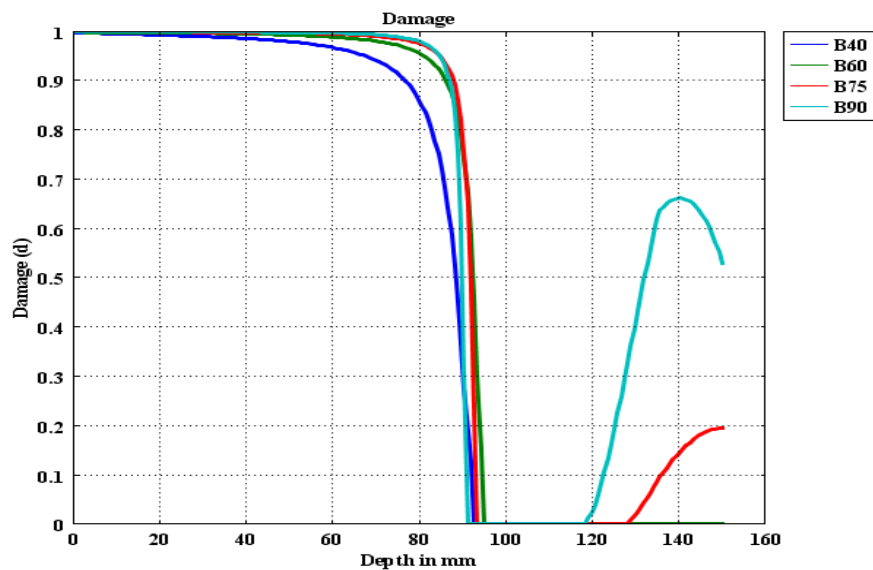


Figure 23. Damage Distribution across the Beam Section at Mid Span (Constant Moment Zone, $x = 550$ mm).

3.3.5 Cracks Development in RC Beams

To verify the COMSOL model with experimental results at crack positions in RC beams with different loading levels, the axial strain (ϵ_x) was plotted at crack positions in the RC beams as shown in Fig. 24 through 27. It was assumed that the crack would propagate when (ϵ_x) is more than the crack normal strain ($\epsilon_{cr} = 1.55 \times 10^{-3}$). Fig. 24 shows the normal strain (ϵ_x) along the position of cracks at distances of 400 and 530 mm from the support in RC beams subjected to 40 % of their ultimate flexural loading. From Fig. 24, it can be noted that the crack depths were found to be about 75 and 85 mm at distances of 400 and 530 mm, respectively, and these results match well with experimental crack maps shown in Fig. 12. The number of cracks and the crack depths increase with the increase of the applied flexural loading. As shown in Fig. 25, the crack depths were increased as the applied flexural loading increased up to 60 % of ultimate loading and were about 82 and 90 mm from crack positions at distance of 360 and 540 mm from the support of the RC beam. One more crack was developed when the RC beams were loaded up to 75 % of their flexural loading as shown in Fig. 26. The crack depths were found to be 50, 85, and 90 mm for cracks at distances of 95, 400 and 520 mm, respectively, from the support of the RC beam. Fig. 27 shows the normal strain (ϵ_x) at RC beams subjected to 90 % flexural loading and it can be noted that the crack depths were 70, 87 and 90 mm for cracks at distances of 100, 400, and 550 mm, respectively.

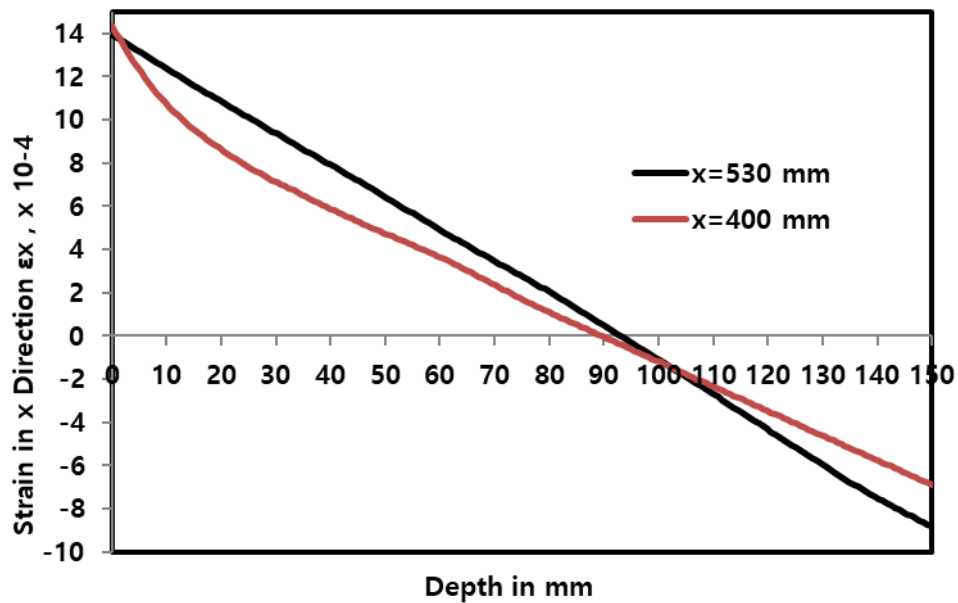


Figure 24. Axial Strain ϵ_x at Cracks in $x = 530$ mm and $x = 400$ mm for B40.

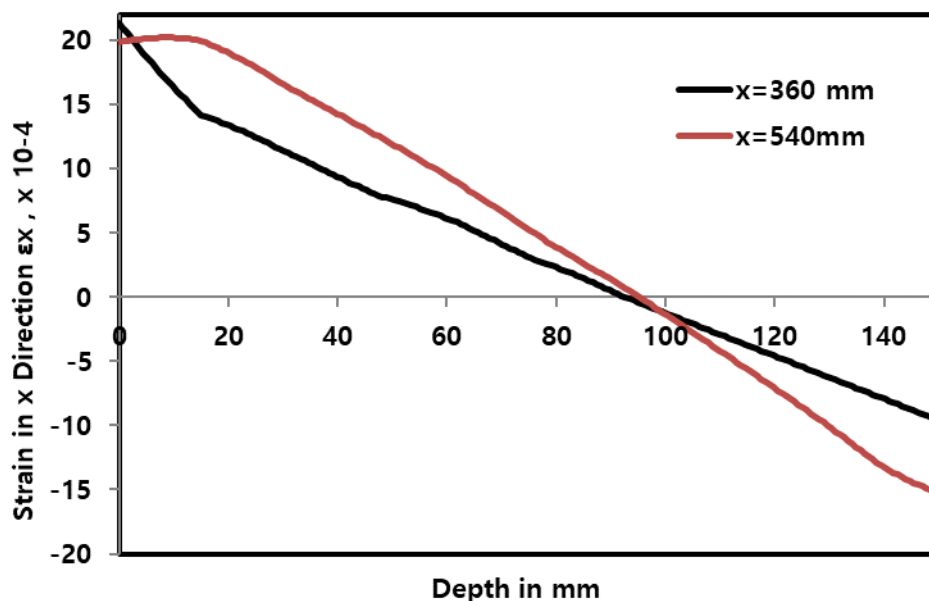


Figure 25. Axial Strain ϵ_x at Cracks in $x = 540$ mm and $x = 360$ mm for B60.

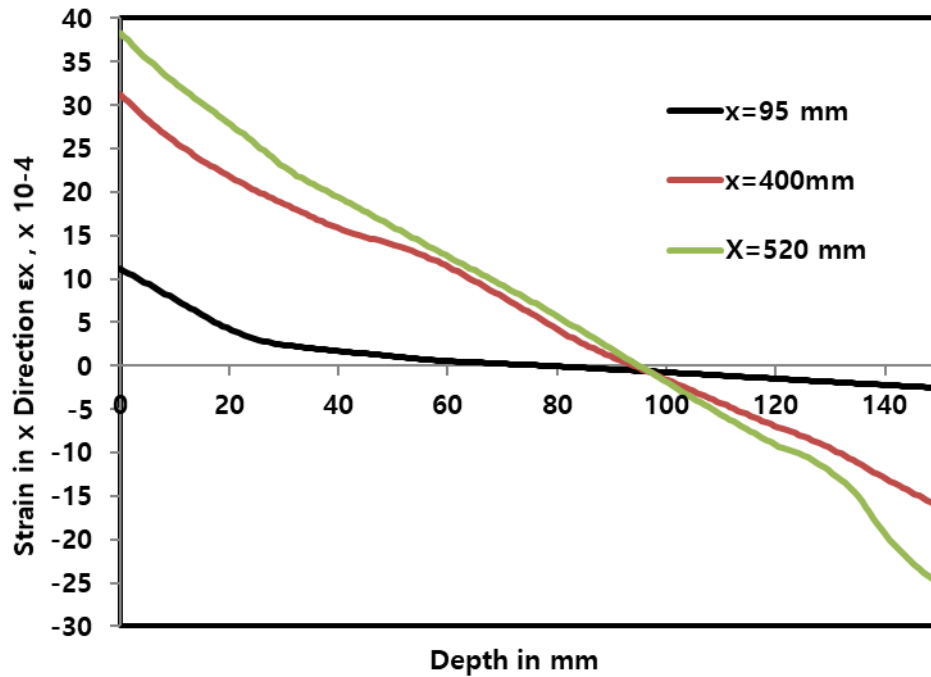


Figure 26. Axial Strain ϵ_x at Cracks in $x = 95, 400$ and 520 mm for B75.

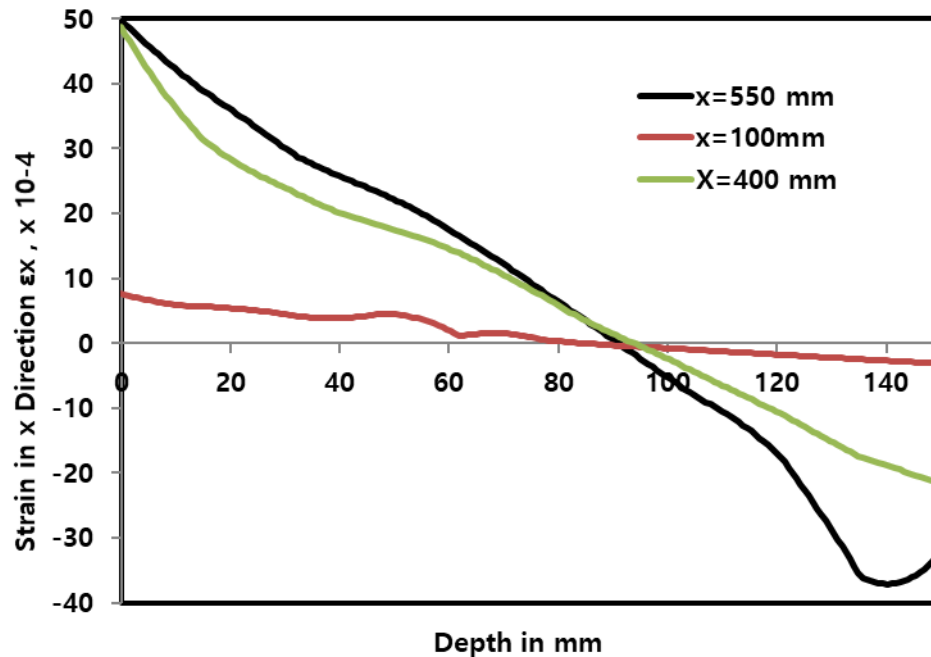


Figure 27. Axial Strain ϵ_x at Cracks in $x = 100, 400$ and 550 mm for B90.

4. Conclusions

1. An experimental and FE analysis study using an elasto-damage model was conducted to simulate the failure of RC beams subjected to 40 %, 60 %, 75%, and 90 % of ultimate flexural loading.
2. The numerical finite element solution using the COMSOL package was calibrated using load-deflection and reinforcement axial strain experimental results. Besides, empirical formulas for crack depth and spacing were used in this study.
3. The proposed elasto-damage model predicted an ultimate load with 94 kN compared to 95 kN achieved in the experimental flexural tests with 1 % error. The proposed model showed similar ability to predict the axial strain for the reinforcement steel as the maximum strain in tensile reinforcement was found to be $3500 \mu\text{m}$ at the maximum mid-span deflection of about 7.5 mm these results match well with the experimental results.

4. The accuracy of these results were compared with other constitutive models for concrete such as elasto-plastic damage model reported in literature in which those models were predicted the ultimate loads in RC beams with 4 % estimated error.

5. The numerical results match well with the proposed scalar damage parameters based on an elasto-damage constitutive model. The outcome of this research paper provides engineers a simplified approach for analyzing the behavior of RC beams subjected to flexural loading using elasto- damage model.

References

1. Kachanov, L. Time of the rupture process under creep conditions. *Izvestiia Akademii Nauk SSSR, Otdelenie Teckhnicheskikh Nauk*. 1958. 8. Pp. 26–31.
2. Mazars, J., Pijaudier-Cabot, G. Continuum damage theory: Application to concrete. *ASCE J Engng Mech*. 1989. 115. Pp. 345–365.
3. Taher S., Baluch, M.H., Al-Gadhib, A.H. Towards a canonical elastoplastic damage model. *Eng. Fract Mech*. 1994. 48 (2). Pp. 151–66.
4. Sun Ming, Xin Dabo, Zou Chaoying. Damage evolution and plasticity development of concrete materials subjected to freeze-thaw during the load process. *Mechanics of Materials*. 2019. 139. Pp. 103–192.
5. Sarikaya, A. and Erkmen, R.E. A plastic-damage model for concrete under compression. *International Journal of Mechanical Sciences*. 2019.150. Pp. 584–593.
6. Javanmardi, M.R., and Mahmoud, R. Maheri. Extended finite element method and anisotropic damage plasticity for modelling crack propagation in concrete. *Finite Elements in Analysis and Design*. 2019. 165. Pp. 1–20.
7. Benin, A.V., Semenov, A.S., Semenov, S.G., Beliaev, M.O., Modestov, V.S. Methods of identification of concrete elastic-plastic-damage models. *Magazine of Civil Engineering*. 2017. 76(8). Pp. 279–297.
8. Bilal, A., George Z.Voyiadjib, Taehyo Parka. Damaged plasticity model for concrete using scalar damage variables with a novel stress decomposition. *International Journal of Solids and Structures*. 2019. <https://doi.org/10.1016/j.ijsolstr.2019.11.023>
9. Roberto, S., Renato, V., Anna, S., Eugenio, O., Alex, H. A scalar damage model with a shear retention factor for the analysis of reinforced concrete structures: theory and validation. *Computers and structures*. 2001. 79 (7). Pp. 737–755.
10. Voyiadjis, G.Z., Taqieddin, Z.N., Kattan, P.I. Theoretical formulation of a coupled elastic-plastic anisotropic damage model for concrete using the strain energy equivalence concept. *Int.J Damage Mech*. 2009. 18 (7). Pp. 603–68.
11. Lubliner, J., Oliver, J., Oller, S., Onate, E. A plastic-damage model for concrete. *International Journal of Solids and Structures*. 1989. 25 (3). Pp. 299–326.
12. Luccioni, B.M., Rougier, V.C. A plastic damage approach for confined concrete. *Computers & Structures*. 2005. 83 (27). Pp. 2238–2256.
13. Salari, M.R., Saeb, S., Willam, K.J., Patchet, S.J., Carrasco, R.C. A coupled elastoplastic damage model for geomaterials. *Comp. Meth. In Applied Mech. and Eng*. 2004. 193 (27). Pp. 2625–2643.
14. Armero, F., Oller, S. A general framework for continuum damage models. I. Infinitesimal plastic damage models in stress space. *International Journal of Solids and Structures*. 2000. 37 (48-50). Pp. 7409–7436.
15. Labadi, Y., Hannachi, N.E. Numerical simulation of brittle damage in concrete. *Strength of Materials*. 2005. 37. Pp. 268–281.
16. Tao, X., Phillips, D.V. A simplified isotropic damage model for concrete under bi-axial stress states. *Cement and Concrete Composites*. 2005. 27 (6). Pp. 716–726.
17. Khan, R.K., Al-Gadhib, A.H., Baluch, M.H. Elasto-damage constitutive model for high strength concrete. *Proc. EURO-C Conf. Computational Modeling of Concrete Structures. Austria*. 1998. Pp. 133–42.
18. Al-Kutti, W.A., Muhammad, K.R., Shazali, M.A., Baluch, M.H. Enhancement in chloride diffusivity due to flexural damage in reinforced concrete beams. *Journal of Materials in Civil Engineering*. 2014. 26 (4). Pp. 658–667.
19. Willam, K., Rhee, I., Beylkin, G. Multiresolution analysis of elastic degradation in eterogeneous materials. *Meccanica*. 2001. 36(1). Pp. 131–150.
20. Júnior, F.S., Venturini, W.S. Damage modelling of reinforced concrete beams. *Advances in Engineering Software*. 2007. 38 (8-9). Pp. 538–546.
21. Khabidolda, O., Bakirov, Zh.B., Nuguzhinov, Zh.S., Vatin, N.I. Determining stress intensity factor in bending reinforced concrete beams. *Bulletin of the Karaganda University-Mathematics*. – 2019. – Volume 92. – Issue 4. – Pp. 139–147.
22. Popovics S. A numerical approach to the complete stress-strain curve of concrete. *Cem Conc Res*. 1973. 3. Pp. 583–99.
23. ACI 224 R1.01 Control of Cracking in Concrete Structures, ACI, 2001.
24. COMSOL Multiphysics. User guide (<http://www.comsol.com>). 2012
25. Abdulsamee, M.H., Yazan B.A., Amin, H.A., George Z.V. The effect of shape memory alloys on the ductility of exterior reinforced concrete beam-column joints using the damage plasticity model. *Engineering Structures*. 2019. 200. Pp.109676.
26. Elghazy, M., El Refai, A., Usama, E., Antonio, N. Experimental results and modelling of corrosion-damaged concrete beams strengthened with externally-bonded composites. *Engineering Structures*. 2018. 172. Pp. 172–186.
27. Stéphanie, F., La Borderie, C., Gilles Pijaudier-Cabot. Isotropic and anisotropic descriptions of damage in concrete structures. *Mechanics of Cohesive-frictional Materials*. 1999. 4(4). Pp. 339–359.

Contacts:

Walid Al-Kutti, wasalem@iau.edu.sa

Tamara Chernykh, chernykh@susu.ru



DOI: 10.34910/MCE.107.15

Improvement of mechanical characteristics of mortar by using of wollastonite

A.V. Kozin^a , R.S. Fediuk^{*a} , S.B. Yarusova^b , P.S. Gordienko^b , V.S. Lesovik^{c,d} ,
M.A. Mosaberpanah^e , Y.H. Mugahed Amran^f , G. Murali^g 

^a Far Eastern Federal University, Vladivostok, Russia

^b Institute of Chemistry, Far Eastern Branch of the Russian Academy of Sciences, Vladivostok, Russia

^c V.G. Shukhov Belgorod State Technological University, Belgorod, Russia

^d Central Research and Design Institute of the Ministry of Construction and Housing and Communal Services of the Russian Federation, Moscow, Russia

^e Cyprus International University, North Cyprus, Turkey

^f Prince Sattam Bin Abdulaziz University, Alkharj, Saudi Arabia

^g SASTRA to be Demeed University, Tamil Nadu, India

*E-mail: roman44@yandex.ru

Keywords: binder, cement, wollastonite, superplasticizer, quartz sand, mortar, strength

Abstract. Geomimetic (nature-like) principles are proposed for optimizing the strength properties of cement mortar, consisting in the integrated effect of wollastonite on the processes of structure formation of cement paste. At the same time, wollastonite (2, 4, 6 and 8 % of the weight of cement) in the composition of mortar has a double function: it serves as a filler (silica-containing component) and microfiber. It was revealed that the incorporation of wollastonite into the mortar mix makes the material easier without sacrificing strength. It has been proven that in the initial period of hardening (3 and 7 days), hydration processes are accelerated, and early strength for all formulations developed with the addition of wollastonite is higher than for the control specimen. An analysis of the structure formation of cement paste from the standpoint of geomimetics reveals the similarity of wollastonite CaSiO_3 to the main minerals of the Portland cement clinker Ca_2SiO_4 (belite) and Ca_3SiO_5 (alite). This similarity leads to the creation of a chemically uniform and, accordingly, strong microstructure. Micro reinforcement of the mortar matrix with wollastonite occurs due to the elongated shape of the microfiber and its good adhesion to the mortar matrix. The results can be used by technologists in the design of mortar mixes for the construction of buildings and structures for various purposes.

1. Introduction

The trend of building materials science is aimed at reducing the amount of cement in building materials, which is achieved by using various mineral raw materials of natural and technogenic origin in binders in the preparation of mortars and mortar mixes [1–3]. To control the structure formation of the cement composite, it is necessary to use new components. At the same time, the prospect of using

Kozin, A.V., Fediuk, R.S., Yarusova, S.B., Gordienko, P.S., Lesovik, V.S., Mosaberpanah, M.A., Mugahed Amran, Y.A., Murali, G. Improvement of mechanical characteristics of mortar by using of wollastonite. Magazine of Civil Engineering. 2021. 107(1). Article No. 10715. DOI: 10.34910/MCE.107.15

© Kozin A.V., Fediuk R.S., Yarusova S.B., Gordienko P.S., Lesovik V.S., Mosaberpanah M.A., Mugahed Amran, Y.H., Murali G., 2021. Published by Peter the Great St. Petersburg Polytechnic University.



This work is licensed under a CC BY-NC 4.0

components increases if they are extracted from industrial waste. Moreover, from the standpoint of geomimetics (the science of creating materials from the standpoint of studying geological processes), the mineral composition of the binder components should be identical to the minerals of Portland cement clinker [4].

The use of such raw materials as various natural pozzolanic ones, as well as industrial waste (fly ash, blast furnace slag, rice husk ash, etc.), has been studied quite well [5–7]. These materials make it possible to obtain high-performance mortars with compressive strength above 100 MPa, flexural strength above 15 MPa and a diverse range of high exploitation characteristics. This allows the creation of materials of construction for a variety of special applications. At the same time, the use of waste of various genesis is a priority in the production of building materials.

A promising material is wollastonite, which is formed as waste from boron production. It was previously proved that wollastonite CaSiO_3 ($\text{Ca}_6\text{Si}_6\text{O}_{18}$) due to the micro-reinforcing effect is able to give mortar enhanced characteristics of strength (tensile, flexural and compression) and impact resistance [8–10]. Natural wollastonite is characterized by an elongated crystal structure, upon cleaving of which grains of needle-shaped form are formed [11–12]. The needle-shaped form of wollastonite grain determines the main direction of its use as a micro-reinforcing filler with the ratio of fiber length to its diameter from 3 : 1 and higher [13–14]. The micro-reinforcing properties of wollastonite ensure non-shrinkage of materials manufactured with its use. In the production of composite building materials and cement-based products, it was found that its physicochemical affinity with cement-containing raw materials, active selective adsorption of binder hydration products, has a significant effect on the rheological parameters of concentrated suspensions and pastes, the formation of structure, strength and deformation properties hardened composites.

According to the law of similarity, as an integral part of geomimetics [15–16], the selection of composite components should be carried out from the point of view of similarity of their characteristics, such as adhesion, for example, coefficient of linear thermal expansion, deformation properties, etc. Mortars with added wollastonite in closed form are very plastic, easy to apply and have good adhesion to various surfaces [17–18]. Wollastonite increases the water retention capacity of closed mixtures, enhances their structure formation and almost completely eliminates shrinkage during hardening. Possessing good adsorption properties, wollastonite eliminates salt formation. Mortar with the addition of wollastonite have good weather- and frost resistance [19–23].

The leading five countries for the production of wollastonite are shown in Fig. 1 [24]. In Russia, mining of wollastonite was previously carried out only in the Altai, but now mining has been discontinued [25]. Therefore, a search for new sources of wollastonite is necessary. Especially promising is the disposal of production waste.

Wollastonite has a wide range of applications: the high-performances cements, paints, varnishes, household and technical ceramics, molding materials, car brake pads, plastics, additives for special glasses against electromagnetic radiation, composite materials against radioactive radiation, in medicine and others. Wollastonite is included in the list of strategic raw materials in the USA, Great Britain and China [8–14]. In this work, it was studied the use of wollastonite in mortar, the resulting waste from boron production.

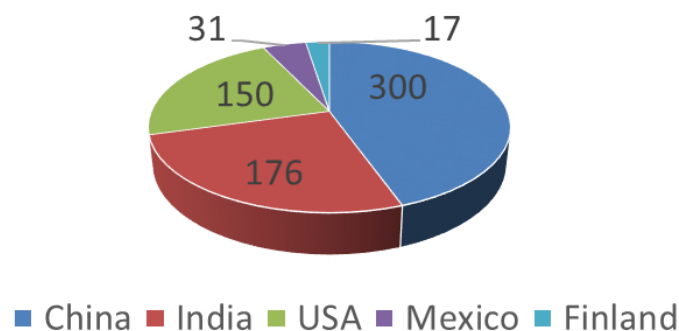


Figure 1. The largest countries for the production of wollastonite (thousands tons).

However, the use of wollastonite as a silica-containing additive that affects the hydration of clinker minerals is not well understood. Thus, the aim of the work is to analyse the effect of wollastonite on the characteristics of mortar, both as a binder filler and reinforcement as microfiber.

To achieve this goal, the following tasks were solved:

- study of the microstructure of wollastonite;

- selection of the optimal amount of wollastonite as a binder filler;
- study of fresh and hardened properties of the modified composite
- comparison of hydration schemes of pure cement and cement-wollastonite binder.

2. Materials and methods

2.1. Materials

Portland cement CEM I 42.5R (Spasskement, Russia) was used as a binder. The chemical and mineralogical composition of the Portland cement is listed in Table 1.

Table 1. Chemical and mineralogical composition of Portland cement CEM I 42.5N.

Chemical composition (%)							Mineralogical composition (%)			
CaO	SiO ₂	Al ₂ O ₃	Fe ₂ O ₃	MgO	SO ₃	Na ₂ O	C ₃ S	C ₂ S	C ₃ A	C ₄ AF
65.94	21.70	5.02	4.20	1.25	0.40	0.78	61.0	16.3	6.2	12.8

The ratio of the content of the main components of the presented cement sample indicates its compliance with the Russian standard GOST 31108-2016 (Table 2). The microstructure of used Portland cement grains is shown in Fig. 2.

Table 2. Physical and mechanical properties of Portland cement used.

Compressive strength, MPa		Setting time, min		Fineness of grinding (passed through a sieve 008), %	Specific surface area, m ² /kg	Standard consistency, %
2 days	28 days	start	end			
14.0–18.8	38.0–47.0	130–240	225–360	88–90	290	22.25–26.25

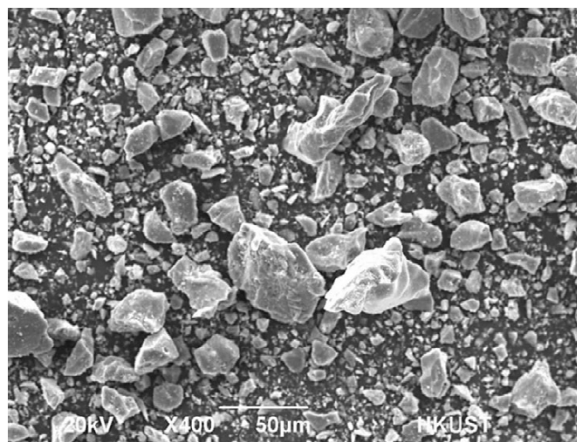


Figure 2. Microstructure of Portland cement grains used.

Wollastonite (calcium silicates CaSiO₃) obtained from the laboratory of protective coatings and marine corrosion of the Institute of Chemistry of the Far Eastern Branch of the Russian Academy of Sciences from borogypsum of technogenic origin (Primorsky Krai) was used as a partial replacement for Portland cement. Among natural minerals, wollastonite is highly resistant to aqueous solutions and solutions of chloride salts; therefore, it was chosen as a filler and aggregate for the developed corrosion-resistant fine-grained concrete. Substitution of Portland cement was carried out in an amount of 2, 4, 6 and 8 % by weight. River sand with medium size modulus (fraction 20–40 mm) was used as a filler (Razdolnoye, Russia). The water absorption of the sand is 5 % and the bulk density is 1,180 kg/m³. Table 3 lists the determination of grain size composition of sand.

For mixing composite binders and making mortars, a water from city pipelines was used that meets the requirements of the Russian standard GOST 23732-2011. The water does not contain harmful impurities and has a pH of 6.52. Its total hardness is 0.41–0.60 mg-eq/l. Mixing water does not contain dissolved acids or alkalis, which hinder the normal setting or hardening of binders, harmful impurities, decomposing plant substances, which can have a harmful effect on mortar hardening. To increase the plasticity of the mortar mixture, S-3 superplasticizer (SP) in liquid form was used (Vladimirsky ZBK, Russia).

Suplasticizer S-3 is an organic synthetic substance based on the condensation product of naphthalenesulfonic acid and formaldehyde with a specific ratio of fractions with different average molecular weight – sodium polynaphthalene methylene sulfonate or methylenebis (naphthalene sulfonate) sodium.

Table 3. Determination of grain size composition of sand.

Content of coarse-grained impurities, %		Residues on sieves, %	Granulometric composition						Fineness module
> 10 mm	> 5 mm		Sieve sizes, mm						
			2.5	1.25	0.63	0.315	0.16	< 0.15	
–	–	partial	2.0	6.5	34.5	41.5	13.0	2.5	2.4
		full	2.0	8.5	43.0	84.5	97.5	100	

2.2. Mix design

Variation of the addition of wollastonite was carried out in the range from 0 to 36 kg per 1 m³ of mortar mix (Table 4).

Table 4. Results of the selection of the optimal composition of CB (per 1 m³ of mortar mix).

Mix ID	CEM I, kg	Wollastonite, kg	Sand, kg	Water, l	SP, l
1	450	-	1500	270	38
2	441	9	1500	270	38
3	432	18	1500	270	38
4	423	27	1500	270	38
5	414	36	1500	270	38

Cement was poured into a bowl of a laboratory planetary mixer (Testing, Germany) and water was added to it, then the mixer was turned on at 140 rpm, stirred for 120 seconds, turn on the sand supply, after another minute switch to accelerated mode, namely 285 rpm min, and interfere with another 150 seconds. Fig. 3 shows the flow chart of specimens preparation.



Figure 3. Flow chart of specimens preparation.

Specimens of 40×40×160 mm in size (for flexural studies) and 100×100 mm (for compression studies) were made. Six specimens of each composition and size were made. The prepared mixture was manually layered in layers in molds and vibrated on a vibrating platform (SMZ-539, Russia) for 5 sec. The mold with the specimens was covered with glass, and after 1 day, the formwork was carried out. The prepared specimens were placed in a normal hardening chamber (model KPU-1M) on pads and stored for 27 days (Fig. 4). The temperature in the chamber is 20 °C, the relative humidity is 95 %. After 28 days from the date of manufacture, the samples were removed from the chamber. For 4 hours, the specimens were in the natural conditions of the room in which they were subsequently tested, i.e., at an air temperature of 20±5 °C and a relative humidity of at least 55 %.



Figure 4. Loading samples into the steam chamber.

2.3. Methods

The density of mortar specimens was determined by dividing the mass of specimens with a size of 100×100 mm by their volume. To determine the average density of concrete, three cubic samples hardened under the same conditions and having the same hardening age (60 days). Saturated samples were weighed to prevent drying cracks. The mass was measured after 2 hours of boiling, followed by immersing the samples in ionized water in an evacuated state for another 24 hours. Then the samples were kept at a temperature of 105 °C for 24 hours to remove water and obtain a dry weight.

The determination of the slump of the mortar mix was carried out using the Abrams cone as follows. First, the cone was filled with a mortar, which was pierced to seal and remove voids, after which it was supplemented with the mix. Then the cone was removed (lifted vertically) and positioned next to the mortar. After that, a plasticity test was carried out.

The compressive and flexural strength of the specimens was tested on a Testing hydraulic press (Germany) according to Russian Standard GOST 310.4-81. The compressive strength of an individual specimen was calculated as the quotient of dividing the value of the breaking load on the working area of the plate. Compressive strength was calculated as the arithmetic mean of the four largest test results on six specimens.

The possibility of using wollastonite, the manufacture of samples and their testing was carried out at the Department of Building Structures and Materials of Far Eastern Federal University by Dr. Kozin. The morphological features of the wollastonite microstructure were studied using a Hitachi S5500 scanning electron microscope (Japan).

Differential thermal studies were carried out on a Shimadzu DTG-60H thermogravimetric analyzer. The programmed heating of the furnaces from 20 to 1500 °C is carried out by an electronic thermal heater at a rate of 20 °C/min. A platinum thermocouple with an accuracy of 5 °C measures the temperature (T), while the signal is recorded on paper with a sweep speed of 2.5 mm/min. The temperature difference (ΔT) between the test substance and the reference, proportional to the thermal effect, is recorded as a DTA curve (sensitivity 500 μV). Simultaneously with the DTA curve, the weight loss curve (TG) and its derivative (DTG) are recorded (sensitivity 500 μV). Sample weight 113 mg. The weighing accuracy was 0.05 mg.

3. Results and Discussion

To understand the mechanisms of the influence of wollastonite additives on the physicomaterial characteristics, the microstructure of wollastonite was considered (Fig. 5). Wollastonite is a white powder with a density. It is characterized by the presence of elongated plate and needle crystals, when cracked which form needle-shaped grains. The elongated structure of microfibers will obviously contribute to the hardening of the cement matrix.

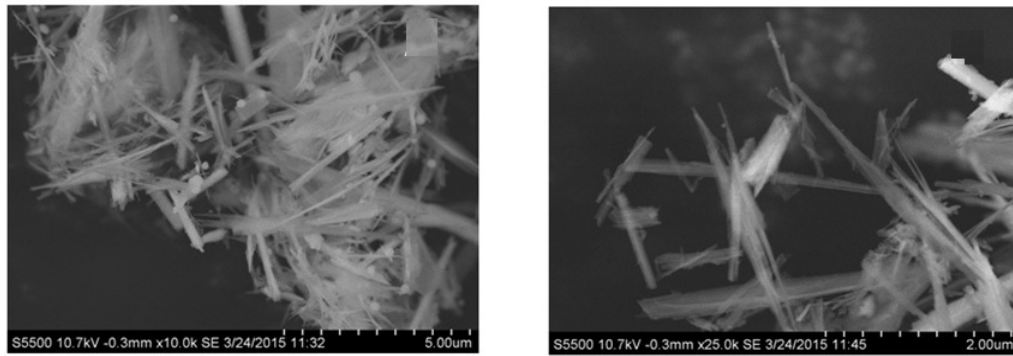


Figure 5. Microstructure of wollastonite fibers.

The slump of the developed mixes is shown in Fig. 6. It is seen that the introduction of wollastonite makes the mix more rigid. This is due to the reinforcing effect of wollastonite. At the same time, even with the maximum introduction of the addition of wollastonite 8 %, the mix shows sufficient fresh characteristics.



Figure 6. Slump test results.

At the same time, a decrease in the density of mortar at the age of 28 days is observed, depending on the increase in the percentage of replacement of Portland cement with wollastonite (Fig. 7), which is explained by a lower density of wollastonite compared to Portland cement. It should be noted that the dependence is not linear, with successive replacement for every 2 %, the density decreases by 25, 29, 40 and 38 kg/m³. This fact, obviously, can be explained by the formation of less dense calcium hydrosilicates due to the secondary hydration of calcium hydroxide released during hydration of alite with wollastonite minerals. Moreover, the positive effect of reducing the specific gravity of the structural material does not adversely affect the strength characteristics. Accordingly, even considering the lower density, there are prerequisites to count on the best characteristics of weather resistance and frost resistance.

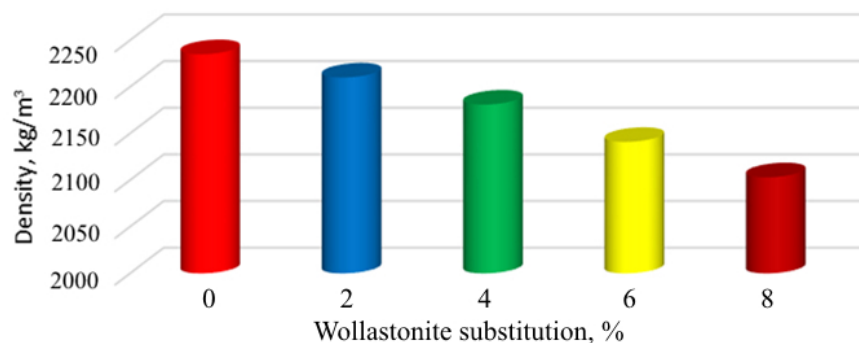


Figure 7. Effect of wollastonite addition on mortar density.

As a result of studying the compressive strength of mortar specimens, it was found that all the studied doses of wollastonite (2–8 %) give an increase in this parameter on days 3, 7 and 28 (Fig. 8).

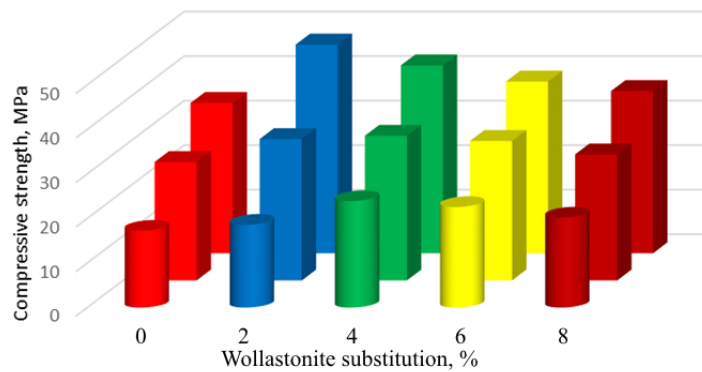


Figure 8. Effect of wollastonite addition on mortar compressive strength (3, 7 and 28 days).

Particles of polymineral cement-wollastonite binder play a complex role in the structure formation of cement paste: firstly, filling the space of micropores, harden the cement paste; secondly, they form active crystallization centers; and, finally, participate in chemical reactions with the formation of new phases, due to which crystalline intergrowths of low-basic CSH are formed with a ratio $C / S \leq 1.0$ instead of primary high-basic hydrosilicates of calcium and portlandite.

In the initial period of hardening (3 and 7 days), acceleration of hydration processes was revealed already in the initial period. The compressive strength on 3 and 7 days for all developed formulations with the addition of wollastonite has a higher value than for the control composition.

At the second stage of hydration of the composite binder, the role of chemical processes is growing, which contribute to a significant modification of the phase composition of the system: the balance shifts from primary crystalline hydrates (calcium hydroxide and highly basic CSH) to more stable secondary fine crystalline hydrates, represented by low-basic calcium hydrosilicates. Obviously, this conclusion is valid until an excessive amount of silica-containing active filler begins to cover the surface of new phases, and this prevents the formation of contacts and the coalescence of crystalline hydrates. Based on the foregoing, we obtain the hypothesis of the presence in the binder of the composition of the optimal volumetric concentration of silica filler, taking into account its pozzolanic activity. As for the inert properties of the filler, its effective dosage will depend directly on the total volume of capillary pore space of the hardening composite necessary for the clogging. The presence of secondary generation hydrosilicates, formed as a result of the binding of CSH with an active silica-containing additive in the composition of cement-wollastonite binder, is noted (Fig. 9).

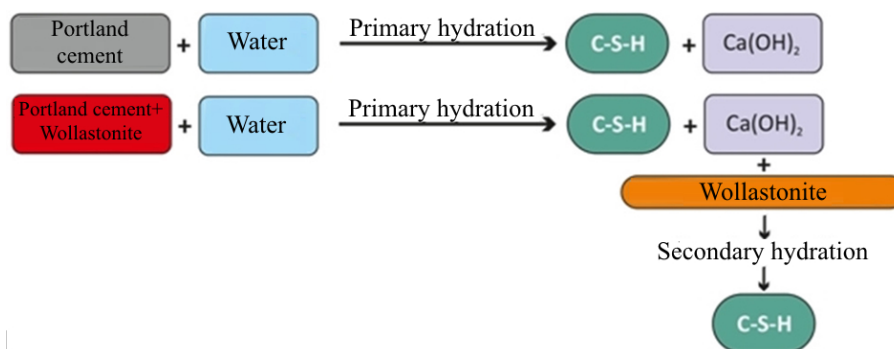


Figure 9. Comparison of hydration schemes of pure cement and cement-wollastonite binder.

The use of the developed composite binder makes it possible to compact the structure of the hardening composite, thus, the controlled structure formation of a rigid matrix with reduced porosity is carried out, and this, accordingly, entails the strengthening of the composite. Clinker grains, as well as individual clinker minerals and wollastonite mineral additives, are large fragments of active solids that form nodes of the spatial lattice of cement paste during hydration. In the course of this, crystalline hydrates, which, depending on the activity of the mineral, are formed simultaneously or sequentially, filling the free space, by partial ingrowth, bind to the already existing framework. Thus, the described processes lead to the formation of a mechanical mixture of crystals, differing in composition, size and shape, and connected by a gel-like mass.

Particles of a polymineral binder play a complex role in the structure formation of a cement-wollastonite paste: firstly, filling the space of micropores, they compact and harden the cement stone; secondly, they form active centers of crystallization; and, finally, they participate in chemical reactions with

the formation of new phases, due to which crystalline intergrowths of low-basic CSH with a C / S ratio of ≤ 1.0 are formed instead of primary highly basic calcium silicate hydrates and portlandite.

The strengthening of the cement composite is confirmed by the results of the DTGA patterns of the specimen, which has 8 % of wollastonite at the age of 3 and 28 days (Fig. 10).

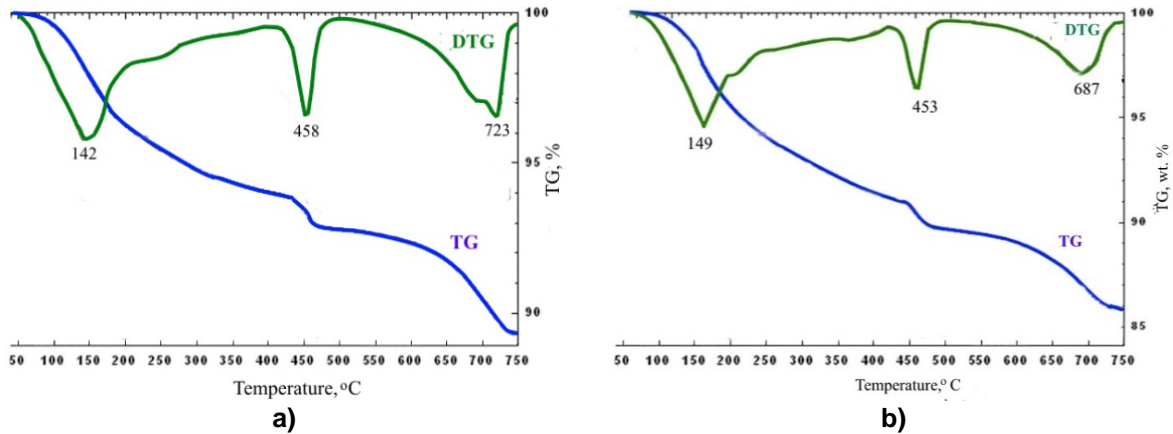


Figure 10. DTA and TG patterns for a specimen with 8 % wollastonite at the age of 3 (a) and 28 (b) days.

As the 3-day specimen, the 28-day one shows a loss of water at all stages with the greatest intensity at temperatures of 70–190 °C. After 200 °C, a decrease in the amount of removed water is also observed. The endothermic peak associated with dehydration below 200 °C is associated with the partial removal of water from ettringite and weakly crystallized and amorphous phases of calcium hydrosilicates. A weak endothermic peak with water loss in the range of 320–410 °C corresponds to the dehydration of weakly crystallized boehmite $\text{AlO}(\text{OH})$ or other products of ettringite decomposition, such as $\text{CaO} \cdot \text{Al}_2\text{O}_3 \cdot 6\text{H}_2\text{O}$ hydrates. A decrease in the amount of $\text{Ca}(\text{OH})_2$, which is an indicator of the pozzolanic reaction, occurs due to its binding during the formation of second generation hydrosilicates.

Analyzing the above from the standpoint of geomimetics, we reveal the similarity of wollastonite CaSiO_3 with the main minerals of the Portland cement clinker Ca_2SiO_4 (belite) and Ca_3SiO_5 (alite), which allows one to obtain a chemically uniform and, accordingly, strong structure of cement paste.

As a result of varying the amount of applied wollastonite additive, it is possible to control the number and dimension of ettringite crystals, which further determines the properties of solutions. In turn, carbonate structures are in close contact with cement stone, which is explained by the occurrence of epitotoxic bonds between the products of cement hydration and wollastonite minerals. Thus, the addition of finely dispersed wollastonite is a chemical factor in increasing the activity of interaction between the active additive and sand. It increases the reactivity of the surface of polymineral additives to cement and therefore activates the hydration process. In the hydration products of composite binders, a redistribution of crystalline phases occurs, both unhydrated clinker minerals (alite, belite, tetracalcium alumoferrite), quartz and calcite, and hydration products (CH – portlandite, $\text{Ca}_6\text{Al}_2(\text{SO}_4)_3(\text{OH})_{12} \cdot 26\text{H}_2\text{O}$ – ettringite).

During the study of the flexural strength of the developed compositions, the microreinforcing effect of wollastonite (Fig. 11, 12), which has an elongated shape and has increased adhesion to cement stone, was confirmed. However, when the optimal dosage of 4 % is exceeded, a decrease in the strength characteristics of mortar specimens at the age of 3, 7 and 28 days is observed.

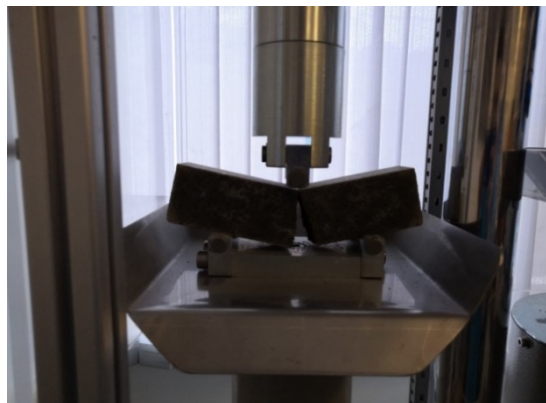


Figure 11. Flexural strength test.

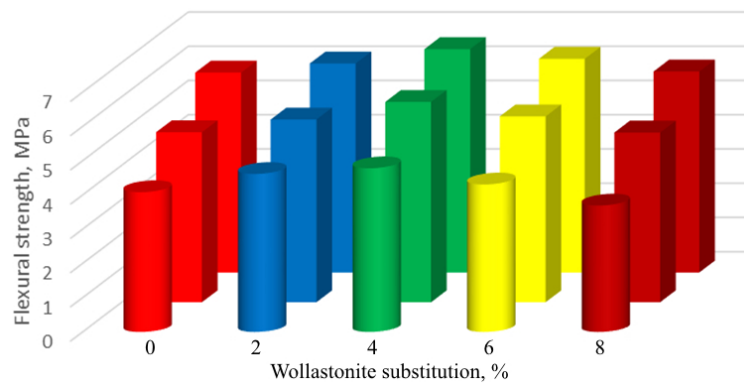


Figure 12. Effect of wollastonite addition on mortar flexural strength (3, 7 and 28 days).

Comparing with articles by other authors who developed mortar with wollastonite [13–17, 24–25], we note that the compressive strength increased by 12–26 %, and the flexural strength – by 24–68 % depending on the dosage of wollastonite.

4. Conclusion

As a result of the study of the physicommechanical characteristics of fine-grained concrete with the replacement of Portland cement with wollastonite in an amount of 2, 4, 6, 8 wt. % revealed the following:

1. Wollastonite in mortar has a dual function: it acts as a filler (silica-containing component) and as microfiber.

2. With an increase in the amount of cement replaced with wollastonite, a decrease in the density of the structural material is observed, which, however, does not adversely affect the strength characteristics. Accordingly, even considering the lower density, there are prerequisites to count on the best characteristics of weather resistance and frost resistance.

3. In the initial period of hardening (days 3 and 7), acceleration of hydration processes was revealed. The compressive strength on days 3 and 7 for all developed compositions with the addition of wollastonite has a higher value than for the control composition.

4. Analyzing the structure formation of cement paste from the standpoint of geomimetics, it was revealed the similarity of wollastonite CaSiO_3 with the main minerals of the Portland cement clinker Ca_2SiO_4 (belite) and Ca_3SiO_5 (alite), which makes it possible to obtain a chemically uniform and, accordingly, strong microstructure.

5. The micro-reinforcing effect of wollastonite is ensured by the elongated shape of the microfiber and its good adhesion to the cement paste.

5. Prospects for further development of the topic

It is advisable to consider interdisciplinary approaches to solving the urgent problems of building materials science, for the development of technologies for the production of mortar with additives of natural calcium silicates for a wide range of building composites, including for the development of the Arctic. The algorithm used in the paper can be used in the development of composite binders to expand the range of production of mortar for various purposes, including to improve a comfortable human environment in architectural and construction design and production of mortar composites.

6. Acknowledgements

This work was financially supported by RFBR grant No. 18-29-24113 “Transdisciplinarity – as a theoretical basis for the rational use of technogenic raw materials for energy-efficient technologies for the production of new generation building composites”.

References

1. Yarusova, S.B., Gordienko, P.S., Kozin, A.V., Zhevtun, I.G., Perfilov, A.V. Influence of synthetic calcium silicates on the strength properties of fine-grained concrete. IOP Conf. Series: Materials Science and Engineering. 2018. No. 347. 012041. DOI: 10.1088/1757-899X/347/1/012041
2. Klyuev, S.V., Khezhev, T.A., Pukharenko, Yu.V., Klyuev, A.V. Fiber Concrete on the basis of composite binder and technogenic raw materials. Materials Science Forum. 2018. No. 931. Pp. 603–607.
3. Sharonova, O.M., Yumashev, V.V., Solovyov, L.A., Anshits, A.G. The fine high-calcium fly ash as the basis of composite cementing material. Magazine of Civil Engineering. 2019. No. 91. Pp. 60–72.

4. Haridharan, M.K., Matheswaran, S., Murali, G., Abid, S.R., Fediuk, R., Mugahed Amran, Y.H., Abdelgader, H.S. Impact response of two-layered grouted aggregate fibrous concrete composite under falling mass impact. *Construction and Building Materials*. 2020. Vol. 263, 120628.
5. Artamonova, O.V., Slavcheva, G.S., Chernyshov, E.M. Effectiveness of Combined Nanoadditives for Cement Systems. *Inorganic Materials*. 2017. 53 (10). Pp. 1105–1110.
6. Fediuk, R. High-strength fibrous concrete of Russian Far East natural materials. *IOP Conference Series: Materials Science and Engineering*. 2016. 116 (1), 012020.
7. Yoo, D.-Y., Banthia, N. Mechanical properties of ultra-high-performance fiber-reinforced concrete: A review. *Cement and Concrete Composites*. 2016. No. 73. Pp. 267–280.
8. Low, N.M.P., Beaudoin, J.J. The effect of wollastonite micro-fibre aspect ratio on reinforcement of Portland cement-based binders. *Cement and Concrete Research*. 1993. No. 23. Pp. 1467–79.
9. Ransinchung, G.D., Kumar, B., Kumar, V. Assessment of water absorption and chloride ion penetration of pavement quality concrete admixed with wollastonite and microsilica. *Construction and Building Materials*. 2009. No. 23. Pp. 1168–1177.
10. Chernysheva, N.V., Lesovik, V.S., Drebezgova, M.Yu. Composite Gypsum Binders with Silica-containing Additives. *IOP Conference Series: Materials Science and Engineering*. 2018. 327 (3), 032015. DOI: 10.1088/1757-899X/327/3/032015
11. Kalla, P., Misra, A., Gupta, R.C., Csetenyi, L., Gahlot, V., Arora, A. Mechanical and durability studies on concrete containing wollastonite–fly ash combination. *Construction and Building Materials*. 2013. No. 40. Pp. 1142–50.
12. Yarusova, S.B., Gordienko, P.S., Sharma, Y.S., Perfilov, A.V., Kozin, A.V. Industrial Waste as Raw Material for Producing Synthetic Wollastonite in Russia. *International Journal of Environmental Science and Development*. 2017. 8 (2).
13. Mathur, R., Misra, A.K., Goel, P. Influence of wollastonite on mechanical properties of concrete. *Journal of Scientific & Industrial Research*. 2007. No. 66. Pp. 1029–1034.
14. Jindal, A., Ransinchung, R.N., Kumar, P. Behavioral study of self-compacting concrete with wollastonite microfiber as part replacement of sand for pavement quality concrete (PQC). *International Journal of Transportation Science and Technology*. 2019. <https://doi.org/10.1016/j.ijtst.2019.06.002>
15. Sharma, S.K. Properties of SCC containing pozzolans, wollastonite micro fiber, and recycled aggregates. *Heliyon*. 2019. 5 (8). e02081. DOI: 10.1016/j.heliyon.2019.e02081
16. Kumar, B.J., Ramujee, K. Mechanical and Durability Characteristics of Wollastonite Based Cement Concrete. *I-manager's Journal on Civil Engineering*. 2017. 7 (1). Pp. 1–7. <https://doi.org/10.26634/jce.7.1.10363>
17. Lukutsova, N.P., Karpikov, E.G., Golovin, S.N. Highly-Dispersed Wollastonite-Based Additive and its Effect on Fine Concrete Strength. *Solid State Phenomena*. 2018. No. 284. Pp. 1005–1011. DOI: 10.4028/www.scientific.net/SSP.284.1005
18. Hossain, S.K.S., Yadav, S., Majumdar, S., Krishnamurthy, S., Pyare, R., Roy, P. A comparative study of physico-mechanical, bioactivity and hemolysis properties of pseudo-wollastonite and wollastonite glass-ceramic synthesized from solid wastes. *Ceramics International*. 2019. DOI: 10.1016/j.ceramint.2019.09.039
19. Fediuk, R.S., Ibragimov, R.A., Lesovik, V.S., Stoyushko, N.Y., Gladkova, N.A., et al. Processing equipment for grinding of building powders. *IOP Conference Series: Materials Science and Engineering*. 2018. 327 (4). 042029.
20. Klyuev, S.V., Khezhev, T.A., Pukhareenko, Yu.V., Klyuev, A.V. Fiber concrete on the basis of composite binder and technogenic raw materials. *Materials Science Forum*. 2018. No. 931. Pp. 603–607.
21. Sorelli, L., Constantinides, G., Ulm, F.J., Toutlemonde, F. The nano-mechanical signature of ultra high performance concrete by statistical nanoindentation techniques. *Cement and Concrete Research*. 2008. 12 (38). Pp. 1447–1456. DOI: 10.1016/j.cemconres.2008.09.002
22. Lukutsova, N.P., Karpikov, E.G., Luginina, I.G., Pykin, A.A., Ustinov, A.G., Pinchukova, I.N. High-performance fine concrete modified with nano-dispersion additive, *International Journal of Applied Engineering Research*. 2014. 9 (22). Pp.16725–16731.
23. Klyuev, S.V., Khezhev, T.A., Pukhareenko, Yu.V., Klyuev, A.V. The fiber-reinforced concrete constructions experimental research. *Materials Science Forum*. 2018. No. 931. Pp. 598–602.
24. Bong, S.H., Nematollahi, B., Xia, M., Nazari, A., Sanjayan, J. Properties of one-part geopolymer incorporating wollastonite as partial replacement of geopolymer precursor.
25. Sedelnikova, M.B., Sharkeev, Yu.P., Komarova, E.G., Khlusov, I.A., Chebodaeva, V.V. Structure and properties of the wollastonite – calcium phosphate coatings deposited on titanium and titanium – niobium alloy using microarc oxidation method. *Surface and Coatings Technology*. 2016.307 (C15). Pp. 1274–1283.

Contacts:

Andrey Kozin, prosek@mail.ru

Roman Fediuk, roman44@yandex.ru

Sofya Yarusova, yarusova@mail.ru

Pavel Gordienko, gordienko@mail.ru

Valeriy Lesovik, naukavs@mail.ru

Mohammad Ali Mosaberpanah, mmosaberpanah@ciu.edu.tr

Yahya Hussein Mugahed Amran, mugahed_amran@hotmail.com

Gunasekaran Murali, murali_220984@yahoo.co.in



ПОЛИТЕХ
Санкт-Петербургский
политехнический университет
Петра Великого

Инженерно-строительный институт
Центр дополнительных профессиональных программ

195251, г. Санкт-Петербург, Политехническая ул., 29,
тел/факс: 552-94-60, www.stroikursi.spbstu.ru,
stroikursi@mail.ru

Приглашает специалистов проектных и строительных организаций,
не имеющих базового профильного высшего образования
на курсы профессиональной переподготовки (от 500 часов)
по направлению «Строительство» по программам:

П-01 «Промышленное и гражданское строительство»

Программа включает учебные разделы:

- Основы строительного дела
- Инженерное оборудование зданий и сооружений
- Технология и контроль качества строительства
- Основы проектирования зданий и сооружений
- Автоматизация проектных работ с использованием AutoCAD
- Автоматизация сметного дела в строительстве
- Управление строительной организацией
- Управление инвестиционно-строительными проектами. Выполнение функций технического заказчика

П-02 «Экономика и управление в строительстве»

Программа включает учебные разделы:

- Основы строительного дела
- Инженерное оборудование зданий и сооружений
- Технология и контроль качества строительства
- Управление инвестиционно-строительными проектами. Выполнение функций технического заказчика и генерального подрядчика
- Управление строительной организацией
- Экономика и ценообразование в строительстве
- Управление строительной организацией
- Организация, управление и планирование в строительстве
- Автоматизация сметного дела в строительстве

П-03 «Инженерные системы зданий и сооружений»

Программа включает учебные разделы:

- Основы механики жидкости и газа
- Инженерное оборудование зданий и сооружений
- Проектирование, монтаж и эксплуатация систем вентиляции и кондиционирования
- Проектирование, монтаж и эксплуатация систем отопления и теплоснабжения
- Проектирование, монтаж и эксплуатация систем водоснабжения и водоотведения
- Автоматизация проектных работ с использованием AutoCAD
- Электроснабжение и электрооборудование объектов

П-04 «Проектирование и конструирование зданий и сооружений»

Программа включает учебные разделы:

- Основы сопротивления материалов и механики стержневых систем
- Проектирование и расчет оснований и фундаментов зданий и сооружений
- Проектирование и расчет железобетонных конструкций
- Проектирование и расчет металлических конструкций
- Проектирование зданий и сооружений с использованием AutoCAD
- Расчет строительных конструкций с использованием SCAD Office

П-05 «Контроль качества строительства»

Программа включает учебные разделы:

- Основы строительного дела
- Инженерное оборудование зданий и сооружений
- Технология и контроль качества строительства
- Проектирование и расчет железобетонных конструкций
- Проектирование и расчет металлических конструкций
- Обследование строительных конструкций зданий и сооружений
- Выполнение функций технического заказчика и генерального подрядчика

По окончании курса слушателю выдается диплом о профессиональной переподготовке
установленного образца, дающий право на ведение профессиональной деятельности

